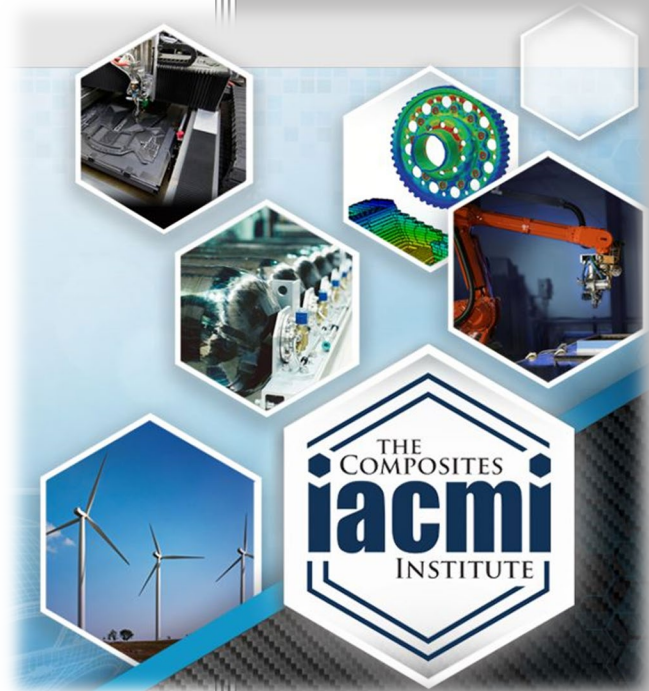


DEVELOPMENT OF NDE/NDT TOOLS FOR HIGH-VOLUME & HIGH-SPEED INSPECTION OF CFRP STRUCTURES IN AUTOMOTIVE MANUFACTURING

Author: Dr. Oleksii Karpenko
Date: 09/06/2021



**Final Technical Report
PA16-0349-3.13-01**

**Approved for Public Release.
Distribution is Unlimited.**



THE
COMPOSITES
INSTITUTE

U.S. DEPARTMENT OF
ENERGY

DOCUMENT AVAILABILITY

Reports produced after January 1, 1996, are generally available free via US Department of Energy (DOE) SciTech Connect.

Website <http://www.osti.gov/scitech/>

Reports produced before January 1, 1996, may be purchased by members of the public from the following source:

National Technical Information Service
5285 Port Royal Road
Springfield, VA 22161
Telephone 703-605-6000 (1-800-553-6847)
TDD 703-487-4639
Fax 703-605-6900
E-mail info@ntis.gov
Website <http://www.ntis.gov/help/ordermethods.aspx>

Reports are available to DOE employees, DOE contractors, Energy Technology Data Exchange representatives, and International Nuclear Information System representatives from the following source:

Office of Scientific and Technical Information PO
Box 62
Oak Ridge, TN 37831
Telephone 865-576-8401
Fax 865-576-5728
E-mail reports@osti.gov
Website <http://www.osti.gov/contact.html>

Disclaimer: "The information, data, or work presented herein was funded in part by an agency of the United States Government. Neither the United States Government nor any agency thereof, nor any of their employees, makes any warranty, express or implied, or assumes any legal liability or responsibility for the accuracy, completeness, or usefulness of any information, apparatus, product, or process disclosed, or represents that its use would not infringe privately owned rights. Reference herein to any specific commercial product, process, or service by trade name, trademark, manufacturer, or otherwise does not necessarily constitute or imply its endorsement, recommendation, or favoring by the United States Government or any agency thereof. The views and opinions of authors expressed herein do not necessarily state or reflect those of the United States Government or any agency thereof."

The information, data, or work presented herein was funded in part by the Office of Energy Efficiency and Renewable Energy (EERE), U.S. Department of Energy, under Award DE-EE0006926

Development of NDE/NDT Tools for High-Volume & High-Speed Inspection of CFRP Structures in Automotive Manufacturing

Principal Investigators: Dr. Oleksii Karpenko, Prof. Lalita Udpa, Prof. Mahmoodul Haq
Co-authors: Ciaron Hamilton, Erik Tarkleson, Prof. Yiming Deng

Organization: Michigan State University / Composite Vehicle Research Center
Address: 3610 Forest Rd, Lansing MI 48910
Phone: 517-402-0634
Email: karpenko@msu.edu

Date Published: (September 2021)

Prepared by:
Institute for Advanced Composites Manufacturing Innovation
Knoxville, TN 37932
Managed by Collaborative Composite Solutions, Inc.
For the
U.S. DEPARTMENT OF ENERGY
Under contract DE- EE0006926

Project Period:
(03/2019 – 07/2021)

Approved For Public Release

TABLE OF CONTENTS

Table of Contents	iv
List of Acronyms	vi
List of Figures	viii
List of Tables	xvii
Executive summary.....	xviii
1. Introduction	1
2. Air Coupled Ultrasonic (ACUT) NDE.....	2
2.1 Optimization of Inspection Parameters for Through-Transmission (TT) and Single-Side Access (SSA) ACUT.....	2
2.1.1. Experiments using Ultrapac II pulser-receiver	4
2.2 Novel ACUT Hardware: Multi-Channel Pulser-Receiver, Piezocomposite and Multi-Element Probes	16
2.2.1 Evaluation of multi-channel pulser-receiver at Sonotec facility.....	17
2.2.2. Piezoceramic and piezocomposite ACUT probes for optimal sensing.....	19
2.2.3. Experimental TT-ACUT C-scans using CF200, CF300 and CF400 probes	22
2.2.4. Comparisons of TT-ACUT C-Scans with Projection X-Ray Radiography.....	23
2.3 High-Speed Multi-Channel ACUT Gantry System at CVRC.....	26
2.3.1. Hardware integration and software development	26
2.3.2. Validation of high-speed ACUT gantry system: 1-channel data acquisition in TT mode	31
2.3.3. Image processing algorithm for quantitative estimation of damage size.....	33
2.3.4. Design and optimization of TT-ACUT array probes.....	35
2.3.5. Validation of high-speed ACUT gantry system: 4-channel data acquisition in TT mode	54
2.3.6. Design and development of SSA-ACUT probes	65
2.3.7. Validation of high-speed ACUT gantry system: 1-channel data acquisition in SSA mode	66
3. Electromagnetic (EM) NDE.....	68
3.1. Hardware for Rapid Eddy Current and Capacitive NDE of CFRP Parts	68
3.1.1. Experimental setup from Phase I	68
3.1.2. Experimental setup for Phase II.....	69
3.2. Eddy Current Testing (ECT).....	71
3.2.1. Modeling of coil sensors for NDE of CFRP and GFRP composites	71
3.2.2. FE simulations: ABS and STDR coil sensors, dielectric FRP	75
3.2.3. Configurations of array coil sensors	80

3.2.4.	Commercial coil array probe	85
3.2.5.	MSU coil array probes for NDE of CFRP composites	86
3.3.	Capacitive Imaging (CI).....	102
3.3.1.	Modeling of capacitive sensors for NDE of FRP composites	102
3.3.2.	Design and optimization of capacitive array probes.....	109
3.3.3.	MSU capacitor array probes for NDE of FRP composites	115
3.4.	Dual-Mode Imaging (Inductive + Capacitive).....	126
3.4.1.	Dual-mode sensing technique for NDE of FRP.....	126
3.4.2.	Array implementation of dual-mode sensing.....	127
3.4.3.	MSU dual-mode probe for NDE of FRP composites	128
4.	Robotic NDE Platform.....	134
4.1.	Robotic NDE Platform Development	134
4.1.1.	Robotic NDE platform design	134
4.1.2.	Acquisition of robotic manipulators	135
4.1.3.	Installation of robotic workcell at MSU/CVRC	135
4.2.	Robotic NDE Pipeline.....	137
4.2.1.	Part's profile reconstruction using stereovision.....	137
4.2.2.	Automated toolpath generation for NDE sensors	139
4.2.3.	Execution of scan programs and parallel data acquisition.....	141
4.2.4.	3D data rendering and defect detection	142
4.3.	Robotic SSA-ACUT	143
4.3.1.	ACUT hardware and software integration with robotic platform.....	143
4.3.2.	Experimental validation of robotic SSA-ACUT.....	144
5.	Conclusions and Recommendations for Future Work.....	149
6.	Commercialization Plan	149
7.	Academic Impact.....	150
8.	References	150

List of Acronyms

ABS – absolute
ACUT – air coupled ultrasound testing
ADC – analog-to-digital converter
API – application programming interface
A-Scan – acquired signal as a function of time
BNC – Bayonet Neill-Concelman
BPF – band-pass filter
BVP – boundary value problem
CAD – computer aided design
CFRP – carbon fiber reinforced polymer
CI – capacitive imaging
C-Scan – diagnostic image obtained using multiple A-scans
CVRC – Composite Vehicle Research Center
DDS – direct digital synthesis
DIFF – differential
DM – dual-mode
EC – eddy current
ECT – eddy current testing
EM – electromagnetic
EMT – electromagnetic testing
OEM – original equipment manufacturer
ES – electrostatic
EQS – electro quasi-static
FE – finite element
FPGA – field programmable gate array
FRP – fiber reinforced polymer
GFRP – glass fiber reinforced polymer
GUI – graphical user interface
GW – guided waves
HPF – high-pass filter
IM – imaginary part
LPF – low-pass filter
LSD – long single driver
MR - magneto resistive
MSU – Michigan State University
NDE – nondestructive evaluation
NDI – nondestructive inspection
NDT – nondestructive testing
NHTSA – National Highway Traffic Safety Administration
P – pulser
PC – personal computer
PCB – printed circuit board
PCDK – personal computer development kit
PE – pulse-echo
PRF – pulse repetition frequency
R – receiver
RE – real part
RHS – right hand side

ROI – region of interest
RAM – random-access memory
SDD – short double driver
SDK – software development kit
SNR – signal-to-noise ratio
SS – single-side
STDN – single transmitter / differential receiver
T – transmitter
TP – teach pendant
TRL – technology readiness level
TT – through-transmission
TTL – transistor-transistor logic
UT – ultrasonic
w.r.t. – with respect to
e.g. – for example

List of Figures

Figure 1. (a) Experimental setups for single-side and through-transmission inspections of CFRP calibration panel #1 with delaminations in different layers; (b) schematic configuration of probes for through-transmission ACUT; (c) schematic configuration of probes for single-side pitch-catch ACUT.	4
Figure 2. Images of air-coupled probes: (a) Sonoscan CF200 probe; (b) Sonoscan CF300.	5
Figure 3. (a) Configuration of air-coupled probes CF300 for inspection in through-transmission mode at normal incidence ($\theta_c = 0^\circ$), $f = 300$ kHz; (b) CFRP calibration panel #1 and corresponding C-scan of the region with delaminations in different layers. True locations of delaminations and their sizes are marked as dotted squares: top layers – red, midplane – black; bottom layers – white.	6
Figure 4. (a) Configuration of air-coupled probes CF200 for inspection in through-transmission mode at normal incidence ($\theta_c = 0^\circ$), $f = 200$ kHz; (b) CFRP calibration panel #1 and corresponding C-scan of the region with delaminations in different layers. True locations of delaminations and their sizes are marked as dotted squares: top layers – red, midplane – black; bottom layers – white.	7
Figure 5. Photo of CF200 probes scanning calibration panel #1 at in through-transmission mode at $\theta_c = 17^\circ$ and zero offset.	7
Figure 6. (a) Configuration of air-coupled probes CF200 for inspection in through-transmission mode at $\theta_c = 17^\circ$, $f = 200$ kHz; (b) CFRP calibration panel #1 and corresponding C-scan of the region with delaminations in different layers. True locations of delaminations and their sizes are marked as dotted squares: top layers – red, midplane – black; bottom layers – white.	8
Figure 7. Photo of CF200 probes scanning calibration panel #1 at in through-transmission mode at $\theta_c = 12^\circ$ and 25 mm offset between their axes.	8
Figure 8. (a) Configuration of air-coupled probes CF200 for inspection in through-transmission mode at $\theta_c = 12^\circ$, $f = 200$ kHz. Axes of transducers are 25 mm apart. (b) Corresponding C-Scan of CFRP calibration panel #1. True locations of delaminations are shown as dotted squares: top layers – red, midplane – black; bottom layers – white.	9
Figure 9. Scanning of calibration panel 1 in through-transmission mode at $\theta_c = 14^\circ$ and 5 mm offset between the axes of air-coupled probes CF200.	9
Figure 10. (a) Configuration of air-coupled probes CF200 for inspection in through-transmission mode at $\theta_c = 14^\circ$, $f = 200$ kHz. Axes of transducers are 5 mm apart. (b) Corresponding C-Scan of CFRP calibration panel #1. True locations of delaminations are shown as dotted squares: top layers – red, midplane – black; bottom layers – white.	10
Figure 11. Schematic configuration of ACUT probes for excitation and sensing of guided waves in thin plates from single side.	11
Figure 12. Guided waves in a 5 mm thick aluminum plate: (a) analytic dispersion relation; (b) snapshot of two fundamental modes A0 and S0 (excited using a 4-count sinusoidal tone burst at 200 kHz) propagating in the plate simultaneously at 100 μ s after the excitation, FE simulation in Abaqus CAE; (c) deformation of the plate's cross-section due to the A0 mode at 200 kHz; (d) deformation of the plate's cross-section due to the S0 mode at 200 kHz.	11
Figure 13. Excitability of guided waves in a 5 mm thick aluminum plate: (a) schematic configuration of probes for exciting the A0 mode at 200 kHz through the water; (b) schematic configuration of probes for exciting the A0 mode at 200 kHz through the air; (c) coincidence angles for exciting fundamental A0 and S0 modes in the water; (d) coincidence angles for exciting fundamental A0 and S0 modes in the air.	12
Figure 14. Model of a 3D printed fixture for guided wave measurements.	13
Figure 15. Guided wave propagation in the defect-free region of CFRP Calibration panel #1: (a) schematic; (b) A-scan with a time gate.	13
Figure 16. Guided wave propagation in the region with a 0.5 in delamination closer to the bottom surface of the CFRP Calibration panel #1: (a) schematic; (b) A-scan with a time gate.	14
Figure 17. Guided wave propagation in the region with a 1 in delamination closer to the top surface of the CFRP Calibration panel #1: (a) schematic; (b) A-scan with a time gate.	14

Figure 18. Pitch-catch C-scans of the Calibration panel #1 using CF300 probes at $\theta = 8^\circ$ with 25 mm offset between the probes. (a) Schematic of the Calibration panel #1 with 9 delaminations; (b) C-scan from the top side; (c) C-scan from the bottom side.	15
Figure 19. Block-diagram of the ACUT system for high-speed NDE of composite parts.	16
Figure 20. Block-diagram of the high-power 4-channel pulser-receiver module for ACUT.	16
Figure 21. Module for rapid ACUT NDE of composites: (a) photo of the module; (b) characteristics of the hardware.	17
Figure 22. ACUT experimental setup for testing 4-channel pulser-receiver and probes on CFRP samples.	18
Figure 23. Typical excitation signal and resulting A-scan (CF200 probe, $f = 200$ kHz).	18
Figure 24. Wave propagation in through-transmission mode at normal incidence and acquisition of the resulting received signal (A-scan).	19
Figure 25. Design of a typical ACUT transducer.	19
Figure 26. (a) Piezocomposite disk for ACUT transducers; (b) dice & fill technique for manufacturing piezocomposite elements.	20
Figure 27. Actuator transect: (a) mode shape of a regular PZT transducer; (b) mode shape of a piezocomposite transducer. Large displacements are shown in red color, and small displacements are shown in blue color. Color bars are normalized for each plot (courtesy of Sonotec US).	21
Figure 28. Optimal frequencies that maximize intensities of generated and sensed sound pressure.	21
Figure 29. CF400 4-element piezocomposite ACUT probe: (a) photo of the probe with connectors; (b) designs of the actuating elements; (c) FE model showing electronic beam forming process (courtesy of Sonotec US).	22
Figure 30. C-scans of Nomad honeycomb CFRP panel with two delaminations between the top skin and the core. Data was acquired using ACUT probes with three different excitation frequencies (200 kHz, 300 kHz and 400 kHz). Courtesy of Sonotec US.	23
Figure 31. (a) ACUT C-scan of the honeycomb part; (b) X-ray image of the honeycomb part (courtesy of Sonotec US). Region 1 – damaged honeycombs; region 2 – excessive glue between the CFRP skin and honeycomb structure.	24
Figure 32. (a) CFRP sample 1 after low velocity impact; (b) corresponding ACUT C-scan; (c) X-ray image (courtesy of Sonotec US).	25
Figure 33. (a) CFRP sample 2 after low velocity impact; (b) corresponding ACUT C-scan; (c) X-ray image (courtesy of Sonotec US).	25
Figure 34. Ruggedized NDE system and XYZ gantry for inspection of CFRP parts.	27
Figure 35. Block-diagram of the pulser-receiver: testing of signal generator and power amplifier (red box).	27
Figure 36. Developed graphical user interface for pulser-receiver control.	28
Figure 37. Experimental validation of ACUT power amplifier outputs: (a) identical pulse sequences on all channels; (b) frequency modulated square pulses; (c) pulse trains of different durations; (d) pulse trains with different time offsets.	29
Figure 38. Block-diagram of the pulser-receiver: testing of receiving amplifier and digitizer (red box).	30
Figure 39. Experimental validation of ACUT receiving amplifier and ADC (digitizer).	30
Figure 40. Developed graphical user interface for digitizer control and sensor data display.	31
Figure 41. Gantry set-up for scanning X-brace part: (a) front view; (b) rear view; (c) typical ACUT signal (A-scan), V_{pp} peak-to-peak voltage is measured in order to plot a C-scan.	31
Figure 42. Immersion UT inspection of X-brace part: (a) scanned region; (b) immersion C-scan (pulse-echo mode, $f = 5$ MHz, spherically focused transducer, $\varnothing 12$ mm).	32
Figure 43. ACUT inspection of X-brace part: (a) high-resolution, low speed C-scan; (b) ~ 2 mm resolution, high-speed C-scan.	32
Figure 44. Post processing of water immersion UT C-scan: image segmentation and defect sizing.	33
Figure 45. Post processing of ACUT C-scan: image segmentation and defect sizing.	34
Figure 46. Comparisons of delamination sizes obtained by post-processing of water immersion UT and	

ACUT C-scans.	34
Figure 47. CF-200 ACUT transducers arranged as a (a) linear array; (b) staggered array.	36
Figure 48. Experimental setup for ACUT transducer characterization.	36
Figure 49. CF-200 transducer characterization: (a) acoustic beam shape in the air; (b) directivity pattern.	37
Figure 50. Linear ACUT array: (a) top view; (b) side view.	37
Figure 51. Strategies for reducing beam interference: (a) crosstalk between the probes; (b) spatial separation of the probes; (c) beam focusing & clipping; (d) time-gated excitation & sensing.	38
Figure 52. Experimental study I. Setup for measuring crosstalk between three CF-300 ACUT probes. ...	39
Figure 53. Experimental study I. Crosstalk between CF-300 probes in the air, typical A-scan. Receiver is aligned with Transmitter 1 (T1).	39
Figure 54. Experimental study I. C-scans, activated transmitters: (a) Transmitter 1 (T1); (b) Transmitter 2 (T2); (c) Transmitter 3 (T3); (d) all transmitters at the same time (T1, T2, T3).	40
Figure 55. Experimental study I. Time-gated excitation: (a) pulse trains with time delays [0, 120, 240] μ s; (b) typical A-scan acquired when the receiver is aligned with Transmitter 3 (T3).	40
Figure 56. Experimental study I. Time-gated excitation with different time delays between consecutive transmitters/channels: (a) 20 μ s; (b) 40 μ s; (c) 60 μ s; (d) 80 μ s; (e) 100 μ s and (f) 120 μ s.	41
Figure 57. Experimental study II. Setup for measuring crosstalk between four CF-200 ACUT probes. ...	42
Figure 58. Experimental study II. C-scans: (a) One transmitter at a time (T1, T2, T3 and T4); (b) multiple transmitters simultaneously ([T1,T2], [T1,T2,T3] and [T1,T2,T3,T4]).	42
Figure 59. Experimental study II. Time-gated excitation with different time delays between consecutive transmitters/channels: (a) 200 μ s; (b) 300 μ s.	43
Figure 60. Experimental study III. 3D printed focusing cones attached to CF-200 transducers: (a) 5 mm apertures; (b) 12 mm apertures for transmitters and 5 mm aperture for receiver.	44
Figure 61. Experimental study III. Beam clipping using acoustic cones. C-scans: (a) transmitters and receiver have 5 mm apertures, [T1,T2,T3,T4] excited simultaneously; (b) transmitters and receiver have 12 mm apertures, [T1,T2,T3,T4] excited simultaneously; (c) transmitters have 12 mm aperture and receiver has 5 mm aperture, [T1,T2,T3,T4] excited simultaneously; (d) transmitter T1 has 12 mm aperture and receiver has 5 mm aperture, only T1 is excited.	44
Figure 62. Experimental study IV. Evaluation of surface reflections: (a) setup with linear array of CF-200 transducers; (b) formation of 2 nd order reflections.	45
Figure 63. Experimental study IV. Typical A-scan with multiple surface reflections (receiver probe is aligned with T1, only T1 is activated).	46
Figure 64. Experimental study IV. Surface reflections and time-gated excitation of a linear array of 4 CF-200 transmitters (T1-T2-T3-T4 sequence).	46
Figure 65. Experimental study IV. Typical A-scan: linear array configuration, time-gated excitation with 1500 μ s delays between consecutive channels (T1-T2-T3-T4 sequence). Receiver is aligned with Transmitter 4 (T4).	47
Figure 66. Experimental Study V. Snapshots of wave propagation in calibration panel #1. Transmitter 1 (T1) is activated: (a) time lapse/C-scan arrangement: left to right & top to bottom; (b) gif video.	48
Figure 67. Experimental Study V. Snapshots of wave propagation in calibration panel #1. ACUT probes CF-200. Two transmitters T1 and T2 are activated simultaneously. Time lapse/C-scan arrangement: (a) left to right & top to bottom; (b) gif video.	49
Figure 68. Experimental Study V. Snapshots of wave propagation in calibration panel #1. ACUT probes CF-200. Three transmitters T1, T2 and T3 are activated simultaneously. Time lapse/C-scan arrangement: (a) left to right & top to bottom; (b) gif video.	50
Figure 69. Experimental Study V. Snapshots of wave propagation in calibration panel #1. ACUT probes CF-200. Four transmitters T1, T2, T3 and T4 are activated simultaneously. Time lapse/C-scan arrangement: (a) left to right & top to bottom; (b) gif video.	51
Figure 70. Experimental Study V. Snapshots of wave propagation in calibration panel #1. Time-gated excitation, T1-T2-T3-T4 sequence, time delay of 300 μ s between the consecutive channels. Time lapse/C-	

scan arrangement: (a) left to right & top to bottom; (b) gif video.	52
Figure 71. Snapshots of wave propagation in calibration panel #1. Time-gated excitation, T1-T2-T3-T4 sequence, time delay of 1000 μ s between the consecutive channels. Time lapse/C-scan arrangement: (a) left to right & top to bottom; (b) gif video.	53
Figure 72. Experimental Study VI. Configurations of transducers (top pair): (a) no cones; (b) long 12-mm OD cones; (c) short 12-mm OD cones with foam rubber.	53
Figure 73. Experimental Study VI. Suppression of surface reflections: (a) no cones; (b) long PLA cones, 12-mm OD; (c) short PLA cones with foam rubber, 12-mm OD.	54
Figure 74. Upgraded XYZ gantry system at CVRC for high-speed ACUT NDE.	54
Figure 75. Schematic block-diagram of the gantry system for ACUT NDE.	55
Figure 76. The 4-element (4-channel) linear ACUT array: (a) sensor pitch and orientation with respect to scan path; (b) array data acquisition in through-transmission mode.	55
Figure 77. Linear array fixtures: (a) CAD model, front view; (b) 3D printed parts with installed CF-200 ACUT sensors and focusing cones.	56
Figure 78. Scan settings for validation of 4-channel linear ACUT array: (a) 2.5-mm scan increment for testing the uniformity of channels; (b) 10-mm scan increment for parallel data acquisition and high-speed inspection.	56
Figure 79. Video of multi-channel ACUT inspection of X-brace #3 using gantry system.	57
Figure 80. Typical A-scans acquired in the multi-channel ACUT inspection of X-braces.	57
Figure 81. Multi-channel ACUT C-scan of X-brace #3. Scan increment: 2.5 mm.	58
Figure 82. Multi-channel ACUT C-scan of X-brace #3. Scan increment: 10 mm.	58
Figure 83. ACUT C-scans of X-brace #3: (a) single channel (CH1), scan increment 2.5 mm, scan time ~6 min; (b) merged multi-channel (CH1+CH2+CH3+CH4), scan increment 10 mm, scan time ~1 min 30 s.	59
Figure 84. Multi-channel ACUT C-scan of X-brace #1. Scan increment: 2.5 mm.	60
Figure 85. Multi-channel ACUT C-scan of X-brace #1. Scan increment: 10 mm.	60
Figure 86. ACUT C-scans of X-brace #1: (a) single channel (CH1), scan increment 2.5 mm, scan time ~6 min; (b) merged multi-channel (CH1+CH2+CH3+CH4), scan increment 10 mm, scan time ~1 min 30 s.	61
Figure 87. CFRP panel #3: (a) front view; (b) rear view.	62
Figure 88. Implementation of floating time-gates for feature extraction from A-scans.	62
Figure 89. Multi-channel ACUT C-scan of CFRP panel #3 acquired in TT mode at 200 kHz.	63
Figure 90. Manufacturing flaws in CFRP panel #3: (a) photograph of the ROI, region with defects is marked with white paint, possibly dry fibers and/or agglomeration of air bubbles; (b) corresponding ACUT C-scan showing acoustic reflections.	63
Figure 91. Setup for qualitative comparison of ACUT probes: (a) piezoceramic probes CF-200; (b) piezocomposite probes CFC-230.	64
Figure 92. Comparison of piezoceramic and piezocomposite ACUT probes. Typical A-scans: (a) CF-200; (b) CFC-230.	64
Figure 93. Comparison of piezoceramic and piezocomposite ACUT probes. C-scans of central section of X-brace #3: (a) CF-200; (b) CFC-230.	65
Figure 94. Single-side access ACUT of calibration panel #1: (a) locations of delaminations and scanned region; (b) configuration of the SSA-ACUT probe.	66
Figure 95. Experimental validation of single-side access ACUT on Calibration panel #1: (a) CF-200 probes, $f = 200$ kHz, vertical probe orientation; (b) CF-300 probes, $f = 300$ kHz, horizontal probe orientation. (T - transmitter, R - receiver).	66
Figure 96. Experimental validation of single-side access ACUT on X-brace 3 (CF-200 probes, $f = 200$ kHz, horizontal probe orientation).	67
Figure 97. (a) Experimental setup for eddy current NDE and capacitive sensing from Phase I; (b) corresponding block-diagram.	68
Figure 98. Ectane 2 system for EM NDE.	69

Figure 99. Cable for interfacing array probes with the ECA connector: (a) stripped wire ends; (b) pins attached to ends; (c) pins and μ BNC connection with PCB.	70
Figure 100. Cross section, electrical and mechanical properties of the cable.	70
Figure 101. Schematics of the single transmitter / differential receiver (STD R) coil sensor.	72
Figure 102. The electric field around the absolute coil (xz -cross section).	75
Figure 103. C-scan image over a hole with 2 mm radius (dashed line). Coil sensor with OD = 10 mm, ID = 9 mm, height = 1 mm, liftoff = 1 mm, N=25.	76
Figure 104. Three configurations of a single coil sensor.	76
Figure 105. Sensitivity for different coil geometries (absolute sensor) as a function of: (a) defect radius, (b) dielectric constant of test material, (c) sensor lift-off (defect radius of 2 mm) and (d) defect depth under the surface (defect radius of 5 mm).	77
Figure 106. Three configurations of a single transmitter/differential receiver sensor.	78
Figure 107. Sensitivity for different geometries of single transmitter/differential receiver coil as a function of: (a) defect radius, (b) dielectric constant of test material, (c) sensor lift-off (defect radius of 2 mm) and (d) defect depth under the surface (defect radius of 5 mm).	79
Figure 108. Electrical connection of coils of the array probe to MUX.	80
Figure 109. Absolute (ABS) sensing topology: 1) corresponding electric circuit for one channel; 2) switching sequence for measurements in time gates T1-T3.	81
Figure 110. Differential (DIFF) sensing topology: 1) corresponding electric circuit for one channel; 2) switching sequence for measurements in time gates T1-T3.	81
Figure 111. Reflection (T/R) sensing topology: electric circuit for one channel measurement using a single transmitter coil L1 and a single receiver coil L2.	82
Figure 112. SSD sensing topology: switching sequence for measurements in time gates T1-T3.	83
Figure 113. SSD axial topology: switching sequence for measurements in time gates T1-T3.	83
Figure 114. SSD transverse topology: switching sequence for measurements in time gates T1-T3.	83
Figure 115. LSD axial topology: switching sequence for measurements in time gates T1-T3.	84
Figure 116. LSD transverse topology: switching sequence for measurements in time gates T1-T3.	84
Figure 117. Commercial flex coil for detecting surface barking cracks in metallic parts; (b) manual scanning of CFRP sample with calibrated defects.	85
Figure 118. CFRP sample #7 with calibrated notches: (a) top view; (b) bottom view; (c) schematic drawing; (d) eddy current C-scan of top row of defects acquired at 1 MHz using Eddify flex probe with LSD topology.	86
Figure 119. MSU array probes: (a) E-1a array (10 mm coils) and E-1b array (5 mm coils); (b) two-layer coil design, windings printed on top and bottom sides of PCB.	87
Figure 120. (a) Impedance of one coil from E-1a probe and its equivalent RLC circuit (shown as graph insert); (b) typical dependence of coil impedance $ Z $ on excitation frequency.	87
Figure 121. MSU experimental set-up for initial testing of E-1a and E-1b array probes: (a) gantry, lock-in amplifiers, ADC and probe fixtures; (b) schematic block-diagram.	88
Figure 122. Experimental validation of E-1b probe in DIFF mode using lock-in amplifier: (a) CFRP sample #7 with defects that simulate fiber damage; (b) locations and sizes of machined defects; (c) corresponding C-scan acquired with a 5-mm coil at $f = 10$ MHz.	89
Figure 123. Experimental validation of E-1b probe in T/R SSD mode using Ectane 2: (a) experimental setup; (b) activated coils (T – transmitter, R – receivers).	89
Figure 124. Calibration CFRP sample #7 with fiber damage: (a) top view; (b) bottom view; (c) schematics and locations of introduced notches.	90
Figure 125. Validation of the E-1b probe connected through EET. C-scans of CFRP test sample from the bottom side (SSD topology, left receiver R, $f = 5$ MHz): (a) real part; (b) imaginary part; and (c) absolute value.	90
Figure 126. Validation of the E-1b probe connected through EET. C-scans of CFRP test sample from the top side (SSD topology, left receiver R, $f = 5$ MHz): (a) real part; (b) imaginary part; and (c) absolute value.	90

Figure 127. Array probe E-1c with driver coils on top of receiver coils: (a) top view; (b) bottom view. ...	91
Figure 128. Experimental validation of E-1c probe in T/R SSD mode.	91
Figure 129. Electrical connections between the EET connector and E-1c array probe.	92
Figure 130. Two row 8-channel coil array operating in the T/R mode. Transmitters on the top, receiver on the bottom. C-scans of CFRP test sample from the top side, $f = 2.5$ MHz, CH1.	92
Figure 131. Two row 8-channel coil array operating in the T/R mode. Transmitters on the top, receiver on the bottom. C-scans of CFRP test sample from the bottom side (absolute value, 2.5 MHz): (a) CH1; (b) CH2; (c) CH3; (d) CH4; (e) CH5; (f) CH6; (g) CH7; and (h) CH8.....	93
Figure 132. Prototype E-2a: (a) PCB design of a staggered 18-CH array; (b) PCB design of a single channel with solder pads for μ BNC connector; (c) fabricated array interfaced to the Ectane.	94
Figure 133. Interfacing array probe E-2a with the Ectane: (a) the ECA connector on the Ectane's front panel; (b) cable with the E-2a probe attached; (c) E-2a probe scanning a CFRP sample.....	95
Figure 134. Fast scanning of the CFRP calibration sample #7 using the array probe E2-a ($t = 10.7$ s). Note that the figure includes a gif video.....	96
Figure 135. C-scan of the calibration CFRP sample using the array probe E-2a, bottom side, $f = 2$ MHz in the ABS mode: (a) locations of defects; (b) real part (RE); (c) imaginary part (IM).	97
Figure 136. C-scan of the calibration CFRP sample using the array probe E-2a, bottom side, $f = 2$ MHz in the ABS mode: (a) locations of defects; (b) x-gradient of the real part (RE); (c) x-gradient of the imaginary part (IM).....	97
Figure 137. C-scan of the calibration CFRP sample using the array probe E-2a, bottom side, $f = 2$ MHz in the ABS mode: (a) locations of defects; (b) y-gradient of the real part (RE); (c) y-gradient of the imaginary part (IM).....	97
Figure 138. C-scan of the calibration CFRP sample using the array probe E-2a, top side, $f = 1.3$ MHz in the ABS mode: (a) locations of defects; (b) the imaginary part; (c) y-gradient of the imaginary part.	98
Figure 139. C-scan of the calibration CFRP sample using the sensor array E-2a, bottom side, $f = 2$ MHz in the SDD axial mode: (a) locations of defects; (b) the real part; (c) the imaginary part.	98
Figure 140. C-scan of the calibration CFRP sample using the sensor array E-2a, bottom side, $f = 2$ MHz in the SDD axial mode: (a) locations of defects; (b) x-gradient of the real part; (c) x-gradient of the imaginary part.	99
Figure 141. C-scan of the calibration CFRP sample using the sensor array E-2a, bottom side, $f = 2$ MHz in the SDD axial mode: (a) locations of defects; (b) y-gradient of the real part; (c) y-gradient of the imaginary part.	99
Figure 142. C-scan of the calibration CFRP sample using the sensor array E-2a, top side, $f = 1.3$ MHz in the SDD axial mode: (a) locations of defects; (b) the imaginary part; (c) y-gradient of the imaginary part.	99
Figure 143. C-scan of the sample #7 using the E-2a array, bottom side, $f = 2$ MHz in the SDD transverse mode: (a) locations of defects; (b) the real part (RE); (c) the imaginary part (IM).	100
Figure 144. C-scan of the CFRP sample #7 using the E-2a array, bottom side, $f = 2$ MHz in the SDD transverse mode: (a) locations of defects; (b) x-gradient of RE; (c) x-gradient of IM.	100
Figure 145. C-scan of the calibration CFRP sample using the E-2a array, bottom side, $f = 2$ MHz in the SDD transverse mode: (a) locations of defects; (b) y-gradient of RE; (c) y-gradient of IM.	100
Figure 146. C-scan of the calibration CFRP sample using the sensor array E-2a, top side, $f = 1.3$ MHz in the SDD transverse mode: (a) locations of defects; (b) the imaginary part; (c) y-gradient of the imaginary part.	101
Figure 147. Drawings of array probes E-2b (4-layer) and E-2c (2-layer): (a) PCB top view; (b) multi-layer PCB structure.....	101
Figure 148. Designs of capacitive sensors for NDE of FRP composites: (a) capacitor with rectangular electrodes; (b) capacitor with disk electrodes.	102
Figure 149. Schematics of the open-plate capacitor and surface breaking defect.	103
Figure 150. The electric field in the sample under the open plate capacitor (xz -cross section).....	105
Figure 151. Capacitive C-scan over a hole with 2 mm radius (dashed line). Capacitive sensor with $W=L=10$	

mm, lift-off=1 mm, gap=1 mm.	106
Figure 152. Five configurations of open-plate capacitors used in FE simulations.	107
Figure 153. Sensitivity for different capacitor geometries as a function of: (a) defect radius, (b) dielectric constant of test material, (c) sensor lift-off (defect radius of 2 mm) and (d) defect depth under the surface (defect radius of 5 mm).	107
Figure 154. Electric field in the transect of the test specimen generated by: (a) capacitor with narrow gap; (b) capacitor with wide gap.	108
Figure 155. Open-plate capacitive probes: (a) absolute topology; and (b) differential topology.	109
Figure 156. Schematics of linear capacitor arrays with rectangular electrodes: (a) wide electrodes; (b) narrow electrodes.	109
Figure 157. A typical design of a 2-electrode open-plate capacitor: (a) schematic geometry; (b) electric field distribution in the air (xz-plane) at 10 kHz.	110
Figure 158. The 2-electrode open-plate capacitor after splitting the electrodes along the y-axis: (a) schematic geometry; (b) electric field distribution in the air (xz-plane).	110
Figure 159. The 2-electrode open-plate capacitor after splitting the electrodes along the x-axis: (a) schematic geometry; (b) electric field distribution in the air (xz-plane); (c) electric field distribution in the air right under the electrodes (xy-plane).	111
Figure 160. The differential open-plate capacitor with 3 split electrodes: (a) schematic geometry; (b) electric field distribution in the air (xz-plane); (c) electric field distribution in the air right under the electrodes (xy-plane).	111
Figure 161. A linear 10-electrode capacitor array with differential (DIFF) measurement topology: (a) schematic geometry; (b) multi-channel switching sequence. Note that the figure contains a gif video.	112
Figure 162. A linear 10-electrode capacitor array with absolute (ABS) measurement topology: (a) schematic geometry; (b) multi-channel switching sequence. Note that the figure contains a gif video.	112
Figure 163. A circular 2-electrode capacitor with wide outer ring electrode: (a) schematic geometry; (b) electric field distribution in the air (xz-plane).	113
Figure 164. A circular 2-electrode capacitor with narrow outer ring electrode: (a) schematic geometry; (b) electric field distribution in the air (xz-plane).	113
Figure 165. An 18-channel circular capacitor array with common ground electrode: (a) schematic geometry; (b) mesh for finite element simulations.	114
Figure 166. FEM result, electric field distribution in the air: (a) cut xy-plane; (b) z-component of the electric field.	114
Figure 167. FEM result, electric field distribution in the air: (a) cut xz-plane; (b) z-component of the electric field.	114
Figure 168. Capacitive probe C-1a: (a) schematics; (b) driving circuit (EET connector)	115
Figure 169. Region of the CFRP test panel #7 scanned using capacitor probe C-1a.	116
Figure 170. Capacitor probe C-1a. C-scans of selected region on CFRP test panel: (a) CH1 real part; (b) CH1 imaginary part; (c) CH2 real part; (d) CH2 imaginary part; (e) CH3 real part; (f) CH3 imaginary part. CH1 and CH2 are ABS, CH3 is DIFF.	116
Figure 171. Differential capacitive probes: (a) electric circuit showing connection to the EET connector; (b) C-1b; and (c) C-1c.	117
Figure 172. Impedance of C1 open-plate capacitor in C-1b probe: (a) magnitude; (b) phase.	117
Figure 173. Calibration panel #1: (a) top view; (b) bottom view.	118
Figure 174. Baseline UT imaging of Calibration Panel #1: (a) locations of delaminations; (b) ultrasonic pulse-echo C-scan at 2.25 MHz.	118
Figure 175. Capacitive C-scans of Calibration Panel #1 acquired using C-1b probe at 9.9 MHz: (a) real part; (b) imaginary part.	119
Figure 176. Capacitive C-scans of Calibration Panel #1 acquired using C-1b probe at 6.4 MHz: (a) real part; (b) imaginary part.	119
Figure 177. Capacitive C-scan of mid-size (0.5 in × 0.5 in) delamination “M” close to the top surface of Calibration Panel #1. Data acquired using probe C-1b at 1 MHz.	120

Figure 178. Capacitive C-scan of a small (0.25 in \times 0.25 in) delamination “S” close to the top surface of Calibration Panel #1. Data acquired using probe C-1b at 1 MHz.	120
Figure 179. Capacitive C-scan of the CFRP panel with fiber damage (notches). Data acquired using probe C-1c at 1 MHz: (a) scanned region; (b) real part; (c) imaginary part.	120
Figure 180. Capacitive imaging of interlaminar delaminations using capacitor prototype C-2a: (a) capacitive sensor with 10 mm \times 5 mm rectangular electrodes; (b) CFRP laminate; (c) processed C-scan image ($f = 5$ MHz) highlighting delaminations and variations of dielectric constant of the laminate.	121
Figure 181. Capacitive imaging of interlaminar delaminations using capacitor prototype C-2b: (a) capacitive sensor with ring electrodes (inner radius of 4 mm, outer radius of 7 mm, ring width of 2 mm); (b) CFRP laminate; (c) processed C-scan image ($f = 5$ MHz) highlighting delaminations and variations of dielectric constant of the laminate.	121
Figure 182. Array probe C-3a with rectangular capacitor electrodes: (a) PCB design; (b) fabricated prototype.	122
Figure 183. Experimental setup for calibration of C-3a capacitive array: (a) XYZ gantry with Ectane system; (b) array probe on top of GFRP sample with defects.	122
Figure 184. Validation of array probe C-3a on GFRP calibration sample: (a) locations of defects; (b) C-scan at $f = 1$ MHz (real part, normalized); (c) C-scan at $f = 5$ MHz (real part, normalized).	123
Figure 185. Validation of array probe C-3a on CFRP calibration sample #1: (a) locations of delaminations and scanned region; (b) direction of line scans; (c) typical C-scan (real part), $f = 1$ MHz.	124
Figure 186. Array probe C-3b with circ capacitor electrodes: (a) PCB design; (b) fabricated prototype.	124
Figure 187. Validation of array probe C-3b on GFRP calibration sample: (a) locations of defects; (b) C-scan at $f = 1$ MHz (real part, raw image); (c) C-scan at $f = 1$ MHz (real part, processed image).	125
Figure 188. Validation of array probe C-3b on CFRP calibration sample #1: (a) locations of delaminations and scanned region; (b) direction of line scans; (c) typical C-scan (real part).	125
Figure 189. A dual-mode sensor comprising of two rectangular coils and one open-plate capacitor.	126
Figure 190. A circuit diagram for: (a) driving the rectangular coil sensors in the absolute mode; (b) driving the open-plate capacitor formed by two rectangular coils as electrodes.	127
Figure 191. Dual-mode array sensor prototype: an array of rectangular coil/capacitive sensors that supports two orthogonal orientations of measurements. (An example of the open-plate capacitor with $+45^\circ$ orientation is highlighted as a green box. The open-plate capacitor with -45° orientation is highlighted as a red box).	127
Figure 192. Possible PCB design of the array dual-mode sensor prototype.	128
Figure 193. Design of the dual-mode (hybrid) probe D-1a (single transmitter / dual receiver).	128
Figure 194. Fabricated 2-layer PCB with multiple sensors: (a) side view; (b) front view.	129
Figure 195. Fabricated hybrid probe D-1a: (a) PCB; (b) fixture and connectors.	129
Figure 196. Validation of hybrid probe D-1a on CFRP calibration sample #7: (a) locations of notches; (b) receiver coil 1 (real part); (c) receiver coil 1 (imaginary part), $f = 2$ MHz.	130
Figure 197. Validation of hybrid probe D-1a on CFRP calibration sample #7: (a) locations of notches; (b) receiver coil 2 (real part); (c) receiver coil 2 (imaginary part), $f = 2$ MHz.	130
Figure 198. Validation of hybrid probe D-1a on CFRP calibration sample #7: (a) locations of notches; (b) difference [coil 1 – coil 2] (real part); (c) difference [coil 1 – coil 2] (imaginary part), $f = 2$ MHz. Images normalized by peak magnitude.	131
Figure 199. Validation of hybrid probe D-1a on CFRP calibration sample #1: (a) locations of delaminations and scanned region; (b) probe scanning the sample; (c) typical C-scan acquired in differential STDR mode, $f = 2$ MHz. Only positive lobes are shown.	131
Figure 200. Validation of hybrid probe D-1a on CFRP calibration sample #1: (a) locations of delaminations and scanned region; (b) probe scanning the sample; (c) typical C-scan in CI mode, $f = 1$ MHz.	132
Figure 201. Validation of hybrid probe D-1a on GFRP calibration sample #8: (a) locations of delaminations and scanned region; (b) probe scanning the sample; (c) typical C-scan in T/R mode, $f = 2$ MHz, real part.	133
Figure 202. Validation of hybrid probe D-1a on CFRP calibration sample #8: (a) locations of delaminations	

and scanned region; (b) probe scanning the sample; (c) typical C-scan in CI mode, $f = 1$ MHz, real part.	133
Figure 203. Design of the robotic platform for high-speed ACUT and EM NDE.	134
Figure 204. Robotic platform assembly and testing at Slipstream Technologies' warehouse (Chattanooga, TN).	135
Figure 205. Installation of robotic workcell at MSU/CVRC (Lansing, MI).	136
Figure 206. Part profile reconstruction using a stereo camera: (a) Intel RealSense D435i stereo depth camera; (b) principle of a stereo camera setup (adapted from S. Grehel <i>et al</i> , 2015 https://www.researchgate.net/publication/303307354); (c) reconstruction using multiple view angles.	138
Figure 207. Stereo cameras taking depth images of the test part at a few locations on the imaginary sphere that encapsulates the test part.	138
Figure 208. Reconstructed 3D face profile using stereo camera rotation at a fixed position: (a) front view; (b) view from the left; (c) view from the right.	139
Figure 209. Stereo images of CFRP parts: (a) composite panel #3; (b) composite panel #4 (front splitter section) with embedded honeycomb structure.	139
Figure 210. Zig-zag scan pattern formed by rays intersecting a 3D test object: (a) front view; (b) top view.	140
Figure 211. A demo showing a zig-zag tool path for composite panel #4. Simulation executed in RoboDK for Fanuc Arc Mate 120iB robot with no sensor attached to the end effector.	140
Figure 212. MSU software (based on RoboDK API and OpenTK) for scan simulation and real-time data display: main window – 3D point cloud showing scan positions of the lead end effector; insert – dual robots scanning the X-brace.	141
Figure 213. MSU 3D visualization of simulated scan data: (a) point cloud; (b) gif demo of the colored surface obtained after Delaunay triangulation.	142
Figure 214. Robotic workcell configured for 1 channel single-side access ACUT NDE: (a) rack stand with ACUT hardware; (b) ACUT fixturing, probes and the preamplifier attached to the robot flange.	143
Figure 215. Aluminum fixtures for ACUT probes with adjustable angle of attack.	143
Figure 216. Robotic SSA-ACUT scan of calibration panel #1 (1 channel).	144
Figure 217. Robotic SSA-ACUT results on CFRP panel #1: (a) sample geometry showing scanned region and location of interlaminar delaminations; (b) C-scan at 200 kHz after automated MSU image processing (1 channel).	144
Figure 218. RoboDK simulation showing horizontal zig-zag scan of central part of X-brace #3.	145
Figure 219. Validation of robotic SSA-ACUT on X-brace #3 (horizontal zig-zag pattern, 1 channel).	145
Figure 220. Robotic SSA-ACUT inspection of X-brace #3: (a) horizontal zig-zag scan pattern (motion from red to blue); (b) corresponding 3D image of X-brace #3 (1 channel).	146
Figure 221. RoboDK simulation showing slanted zig-zag scan of central part of X-brace #3.	146
Figure 222. Validation of robotic SSA-ACUT on X-brace #3 (slanted zig-zag pattern, 1 channel).	147
Figure 223. Robotic SSA-ACUT inspection of X-brace #3: (a) slanted zig-zag scan pattern (motion from red to blue); (b) corresponding 3D image of X-brace #3 (1 channel).	147
Figure 224. SSA-ACUT probe with 1 transmitter and 3 receivers for high-speed NDE.	148
Figure 225. Robotic SSA-ACUT inspection of X-brace #3: 3D image of X-brace #3 (3 channels).	148

List of Tables

Table 1. Characteristics of air-coupled probes used in experiments.....	5
Table 2. Salient features of Ectane 2 system.	69
Table 3. Comparisons of coil properties for the probes E-1c and E-2a.	95
Table 4. Comparisons of times required to scan a calibration CFRP sample #7 using different MSU probes (150 mm × 150 mm scan area, scan resolution of 2 mm).	96
Table 5. Connections of terminals corresponding to: (a) driving two rectangular coil sensors; (b) driving the open-plate capacitor formed by two rectangular coils as electrodes.....	127
Table 6. Specifications of the acquired Fanuc ArcMate 100iB robots: (a) general; (b) angular speeds and motion ranges of the axes.	135

EXECUTIVE SUMMARY

Main advantages of the air-coupled ultrasound testing (ACUT) and electromagnetic testing (EMT) techniques for NDE of CFRP composites were non-contact sensing, scalability for high-speed inspection, cost-effectiveness, and non-hazardous operation. Despite these advantages, no systems that would satisfy the project requirements were commercially available. Hence, one of the major efforts of the Michigan State University (MSU) team at the initial stage of the project was to close this technological gap by developing, optimizing, and validating array sensors that would provide sufficient sensitivity, spatial coverage, and resolution for robust defect detection. Optimization of the ACUT and EMT sensor designs was performed using experimentally validated finite element models. Initial experiments using array probes were conducted on relatively flat CFRP samples. In parallel, the MSU team designed and assembled a portable platform with two robotic arms. The robots were equipped with newly designed sensors that enabled high-speed NDE of curved CFRP parts. Presently, the developed robotic platform can be used as a demo/template NDE system, which is easily adaptable to manufacturing environments and in-line NDE.

The ACUT NDE system developed by the MSU team used a high-power 4-channel pulser receiver for parallel data acquisition. The array probes were designed by stacking commercially available ACUT transducers, which operated in the frequency range between 100 kHz and 500 kHz. MSU optimized the excitation procedure and developed wave focusing cones so as to reduce the crosstalk between the transducers and to provide higher pulse repetition frequency (PRF). The through-transmission (TT) and single-side access (SSA) inspection modes were successfully implemented. In the TT-ACUT, structural defects in CFRP were detected by passing ultrasonic waves through the test part. Hence, the ACUT transmitters and receivers needed to be placed on the opposite sides of the test part. In the SSA-ACUT, guided waves (GW) were excited in the test part using the transmitters and were sensed by the receivers from the same side. Multi-channel TT-ACUT and SSA-ACUT provided high-speed NDE, and were successfully validated on CFRP test samples with interlaminar delaminations and other embedded defects.

The EM techniques developed by the MSU team included: 1) eddy current testing (ECT), 2) capacitive imaging (CI) and hybrid dual-mode imaging. In ECT, structural damage was detected in CFRP using coils sensor arrays. In ECT, the excitation magnetic field is generated by passing an alternating current through a coil, which is placed above the test sample. The excitation field penetrates the conductive sample and induces the eddy currents in its transect. In turn, the eddy currents generate the reaction field, which affects the total field sensed by a coil. Hence, the presence of structural flaws will alter the eddy current flow and the picked-up signal. ECT is mostly sensitive to local changes of the electric conductivity of the test sample, and CFRPs are mostly conductive in the direction of carbon fibers. Hence, ECT was well suited for the detection of fiber damage/fiber irregularities. The MSU team developed printed circuit boards (PCB) with coil sensor arrays optimized for NDE of CFRP. Unlike most commercial probes designed for ECT of metallic structures, the MSU array probes were designed for operation in [1-10] MHz frequency range, which was optimal for low-conductive CFRP. Multiple sensing topologies (coil groups excitation/sensing arrangements) were implemented and successfully validated.

Capacitive Imaging (CI) technique developed by MSU was complementary to ECT. In contrast to ECT, which was sensitive to local changes of the electrical conductivity, the CI was sensitive to local changes of the dielectric constant. Therefore, CI could provide information about matrix damage/matrix irregularities in CFRP. The MSU CI sensor arrays were made of multiple circular or rectangular open-plate capacitors printed on PCB. Sensors of this type are not commercially available.

In addition to ECT and CI, the MSU team developed a hybrid (dual-mode) inductive/capacitive measurement technique that synergistically combined the benefits of inductive and capacitive sensing for rapid NDE of fiber reinforced polymer (FRP) composite structures. Fiber damage and fiber irregularities in

FRPs were detected by configuring hybrid sensors as coil sensors. Similarly, matrix damage, matrix irregularities and interlaminar delaminations were detected by configuring hybrid sensors as capacitive sensors. ECT and CI were performed sequentially by means of electronic switching. Hence, eliminating the need for mounting two separate sensor arrays on the probe.

Portable robotic platform was developed by MSU for multi-technique high-speed NDE of CFRP test parts. The platform had two 6-axis robots, which enabled inspection of curved parts in approximately a 6×6×6 ft³ active scan area. On the software side, the MSU team integrated scripts for NDE hardware control with scripts for robot motion control. MSU also implemented automated path planning for the robots, reconstruction of part's surfaces via stereovision, 3D rendering of inspection data, and image processing algorithms for enhanced defect detection.

Automotive composite parts manufactured by Plasan Composites from Phase I were used to validate the ACUT and EMT techniques on representative testbeds. Among those parts were three X-braces for a Dodge Viper, one composite calibration plaque with known defects at known locations, and four other test sections, including sections from a front splitter, a corner section from a composite hood, and a high-pressure RTM panel made using non crimp fabric. Other test samples included CFRP and GFRP calibration plates with fiber/matrix defects fabricated at MSU/CVRC.

1. INTRODUCTION

Rapid, cost-effective nondestructive inspection is necessary to drive the wide scale adoption of advanced carbon fiber reinforced polymer (CFRP) composites in the automotive sector. Before carbon fibers can be applied towards high volume automotive production, several technical hurdles exist. Among these hurdles is the inability to manufacture structural composite parts at high volumes and insure consistent, defect-free parts. High speed inspection for high volume production of advanced composite CFRP components and structures is needed to ensure the integrity, safety, and overall quality of the component/structure. The ability to inspect every part with advanced nondestructive evaluation (NDE) technology will enable increased use of advanced composites/CFRP materials in auto body structures, which will lead to significant lightweighting and improved strength for fuel efficiency and crashworthiness. This effort is applicable to lightweight composite door intrusion beams, bumpers, B pillar reinforcements, crush tubes, hybrid composite/metallic parts, as well as composite bonded assemblies.

The National Highway Traffic Safety Administration (NHTSA) and manufacturers in the automotive sector are necessarily cautious regarding new materials. NHTSA does not want automakers and their suppliers producing defective parts, particularly those parts that affect occupant safety when incorporating new materials in their vehicle designs. For the industry, risks of legal liabilities for warranty of structural automotive composites are a significant concern throughout the supply chain and need to be managed. These risks could be greatly reduced by implementing a 100% endpoint inspection of every part at the manufacturing line. These efforts are also applicable further upstream in the component manufacturing process (Tier I) as well as in the OEM assembly plants/field. Hence, development of the endpoint NDE inspection prototype will eliminate a key barrier for U.S. automakers knowing that the component integrity/validation will be highly controlled enabling them to have the confidence to embrace design and production of mainstream vehicle platforms with advanced composites/CFRP. This will result in larger, lightweight component usage, lower manufacturing costs, less energy consumption and significantly reduced CFRP scrap. The resulting rapid NDE inspection technologies will also be a key enabler for high volume production of CFRP composites for clean energy products (e.g., wind turbine blade and compressed gas storage manufacturing).

Current destructive mechanical tests are inefficient as they represent, at best, a sample of the overall parts produced, compounded with the fact that destructive testing is very inefficient and costly, particularly for CFRP components. On the other hand, existing “off-the-shelf” NDE technologies are precise and provide reasonably high sensitivity to defects in CFRP parts. However, it was determined in the IACMI Project 3.8 (Phase I) [1] that these technologies are not yet optimized for high-speed production with 1-3 minutes cycle times.

After evaluation of multiple NDE techniques in Phase I in terms of sensitivity, scalability, and ease of use in industrial environment, the project management team down selected the air-coupled ultrasound testing (ACUT) and electromagnetic testing (EMT) for further development at Michigan State University (MSU) in Phase II. The major goals in this project were: 1) to increase the technology readiness level (TRL) and adapt the ACUT and EMT techniques for high-speed inspection of CFRP parts by developing novel sensor arrays, data acquisition and signal/image processing algorithms for automated defect detection; 2) to develop a template inspection system, that would enable high speed (3 minute or less) NDE of CFRP parts and that could be easily adapted for in-line production.

2. AIR COUPLED ULTRASONIC (ACUT) NDE

Results obtained in the IACMI Project 3.8 (Phase I) [1] demonstrated the feasibility of air-coupled ultrasound (ACUT) for NDE of automotive parts. In Quarter I of Project 3.13 (Phase II), the MSU team focused on raising the TRL of the ACUT technology. Validation of ACUT for high-speed and high-volume inline inspections required the completion of the following tasks:

- i. optimization of inspection parameters for enhanced sensitivity to damage (e.g., transducer frequency, stand-off distance, wave incidence angle with respect to part's surface, etc.);
- ii. detailed investigation of wave propagation and wave interaction with structural damage in composite parts at ACUT frequencies of 50-400 kHz;
- iii. development and acquisition of hardware for sending and receiving high-power ultrasonic tone bursts through the part;
- iv. development and acquisition of robotic manipulators/gantries for inspection of automotive parts with complex geometries;
- v. development of software for controlling the ultrasonic system, gantries and robotic manipulators;
- vi. development and validation of signal processing algorithms for automatic data analysis and robust damage detection.

2.1 Optimization of Inspection Parameters for Through-Transmission (TT) and Single-Side Access (SSA) ACUT

The ability to inspect test specimens without using couplants is one of the major advantages of the ACUT technique compared to conventional immersion or water-jet ultrasonic NDE. This is important for production facilities since ACUT systems are compact, don't require water tanks, don't wet the test parts, and create no access moisture. However, several technical challenges need to be addressed in order to increase the TRL of the ACUT technique and make it practical for high-speed NDE of automotive composites. The biggest hurdle is the mismatch between the acoustic impedances of piezoelectric elements in ACUT probes, coupling medium (air) and composite test parts. In order to generate the ultrasonic waves of high intensity in the air, ACUT probes require careful design of impedance matching layers. In addition, wave reflections from the surface of the test specimen are much stronger than the reflections from the internal interfaces or defects within the test specimen, which makes the pulse-echo inspection using a single ACUT probe impractical. Hence, separate transmitters and receivers are required for TT and SSA ACUT measurements. Array ACUT probes should be developed for increased spatial coverage and inspection speeds. In this process, multiple parameters need to be optimized (e.g. excitation frequency, incidence angles, shapes of focusing cones, etc.) in order to achieve high sensitivity to flaws in composite test parts and to reduce cross talk between the transducers.

The MSU team performed a series of experiments with in-house ultrasonic gantries and off-the-shelf air-coupled probes in order to determine critical parameters of the ACUT system for rapid NDE of composite parts (Tasks i-ii). The group teamed up with Sonotec US in order to deliver a customized multi-channel pulser-receiver, transducers, and hardware drivers. The MSU team scheduled training with SONOTEC application engineers in Islandia, NY on 07/09/2019 to test all readily available ultrasonic modules and perform initial calibration scans of CFRP panels. Detailed specs of the assembled ACUT system are given in the following sections.

MSU initiated acquisition of two robotic arms in order to manipulate ultrasonic probes within a 6 ft by 6 ft by 6ft cube space. It was envisioned that synchronized robot arms placed on a platform would provide

enough dexterity for efficient ACUT inspections of curved parts in the through-transmission (TT) mode and single-side access (SSA) mode.

The MSU team performed scans of representative composite parts using available ultrasonic pulsers and XYZ gantries in parallel with assembly and acquisition of the new ACUT hardware and robots. This was done in order to determine the best inspection parameters, which would provide maximal sensitivity of air-coupled probes to interlaminar delaminations. ACUT probes were driven by the Ultrapac II system originally designed for immersion ultrasonic testing at frequencies above 500 kHz. Despite serious limitations of the existing system in delivered power and scan speed, ultrasonic wave propagation through CFRP test samples was still detectable after time averaging of multiple ultrasonic waveforms at each scan position. Hence, Ultrapac II was used to identify the best configuration of air-coupled probes for TT and SSA inspection of calibration panel #1.

2.1.1.Experiments using Ultrapac II pulser-receiver

Experimental set-up for 1-channel ACUT of calibration panel #1

TT and SSA ACUT probe configurations

Figure 1a shows the experimental setups for single-side and through-transmission inspection of plate-like CFRP parts. In the through-transmission mode, ACUT transducers are placed on the opposite sides of the test specimen (see Figure 1b). The first probe excites UT waves, and the second probe receives the UT waves propagated through the air interfaces and the specimen. Both probes could be positioned either normal to the part's surface ($\theta = 0^\circ$), or at some arbitrary angles θ° . Note that axes of both probes need not necessarily be collinear and can be offset by a certain distance. For instance, in Figure 1a the probes for through-transmission inspection are positioned at $\theta = 14^\circ$ angles and are offset by 4 mm along the x -axis. Schematic configuration of probes for single-side access inspection is shown in Figure 1c. In contrast to conventional water immersion ultrasound, the same probe cannot be used as both transmitter and receiver due to high acoustic impedances mismatch between air and part that causes strong specular reflection of ultrasonic waves from the part's surface. Hence, inspection is accomplished by placing a transmitter-receiver pair of probes on a single side of a test part (see Figure 1a). Some form of a sound barrier is needed to absorb the ultrasonic wave that propagates straight between the probes through the air. This could be a piece of foam rubber, Styrofoam or an Otoscope cone attachment.

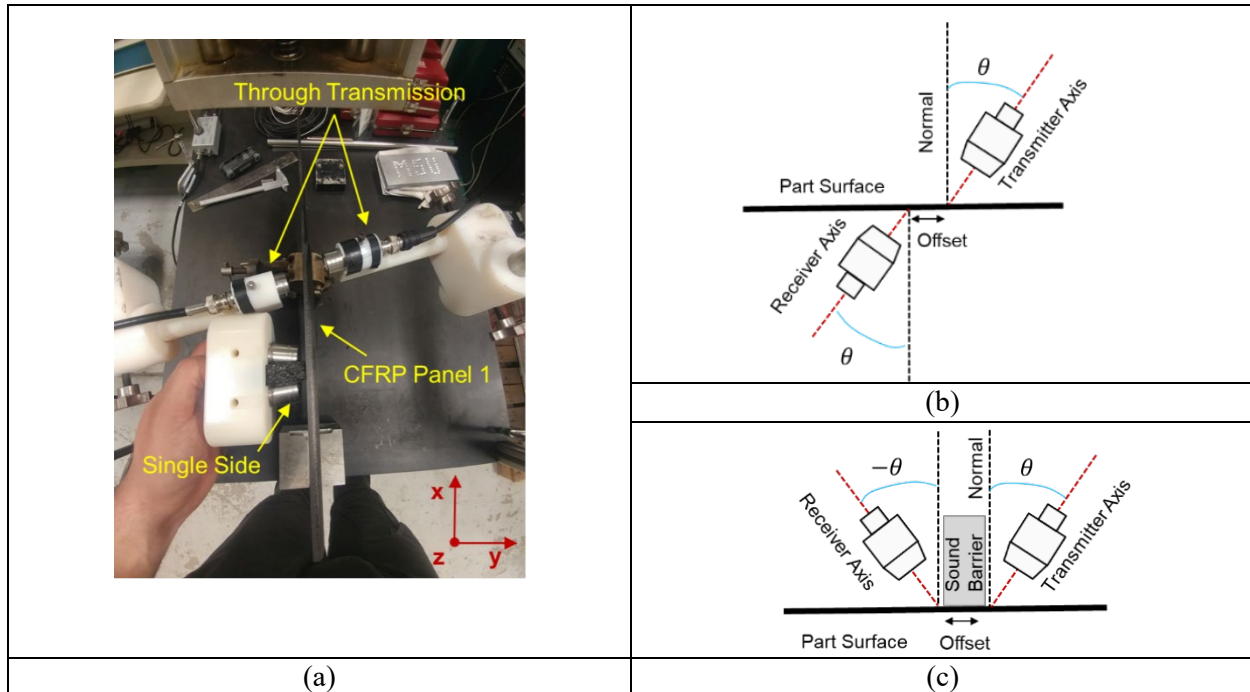


Figure 1. (a) Experimental setups for single-side and through-transmission inspections of CFRP calibration panel #1 with delaminations in different layers; (b) schematic configuration of probes for through-transmission ACUT; (c) schematic configuration of probes for single-side pitch-catch ACUT.

Characteristics of the ACUT transducers

The MSU team used two sets of transducers from the Sonoscan series in experiments: CF200 and CF300 with 200 kHz and 300 kHz center frequencies, respectively. Photos of the transducers and their specs are provided in Figure 2 and Table 1. CF300 transducers generate ultrasonic beam with the smallest diameter that enhances spatial resolution of 2D raster scans (C-scans). On the other hand, acoustic pressure of the CF200 probe is much higher that helps excite strong ultrasonic signals in test specimens. CF200 receivers require less gain, less time averaging and produce cleaner signals compared to CF300.

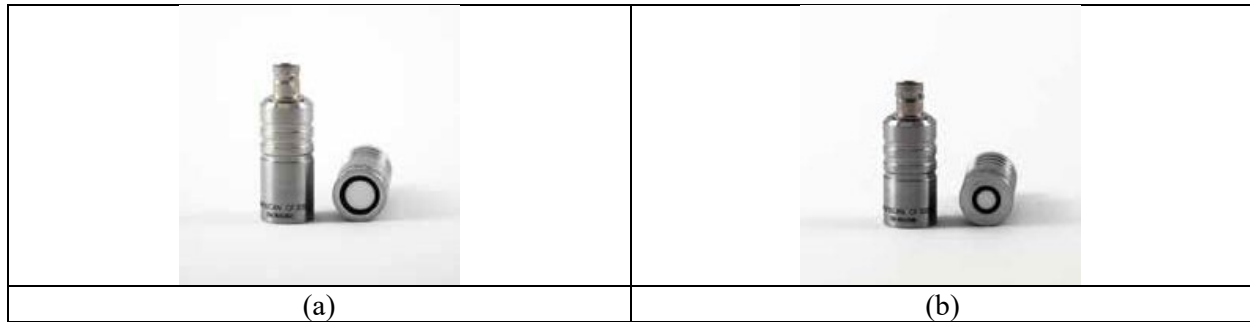


Figure 2. Images of air-coupled probes: (a) Sonoscan CF200 probe; (b) Sonoscan CF300.

Parameters\Probe Type	CF200	CF300
Frequency	200 kHz	300 kHz
Sound beam Ø (-6 dB)	3 mm	2 mm
Wavelength in air	1.7 mm	1.1 mm
Sensitivity (transfer ratio in air)	-35 dB	-52 dB
Near field length	18 mm	12 mm
Dimensions	Ø 19 mm × 43 mm	Ø 19 mm × 38 mm

Table 1. Characteristics of air-coupled probes used in experiments.

Raster scanning, data acquisition and signal processing

Calibration panel #1 was scanned using the Ultrapac-II XYZ-gantry system with UT-Win software designed for immersion UT testing. Ultrasonic waves were excited and sensed at two frequencies (200 kHz and 300 kHz) using pairs of off-the-shelf probes CF200 and CF300, respectively. Stand-off distances between the transducers and corresponding part's surfaces were 18 mm for CF200 transducers and 12 mm for CF300 transducers to avoid operation in near field. The excitation signal was a pulse with peak amplitude of 400 V. Signals from the receiving transducer were amplified with a broadband 60 dB pre-amplifier 2/4/6C from Physical Acoustics Corporation. Second-stage 80 dB gain was added by the receiver's PCI board of the Ultrapac II system.

For the inspection in through-transmission mode, the test sample was placed vertically, and scanning was performed in xz -plane as shown in Figure 1a. In pitch-catch inspection, calibration panel #1 was clamped to the gantry bed, and it was scanned horizontally in xy -plane. In both cases, gantry speed was set to 40 mm/s, and scan resolutions along the horizontal and vertical axes were 2 mm and 2 mm, respectively.

When 2D scanning (raster scanning) of Calibration panel #1 was performed, an ultrasonic signal (A-Scan) was collected at every scan point. Measured signals (A-Scans) were filtered using a 3rd order band-pass filter with cut-off frequencies $f_{min} = f_c - 25 \text{ kHz}$ and $f_{max} = f_c + 25 \text{ kHz}$ around the excitation center frequency f_c and averaged 40 times to reduce the noise. A single feature was selected from each A-scan (for instance, time-of-flight, energy or shape), and it was plotted on a corresponding pixel of a 2D grid thus forming a pseudo-color 3D representation of ultrasonic data, or a C-scan. Energy of the signal measured by the receiving probe at each scan position was the primary feature to analyze, as extracting it from the data was very simple and did not require any sophisticated signal processing. Every signal (A-Scan) was time gated meaning that only a 40 μs window after ultrasonic wave arrival was considered for analysis. The energy of the signal within this window was evaluated and stored using the UT-Win software. Shapes of the signals and their times-of-flight were not considered at this point, since this would be much easier to implement in the new SONOAIR pulser-receiver module. Obtained experimental results are summarized in the next section.

Optimal incidence angles for enhanced defect detection using TT-ACUT

The first configuration of probes is schematically shown in Figure 3a. Region of the calibration panel #1 with 9 delaminations was scanned using CF300 probes at normal wave incidence. Corresponding C-scan is shown in Figure 3b. Results demonstrated that delaminations located closer to the top and bottom surfaces of the laminate were successfully detected. However, signals around midplane delaminations seemed much dimmer in the C-scan. It should be noted that the amplitude of the signals in the regions with delaminations increased compared to damage-free regions. Fiber patterns were also visible in the C-scan, as some fiber tows showed up in horizontal and vertical directions.

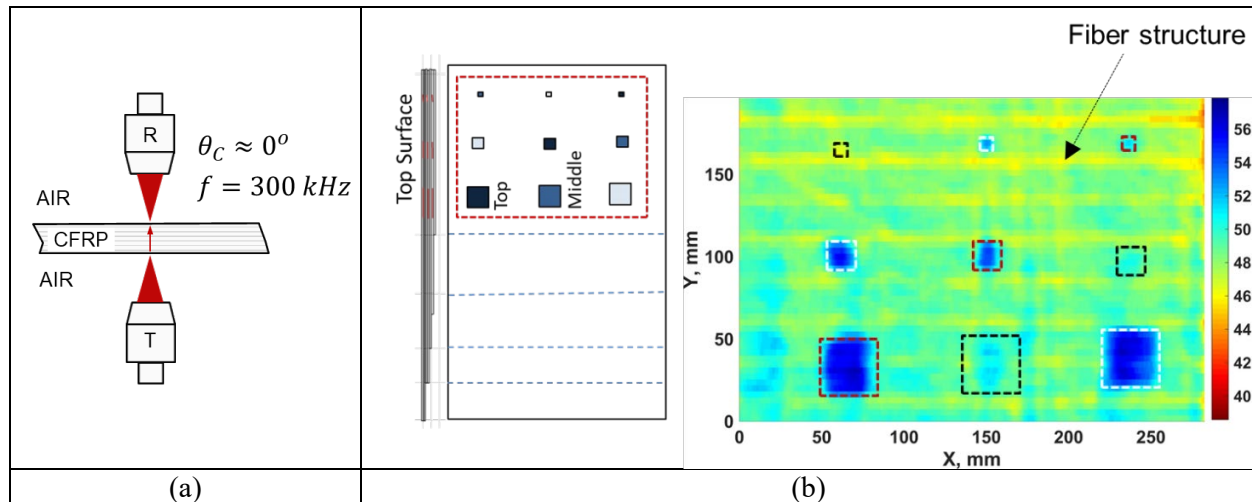


Figure 3. (a) Configuration of air-coupled probes CF300 for inspection in through-transmission mode at normal incidence ($\theta_c = 0^\circ$), $f = 300 \text{ kHz}$; (b) CFRP calibration panel #1 and corresponding C-scan of the region with delaminations in different layers. True locations of delaminations and their sizes are marked as dotted squares: top layers – red, midplane – black; bottom layers – white.

Figure 4 illustrates similar configuration of probes at normal wave incidence, but at this time, the Calibration panel #1 is scanned with CF200 transducers. Obtained results are opposite to Figure 3b. At 200 kHz, only midplane delaminations are seen and the amplitude of the received signal is lower in the regions with delaminations.

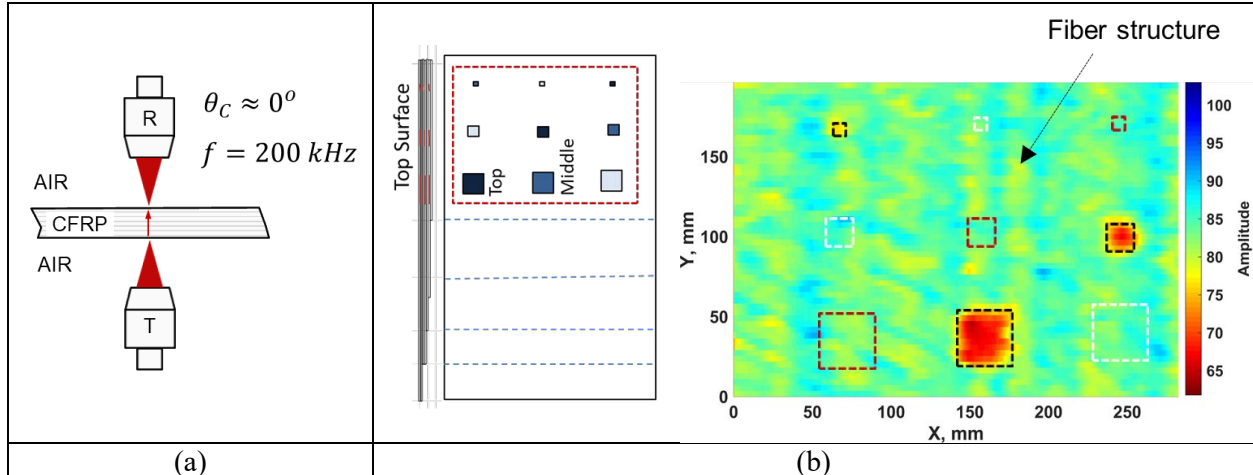


Figure 4. (a) Configuration of air-coupled probes CF200 for inspection in through-transmission mode at normal incidence ($\theta_c = 0^\circ$), $f = 200\text{ kHz}$; (b) CFRP calibration panel #1 and corresponding C-scan of the region with delaminations in different layers. True locations of delaminations and their sizes are marked as dotted squares: top layers – red, midplane – black; bottom layers – white.

Figure 5 and Figure 6 demonstrate the third configuration, in which the sample is scanned with CF200 probes at incidence angle $\theta_c = 17^\circ$. Note that the ACUT probes don't physically touch the sample. C-scan image shows all delaminations with amplitudes higher than the damage-free background. However, as in the case of CF300 probes at normal incidence, delaminations in the midplane of the laminate look dim in the C-scan.

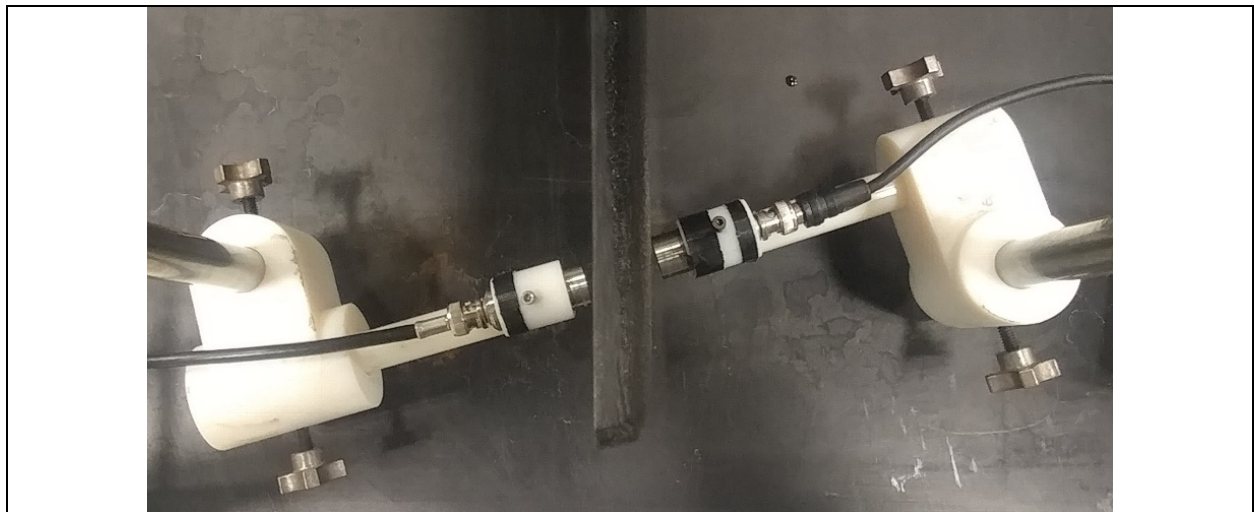


Figure 5. Photo of CF200 probes scanning calibration panel #1 at in through-transmission mode at $\theta_c = 17^\circ$ and zero offset.

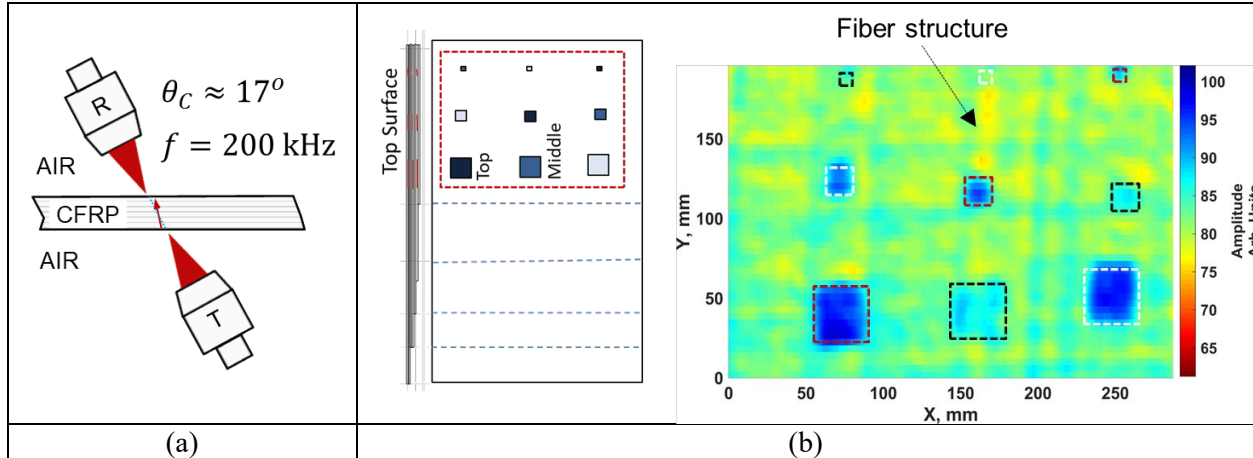


Figure 6. (a) Configuration of air-coupled probes CF200 for inspection in through-transmission mode at $\theta_c = 17^\circ$, $f = 200\text{ kHz}$; (b) CFRP calibration panel #1 and corresponding C-scan of the region with delaminations in different layers. True locations of delaminations and their sizes are marked as dotted squares: top layers – red, midplane – black; bottom layers – white.

Figure 7 and Figure 8 demonstrate the fourth configuration, in which the sample is scanned with CF200 probes at an incidence angle $\theta_c = 12^\circ$ with 25 mm offset between their axes. All delaminations were successfully detected and the contrast between the regions with delaminations and damage-free background was high. Delaminations in top and bottom layers of the laminate introduced high and low amplitude peaks in the C-scans around defect edges. Delaminations in the midplane of the laminate introduced high amplitude regions in the C-scans around defect centers. Notably, maximum and minimum peaks for top and bottom layer delaminations were flipped. Hence, it was possible to determine how deep the defects were in the cross-section of the panel.

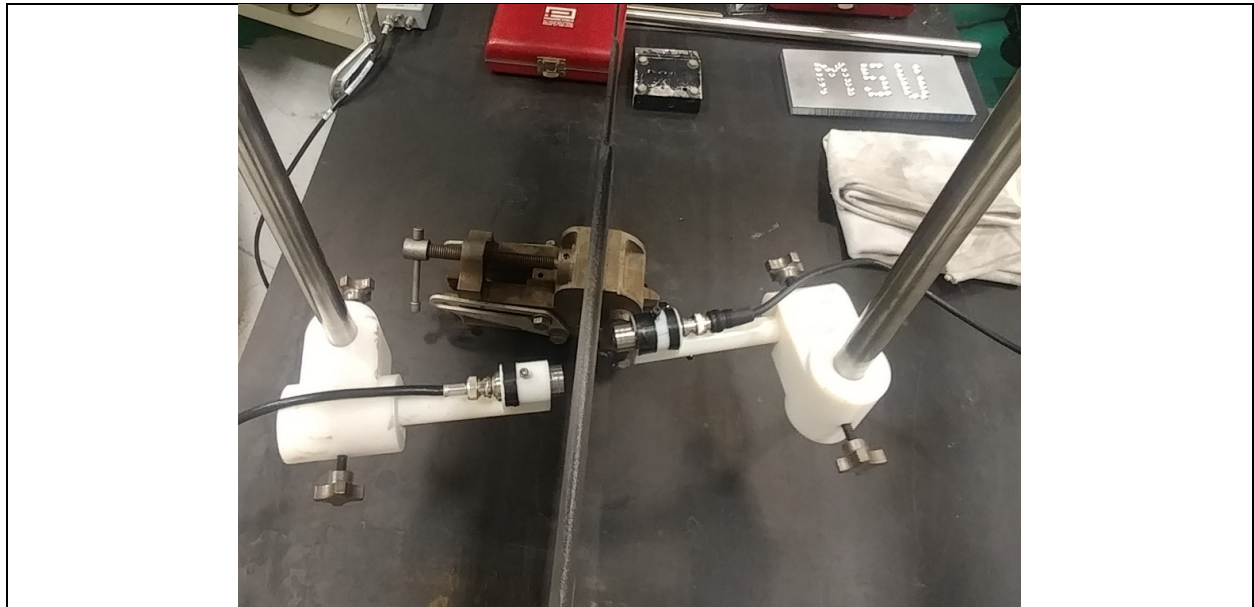


Figure 7. Photo of CF200 probes scanning calibration panel #1 at in through-transmission mode at $\theta_c = 12^\circ$ and 25 mm offset between their axes.

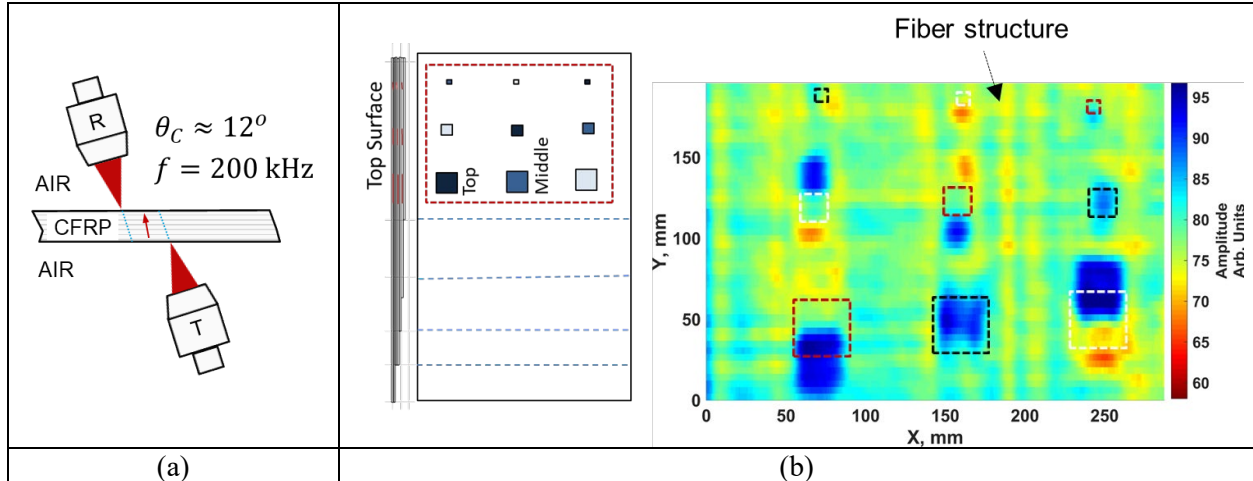


Figure 8. (a) Configuration of air-coupled probes CF200 for inspection in through-transmission mode at $\theta_c \approx 12^\circ$, $f = 200$ kHz. Axes of transducers are 25 mm apart. (b) Corresponding C-Scan of CFRP calibration panel #1. True locations of delaminations are shown as dotted squares: top layers – red, midplane – black; bottom layers – white.

Since the calibration panel #1 is nothing but a 7 mm thick plate in the region with 9 delaminations, a 25 mm offset between the transducer axes was large enough to consider waves propagating in it not as bulk waves, but rather as guided waves (or Lamb waves). The damage indications in Figure 8 weren't perfectly aligned with the actual damage locations owing to the interference of waves propagating above and below the delaminations. This interference depended on the depth of delaminations in the transect of the test specimen. For better accuracy of defect location, it is recommended to keep the offset between the transducers as small as possible.

Figure 9 and Figure 10 show the fifth configuration of ACUT probes in the through-transmission mode. In this case, CF200 probes are at $\theta_c = 14^\circ$ with respect to surface normal, and there was a 5 mm offset between the axes of the probes. C-scan in Figure 10b demonstrates that all delaminations were successfully detected with these settings. Moreover, the high amplitude regions in the C-scans were aligned well with actual positions of delaminations in the panel.

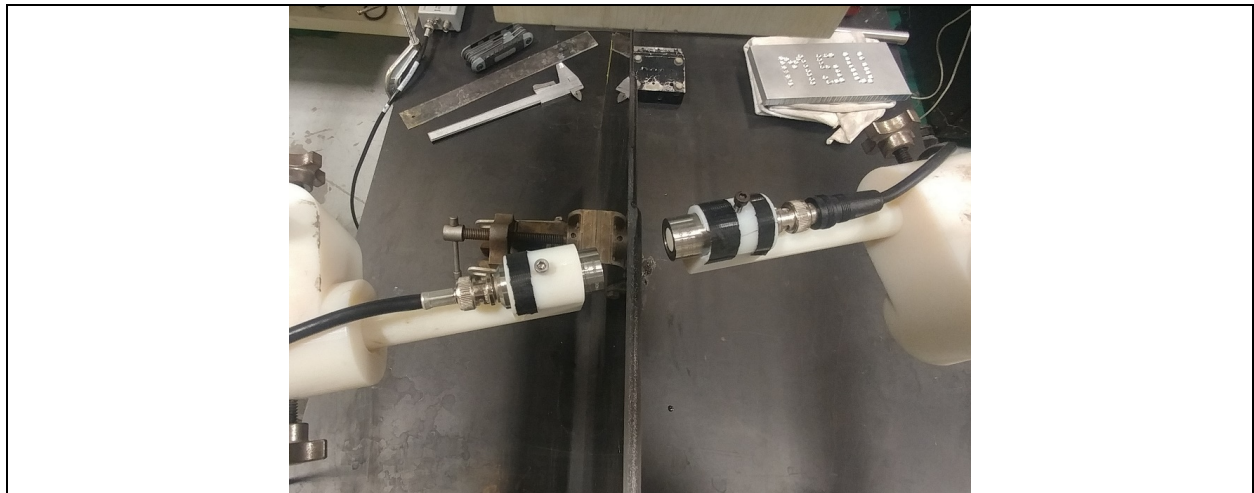


Figure 9. Scanning of calibration panel 1 in through-transmission mode at $\theta_c = 14^\circ$ and 5 mm offset between the axes of air-coupled probes CF200.

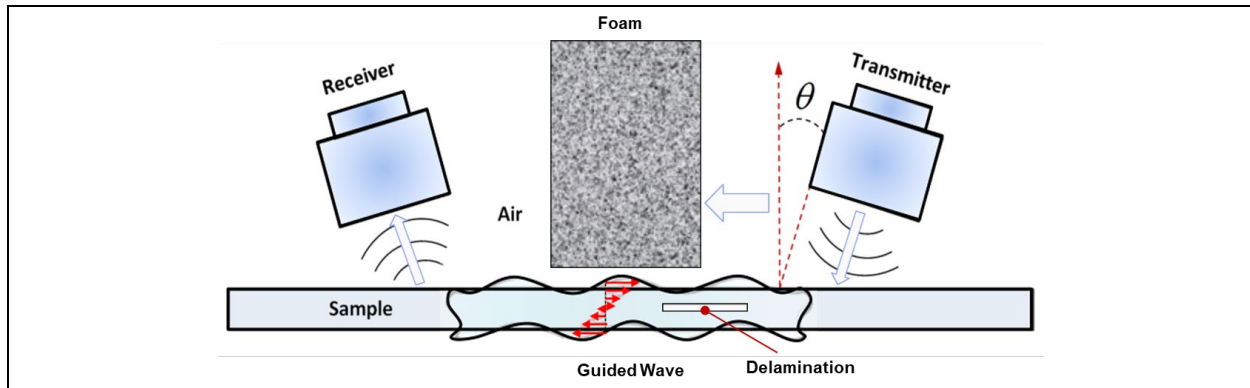


Figure 11. Schematic configuration of ACUT probes for excitation and sensing of guided waves in thin plates from single side.

Guided waves are multimodal, which in simple terms means that a single excitation pulse can generate multiple waves propagating in the structure at the same time with different particle displacement patterns (mode shapes) and group velocities. Guided waves are also dispersive; hence their mode shapes and phase velocities change with frequency. Typical examples of dispersion relations and a snapshot of wave propagation are shown in Figure 12. Figure 12 was included for illustrative purposes only, as it describes guided waves excited around 200 kHz in an isotropic 5 mm thick aluminum plate. When anisotropy, namely stiffness matrices, orientations, and stacking sequences of plies are taken into account, similar wave propagation analysis can be conducted for CFRP and GFRP composite laminates.

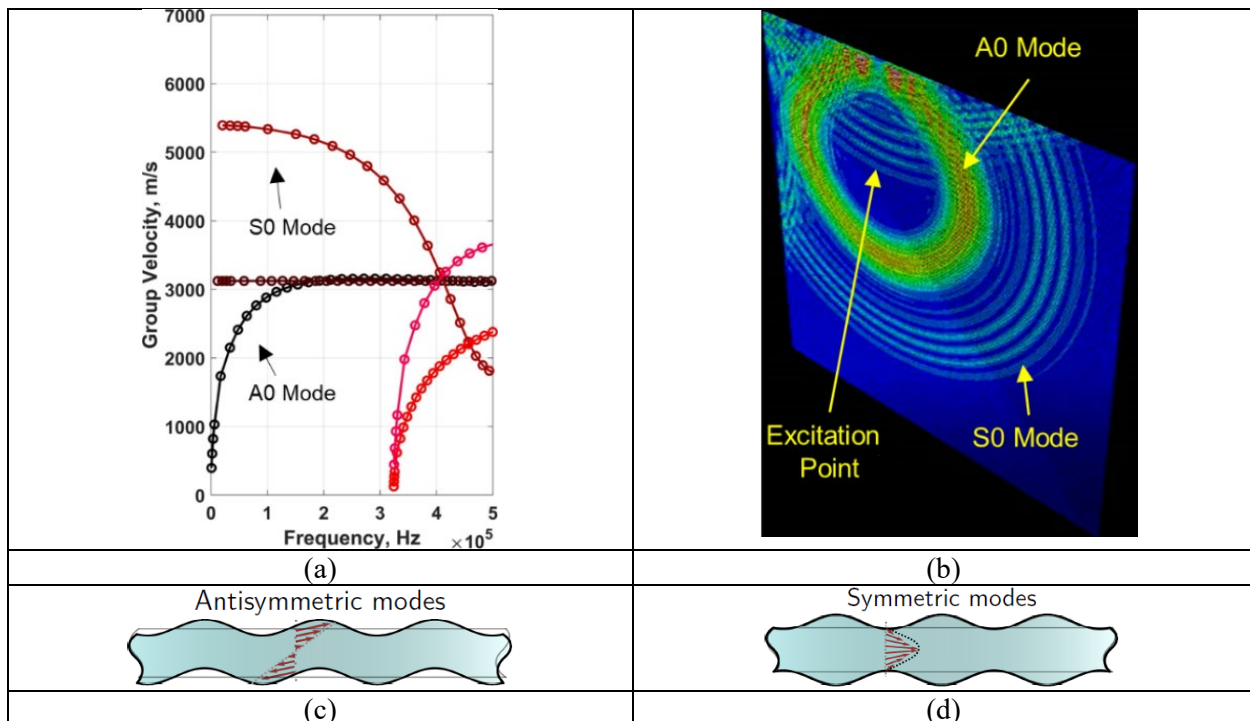


Figure 12. Guided waves in a 5 mm thick aluminum plate: (a) analytic dispersion relation; (b) snapshot of two fundamental modes A0 and S0 (excited using a 4-count sinusoidal tone burst at 200 kHz) propagating in the plate simultaneously at 100 μ s after the excitation, FE simulation in Abaqus CAE; (c) deformation of the plate's cross-section due to the A0 mode at 200 kHz; (d) deformation of the plate's cross-section due to the S0 mode at 200 kHz.

The type of mode excited at a selected frequency can be controlled by adjusting the coincidence angle θ_c . The optimal angle for excitation of specific mode is determined from the Snell's law as

$\theta_c = \sin^{-1} \left(\frac{c_{medium}}{c_{part}} \right),$	(1)
--------------------------------------------------------------------	-----

where c_{medium} is the phase velocity of coupling medium (1500 m/s in the water, and 331 m/s in the air), and c_{part} is the phase velocity of a guided wave in the part. Velocity c_{part} is determined by picking a point on one of the phase velocity dispersion curves of the inspected specimen.

The concept of selective mode excitation is illustrated in Figure 13. The phase velocities from dispersion relations are used in Eq.1 to determine coincidence angles for a given frequency range. For instance, if a 200 kHz probe is in the water, the optimal excitation of the A0 mode in the plate will happen at $\theta_c = 40^\circ$ (see Figure 13c). On the other hand, if the same probe is in the air, the optimal angle would be only $\theta_c = 9.5^\circ$ (see Figure 13d). Hence, in the air-coupled inspection of parts, the angle θ_c will tend to be small in general (~ 0 - 25°), and the axes of transmitter-receiver probes will tend to be close to surface normal in order to excite guided waves of the highest amplitude in the test specimen.

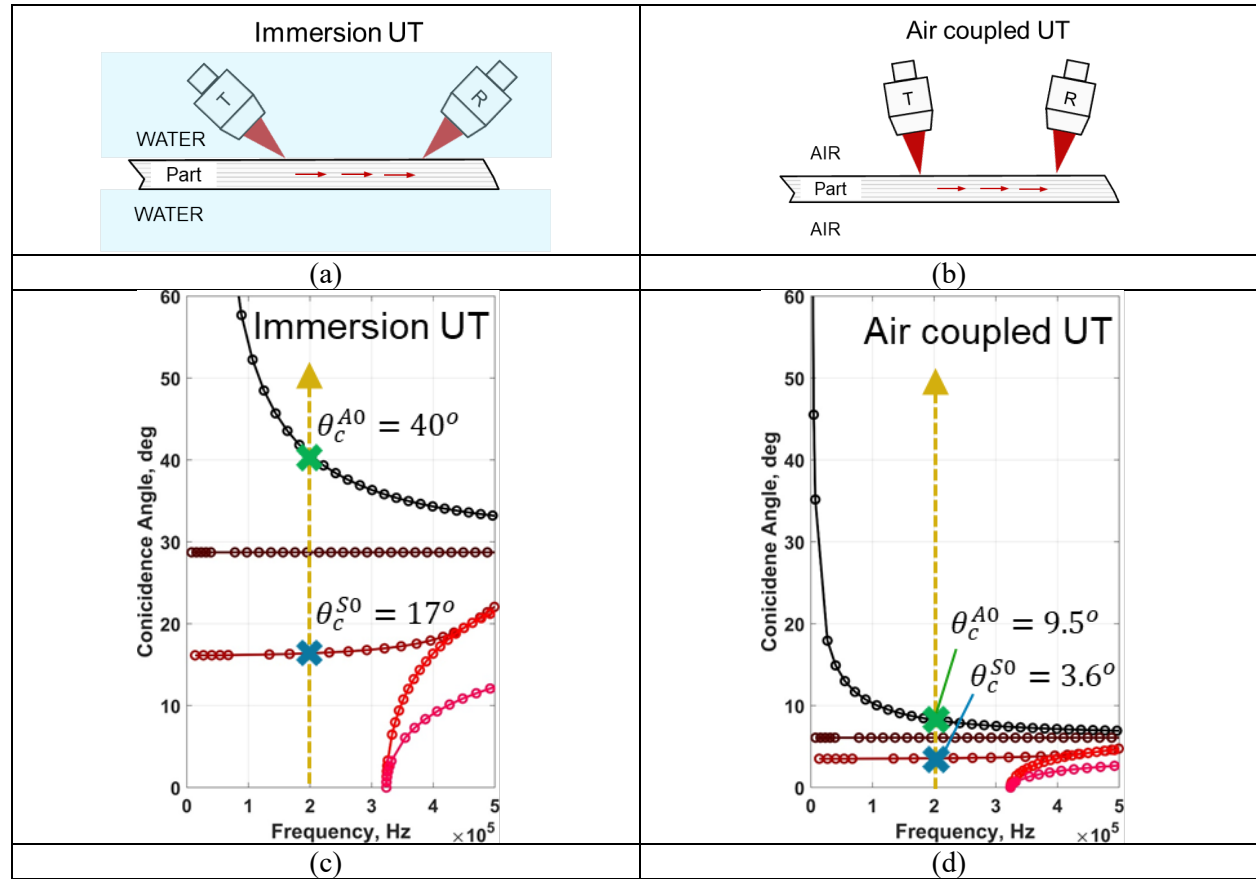


Figure 13. Excitability of guided waves in a 5 mm thick aluminum plate: (a) schematic configuration of probes for exciting the A0 mode at 200 kHz through the water; (b) schematic configuration of probes for exciting the A0 mode at 200 kHz through the air; (c) coincidence angles for exciting fundamental A0 and S0 modes in the water; (d) coincidence angles for exciting fundamental A0 and S0 modes in the air.

Initial experiments with pitch-catch guided wave measurements were conducted by placing the air-coupled probes CF300 in the 3D printed fixture shown in Figure 14. The incidence angle of the probes was $\theta = 8^\circ$. The fixture was attached to the search tube of the XYZ gantry from the top and scanning of the Calibration panel #1 was performed as explained earlier.

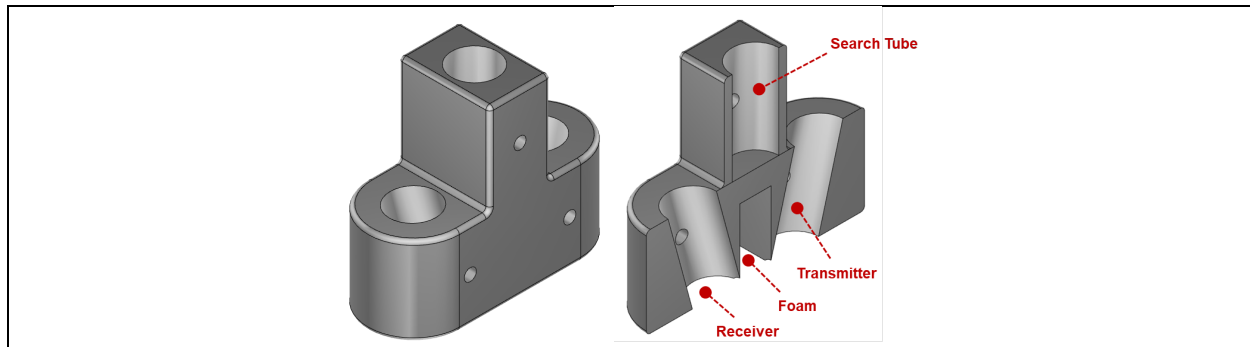


Figure 14. Model of a 3D printed fixture for guided wave measurements.

Figure 15 shows a typical A-scan of the CFRP panel in a defect-free region. The time gate for measuring signal energy is shown as a yellow line segment. Figure 16 and Figure 17 demonstrate similar C-scans in the regions with delaminations closer to the bottom surface of the panel and delaminations closer to the top surface of the panel, respectively. Figure 16b and Figure 17c show that wave packet in the time gate splits in two, and the overall energy of the signal within the gate drops when the probe moves over delaminations. The most probable reason for this observation is that the panel was effectively split in two thinner panels (or waveguides) by a delamination. Guided waves leaked both above and under the defect, thus amplitudes and velocities of these waves depended on the thicknesses of the corresponding top and bottom waveguides. Guided waves leaking though top and bottom added up destructively at the receiver side.

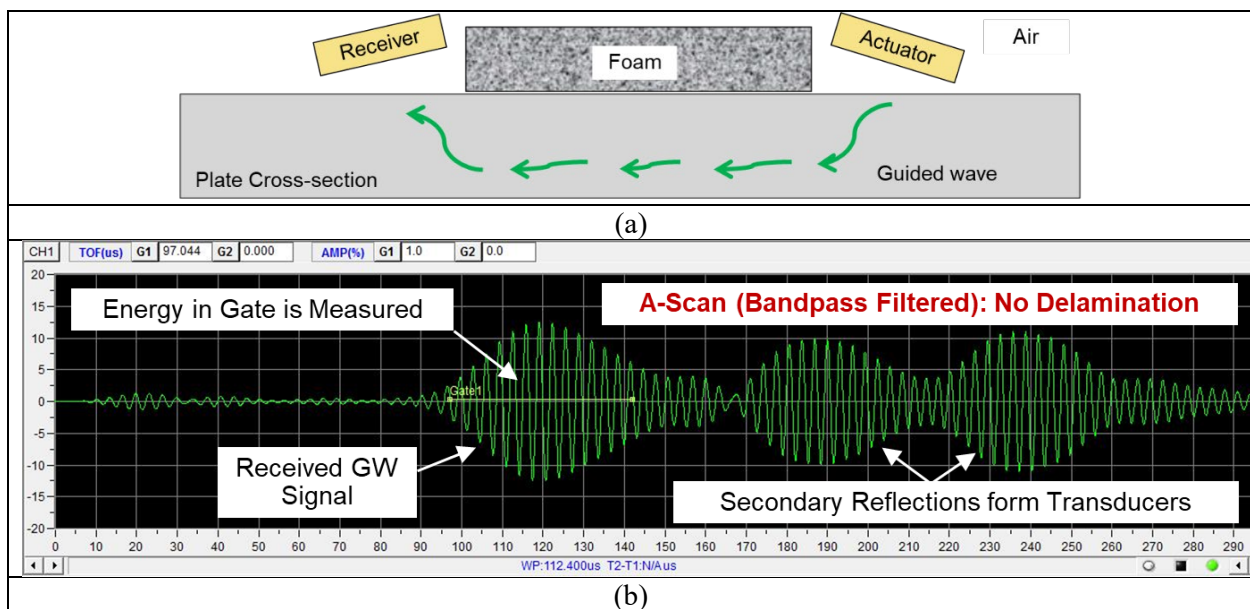


Figure 15. Guided wave propagation in the defect-free region of CFRP Calibration panel #1: (a) schematic; (b) A-scan with a time gate.

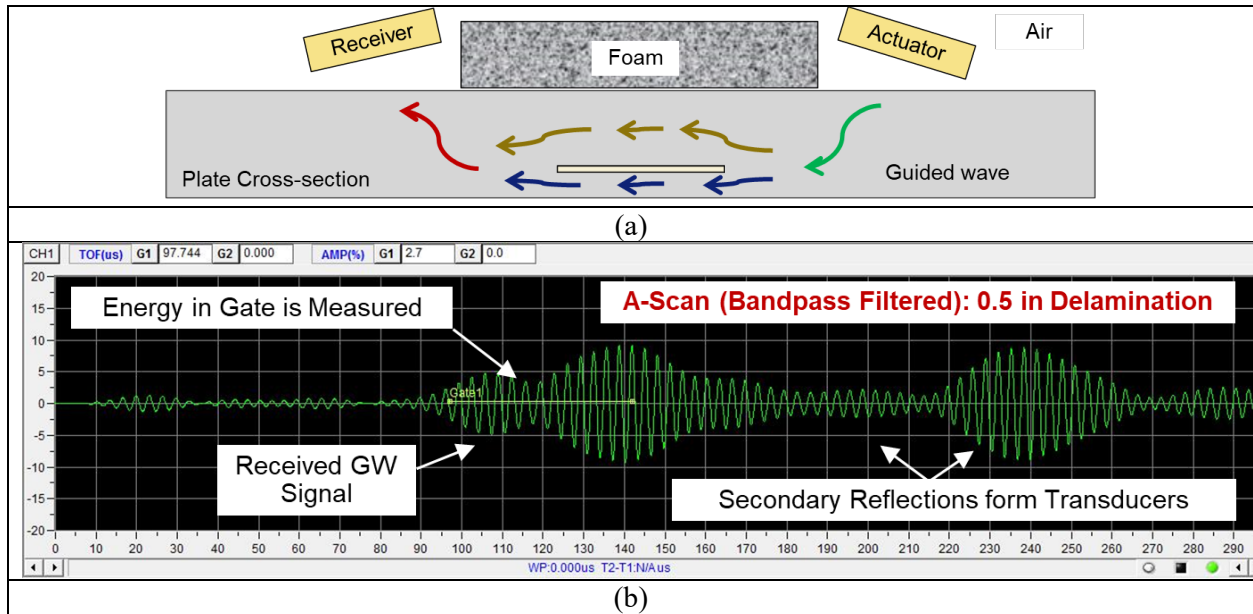


Figure 16. Guided wave propagation in the region with a 0.5 in delamination closer to the bottom surface of the CFRP Calibration panel #1: (a) schematic; (b) A-scan with a time gate.

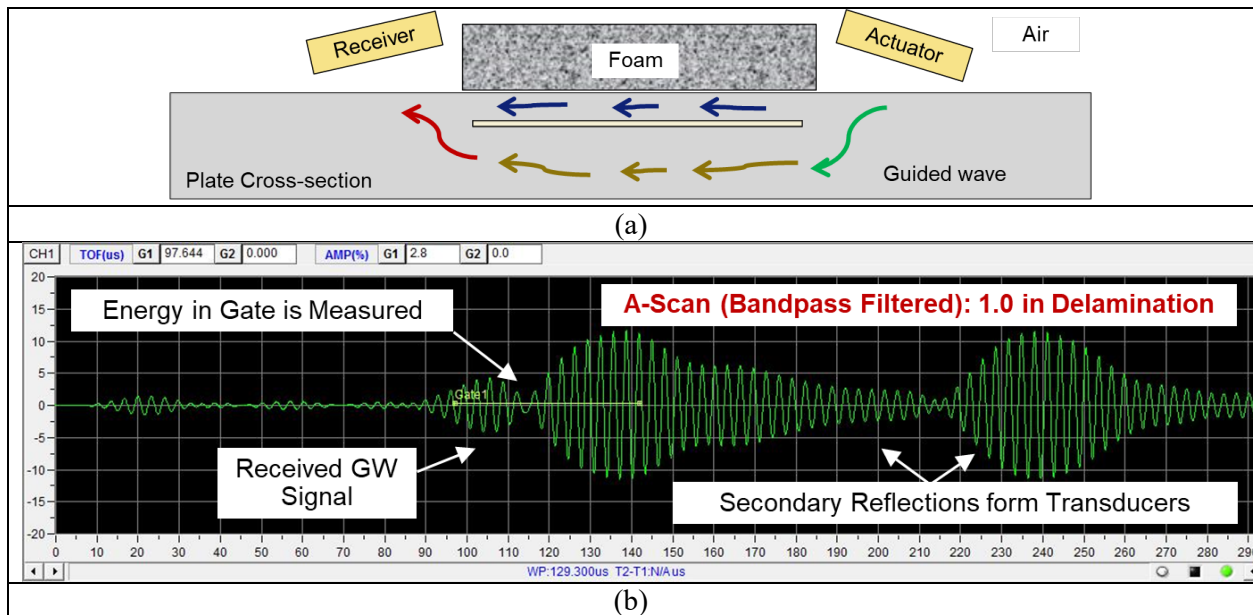


Figure 17. Guided wave propagation in the region with a 1 in delamination closer to the top surface of the CFRP Calibration panel #1: (a) schematic; (b) A-scan with a time gate.

C-scans in pitch-catch mode were acquired from both top and bottom side of the Calibration panel #1. Obtained results are presented in Figure 18b and Figure 18c, respectively. C-scans detected delaminations closer to the top and bottom surfaces of the laminate. However, images of delaminations in the midplane lacked contrast. The results were quite similar to the normal incidence C-scan in the through-transmission mode with the same CF300 probes (see Figure 3). The authors believe that adjusting the incidence angle and excitation frequency like in the case of through-transmission mode inspection will allow for robust detection of all delaminations with the equal sensitivity.

Another observation was that such a simple feature as signal energy in the time gate carried information about the location delaminations in the cross-section of the test panel. Figure 18b and Figure 18c show that images of delaminations closer to the top and bottom surfaces looked differently in the C-scans. Images of the top layer delaminations appeared to have square shapes, and images of the bottom layer delaminations appeared to have round shapes. These patterns remained consistent after the panel was flipped.

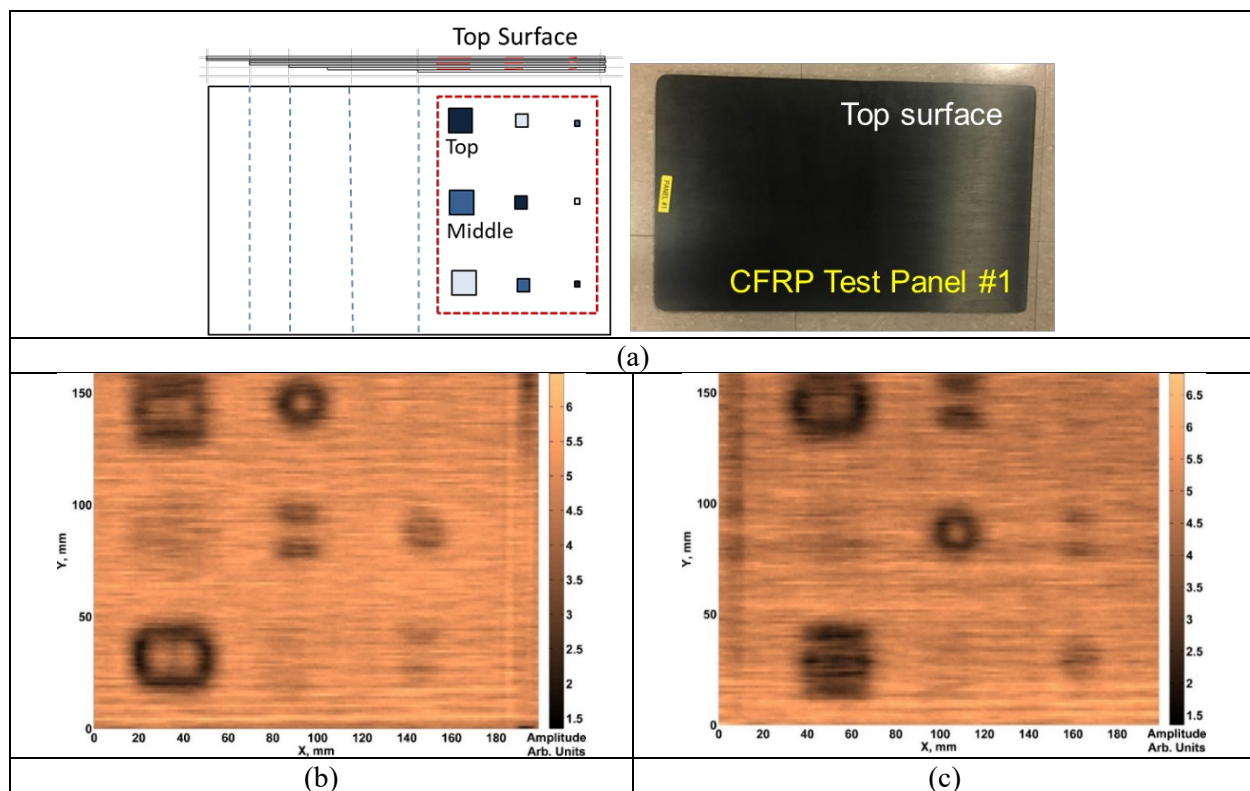


Figure 18. Pitch-catch C-scans of the Calibration panel #1 using CF300 probes at $\theta = 8^\circ$ with 25 mm offset between the probes. (a) Schematic of the Calibration panel #1 with 9 delaminations; (b) C-scan from the top side; (c) C-scan from the bottom side.

The experimental results showed the feasibility of pitch-catch inspection for NDE of CFRP parts. However, more detailed studies of guided wave propagation in the regions with delaminations are needed to confirm experimental findings and explanations of the observed signals.

2.2 Novel ACUT Hardware: Multi-Channel Pulser-Receiver, Piezocomposite and Multi-Element Probes

The MSU team identified the required hardware modules for high-speed and high-volume NDE of composite parts using air-coupled ultrasound (Task iii). MSU teamed up with the Sonotec US to deliver and test the new customized 4-channel pulser-receiver, drivers, and probes. Sonotec provided a software development kit (SDK) in C# to control the hardware and to develop graphical user interface (GUI). The block-diagram of the designed ACUT NDE system is shown in Figure 19.

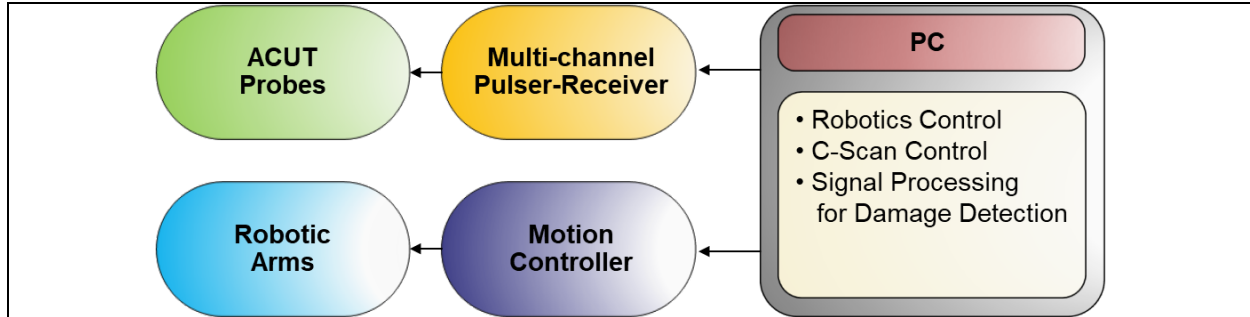


Figure 19. Block-diagram of the ACUT system for high-speed NDE of composite parts.

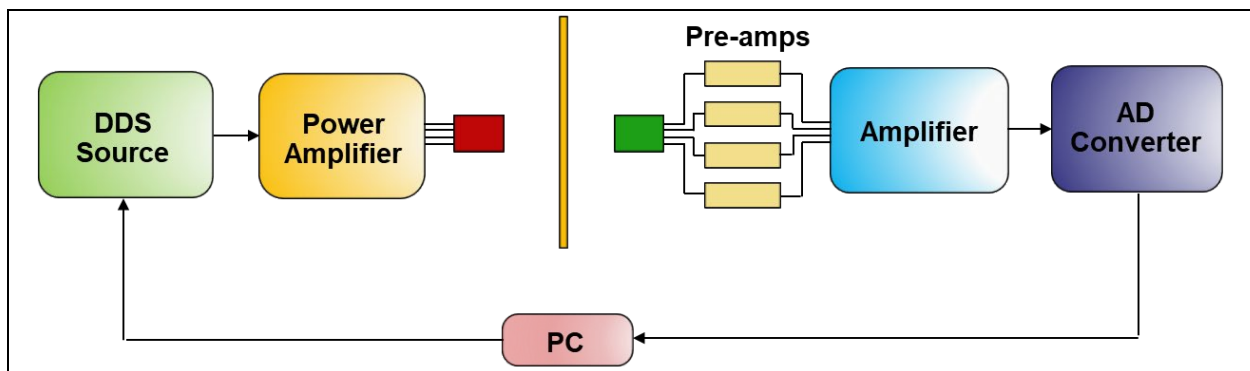


Figure 20. Block-diagram of the high-power 4-channel pulser-receiver module for ACUT.

The new pulser-receiver module was optimized for air-coupled inspection. The block-diagram of the module is presented in Figure 20. The most significant features of the module are the high output power needed to drive the probes at maximal current loads, the digital signal source for generation of arbitrary shaped excitation signals, the FPGA controlled time delays between 4 channels for driving 4 probes synchronously, 4 low-noise pre-amplifiers for acquiring high-SNR measurements, and a 4-channel 100 MS/s ADC. More detailed parameters of the ACUT module are provided in the Figure 21.


	<ul style="list-style-type: none"> • 4 channel system for high-speed inspection • Up to 800 V excitation voltage • Continuous wave operation possible • 2 kW power (burst or single pulse) • Low noise amplification (1 nV/vHz) with up to 120 dB gain • GaGe 16 bit A/D converter • 100 MS/s data acquisition rate
(a)	(b)

Figure 21. Module for rapid ACUT NDE of composites: (a) photo of the module; (b) characteristics of the hardware.

2.2.1 Evaluation of multi-channel pulser-receiver at Sonotec facility

In Quarter II, the new ACUT hardware was successfully tested and acquired. The MSU team made a trip to Islandia, NY in order to evaluate the customized ACUT system built by Sonotec. After a full day of training, the MSU team successfully tested the high-power pulser-receiver module, pre-amplifiers, multi-channel data acquisition hardware and data export libraries. Sonotec provided new line of ACUT transducers with piezocomposite crystals to evaluate their performance on CFRP samples. The ACUT system at Sonotec facility was interfaced to a small demonstration 3D gantry.

The MSU team performed scanning of calibration CFRP parts from IACMI Project 3.8 (Phase I) [1] and of new CFRP honeycomb panels. The acquired ACUT C-scans of honeycomb panels were compared with high-resolution X-ray images. ACUT hardware components were later successfully delivered to MSU.

A photo of the ACUT experimental setup at Sonotec facility is shown in Figure 22. The ACUT system was interfaced to a motion controller of a demo 3D gantry, which allowed the MSU team to perform scans of relatively flat CFRP samples. After all hardware components passed basic electric tests, the MSU team proceeded to scanning the CFRP parts using the available GUI from Sonotec.

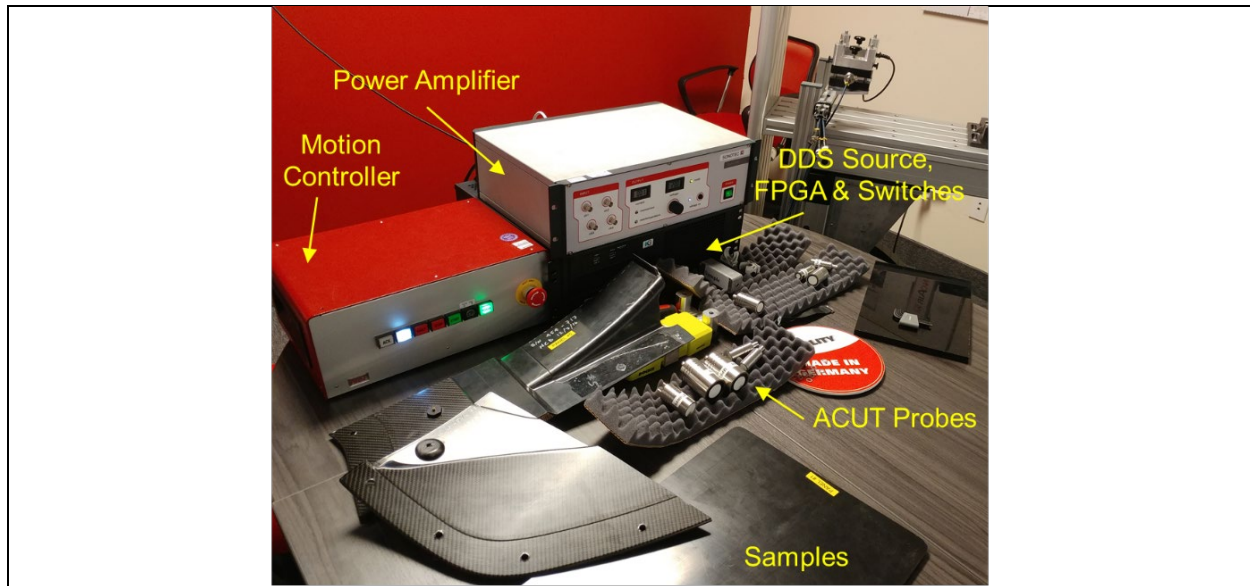


Figure 22. ACUT experimental setup for testing 4-channel pulser-receiver and probes on CFRP samples.

All C-scans (raster scans) in the training session were acquired in the through-transmission mode at normal incidence. One air coupled probe excited ultrasonic waves in the test sample, whereas another probe on the opposite side was used as a receiver. Figure 23 demonstrates a typical excitation voltage applied to the driving probe and a typical signal (A-scan) acquired by the receiving ACUT probe.

In the current system, excitation voltage represented a trail of unipolar square pulses with amplitudes up to 400-500 V. High voltage and power applied to the excitation probe allowed for large displacements and stronger waves to be generated in the air. Bipolar pulsing was not allowed so as to avoid poling of piezoelectric crystals in the opposite direction. Direct digital synthesis (DDS) source and field programmable gate array (FPGA) inside the pulser-receiver provided the capability to apply different excitation signals and to perform frequency sweeps by changing the widths of pulses. All 4 channels could be driven independently with precision time delays between excitation waveforms set by the FPGA.

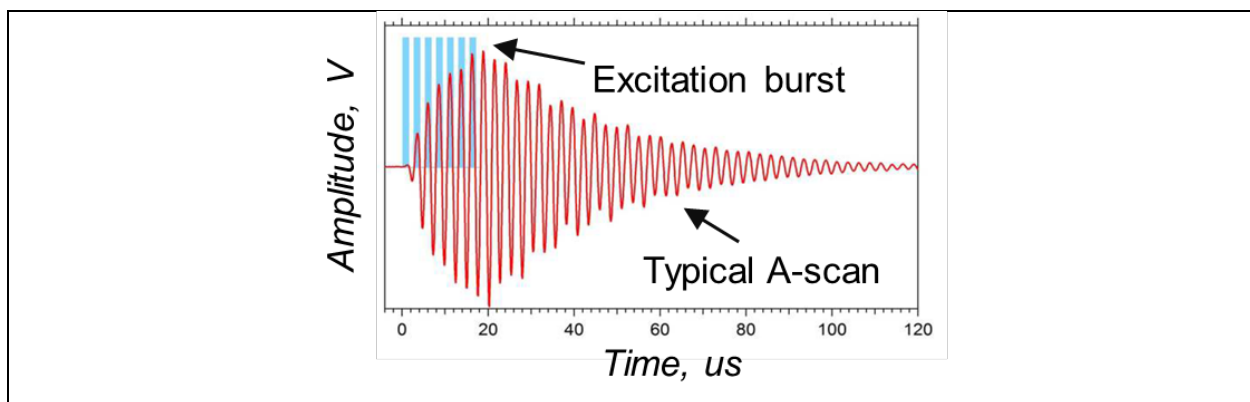


Figure 23. Typical excitation signal and resulting A-scan (CF200 probe, $f = 200$ kHz).

Figure 23 shows that the received signal (red) has longer time support than the excitation signal (blue). This happens owing to superposition of multiple wave reflections between the sample and ACUT probes as shown in Figure 24.

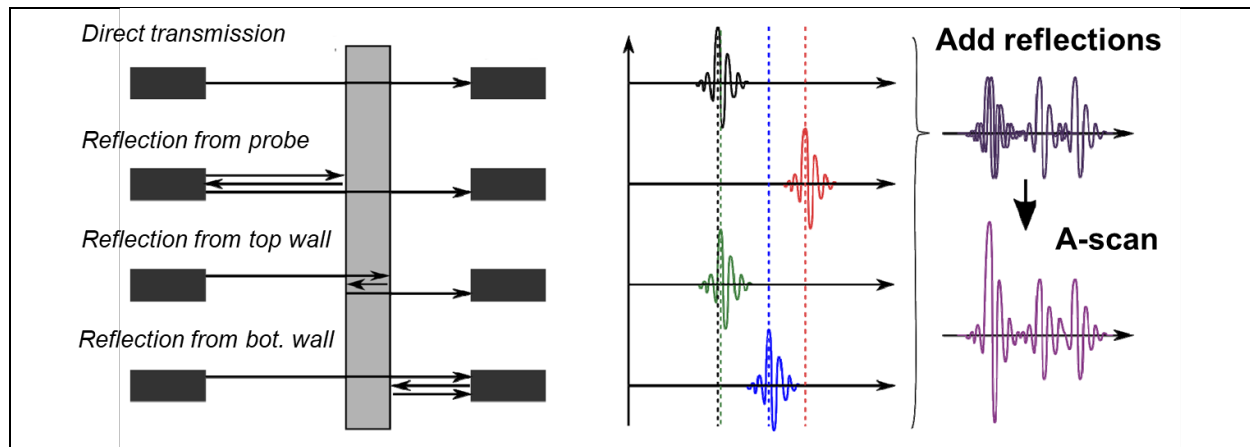


Figure 24. Wave propagation in through-transmission mode at normal incidence and acquisition of the resulting received signal (A-scan).

Directly transmitted wave packet (black) and its reverberation inside the sample (green) carry most information about structural damage in the transect. Second order reflections from the probes (blue and red) can be reduced by increasing the stand-off distances between the probes and the test sample that comes at a cost of increased wave attenuation through the air and smaller amplitude of received signal.

2.2.2. Piezoceramic and piezocomposite ACUT probes for optimal sensing

Design of a typical ACUT transducer is illustrated in Figure 25. An actuator is a disc made of piezoceramic perovskite material (usually PZT $\text{Pb}[\text{Zr}_x\text{Ti}_{1-x}]\text{O}_3$ ($0 \leq x \leq 1$)). Backing layer is made of epoxy compound that absorbs waves generated at the back face of the disk. Matching layer consists of multiple thin layers of materials that match acoustic impedances between the actuator and air.

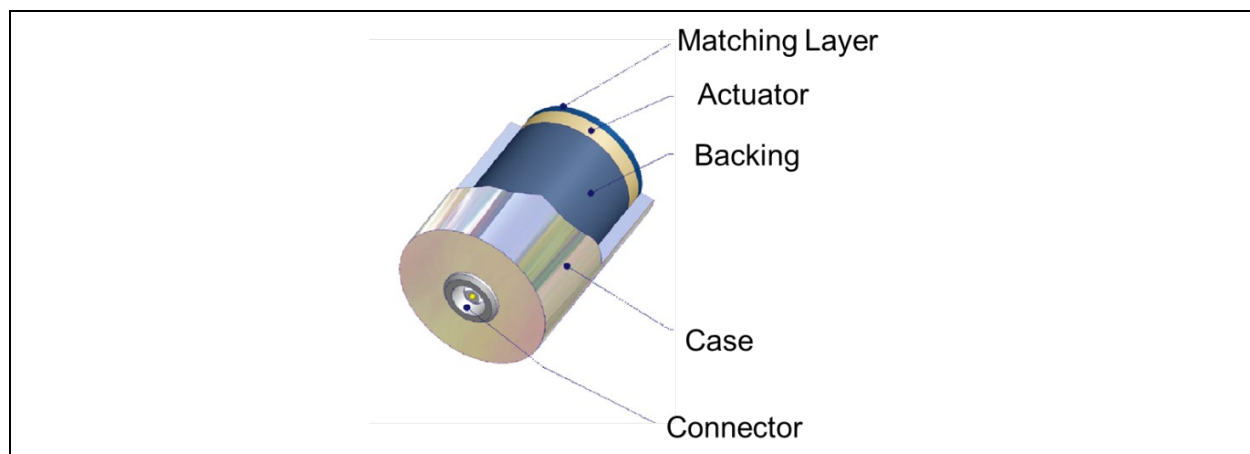


Figure 25. Design of a typical ACUT transducer.

Recently, piezocomposite materials for actuators have shown promise in ACUT applications. During a training session in Islandia, the MSU team evaluated novel piezocomposite transducers compatible with the ACUT system.

Main advantages of piezocomposite elements compared to standard piezoceramic counterparts are: 1) more broadband frequency response, and 2) more uniform distribution of acoustic pressure on the excitation face. Broader frequency response helps resolve shorter wave pulses and reflections from thin interfaces within the structure, and uniformly generated acoustic pressure provides more uniform sensitivity to defects.

Figure 26a demonstrates a piezocomposite actuator disc manufactured using “dice and fill” technique (see Figure 26b). Cutting a standard PZT disc into smaller cubes helps to tailor its frequency response to designed parameters. Stripes of PZT material are removed by precision diamond blades and obtained air gaps are filled with epoxy resin. “Dice and fill” piezocomposite actuators can be easily inserted into standard probe cases shown in Figure 25. Since some of the PZT material is taken away at the manufacturing stage, the displacements of the piezocomposite actuator are inherently weaker than that of a pure PZT. Piezoceramic probes are also more prone to mechanical damage and are more expensive than PZT counterparts (~\$1000 extra per 1 pair).

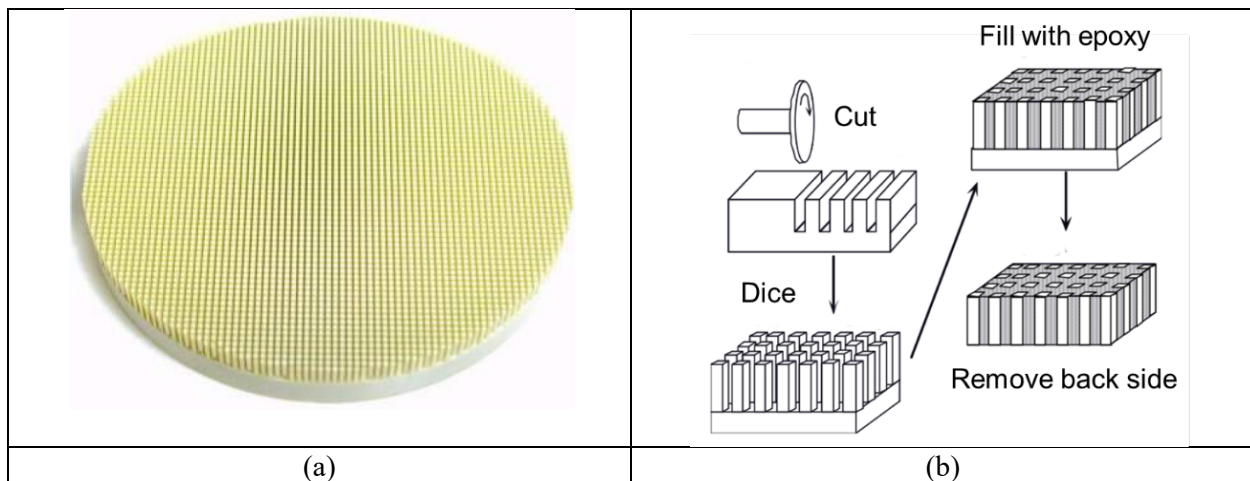


Figure 26. (a) Piezocomposite disk for ACUT transducers; (b) dice & fill technique for manufacturing piezocomposite elements.

Figure 27 shows displacement fields generated by a standard piezoceramic and a piezocomposite disc actuator. In Figure 27a, most displacement is observed at the geometrical center of the disc. In Figure 27b, displacement is distributed more evenly throughout the top and bottom faces.

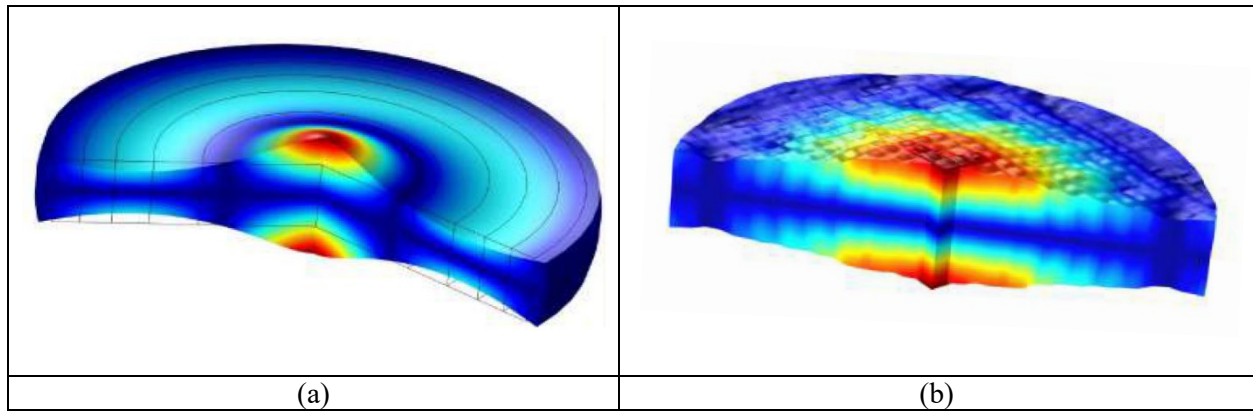


Figure 27. Actuator transect: (a) mode shape of a regular PZT transducer; (b) mode shape of a piezocomposite transducer. Large displacements are shown in red color, and small displacements are shown in blue color. Color bars are normalized for each plot (courtesy of Sonotec US).

Another important observation regarding ACUT transducers is that the same piezocomposite or piezoceramic disc has slightly different optimal frequencies for wave excitation and sensing. This concept is illustrated in Figure 28. Blue curve shows the magnitude of impedance $|Z|$ of a disc, green curve shows the sound intensity when a disc is used as an actuator, and red curve shows sound intensity sensed by a disc.

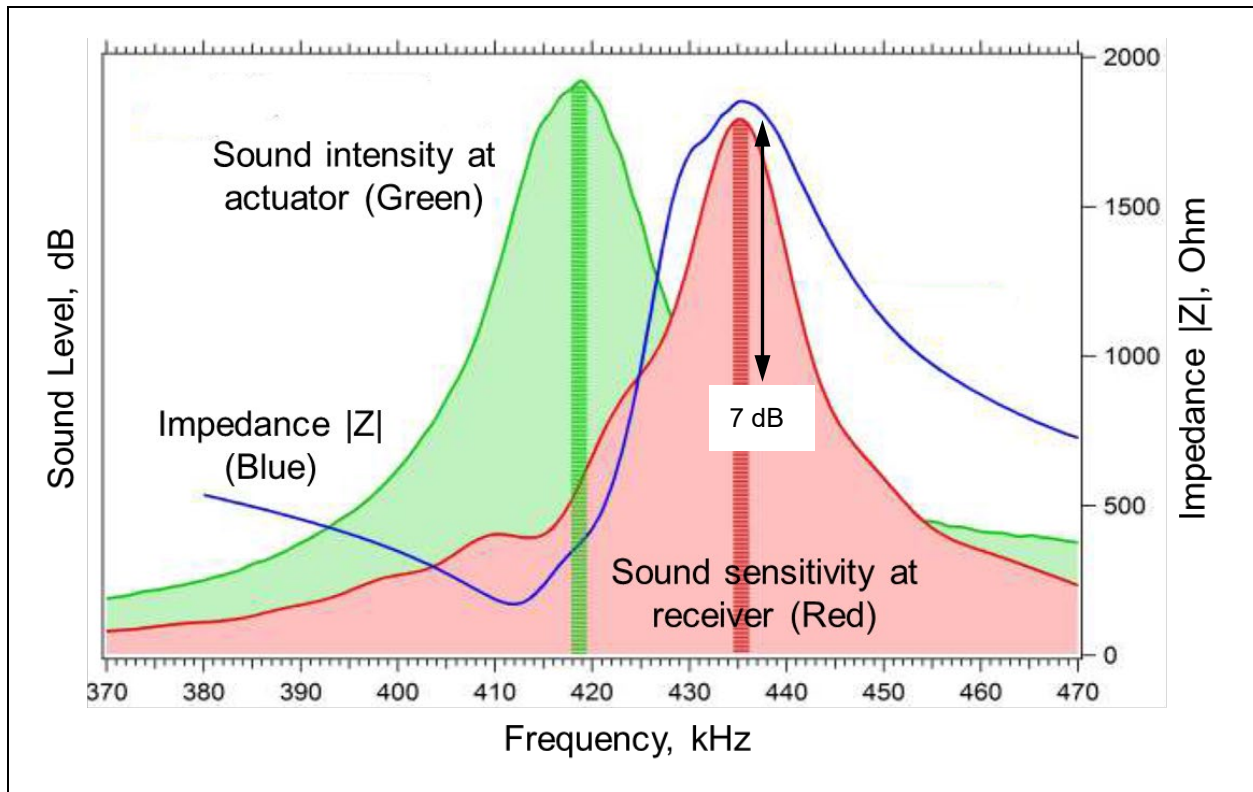


Figure 28. Optimal frequencies that maximize intensities of generated and sensed sound pressure.

Anti-resonance of a disc at $f = 419$ kHz is a sweet spot for excitation, and resonance at $f = 436$ kHz is a sweet spot for sensing. Hence, the optimal configuration of the actuator and receiver for ACUT would have two probes with slightly offset resonant frequencies. If identical probes are used and both are driven at a frequency optimal for sensing ($f = 436$ kHz), the resulting signal strength would be reduced by ~ 7 dB compared to the ideal configuration.

2.2.3. Experimental TT-ACUT C-scans using CF200, CF300 and CF400 probes

The MSU team scanned calibration panel #1 using CF200 and CF300 probes at Sonotec facility, and the results were qualitatively similar to C-scans from Quarter I. Hence, additional probes (e.g., piezocomposite and multi-element) and additional CFRP samples were considered for testing. One of the most advanced probes was the CF400, a 4-element piezocomposite probe with the shortest wavelength in the air, electronic beam focusing, and the highest spatial resolution among others (see Figure 29a). CF400 uses all 4 channels of the pulser-receiver simultaneously; therefore, it is envisioned that it can be used only for acquiring detailed high-definition scans of selected regions on parts, initially screened with truly parallel arrays of CF200 or CF300 probes. CF400 has a disc element in the center of the probe surrounded by three ring elements as shown in Figure 29b. Activating all four elements with preprogrammed time delays allows for generation of a tight beam in the air ($d \sim 2$ mm) by cancelling side lobes introduced by the central disc. The simulated distribution of acoustic pressure around CF400 probe is shown in Figure 29c.

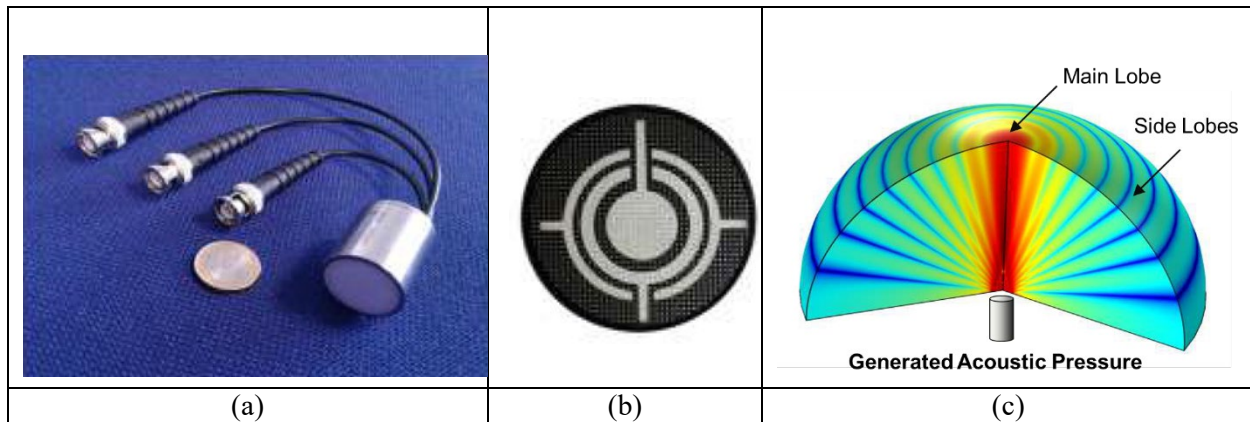


Figure 29. CF400 4-element piezocomposite ACUT probe: (a) photo of the probe with connectors; (b) designs of the actuating elements; (c) FE model showing electronic beam forming process (courtesy of Sonotec US).

CF200, CF300 and CF400 probes were used to scan the Nomad CFRP honeycomb panel shown in the bottom of Figure 30. C-scans were acquired at a pulse repetition rate of 200 pulses/s, linear gantry speed of 100 mm/s and with spatial resolution of 2 mm. For the scans with CF200 and CF300 probes, 2 channels were activated simultaneously as only 4 probes of each type were available at a testing site.

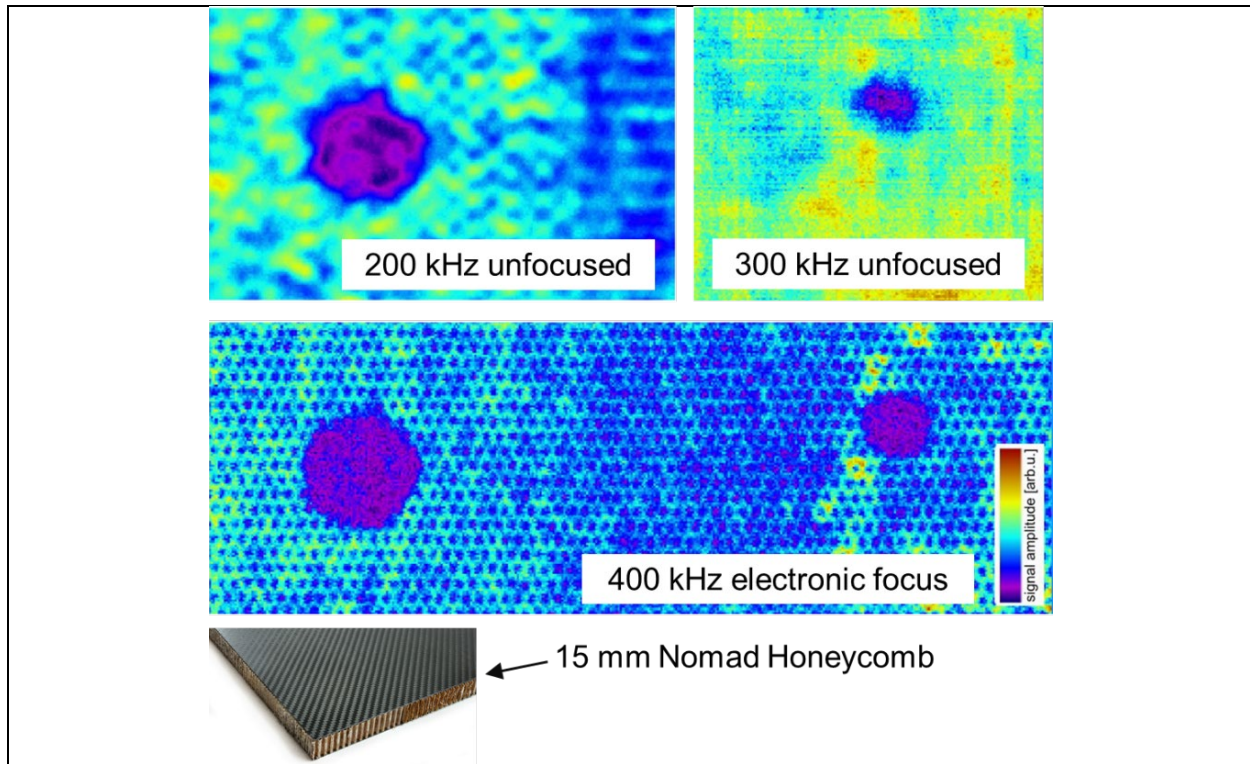


Figure 30. C-scans of Nomad honeycomb CFRP panel with two delaminations between the top skin and the core. Data was acquired using ACUT probes with three different excitation frequencies (200 kHz, 300 kHz and 400 kHz). Courtesy of Sonotec US.

The honeycomb sample had two circular delaminations between the skins and the core, which was successfully confirmed by the C-scans at all frequencies. The full surface of the sample was scanned using CF400 probes, and only one delamination at a time using CF200 and CF300 probes, respectively. Resulting C-scans in Figure 30 revealed that electronic focusing improved the spatial resolution up to a point when individual honeycombs could be seen.

2.2.4. Comparisons of TT-ACUT C-Scans with Projection X-Ray Radiography

Simulated damage: detection of open delamination (Teflon inserts) and excessive glue

A CFRP honeycomb panel with 18 circular Teflon inserts, damaged honeycombs and excessive adhesive glue was scanned using CF200 probes at normal incidence with 2 mm step resolution. Sizes of inserts were 20 mm, 10 mm and 5 mm in diameter. Most inserts were placed in different CFRP layers and some between the CFRP skins and honeycomb. Hence, physical gaps existed between the layers, and delaminations could be classified as open delaminations. Corresponding ACUT C-scan is shown in Figure 31a. Projection X-ray imaging of the same panel was done by Sonotec partners using a high-definition X-ray camera at normal ray incidence. X-ray result is presented in Figure 31b.

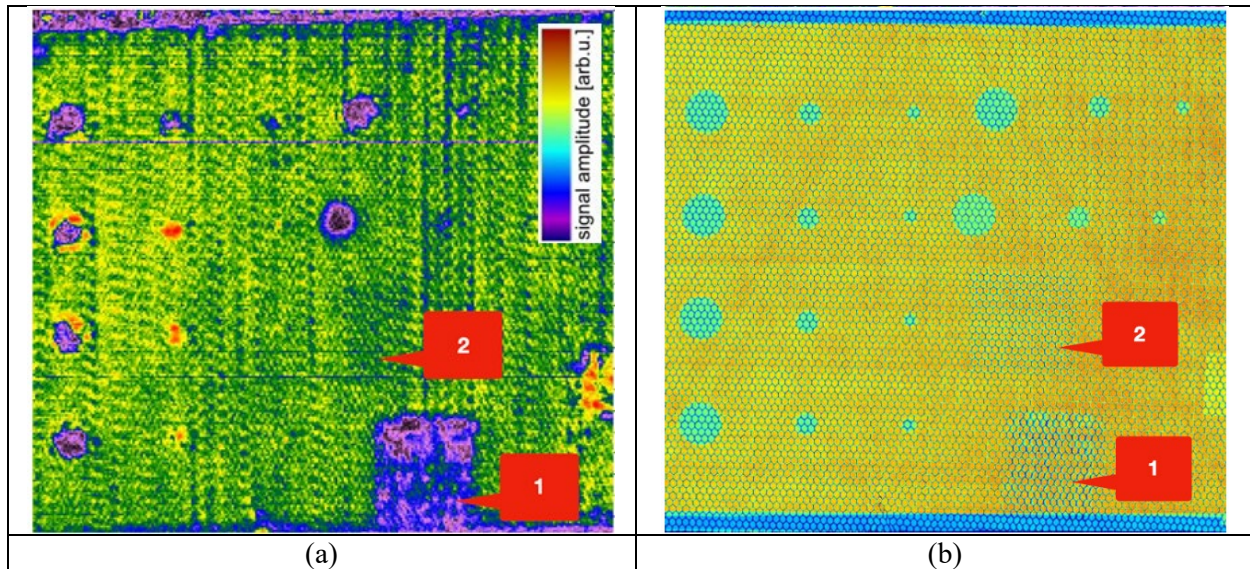


Figure 31. (a) ACUT C-scan of the honeycomb part; (b) X-ray image of the honeycomb part (courtesy of Sonotec US). Region 1 – damaged honeycombs; region 2 – excessive glue between the CFRP skin and honeycomb structure.

Comparing Figure 31a and Figure 31b reveals that X-ray detected all simulated damages in the panel, while ACUT missed some of the smallest Teflon inserts. However, the ACUT scan configuration was not optimal in the experiment. Findings in Quarter I of the report showed that the ACUT results could be significantly improved by properly adjusting the incidence angle θ of the transmitting and receiving probes. Projection X-ray highlighted all damages in the panel since Teflon inserts (open delaminations) and excessive glue introduced detectable attenuation of the emitted radiation.

Realistic damage: characterization of closed delamination after low velocity impact

Figure 32 and Figure 33 demonstrate performance of ACUT and projection X-ray on multi-layer CFRP samples with delaminations introduced by low velocity impacts. In this case, the delaminations were considered closed since there were no Teflon inserts and the laminas could be in contact. ACUT C-scans and X-ray images are plotted in gray scale for better visual comparisons.

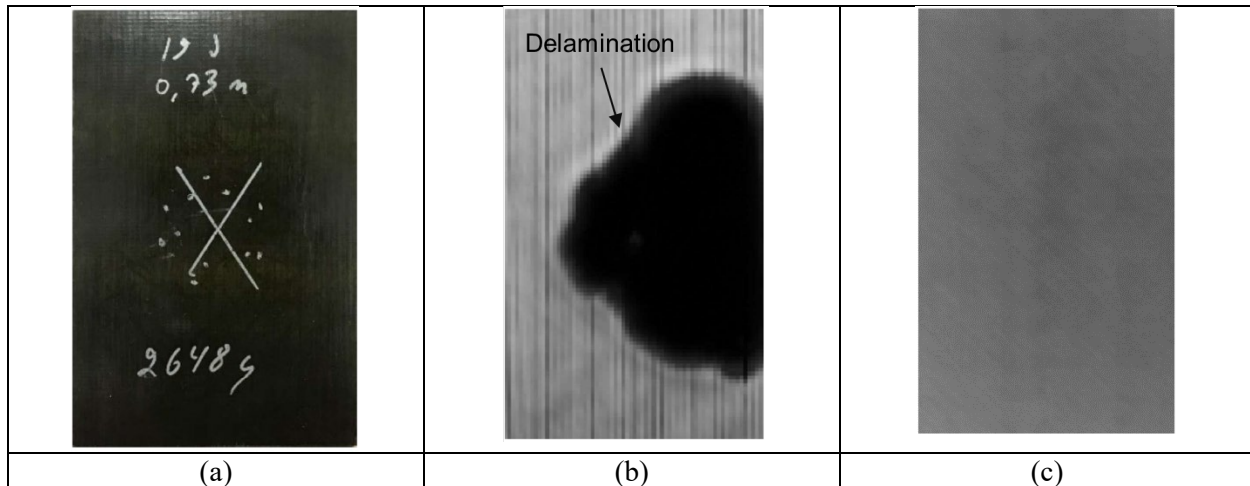


Figure 32. (a) CFRP sample 1 after low velocity impact; (b) corresponding ACUT C-scan; (c) X-ray image (courtesy of Sonotec US).

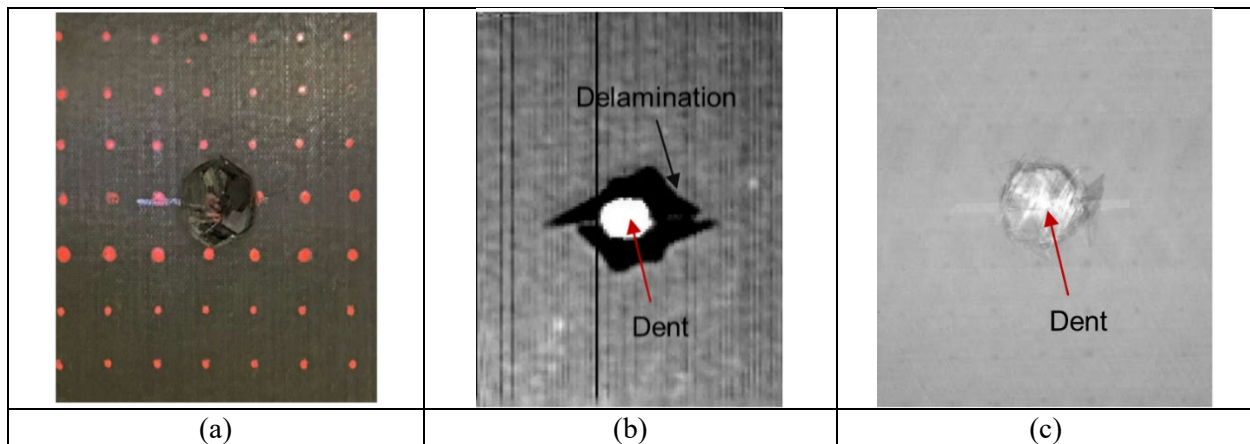


Figure 33. (a) CFRP sample 2 after low velocity impact; (b) corresponding ACUT C-scan; (c) X-ray image (courtesy of Sonotec US).

Obtained results show that ACUT accurately detects closed interlaminar delaminations. In the case of ultrasonic wave propagation through the test sample, delamination introduces a microscopic interface that reflects the incident wave energy. In contrast, projection X-ray radiography provides poor detection of closed delaminations since the introduced attenuation is minimal and often goes beyond the sensitivity and spatial resolution of the X-ray system. X-ray imaging of impact damage in CFRP test parts can be enhanced by using liquid dye penetrants or by implementing more advanced techniques such as laminography. Both ACUT and X-ray systems can successfully detect fiber damage and matrix cracking in the form of a dent left by an impactor tip. This is explained by the fact that both ultrasonic waves and X-rays are scattered in this region.

2.3 High-Speed Multi-Channel ACUT Gantry System at CVRC

In Quarter III, the MSU team integrated the acquired ACUT module with in-house XYZ gantry at CVRC. (Tasks iv-vi). The ACUT system was successfully validated on X-brace parts. Key accomplishments of Quarter III are summarized below:

- a. developed and debugged C#, LabView scripts and graphical user interfaces (GUI) for control of the high-power pulser-receiver (Sonoair) and high-speed ADC converter (GaGe);
- b. successfully verified performance of each 4-channel hardware module in the ACUT system (signal generator & pulse amplifier, receiving amplifier and ADC);
- c. ruggedized setup; successfully integrated new ACUT system with in-house XYZ gantry;
- d. identified optimal inspection parameters and successfully acquired first through-transmission C-scans of X-brace test parts by activating one channel of the ACUT system; accurately detected all embedded defects (Teflon inserts) in X-braces and achieved <2 min scan time per a single channel (scan area: $\sim 8 \times 10 \text{ in}^2$); made quantitative comparisons of the obtained results with high-resolution water immersion ultrasonic scans;
- e. established advanced signal processing algorithms for defect detection and sizing using ACUT scan data; validated the algorithm on C-scans of X-brace parts by detecting delaminations from $\sim 0.25 \times 0.25 \text{ in}^2$ to $\sim 0.75 \times 0.75 \text{ in}^2$;
- f. ordered 3 extra pairs of CF-200 ACUT transducers in order to assemble a 4-element transducer array for rapid scanning.
- g. developed a modular C# interface that ties together all scripts for hardware control including robot controllers, XYZ gantries, position encoders, ACUT pulser-receiver, ADC, and eddy current instruments (e.g., Ectane 2).

2.3.1. Hardware integration and software development

The ACUT pulser-receiver, industrial PC, and other hardware components of the novel NDE system were mounted on a portable rack stand as shown in Figure 34. In order to facilitate experiments with air-coupled probes, the MSU team interfaced the PC to an in-house built XYZ gantry with position encoders. The gantry could fit relatively large and slightly curved CFRP parts.

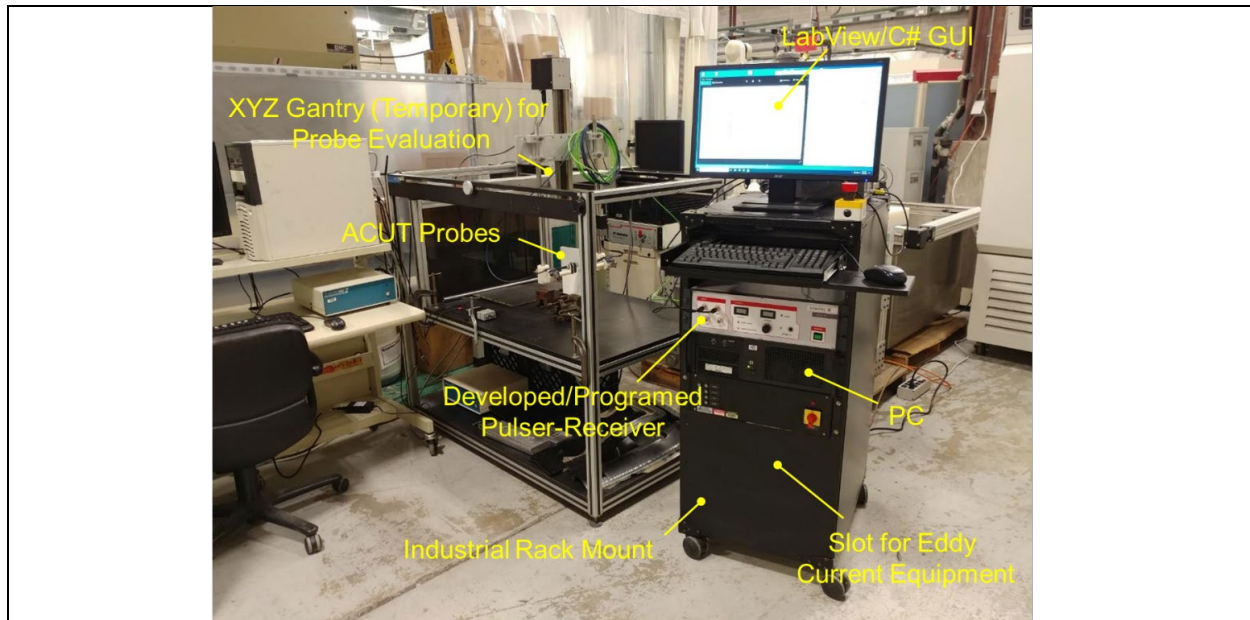


Figure 34. Ruggedized NDE system and XYZ gantry for inspection of CFRP parts.

Scripts and graphical user interfaces (GUI) for control of high-power 4-channel pulser-receiver and ADC digitizer were written in C# and Labview. The MSU team also performed extensive testing of all hardware components to validate their performance.

Testing of multi-channel digital signal generator and sending power amplifier

Block diagram of the ACUT pulser-receiver module is shown in Figure 35. The unit has 4 independent channels controlled via field programmable gate array (FPGA) with 10 ns clock. Generator provides +3.3 V logical signals and drives the sending amplifier. Sending amplifier is a class D amplifier with total power output up to 2 kW. TTL square pulses can be amplified up to 400 V such that ACUT transducers would generate strong acoustic wavefields in the air.

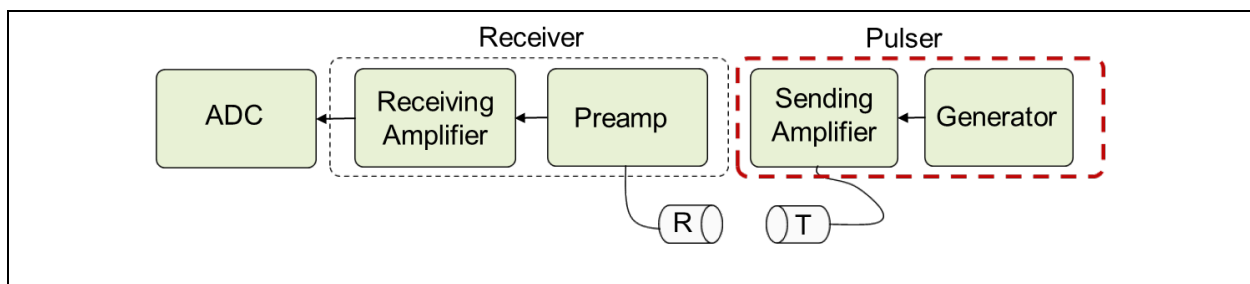


Figure 35. Block-diagram of the pulser-receiver: testing of signal generator and power amplifier (red box).

Figure 36 demonstrates the GUI for pulser-receiver control. User can set such parameters as output voltage, square pulse frequency, phase shift and burst rate for each channel independently that provides much flexibility for rapid ACUT inspections. Menu on the right in Figure 36 shows values of pulser-receiver's state registers as well as feedback from voltage, current and temperature sensors.

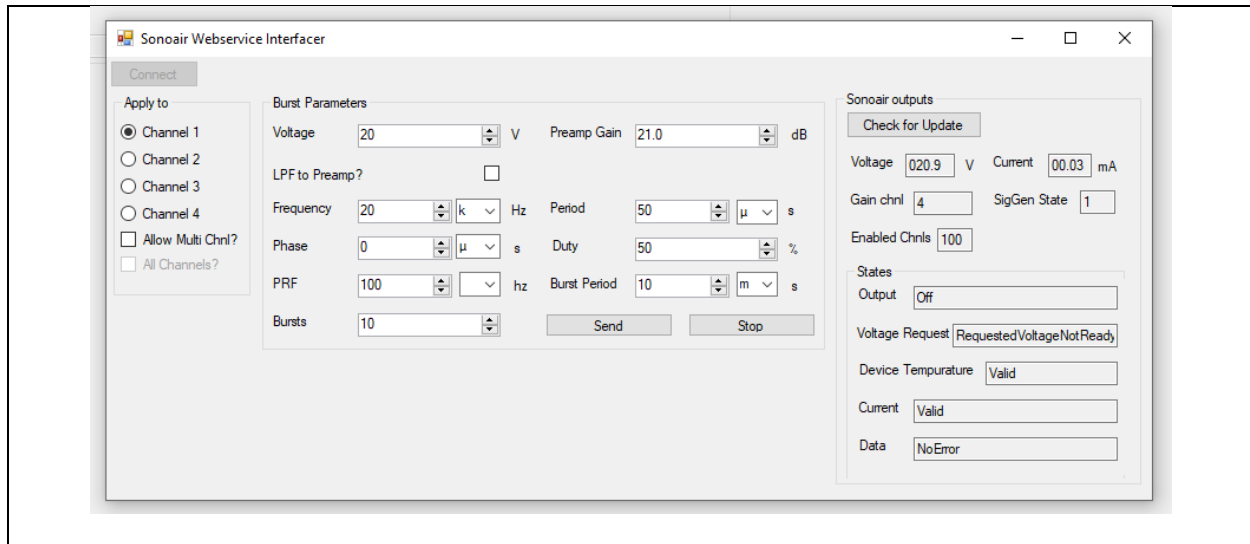


Figure 36. Developed graphical user interface for pulser-receiver control.

ACUT pulser was tested by connecting four CF-300 transducers to its outputs. Voltages across the transducers were measured using a DSO-1004A digital oscilloscope. Four different sets of driving signals were used as illustrated in Figure 37. In Figure 37a, identical driving signals were generated (4 pulses, 100 kHz, 50 Vpp). In Figure 37b, frequency of pulses was successfully modulated (100, 150, 200 and 250 kHz). Figure 37c demonstrates the case with different number of square pulses (2,3,4 and 5). Finally, Figure 37d shows the outputs of the amplifier when it is programmed to generated pulse bursts shifted by a certain period of time (1,4 and 9 μ s w.r.t. channel 1).

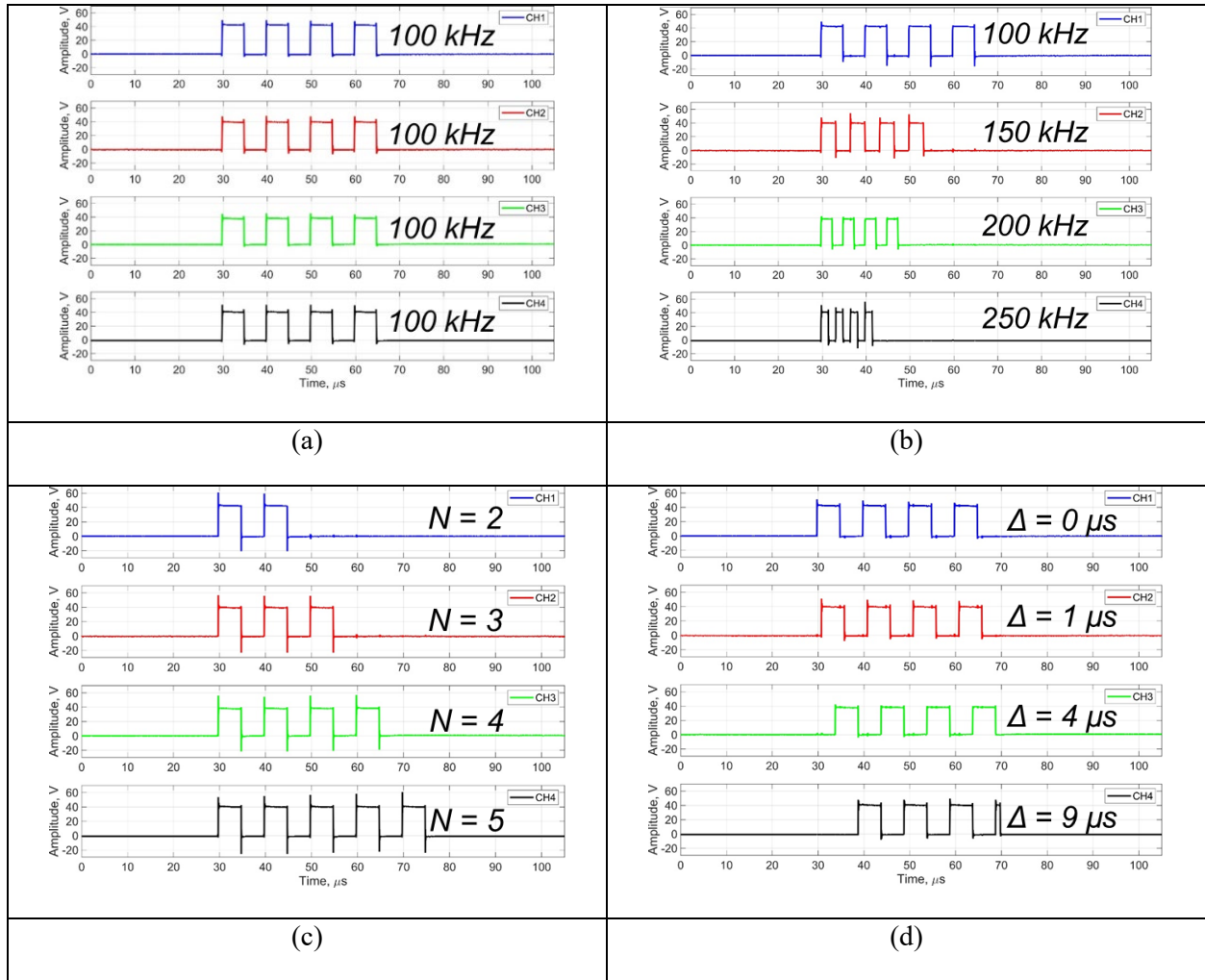


Figure 37. Experimental validation of ACUT power amplifier outputs: (a) identical pulse sequences on all channels; (b) frequency modulated square pulses; (c) pulse trains of different durations; (d) pulse trains with different time offsets.

All test results were accurate and repeatable. Hence, it was concluded that programming was done properly, and the pulser-receiver module functioned without any issues.

Testing of 4-channel receiving amplifier and analog-to-digital converter

Multi-channel receiving amplifier helps to measure weak ultrasonic signals picked up by ACUT probes through the air. Analog-to-digital converter (ADC) digitizes the acquired acoustic signals and transfers data into computer's RAM. Both modules of the pulser-receiver are highlighted in the block-diagram shown in Figure 38.

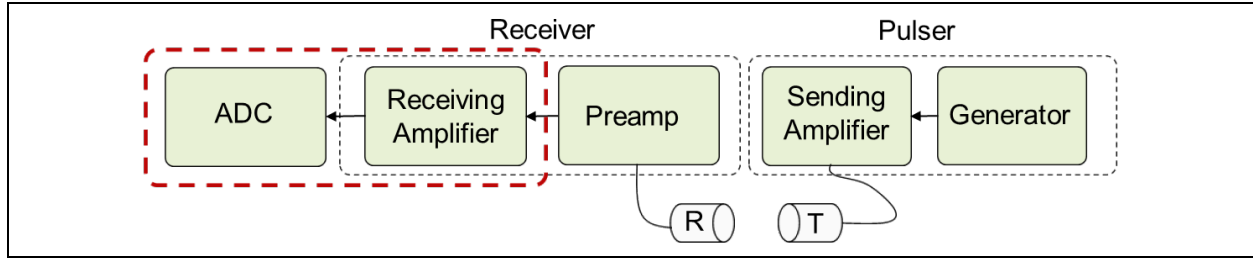


Figure 38. Block-diagram of the pulser-receiver: testing of receiving amplifier and digitizer (red box).

The gain of the receiving amplifier is controlled programmatically and can be set to an arbitrary value between 0 dB and 120 dB. In addition, 40 dB out of 120 dB of total gain are obtained by using four external pre-amplifiers (see Figure 38), which should be kept as close as possible to the ACUT receiving probes. Voltage outputs of the receiving amplifier are limited to $\pm 1.5V$ on the analog level in order to protect sensitive 16-bit ADC (GaGe digitizer) from over-voltage.

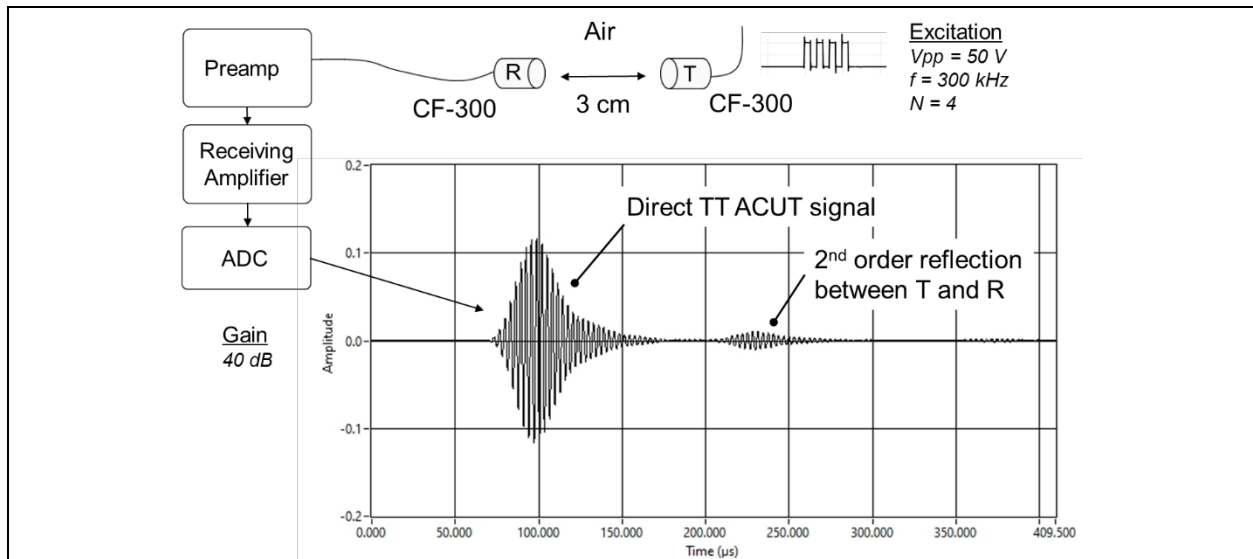


Figure 39. Experimental validation of ACUT receiving amplifier and ADC (digitizer).

Results of receiving amplifier and digitizer testing are shown in Figure 39. In this case, ultrasonic waves were transmitted and received using a pair of CF-300 ACUT probes straight through the air. Gain of the signal was successfully controlled via GUI developed in C#. Acoustic signal of $\sim 400 \mu s$ duration was sampled at a rate of 10 MS/s. ACUT pulser, receiving amplifier and GaGe digitizer were synchronized using TTL logic triggering signals.

The GaGe ADC was programmed to operate as a live scope and to save the acquired multi-channel data at a maximum rate of ~ 600 waveforms per channel per second. Figure 40 displays a snapshot of acoustic waveforms registered by the digitizer and digitizer's GUI.



Figure 40. Developed graphical user interface for digitizer control and sensor data display.

In Figure 40, only channel 1 was activated, and the other three input channels were measuring noise. Developed and debugged GUI for the digitizer allows user to select different options for data acquisition and data display, such as sampling rate, measurement voltage range, data depth, remote triggering and many more.

2.3.2. Validation of high-speed ACUT gantry system: 1-channel data acquisition in TT mode

Performance of the assembled ACUT system was successfully validated by scanning CFRP X-braces from Plasan Composites. X-brace #3 from Phase I was placed in the XYZ gantry as shown in Figure 41a and Figure 41b. Inspection was performed in a through-transmission mode at normal wave incidence using a pair of CF-200 transducers with center frequency of 200 kHz. Only one channel of the digitizer was activated at this time for initial testing. A typical acoustic waveform (A-scan) after wave propagation through the CFRP part is shown in Figure 41c. Waveforms such as the one depicted in Figure 41c are acquired during the scan process, and their maximum amplitudes (peak-to-peak voltages V_{pp}) are automatically measured in order to build a C-scan image of the part.

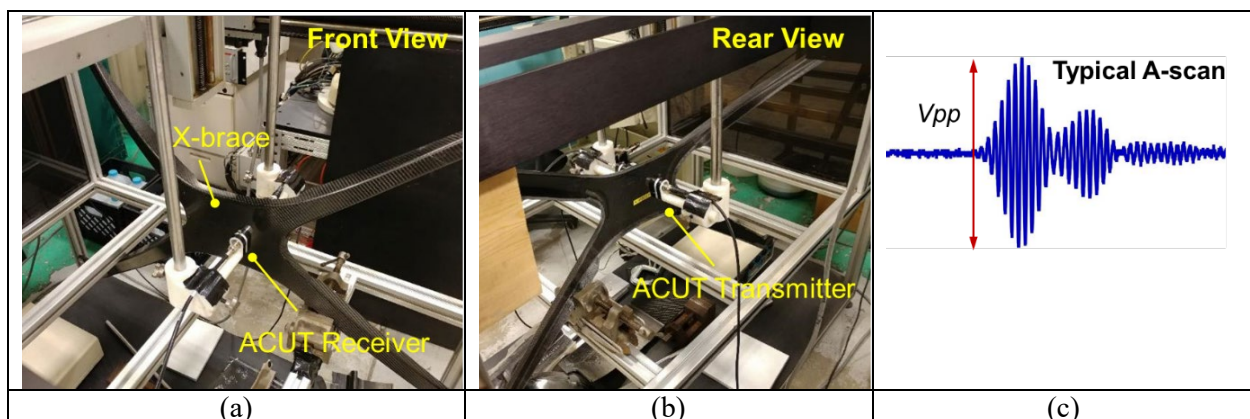


Figure 41. Gantry set-up for scanning X-brace part: (a) front view; (b) rear view; (c) typical ACUT signal (A-scan), V_{pp} peak-to-peak voltage is measured in order to plot a C-scan.

Immersion UT C-scans from Phase I of the Project were used as a ground truth for validating the ACUT technique. Figure 42a shows the central region ($\sim 8 \times 10 \text{ in}^2$) of the X-brace #3 selected for scanning. Immersion UT inspection was conducted in the pulse-echo mode using a focused $\varnothing 12 \text{ mm}$ transducer with resonant frequency of 5 MHz. A-scan waveforms were averaged 8 times. A detailed immersion UT C-scan was acquired with high spatial resolution ($< 1 \text{ mm}$) at a low speed. The corresponding result is presented in Figure 42b. Immersion UT C-scan showed that X-brace #3 had three interlaminar delaminations of different sizes (see Figure 42b).

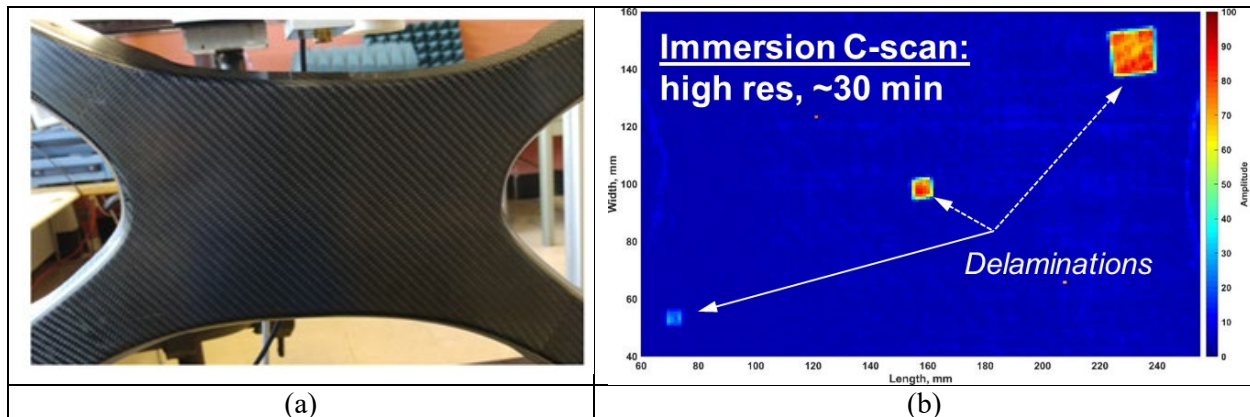


Figure 42. Immersion UT inspection of X-brace part: (a) scanned region; (b) immersion C-scan (pulse-echo mode, $f = 5 \text{ MHz}$, spherically focused transducer, $\varnothing 12 \text{ mm}$).

The same region of X-brace #3 was inspected using the newly developed ACUT system. A-scans were averaged 8 times, and acoustic bursts were generated 400 times/s. Figure 43a demonstrates the ACUT C-scan with spatial resolution comparable to that of the immersion UT C-scan from Figure 42b. In Figure 43a, delaminations could be easily identified that validated the ACUT technology. At the same time, the ACUT C-scan detected a tape label glued to the X-brace #3 (see Figure 41b) and some fiber wrinkles.

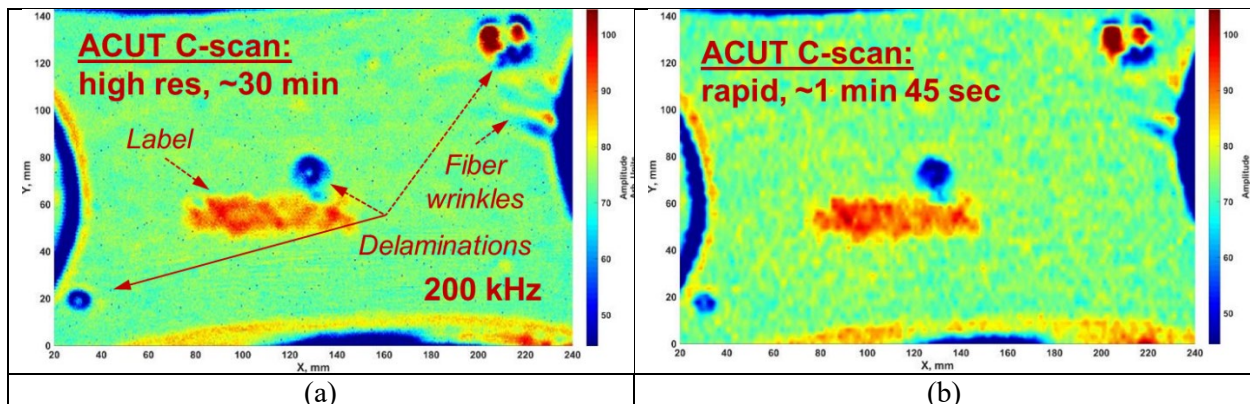


Figure 43. ACUT inspection of X-brace part: (a) high-resolution, low speed C-scan; (b) $\sim 2 \text{ mm}$ resolution, high-speed C-scan.

In order to reduce the time of the ACUT inspection, the A-scan averaging was deactivated, the linear gantry speed was set to its maximum values along both scan and index axes, and the spatial resolution was reduced to $< 2 \text{ mm}$. The C-scan process took $\sim 1 \text{ min } 45 \text{ seconds}$ to complete with the final results presented in Figure 43b. Despite the drastically reduced scan time, the C-scan in Figure 43b showed no significant degradation of image quality as all three delaminations and part label were clearly visible. Rapid ACUT C-scan had more speckles owing to electrical noise and vibrations of the gantry. The noise can be reduced by applying a digital band-pass filter to the A-scans. The scan time can be further reduced 1) by using high-speed robotic

arms and/or 2) by increasing the excitation burst rate.

2.3.3. Image processing algorithm for quantitative estimation of damage size

The MSU team analyzed immersion UT and ACUT inspection data and developed signal processing algorithms for defect detection and sizing (Task vi). C-scan images of X-brace #3 showed that defects in CFRP parts appeared as regions of higher or lower acoustic wave energies compared to defect-free background. These regions can be accurately identified by following a 4-step procedure:

- segment ultrasonic C-scan image by identifying the regions of interest (ROI);
- calculate the median value of the C-scan in order to determine the average “defect-free” image intensity (baseline);
- set the sensitivity threshold based on the estimated power of speckle noise in the image;
- find all pixels with intensities $I > (\text{baseline} + \text{threshold})$ or $I < (\text{baseline} - \text{threshold})$ and calculate damage area.

The flowchart of the proposed algorithm and its intermediate steps are shown on the immersion UT C-scan (Figure 44) and on the ACUT C-scan (Figure 45) of X-brace #3, in which three defects are quantitatively evaluated.

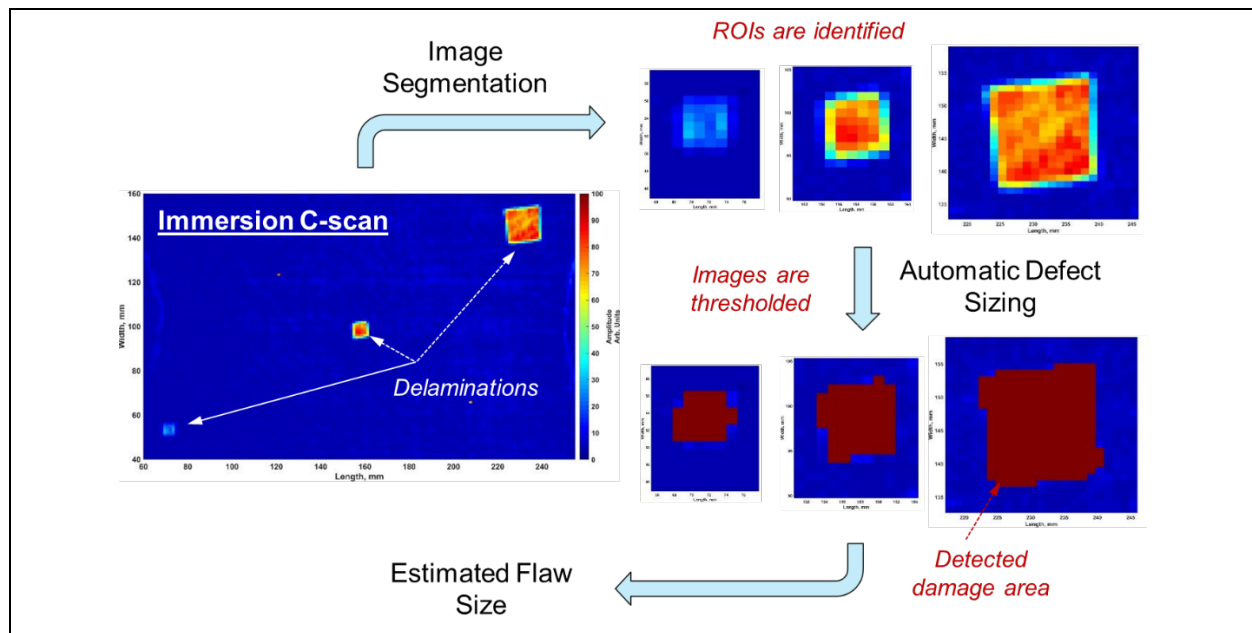


Figure 44. Post processing of water immersion UT C-scan: image segmentation and defect sizing.

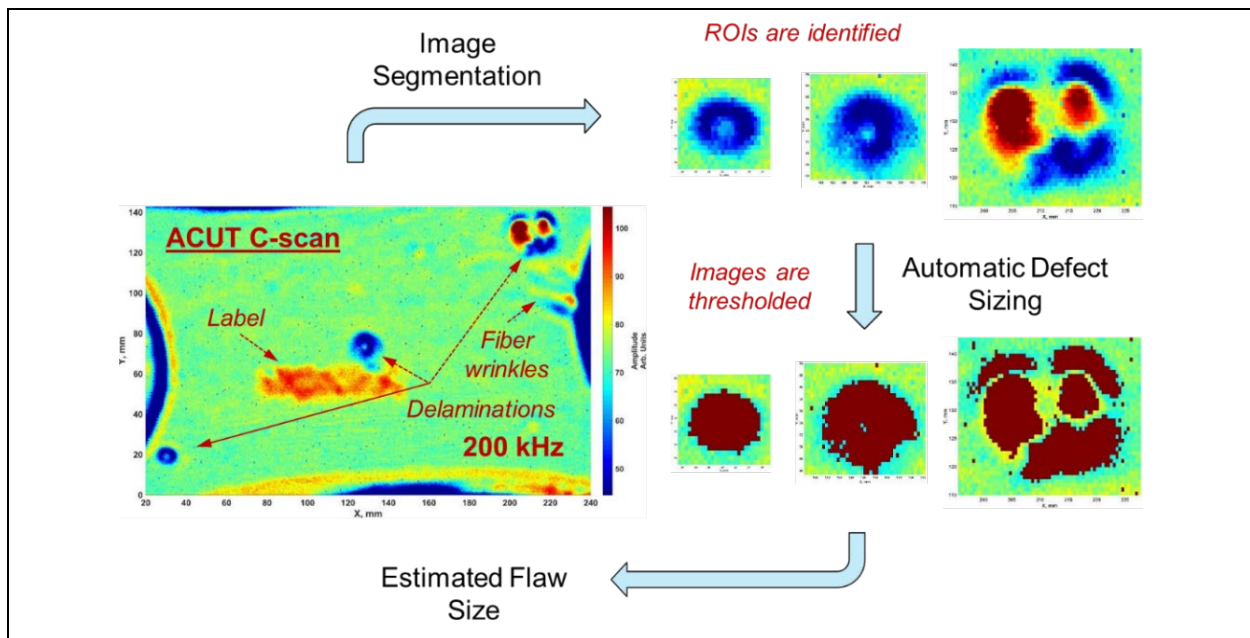


Figure 45. Post processing of ACUT C-scan: image segmentation and defect sizing.

Figure 46 shows quantitative comparisons of delamination areas estimated from the immersion UT and ACUT C-scans. The MSU team didn't have CAD drawings of X-brace #3 with locations and sizes of embedded defects. However, the inspection results indicated that interlaminar delaminations were approximately $6 \times 6 \text{ mm}^2$, $10 \times 10 \text{ mm}^2$ and $18 \times 18 \text{ mm}^2$.

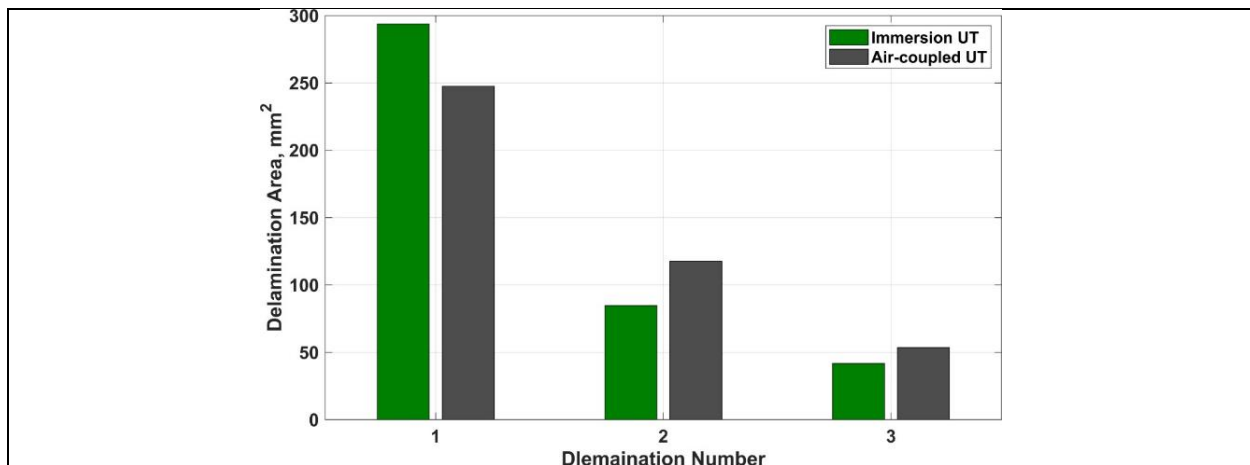


Figure 46. Comparisons of delamination sizes obtained by post-processing of water immersion UT and ACUT C-scans.

Small defects in ACUT C-scans may appear 15% larger compared immersion UT owing to larger aperture size of transducers and larger wavelength of acoustic waves. The largest defect appears 15% smaller in the ACUT C-scan due to ultrasonic wave diffraction around the edges.

2.3.4. Design and optimization of TT-ACUT array probes

In Quarter VI, the MSU team designed and optimized array ACUT probes for high-speed multi-channel NDE of FRP composites. Key accomplishments are summarized below.

Multi-element ACUT probe design & optimization:

- i. performed acoustic wavefield imaging on composite samples and visualized propagation of ultrasonic waves in real time;
- ii. successfully measured beam interference between multiple ACUT transducers;
- iii. studied influence of acoustic wave reflections from part's surface on acquired ACUT signals;
- iv. developed and optimized acoustic cones for beam shaping and minimization of crosstalk;
- v. successfully mitigated crosstalk between the probes using designed cones, time-gated excitation and sensing;
- vi. increased the pulse repetition frequency (PRF) of excitation to 400 pulses/s;
- vii. successfully performed qualitative comparisons of ACUT signals acquired with piezoceramic and piezocomposite probes with integrated pre-amplifiers.

ACUT hardware & software optimization:

- viii. optimized XYZ gantry system for high-speed ACUT data acquisition:
 - improved and debugged C# and LabView scripts;
 - installed 3 optical rotary encoders to accurately track probe's position;
 - installed and programmed multi-channel digital pulse counter from National Instruments for reading encoder outputs;
- ix. successfully programmed high-speed parallel data acquisition using GaGe CSE 447 digitizer;
- x. implemented data saving in binary format and data replay.

Successful validation of high-speed multi-channel ACUT NDE:

- xi. developed & verified signal processing algorithms for merging multi-channel ACUT data;
- xii. successfully performed multi-channel C-scans of composite X-braces (through-transmission mode, 2.5 mm line-to-line resolution) and achieved scan times of ~1 min 30 s for ~12×27 in² scan area (faster scanning is possible; reached maximum speed/acceleration of the available XYZ gantry).

Configurations of ACUT transducers for multi-channel high-speed NDE

Figure 47 demonstrates linear and staggered arrays for acoustic signal pick up. The main advantage of a linear array is the ability to adjust the effective spacing between probe apertures by tilting the array with respect to its scan axis as shown in Figure 47a. It is anticipated that linear array would be more suitable for NDE of flat and slightly curved parts. On the other hand, the staggered array showed in Figure 47b is more compact so that the ultrasonic signals are less affected by changes of part's curvature.

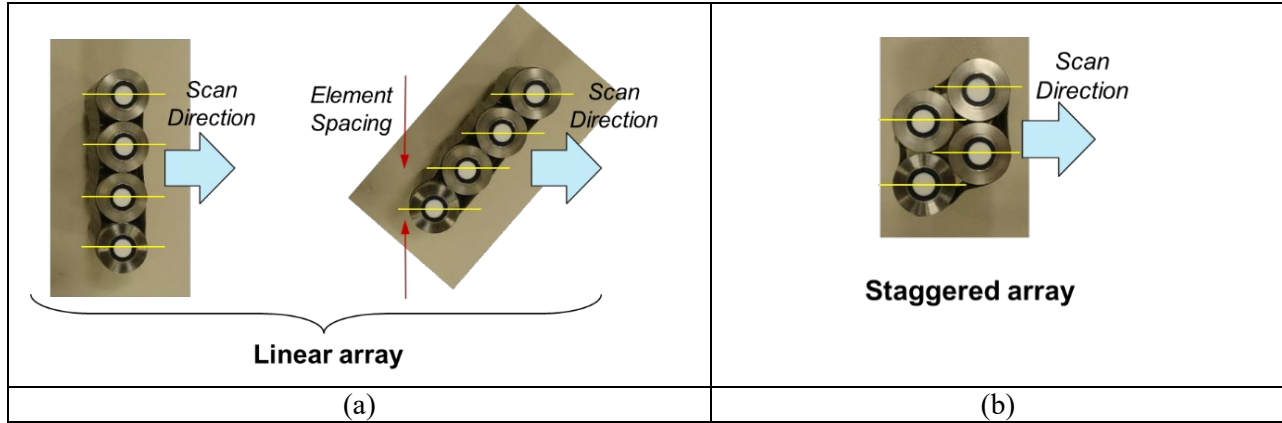


Figure 47. CF-200 ACUT transducers arranged as a (a) linear array; (b) staggered array.

Multi-channel TT-ACUT probe design and optimization

Acoustic characterization of transducers

MSU acquired four pairs of CF-200 transducers ($f = 200$ kHz) and two pairs of CF-300 transducers ($f = 300$ kHz) for ACUT NDE of composites. Their acoustic fields and directivity patterns were characterized using experimental setup shown in Figure 22. Transducers were connected to a square wave pulser, and generated acoustic pressure was measured using a broadband microphone.

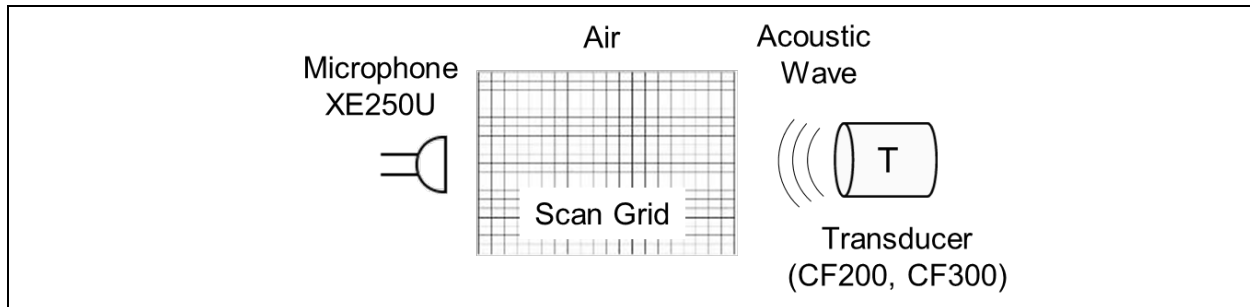


Figure 48. Experimental setup for ACUT transducer characterization.

Typical results of transducer characterization are presented in Figure 49. Figure 49a shows the beam shape of a CF-200 probe, and Figure 49b shows its directivity pattern. CF-200 transducers generate strong acoustic pressure as the level of the received signal drops by 3 dB only at a distance of ~ 35 mm. Their beam waist is ~ 20 mm (see Figure 49a). Weak side lobes (-20 dB) are present at $\pm 20^\circ$ (Figure 49b). The relatively wide beam waist and side lobes indicate that beam shaping and time-gated excitation are necessary to avoid crosstalk between transducers, when array probe is designed.

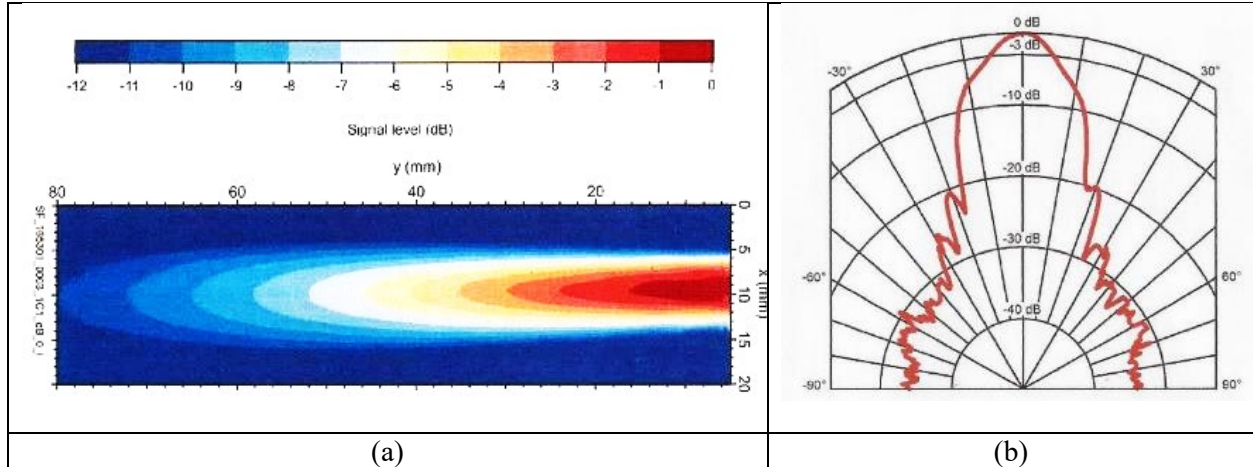


Figure 49. CF-200 transducer characterization: (a) acoustic beam shape in the air; (b) directivity pattern.

Multi-channel excitation and acoustic beam interference

A pair of plastic holders was 3D printed at CVRC for studying beam interference between multiple ACUT probes. Figure 50 shows the 4-channel linear array of CF-200 (or CF300) transducers. A heavy fixture holds excitation transducers in the plane parallel to the gantry bed. Faces of receiving transducers stay parallel to the faces of excitation transducers (no roll, pitch or yaw). However, the receiving sensor array can be moved freely as it is attached to the search tube of the XYZ gantry.

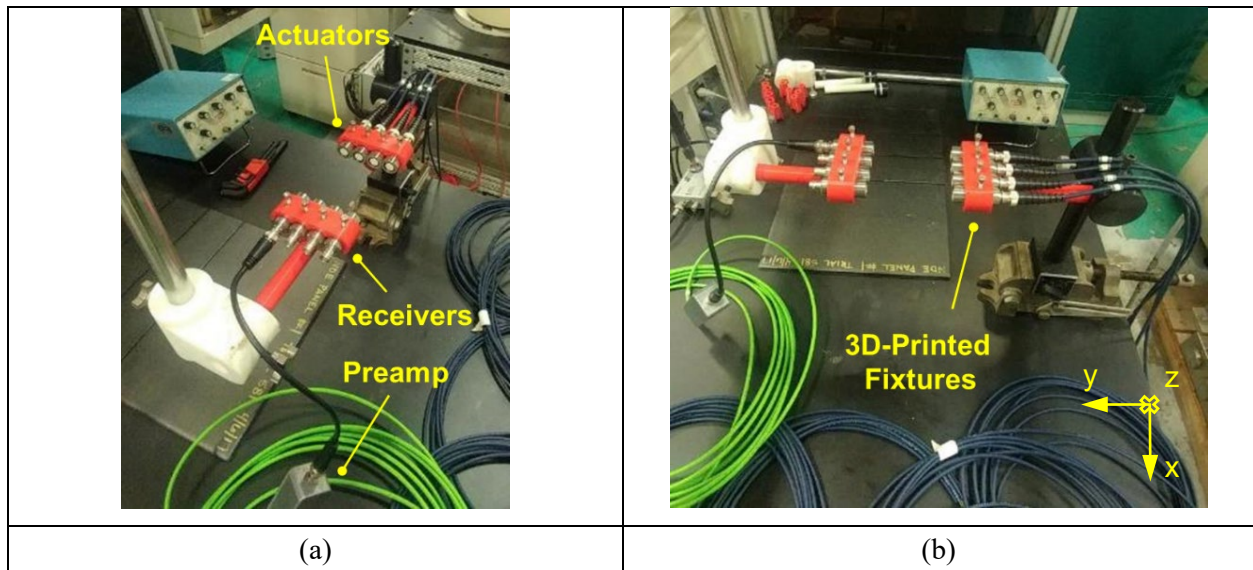


Figure 50. Linear ACUT array: (a) top view; (b) side view.

Actuators are connected to the outputs of the 4-channel pulser. They can be excited simultaneously or with different time delays at 10 ns steps. One receiver is activated in order to measure the acoustic field at some distance from the excitation array. Raster scans are acquired in xz -plane (see Figure 50b).

As shown in Figure 51a, there are no gaps between excitation transducers, which provides the smallest size of the linear array. However, in this case, acoustic beams of transducers will interfere, if excited simultaneously. Beam interference results in constructive and destructive superpositions of acoustic waves depending on their phases, which introduces high and low amplitude spots in measured signals (A-scans). Crosstalk renders signal analysis complicated and may show up as unwanted artifacts in C-scans.

Three different strategies of mitigating crosstalk are schematically illustrated in Figure 51b, Figure 51c and Figure 51d, respectively. The simplest approach is to split the probes in space, which is not an acceptable solution, since it increases the length of the array and reduces the capability to scan edges of composite parts (see Figure 51b). Better options for minimizing crosstalk are beam focusing (see Figure 51c) and time-gated excitation (see Figure 51d).

Beam focusing and clipping is achieved by attaching cones to active faces of ACUT transducers. Cones should be made of materials with high acoustic attenuation (e.g., foams, rubbers, etc.) in order to eliminate multiple beam reflections from their internal surfaces. The shape of a cone, its length and outer diameter can be optimized so as to reduce crosstalk, but at the same to maintain acceptable signal level at the receiver.

Finally, time-gated excitation is the most effective approach for avoiding beam interference. In a time-gated excitation, acoustic transducers are activated in a sequence, and excitations are delayed by certain time intervals. Lengths of these intervals should be sufficiently large to let previously generated waves and their reflections decay rapidly.

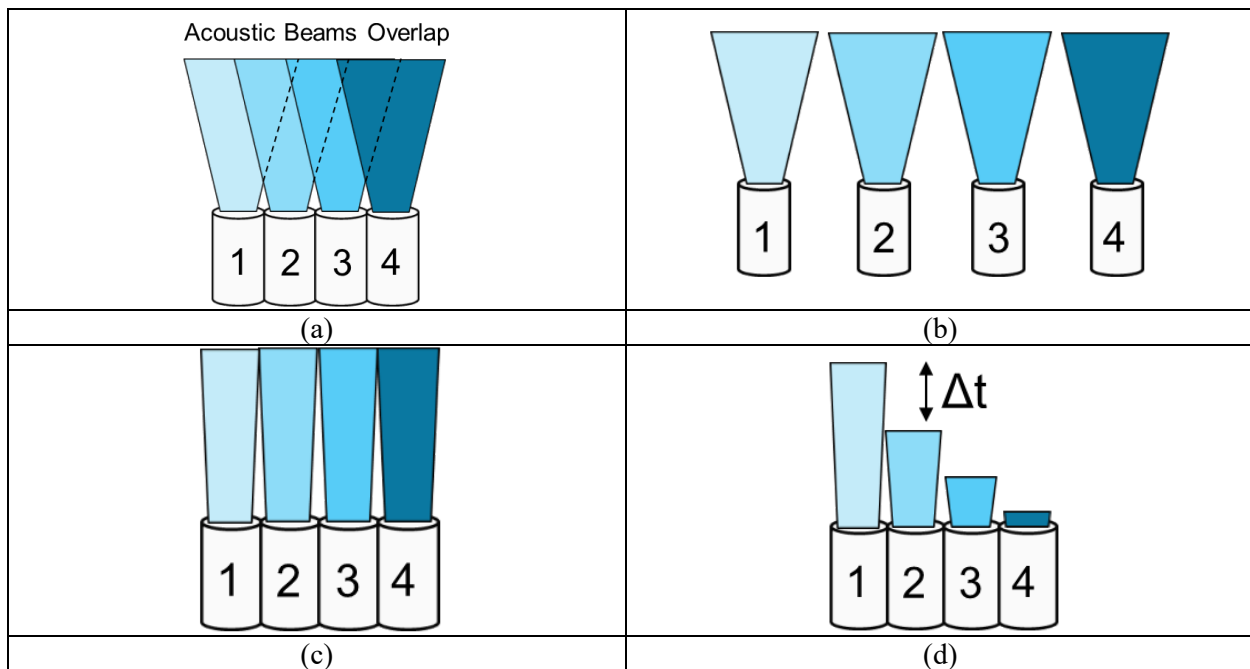


Figure 51. Strategies for reducing beam interference: (a) crosstalk between the probes; (b) spatial separation of the probes; (c) beam focusing & clipping; (d) time-gated excitation & sensing.

Excitation sequence plays important role in time-gated mitigation of crosstalk. For instance, the sequence 1-2-3-4 would be the simplest one to implement. However, the sequence 2-4-1-3 would be more advantageous, since there is more spatial separation between the probes, which provides higher attenuation of acoustic waves and shortens signal decay intervals.

Experimental Study I: Acoustic beam interferences of CF-300 ACUT probes

Acoustic beams of CF-300 probes ($f = 300$ kHz) and their interference patterns in the air were measured using the setup schematically shown in Figure 52. Distance between transmitters and receiver was ~ 70 mm. First three measurements were acquired by activating transmitter probes one at a time as labeled in Figure 52. The 4th measurement was acquired by activating all 3 probes simultaneously. The data acquisition sample rate was 2 Ms/s.

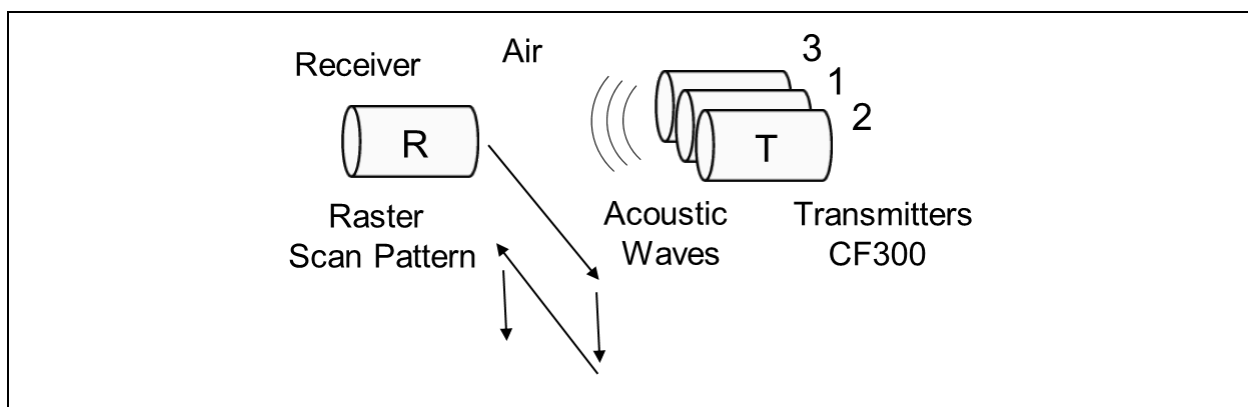


Figure 52. Experimental study I. Setup for measuring crosstalk between three CF-300 ACUT probes.

Typical measurement (A-scan) is shown in Figure 53. In Figure 53, the energy of the signal in the time-gate (Gate 1, labeled as a yellow line segment) is used as a feature for a raster scan (C-scan). Position of the time-gate was the same for all experiments in this study.

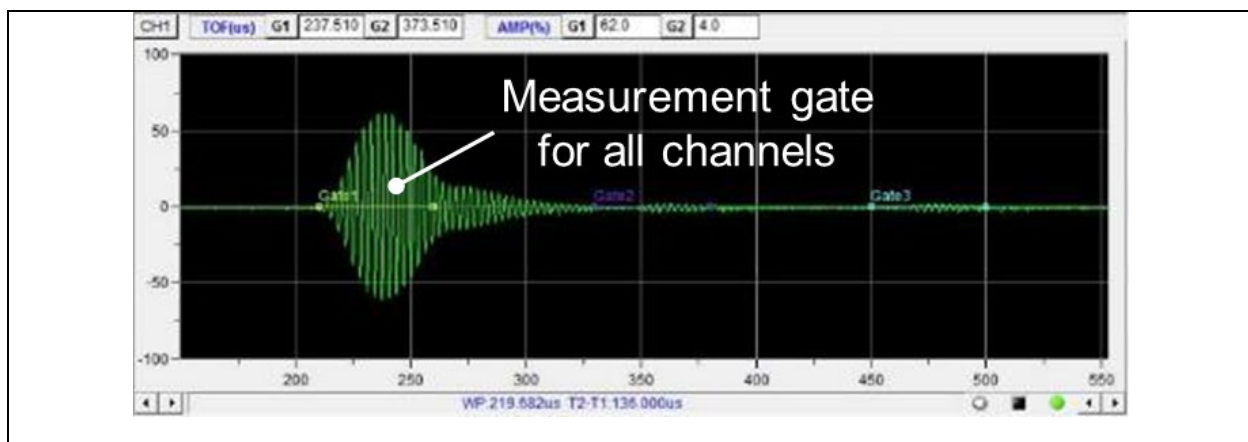


Figure 53. Experimental study I. Crosstalk between CF-300 probes in the air, typical A-scan. Receiver is aligned with Transmitter 1 (T1).

Resulting C-scans are shown in Figure 54. C-scans show that beam cross-sections of CF-300 probes are nearly circular, and that Transmitter 3 (see Figure 54c) generates $\sim 25\%$ less acoustic pressure than Transmitter 1 (see Figure 54a) and Transmitter 2 (see Figure 54b). When all transmitters are activated simultaneously, there is a significant distortion of beam profiles, and the acoustic field is not a mere summation of acoustic fields produced by individual transmitters (see Figure 54d). This is a direct result of beam interference discussed earlier.

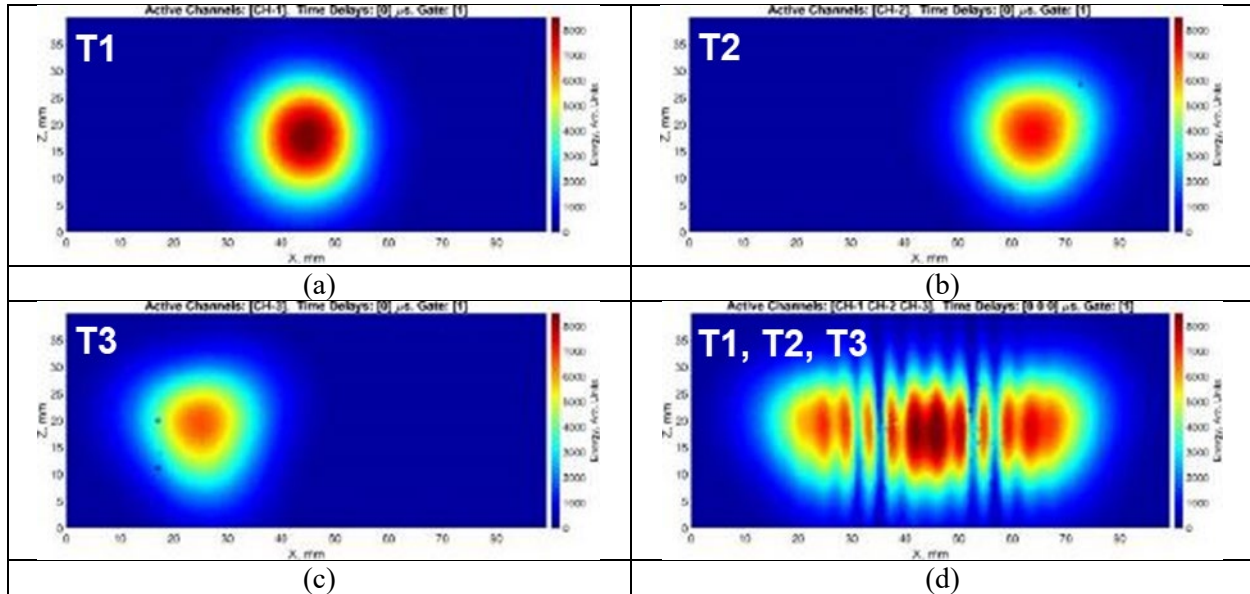


Figure 54. Experimental study I. C-scans, activated transmitters: (a) Transmitter 1 (T1); (b) Transmitter 2 (T2); (c) Transmitter 3 (T3); (d) all transmitters at the same time (T1, T2, T3).

Figure 55 demonstrates time-gated excitation and sensing aimed at reducing the inter-channel crosstalk. Excitation pulse trains of Transmitter 2 and Transmitter 3 are delayed with respect to Transmitter 1 by $120\ \mu\text{s}$ and $240\ \mu\text{s}$, respectively (see Figure 55a). The acoustic signal measured by the receiver is now evaluated in 3 separate gates: Gate 1 (yellow), Gate 2 (purple) and Gate 3 (cyan) as illustrated in Figure 55b. The receiver probe is aligned with the Transmitter 3 (T3).

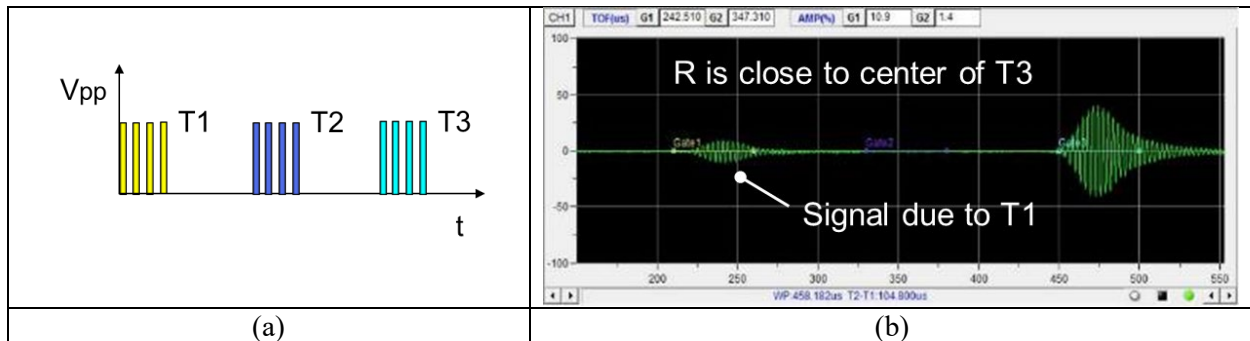


Figure 55. Experimental study I. Time-gated excitation: (a) pulse trains with time delays $[0, 120, 240]\ \mu\text{s}$; (b) typical A-scan acquired when the receiver is aligned with Transmitter 3 (T3).

Figure 55b shows that the receiving probe senses some signal from Transmitter 1 (T1) in Gate 1 and virtually no signal from Transmitter 2 (T2) in Gate 2. As expected, the strongest response is observed in Gate 3, which corresponds to Transmitter 3 (T3). Signals from T1 and T2 have negligible impact on Gate 3, since there is enough temporal separation between acoustic wave packets. The nearly zero response in Gate 2 indicates that Transmitter 2 is farther away from the receiver probe, and the beams don't overlap significantly.

Time delays between the transmitters should be minimized in order to compress the total measurement time and to speed up the ACUT inspection. Shorter acoustic responses allow one to increase the pulse repetition frequency (PRF) of the generator (pulsar) and to implement more agile motions of robotic manipulators. Hence, in order to find the optimal time-gates, a set of interference measurements was acquired with different time-delays ranging from 20 μs to 120 μs . The results are shown in Figure 56.

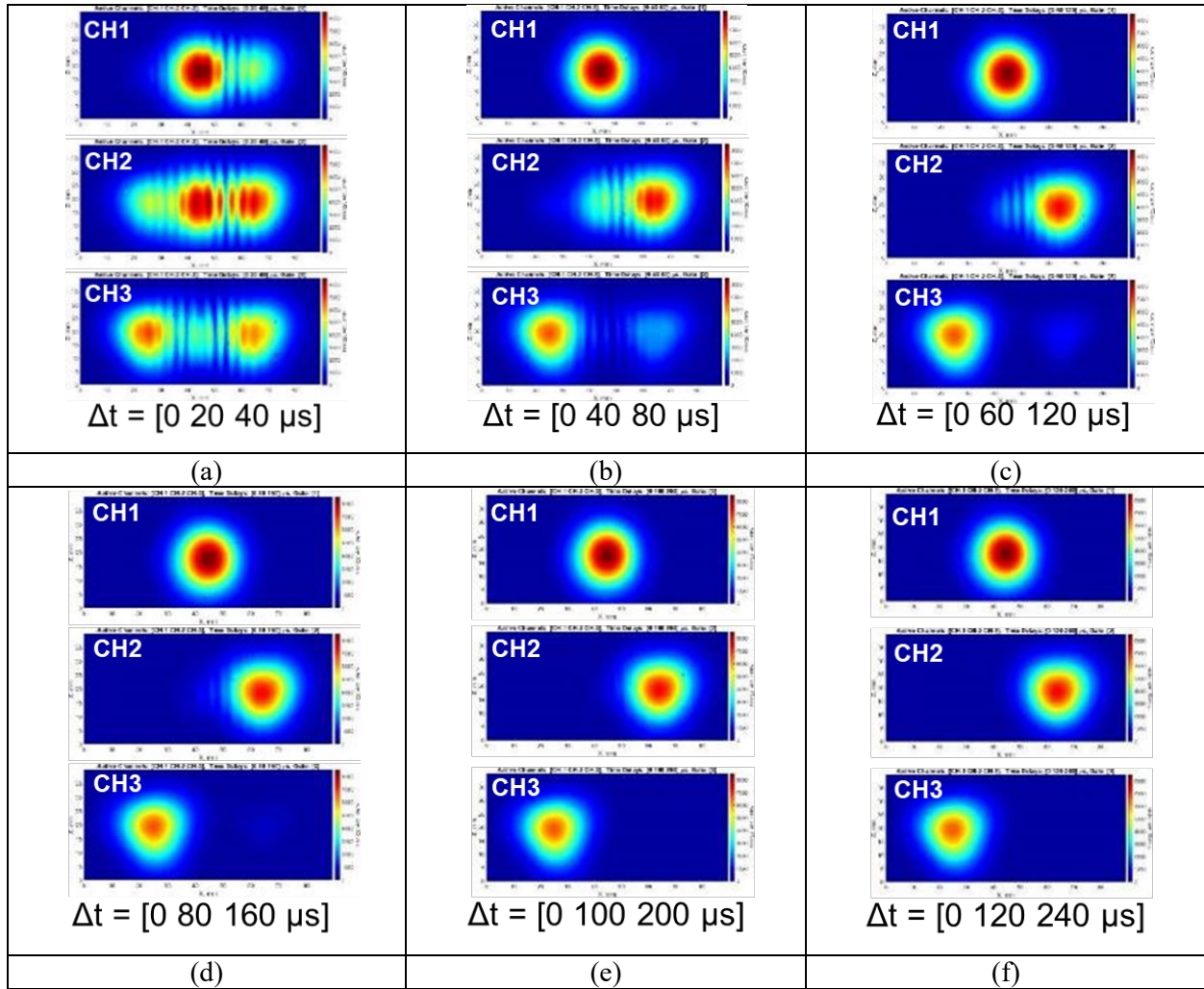


Figure 56. Experimental study I. Time-gated excitation with different time delays between consecutive transmitters/channels: (a) 20 μs ; (b) 40 μs ; (c) 60 μs ; (d) 80 μs ; (e) 100 μs and (f) 120 μs .

Figure 56 demonstrates that increase in time delay visually improves C-scans. The delay of $80\ \mu\text{s}$ between the channels (see Figure 56d) is optimal in this experiment as it is the shortest delay that nearly eliminates ripple distortions.

Experimental Study II: Acoustic beam interferences of CF-200 ACUT probes

Beam interference in the air between CF-200 ACUT probes ($f = 200\ \text{kHz}$) was measured using the setup shown in Figure 57. In this case, a full array of 4 probes was available, and multiple sets of measurements were acquired. The distance between the transmitters and the receiver was $\sim 135\ \text{mm}$.

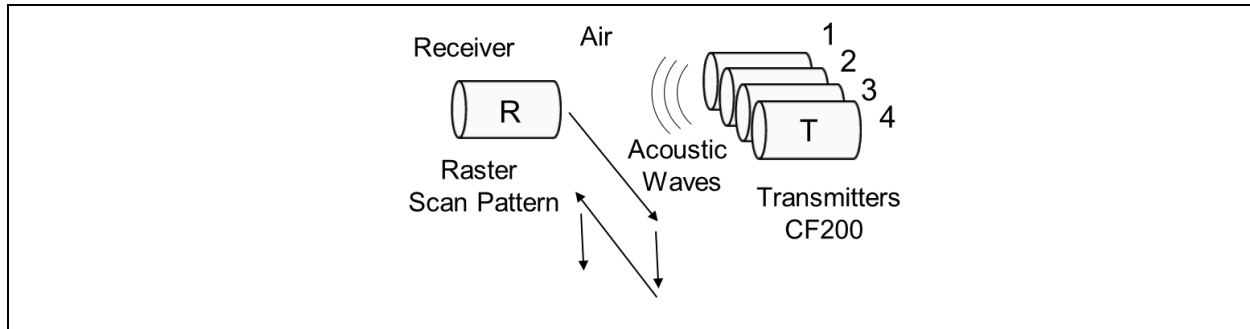


Figure 57. Experimental study II. Setup for measuring crosstalk between four CF-200 ACUT probes.

Figure 58 demonstrates the C-scans corresponding to experiments, in which one transmitter is excited at a time (see Figure 58a) and in which multiple transmitters are excited simultaneously (see Figure 58b). Figure 58a shows that all CF-200 transducers generate similar acoustic pressure. When the transmitters are excited simultaneously, there is considerable interference between the probes, and the acoustic fields are distorted as shown in Figure 58b.

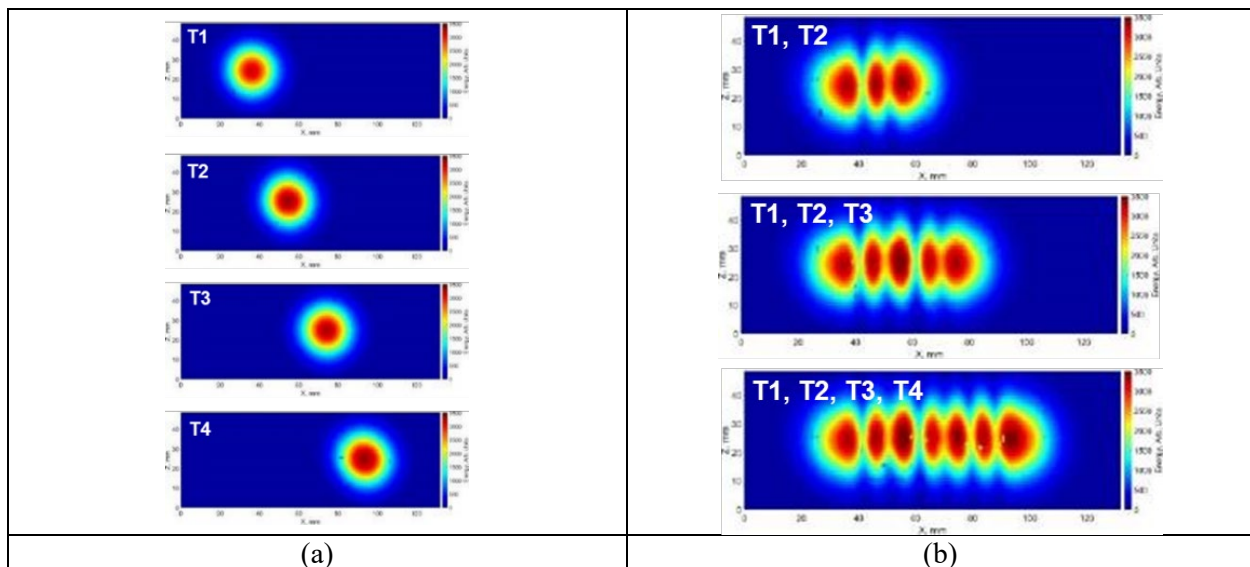


Figure 58. Experimental study II. C-scans: (a) One transmitter at a time (T1, T2, T3 and T4); (b) multiple transmitters simultaneously ([T1,T2], [T1,T2,T3] and [T1,T2,T3,T4]).

C-scans acquired using time-gated excitation are presented in Figure 59. If the time-delay is 200 μs as in Figure 59a, some ripple is observed. This ripple is the strongest for Transmitter/Channel 4. This is due to the fact that when the Receiver is aligned with Transmitter 4, it senses acoustic waves from all other transmitters (T1, T2 and T3). Figure 59b demonstrates that a time delay of 300 μs is sufficient for suppression of the inter-channel crosstalk.

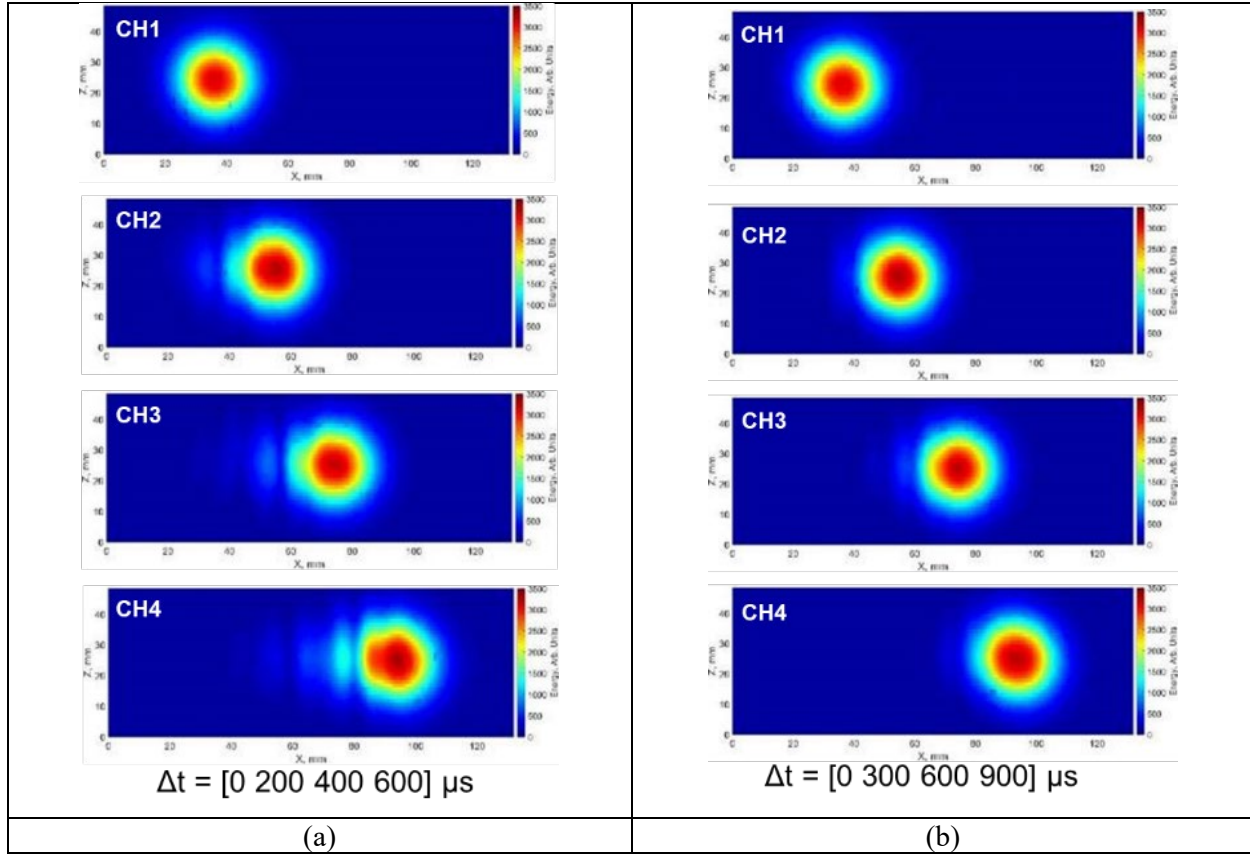


Figure 59. Experimental study II. Time-gated excitation with different time delays between consecutive transmitters/channels: (a) 200 μs ; (b) 300 μs .

Experimental Study III: Beam focusing and clipping using acoustic cones

The MSU team designed multiple cones to be attached to active faces of the ACUT transducers in order to focus and clip generated acoustic beams as explained in Figure 51c. The cones were 3D printed using PLA plastic with 15% infill. Low infill values were chosen for better acoustic impedance matching between the cones and the air. Cones were also filled with hexagonal cells that scattered ultrasonic waves and, therefore, acted like an absorbing material. Experiments were conducted with two sets of plastic cones with output diameters/apertures (OD) of 5 mm and 12 mm as shown in Figure 60. An aperture of 12 mm matched the diameters of the piezoelectric crystals in CF-200 transducers.

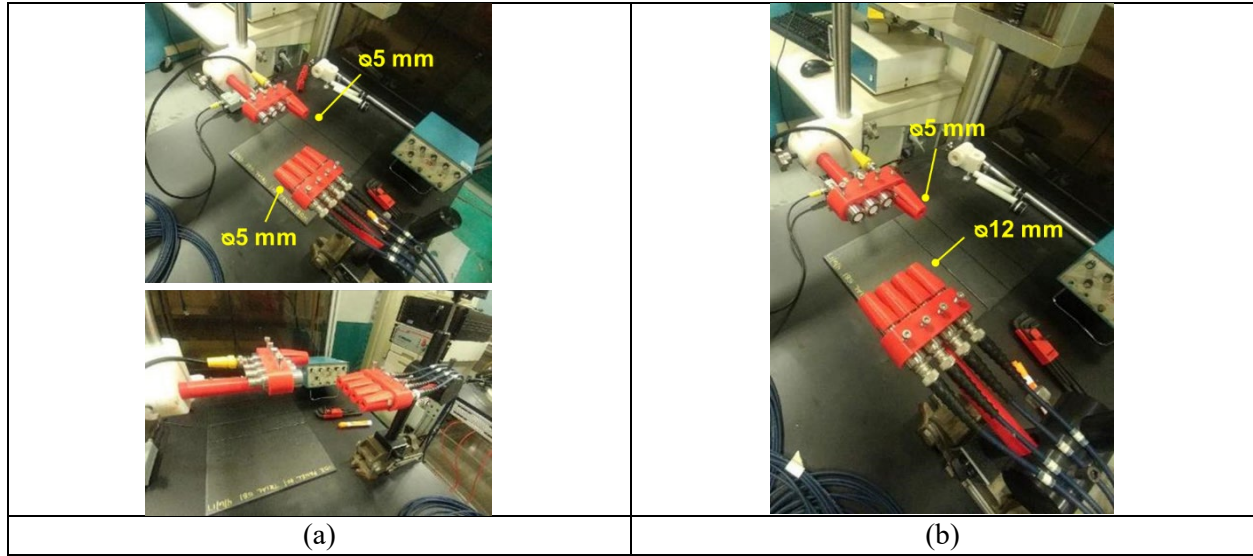


Figure 60. Experimental study III. 3D printed focusing cones attached to CF-200 transducers: (a) 5 mm apertures; (b) 12 mm apertures for transmitters and 5 mm aperture for receiver.

Figure 61 demonstrates how acoustic fields are shaped using attached cones. Cones with 5 mm ODs made the acoustic waves reverberate, and the resulting field pattern is irregular as shown in Figure 61a. On the other hand, cones with 12 mm ODs had a more uniform field pattern (see Figure 61b). Energies of acoustic beams generated by transmitters are mostly focused in the centers of respective apertures. However, some unwanted field lobes can be observed in between the centers of the transmitters. It is desirable that these lobes are suppressed. Amplitudes of signals (A-scans) acquired with 12 mm OD cones are ~ 2.5 times higher than those acquired with 5 mm OD cones.

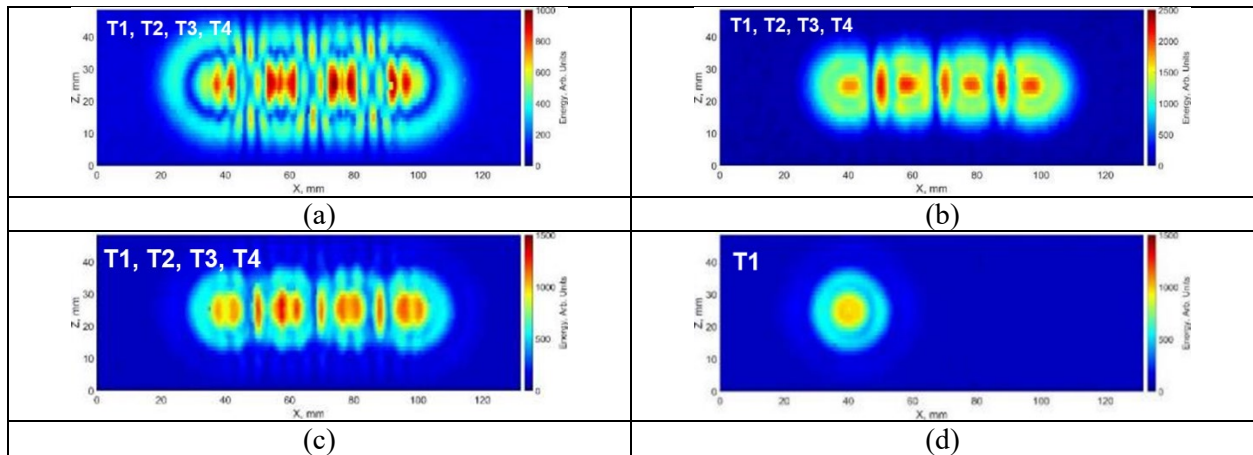


Figure 61. Experimental study III. Beam clipping using acoustic cones. C-scans: (a) transmitters and receiver have 5 mm apertures, [T1,T2,T3,T4] excited simultaneously; (b) transmitters and receiver have 12 mm apertures, [T1,T2,T3,T4] excited simultaneously; (c) transmitters have 12 mm aperture and receiver has 5 mm aperture, [T1,T2,T3,T4] excited simultaneously; (d) transmitter T1 has 12 mm aperture and receiver has 5 mm aperture, only T1 is excited.

Experimental Study IV: Surface reflections in ACUT signals

Previous studies with ACUT probes were conducted without composite samples, and beam interference between transducers was measured in the air. However, it is important to understand how reflections from the surface of the test sample affect the signals. Figure 62 shows a simple setup for acquiring such measurements. Distance between the transmitter array and the receiver is ~60 mm. Calibration panel #1 (CFRP sample from Phase I) is placed in between the transmitting and receiving probes. No cones are attached to the transducers.

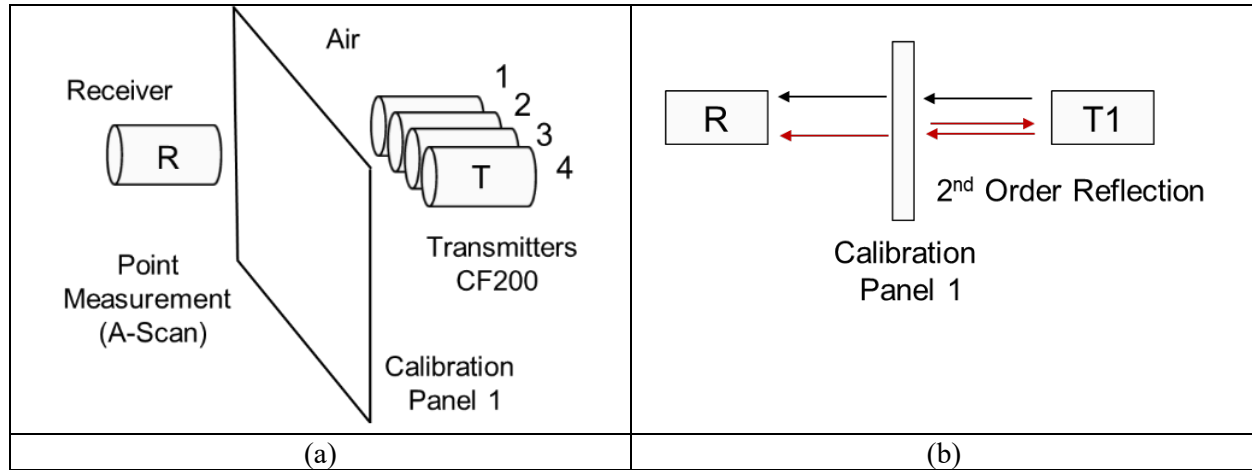


Figure 62. Experimental study IV. Evaluation of surface reflections: (a) setup with linear array of CF-200 transducers; (b) formation of 2nd order reflections.

When the transmitting probe (e.g., Transmitter 1, T1) is activated, an acoustic wave will be generated, and it will reach the surface of the test sample. However, more than 99% of its energy will be reflected at the air/composite interface owing to acoustic impedance mismatch. The reflected wave will hit the active surface of the Transmitter 1 and will back propagate to the surface of the sample, forming a 2nd order reflection. In this process, the wave will undergo attenuation, since its reflections can't be characterized as strictly speckle reflections. As shown in Figure 49, the acoustic beam of T1 is divergent. Hence, some rays from this beam will be incident onto the sample's surface at oblique angles and will be reflected sideways. Similar wave reflections will occur between the sample and the receiver. Acoustic waves will reverberate between the sample and the ACUT probes multiple times before decaying completely. Such reverberations will also happen in the test sample.

A typical signal (A-scan) showing multiple surface reflections is presented in Figure 63. In this case, 2nd and 3rd order reflections are labeled, and up to 6 reflections can be observed. The first wave packet is registered at $t \sim 350 \mu\text{s}$, and the acoustic signal dies out at $t \sim 1500 \mu\text{s}$.

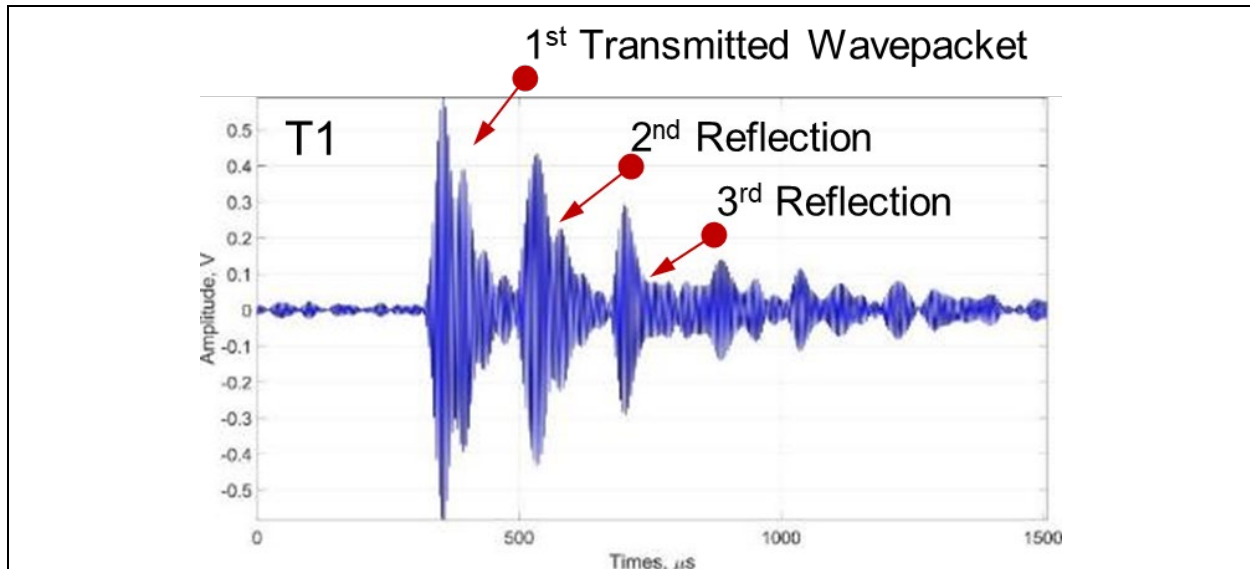


Figure 63. Experimental study IV. Typical A-scan with multiple surface reflections (receiver probe is aligned with T1, only T1 is activated).

Figure 64 demonstrates schematics of the extended setup for measuring surface reflections in a linear array configuration. In this case, Transmitters 1 through 4 are excited with time delays of 1500 μs . The receiver is aligned with Transmitter 4, but the signal is sampled as soon as the first excitation pulse is applied to Transmitter 1.

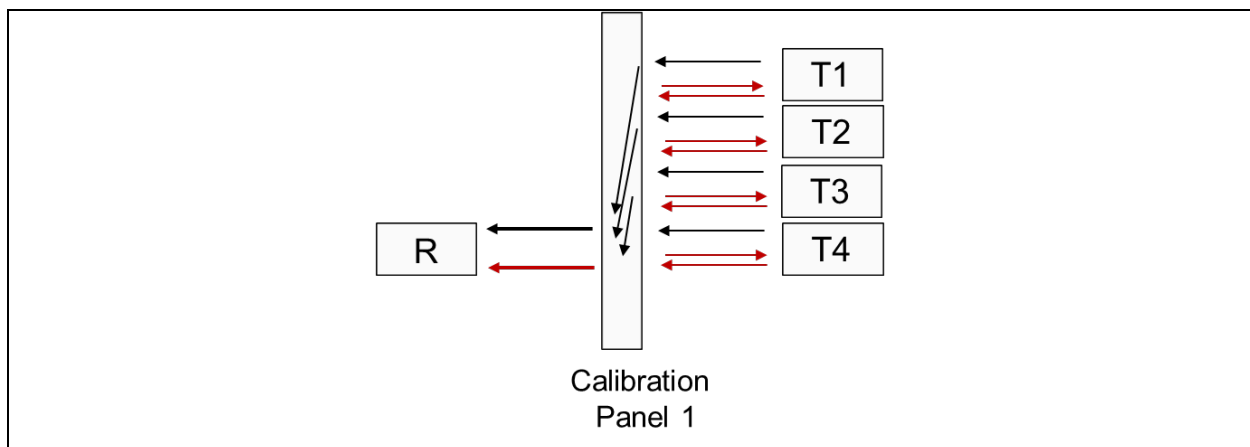


Figure 64. Experimental study IV. Surface reflections and time-gated excitation of a linear array of 4 CF-200 transmitters (T1-T2-T3-T4 sequence).

The resulting A-scan is presented in Figure 65. Figure 65 shows that the receiving probe senses signals generated by all transmitters (T1-T4). Through-transmitted waves and multiple-order surface reflections are labeled accordingly. Signals from T1 are the weakest, and signals from T4 are the strongest, which is explained by different distances between the transmitters T1, T4 and the receiver R. There is no crosstalk between the channels, since time delay of 1500 μs is long enough to let signals from a single channel die out before another channel is activated.

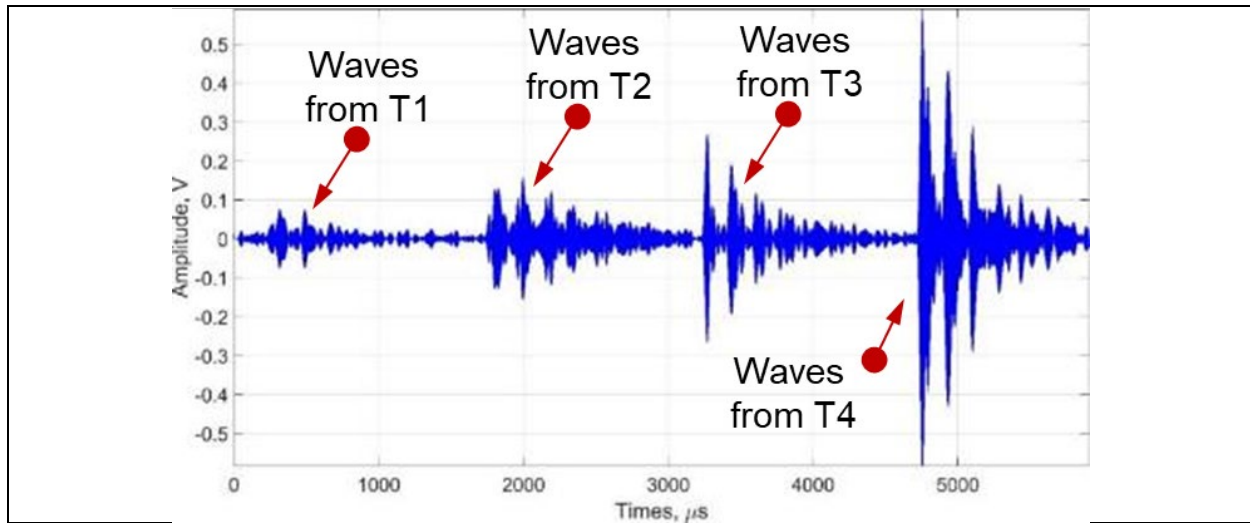


Figure 65. Experimental study IV. Typical A-scan: linear array configuration, time-gated excitation with 1500 μs delays between consecutive channels (T1-T2-T3-T4 sequence). Receiver is aligned with Transmitter 4 (T4).

Comparisons of results obtained in Study II (no part, no surface reflections) and Study IV (multiple order surface reflections) reveal that the minimum time delays required to eliminate crosstalk are increased by $>1000 \mu\text{s}$ for Study IV. Hence, reflections between the part and transmitter need to be attenuated as much as possible.

Experimental Study V: Acoustic wavefield imaging & linear array excitation

This section extends previous experimental work to imaging of elastic wave propagation in CFRP test samples. In this set of experiments, transducer arrangement is similar to the one shown in Figure 62, but the receiving probe can move freely in xz -plane in order to perform raster scans.

Wavefield propagation is imaged as a sequence of C-scans (images). One waveform (A-scan) is acquired at each scan position. Then, a set of waveforms is recorded and is saved as binary files. A C-scan is formed from A-scans by extracting peak amplitude data from a time gate. For instance, taking Figure 63 as an example, the time gate would be centered around the 1st transmitted wave packet. If the time gate is moved to the right along the time axis, a sequence of C-scans is acquired, which corresponds to snapshots of wave propagation in the test sample. All C-scans can be merged into a sprite sheet or a movie file. In the current set of experiments, the gate width was 75 μs .

Figure 66 demonstrates snapshots of wave propagation in Calibration panel #1, when Transmitter 1 (T1) is driven by four square pulses ($V_{pp} = 200 \text{ V}$). Figure 66 shows that vibrations in the sample are mostly focused around the point of incidence of the T1 beam. However, wave propagation is observed along $[0/90/\pm 45]$ directions around the point of incidence. Since the velocity of wave propagation is higher in the regions of higher stiffness, evidently the CFRP part is made of unidirectional plies stacked at 0° , 90° and $\pm 45^\circ$ angles (but exact stacking sequence can't be determined at this point). Twelve snapshots were acquired with time lags of 25 μs . They captured only the 1st transmitted wave packet and the 2nd order reflection from the top surface of the test sample.

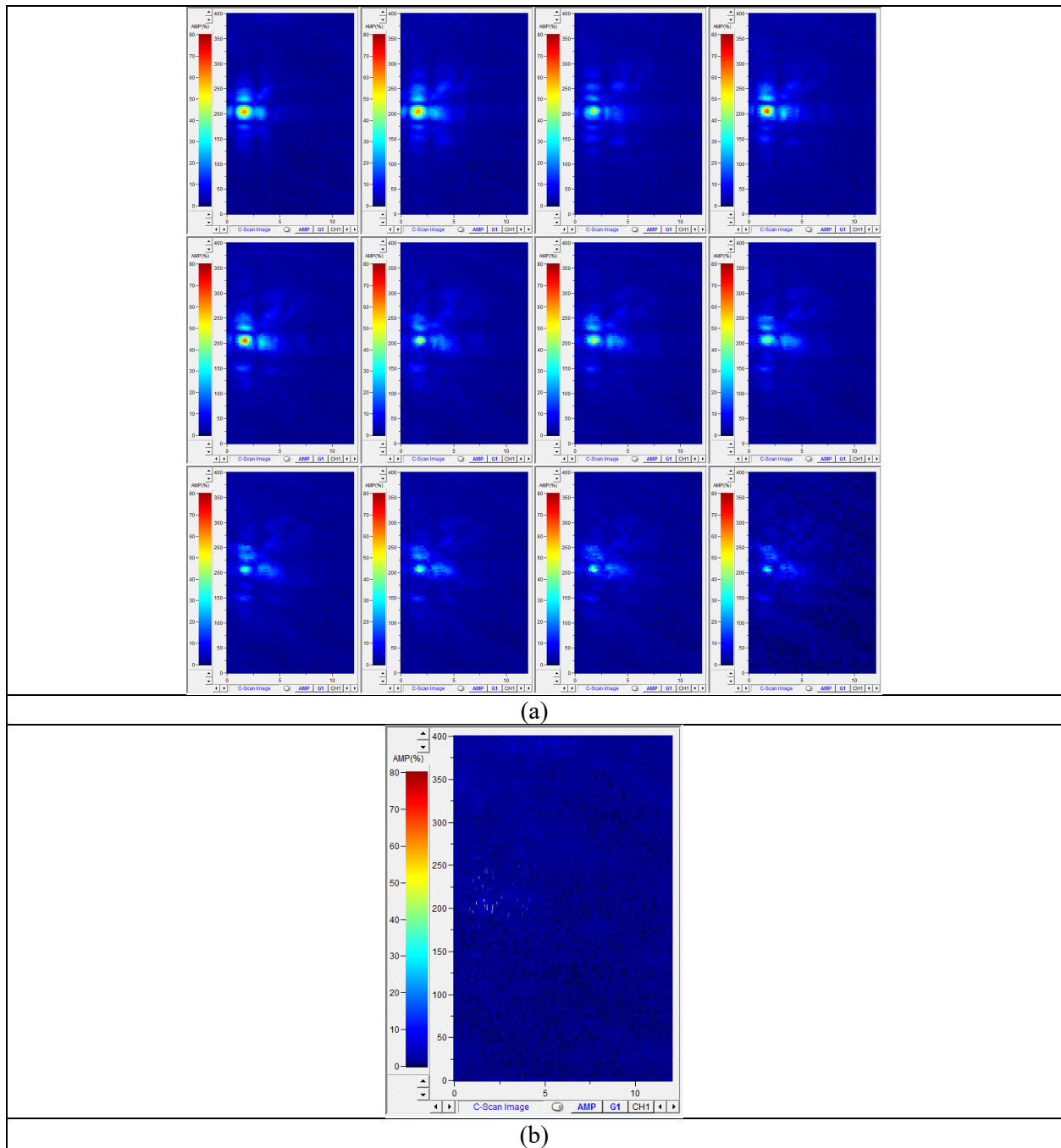


Figure 66. Experimental Study V. Snapshots of wave propagation in calibration panel #1. Transmitter 1 (T1) is activated: (a) time lapse/C-scan arrangement: left to right & top to bottom; (b) gif video.

Figure 67, Figure 68 and Figure 69 show snapshots of elastic wave propagation when two, three, and four CF-200 transmitters are activated simultaneously. The methodology for acquiring snapshots is identical to the methodology used for Figure 66. Obtained results demonstrate interference of acoustic waves inside the CFRP sample. However, elastic waves still tend to propagate more along 0° and 90° directions.

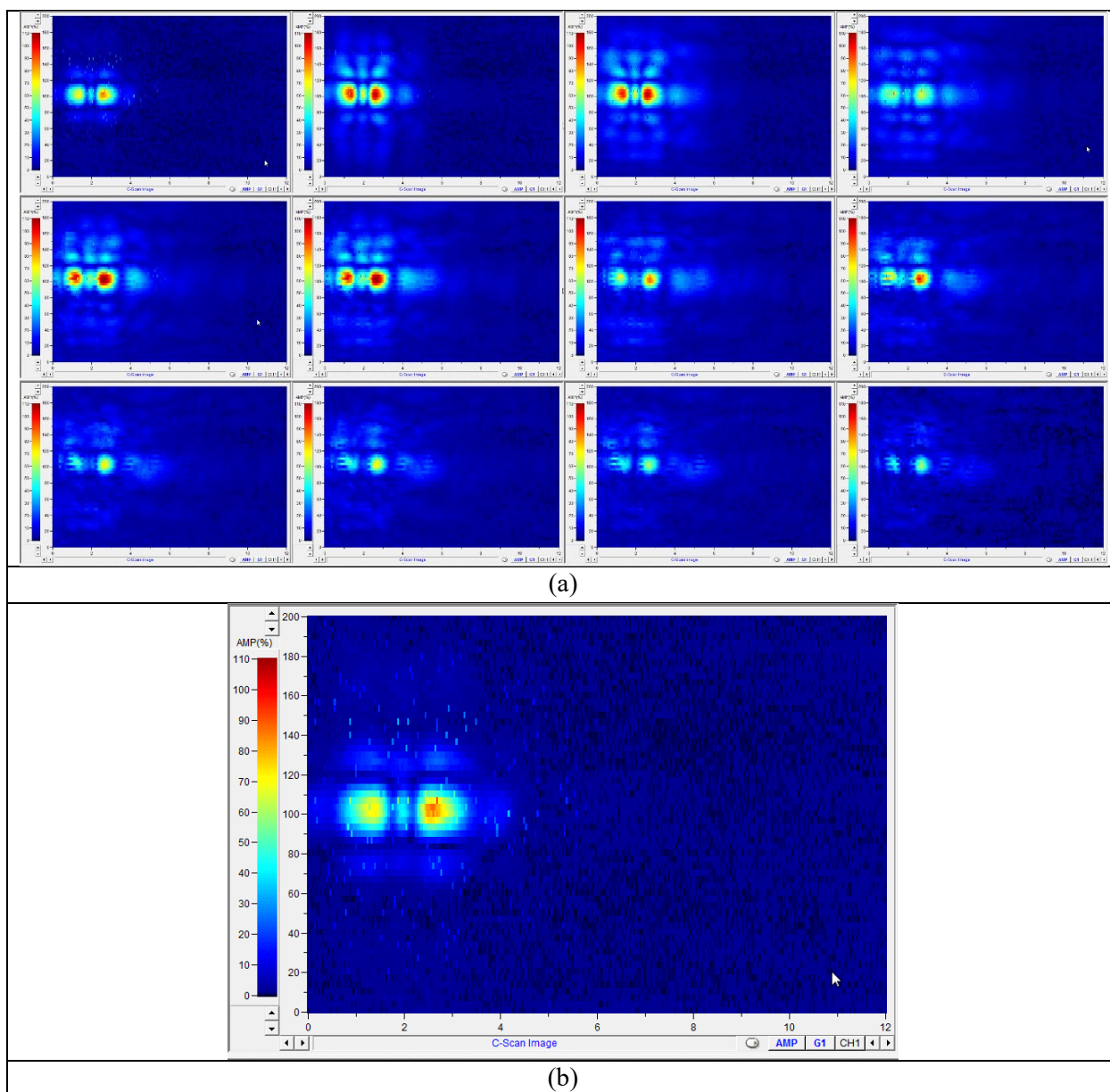


Figure 67. Experimental Study V. Snapshots of wave propagation in calibration panel #1. ACUT probes CF-200. Two transmitters T1 and T2 are activated simultaneously. Time lapse/C-scan arrangement: (a) left to right & top to bottom; (b) gif video.

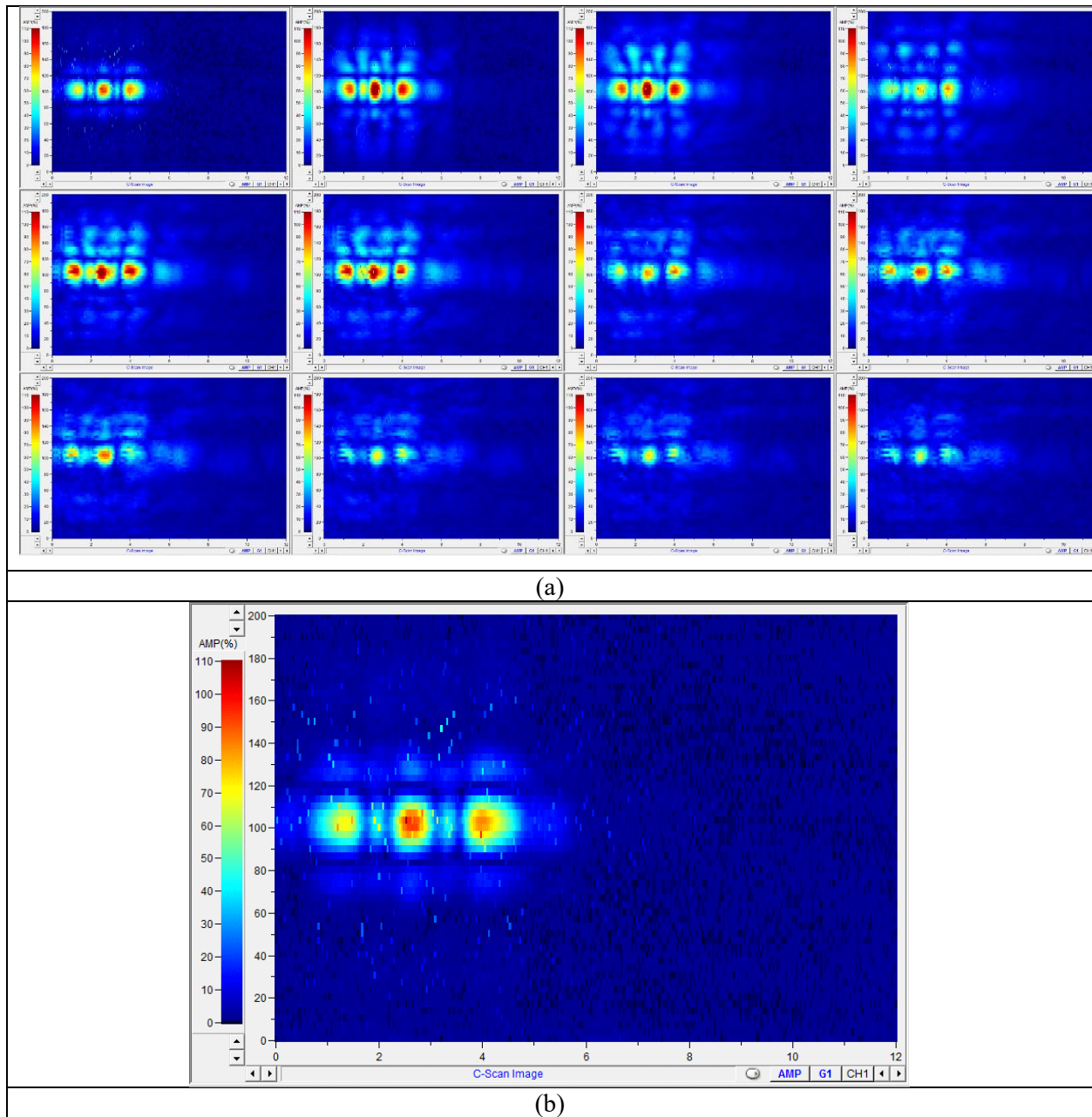


Figure 68. Experimental Study V. Snapshots of wave propagation in calibration panel #1. ACUT probes CF-200. Three transmitters T1, T2 and T3 are activated simultaneously. Time lapse/C-scan arrangement: (a) left to right & top to bottom; (b) gif video.

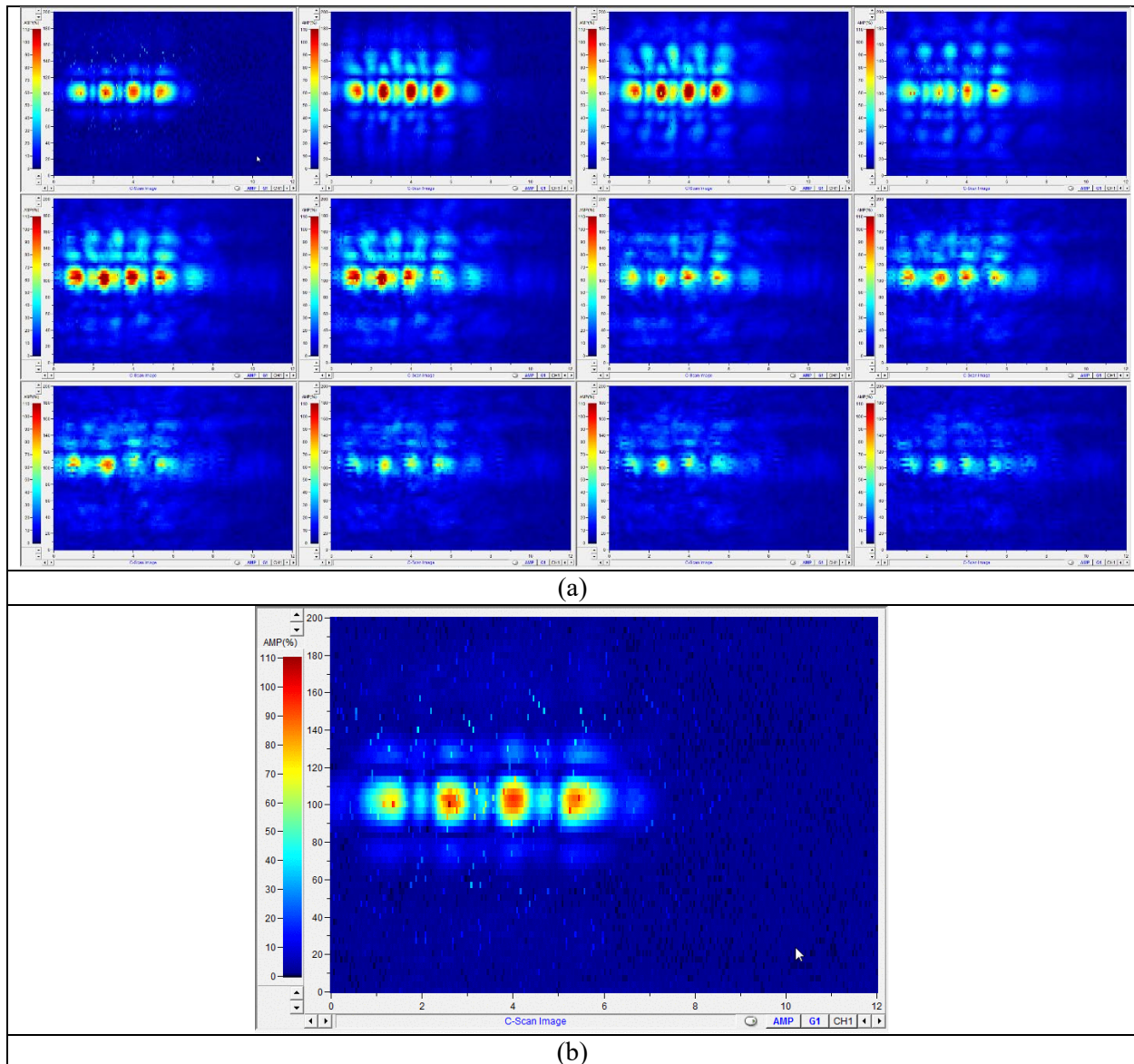


Figure 69. Experimental Study V. Snapshots of wave propagation in calibration panel #1. ACUT probes CF-200. Four transmitters T1, T2, T3 and T4 are activated simultaneously. Time lapse/C-scan arrangement: (a) left to right & top to bottom; (b) gif video.

Figure 70 shows the acoustic wavefield in Calibration panel #1, when time-gated excitation is implemented. Transmitters T1, T2, T3 and T4 are activated with 300 μ s delays. Figure 70 demonstrates that this delay is not long enough to avoid crosstalk. For instance, Transmitter T1 remains active in the top row and 2nd from the top row of C-scans. However, Transmitter T2 starts generating waves before the signal from T1 dies out, and appears in the 2nd from the top row as well. The rightmost image in the 3rd row shows three active transducers, namely T2, T3 and T4.

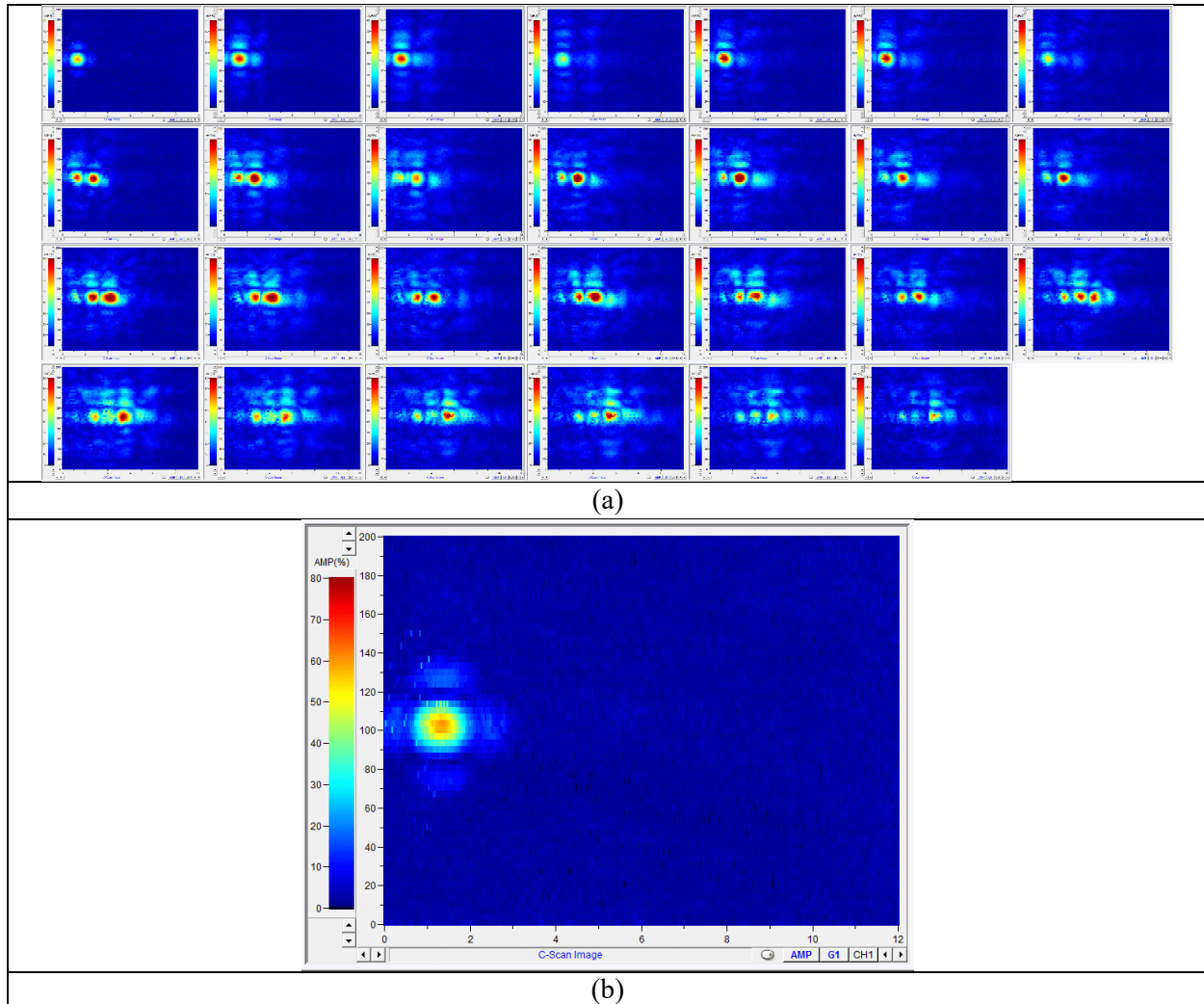


Figure 70. Experimental Study V. Snapshots of wave propagation in calibration panel #1. Time-gated excitation, T1-T2-T3-T4 sequence, time delay of 300 μ s between the consecutive channels. Time lapse/C-scan arrangement: (a) left to right & top to bottom; (b) gif video.

Snapshots of wave propagation in Figure 71 were acquired using similar approach as in Figure 70, but the time delays between excitations T1-T2-T3-T4 were increased to 1000 μ s. Figure 71 demonstrates that in this case no images have more than one red spot, meaning that elastic waves generated by each transmitter attenuate completely before the next transmitter in a sequence is activated.

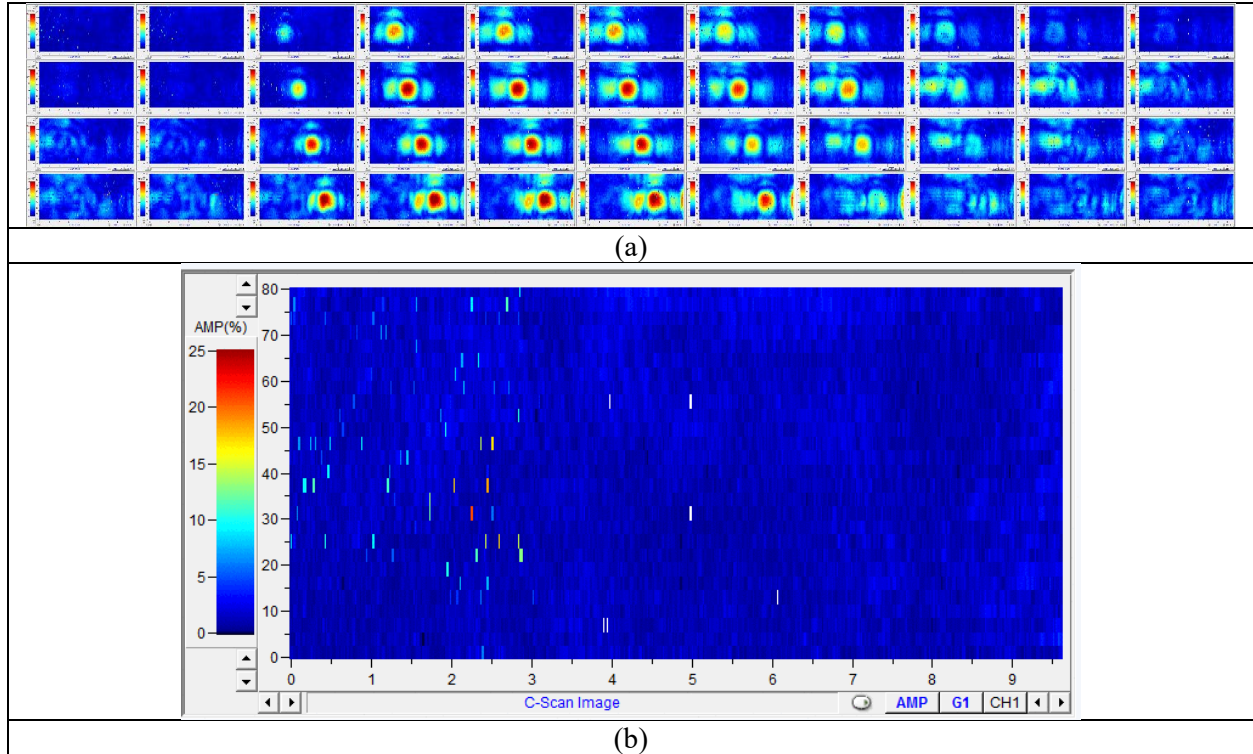


Figure 71. Snapshots of wave propagation in calibration panel #1. Time-gated excitation, T1-T2-T3-T4 sequence, time delay of 1000 μ s between the consecutive channels. Time lapse/C-scan arrangement: (a) left to right & top to bottom; (b) gif video.

Experimental Study VI: Focusing cones with foam rubber for eliminating surface reflections

Based on the results of Experimental Studies III-V, the design of the focusing cones was optimized. PLA cones with 12-mm ODs were made 10 mm shorter, and foam rubber pads were added in order to suppress unwanted beam interferences and surface reflections. The updated cone design is shown in Figure 72c. The previous design is shown in Figure 72b.

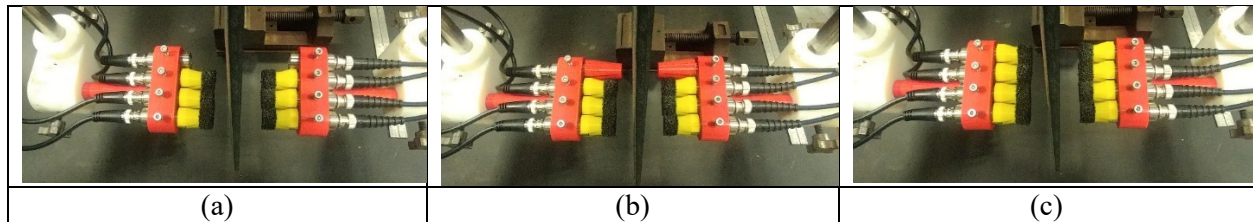


Figure 72. Experimental Study VI. Configurations of transducers (top pair): (a) no cones; (b) long 12-mm OD cones; (c) short 12-mm OD cones with foam rubber.

Performance of new cones was tested using the methodology from Experimental Study IV. Obtained results are shown in Figure 73. Figure 73b and Figure 73c demonstrate that PLA cones effectively remove surface reflections of the 3rd order and higher. However, cones with rubber foam provide the best performance, since the total signal duration is reduced to ~ 600 μ s. The only drawback of PLA cones is the reduction in the amplitudes of transmitted signals by $\sim 38\%$. The energy is lost because only a central part of the acoustic beam is retained and the sidelobes are removed by randomized scattering in the foam. This is not a big issue for ACUT inspection of CFRP parts using the current system, as the pulse voltage and receiver gain can be increased.

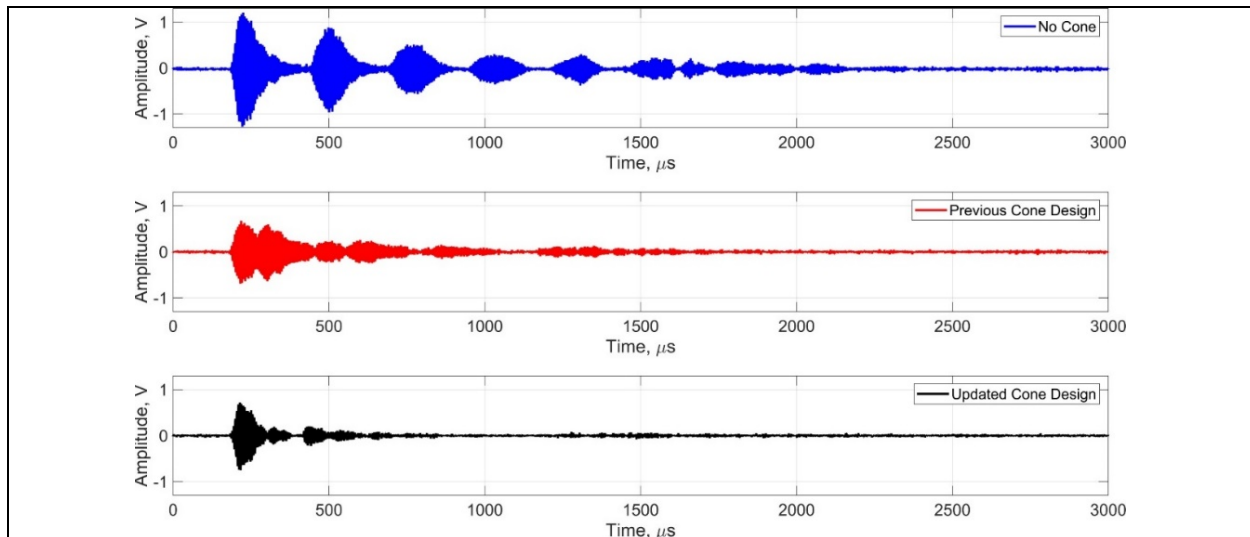


Figure 73. Experimental Study VI. Suppression of surface reflections: (a) no cones; (b) long PLA cones, 12-mm OD; (c) short PLA cones with foam rubber, 12-mm OD.

2.3.5. Validation of high-speed ACUT gantry system: 4-channel data acquisition in TT mode

In Quarter IV, the MSU team optimized the XYZ gantry system for the high-speed ACUT data acquisition. Three precision rotary encoders were installed on the shafts of 5-phase stepper motors to accurately track position of the probe. The MSU team also installed and programmed multi-channel digital pulse counter from National Instruments for reading encoder outputs in real-time. Gantry system was expanded to fit parts of the size of an X-brace as shown in Figure 74.

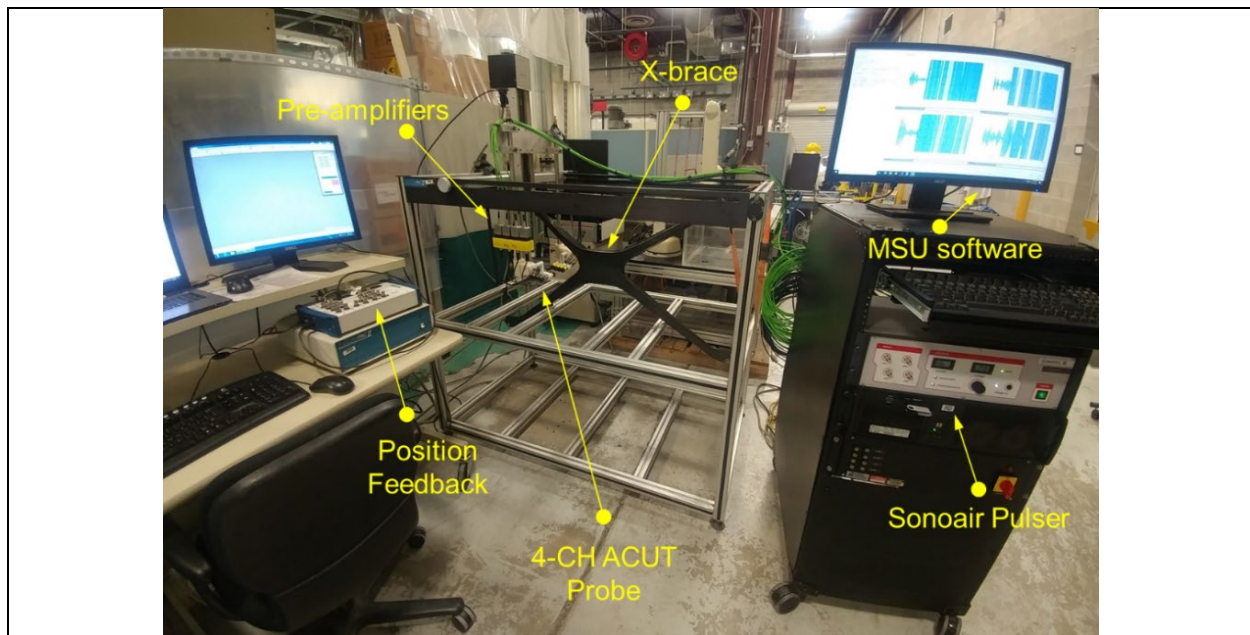


Figure 74. Upgraded XYZ gantry system at CVRC for high-speed ACUT NDE.

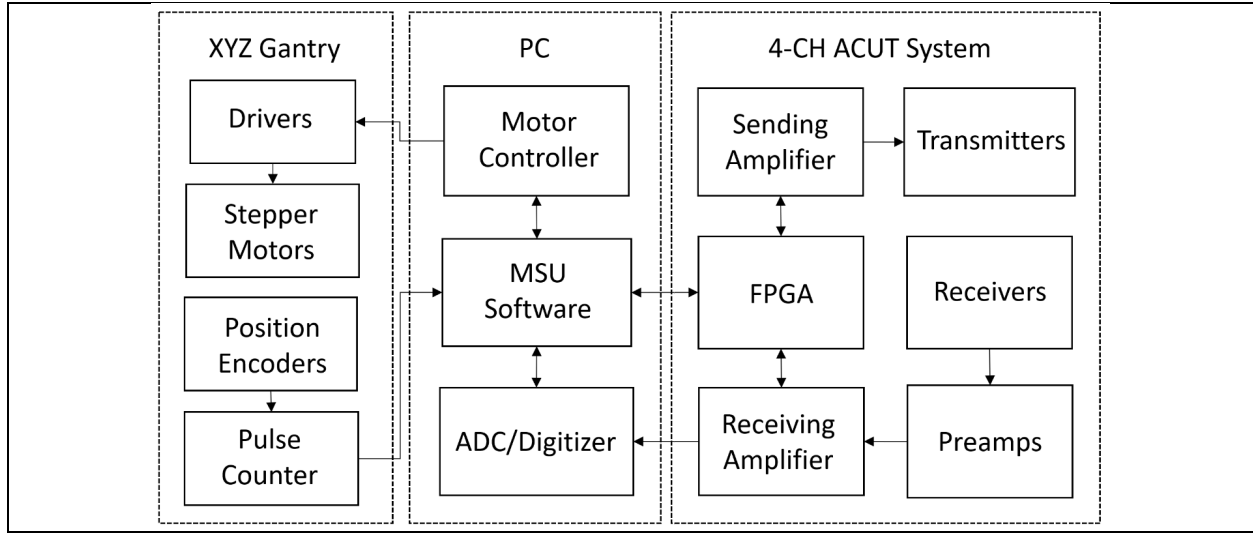


Figure 75. Schematic block-diagram of the gantry system for ACUT NDE.

Figure 75 shows the schematic diagram of the gantry system. Motion controller was programed so as to provide the highest possible speed and acceleration of stepper motors without excessive vibrations or halts. MSU implemented high-speed parallel data acquisition using GaGe CSE-4447 digitizer. The digitizer could simultaneously sample 4 waveforms at a rate of ~ 400 times/s ($F_s = 2$ MHz). Software scripts and graphical user interfaces were also updated in C# and LabView to be able to keep up with high data acquisition rates. The new version of the software could process ACUT signals on the fly. It could also perform time windowing/gating, feature extraction from A-scans, data saving in binary format, and data replay.

Design of linear TT-ACUT sensor array

A series of experiments was performed to validate the performance of the developed linear ACUT array and high-speed data acquisition software. Figure 76 shows the array geometry and configuration for the ACUT inspection in the through-transmission mode. The array is rotated about its central axis by an angle β , which determines the sensor pitch (see Figure 76a). Based on the minimum size of defects that the system is supposed to detect ($\sim 0.25 \times 0.25$ in²) and short inspection time requirements, the sensor pitch was set to 2.5 mm.

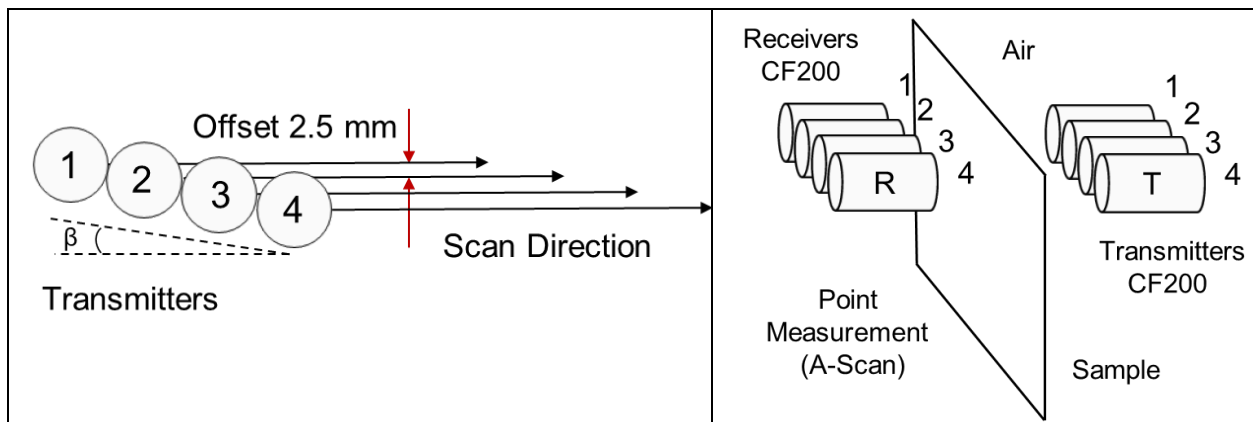


Figure 76. The 4-element (4-channel) linear ACUT array: (a) sensor pitch and orientation with respect to scan path; (b) array data acquisition in through-transmission mode.

Mirrored plastic fixtures with fixed sensor offsets of 2.5 mm were 3D prototyped for initial experiments (see Figure 77a). Fixtures were attached to a fork made of search tubes. CF-200 transducers were inserted into open slots, and cones with rubber foam were attached to active faces of transducers as shown in Figure 77b. Transmitters and receivers were ~140 mm apart in order to account for the curvature of X-brace and to cover most of its surface area in a single C-scan.

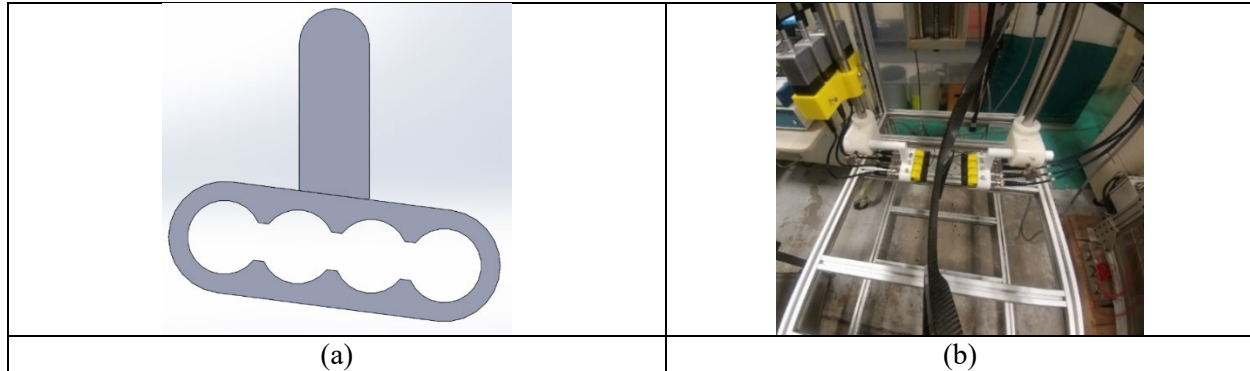


Figure 77. Linear array fixtures: (a) CAD model, front view; (b) 3D printed parts with installed CF-200 ACUT sensors and focusing cones.

A sensor pitch of 2.5 mm increases effective coverage of the array probe to 10 mm. Hence, 10 mm segments of the test sample can be covered in a single scan path. However, before the parallel data acquisition is implemented, it is necessary to evaluate the uniformity of the acquired signals across all four transmit-receive sensor pairs. Hence, two separate C-scans of the test part should be acquired at this point as shown in Figure 78.

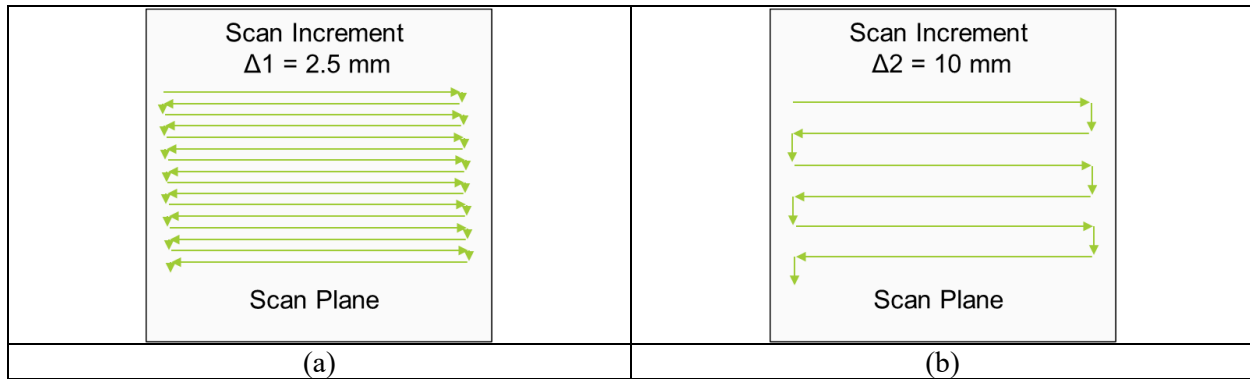


Figure 78. Scan settings for validation of 4-channel linear ACUT array: (a) 2.5-mm scan increment for testing the uniformity of channels; (b) 10-mm scan increment for parallel data acquisition and high-speed inspection.

The first C-scan should have a scan increment equal to the sensor offset of 2.5 mm (see Figure 78a). In this case, all four ACUT transmit-receive pairs (channels) will scan the same geometrical points of the test part, and it is expected that the acquired C-scans for all channels would look similar. The differences in C-scans could be caused by variations in generated acoustic pressure and impulse responses of the probes.

The second C-scan should have a scan increment of 10 mm as shown in Figure 78b. Acquired data will not be repetitive. However, C-scans corresponding to different channels will need to be merged together in order to form a composite image of the test part. In this case, the scan time will be 4 times shorter compared to the 2.5 mm C-scan. Merging of multi-channel data can be easily performed using linear interpolation while keeping track of the geometrical centers of ACUT transducers.

TT-ACUT C-scans of X-brace parts with delaminations

The MSU team successfully verified performance of the upgraded multi-channel ACUT system by scanning two X-brace parts (X-brace #1 and X-brace #3) provided by Plasan Composites in Phase I of the Project. The water jet UT inspection revealed a series of defects embedded in X-brace #3, and scans of X-brace #1 didn't show any apparent defects.

Figure 79 shows the scan process, and Figure 80 demonstrates typical A-scans acquired in the ACUT inspection of X-braces. In Figure 80, orange vertical lines highlight time windows for feature extraction. Time-gated excitation is implemented, and signals are offset by $\sim 440 \mu\text{s}$. The low signal amplitude registered by Channel 3 (CH3, transmitter-receiver pair 3) indicates the presence of a defect.

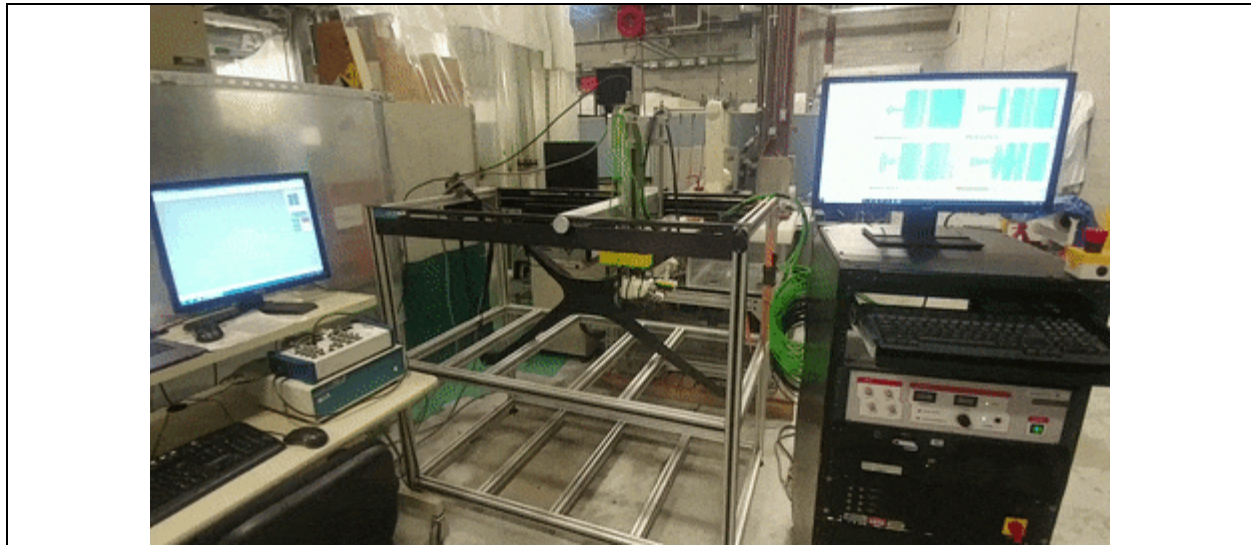


Figure 79. Video of multi-channel ACUT inspection of X-brace #3 using gantry system.

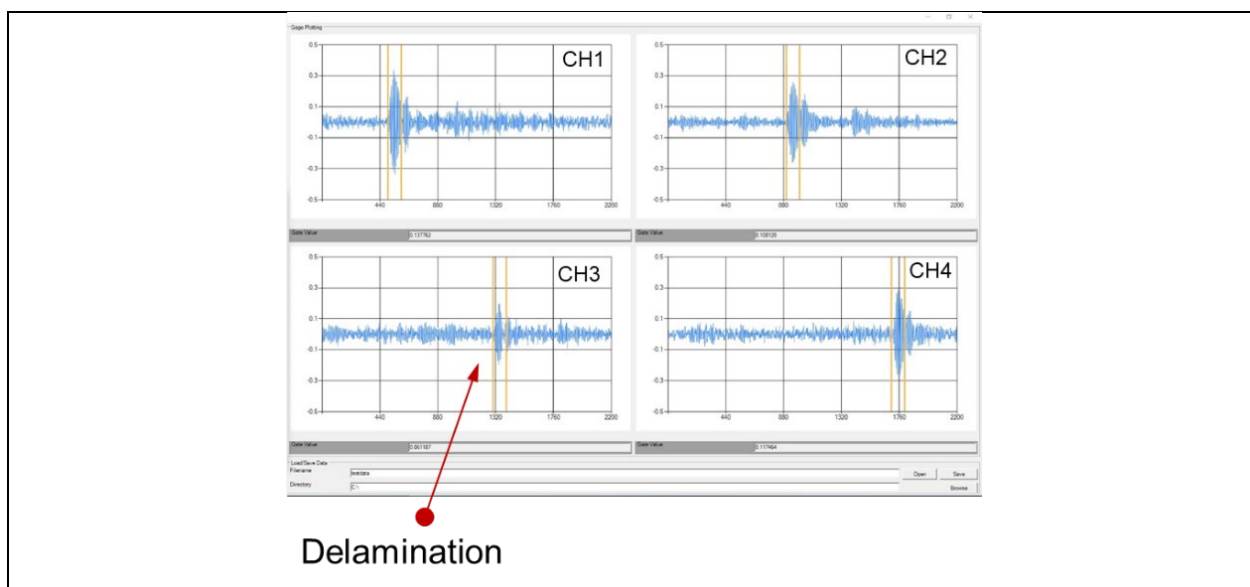


Figure 80. Typical A-scans acquired in the multi-channel ACUT inspection of X-braces.

Figure 81 presents multi-channel ACUT C-scan of X-brace #3 acquired with scan increment of 2.5 mm. Images corresponding to different channels have different fields of view, as geometrical locations of the ACUT transducers are not the same. At the same time, all images are visually similar, which confirms that differences in acoustic pressures between sensor pairs are small. All four channels successfully detected four anomalies in the X-brace #3, which are pointed out with red arrows. The X-brace #3 also had a sticker label that left glue on its bottom surface. Similar results were obtained for multi-channel ACUT C-scan with 10 mm scan increment as shown in Figure 82. In this case, the spatial resolution is low, but the multi-channel data is supposed to be merged.

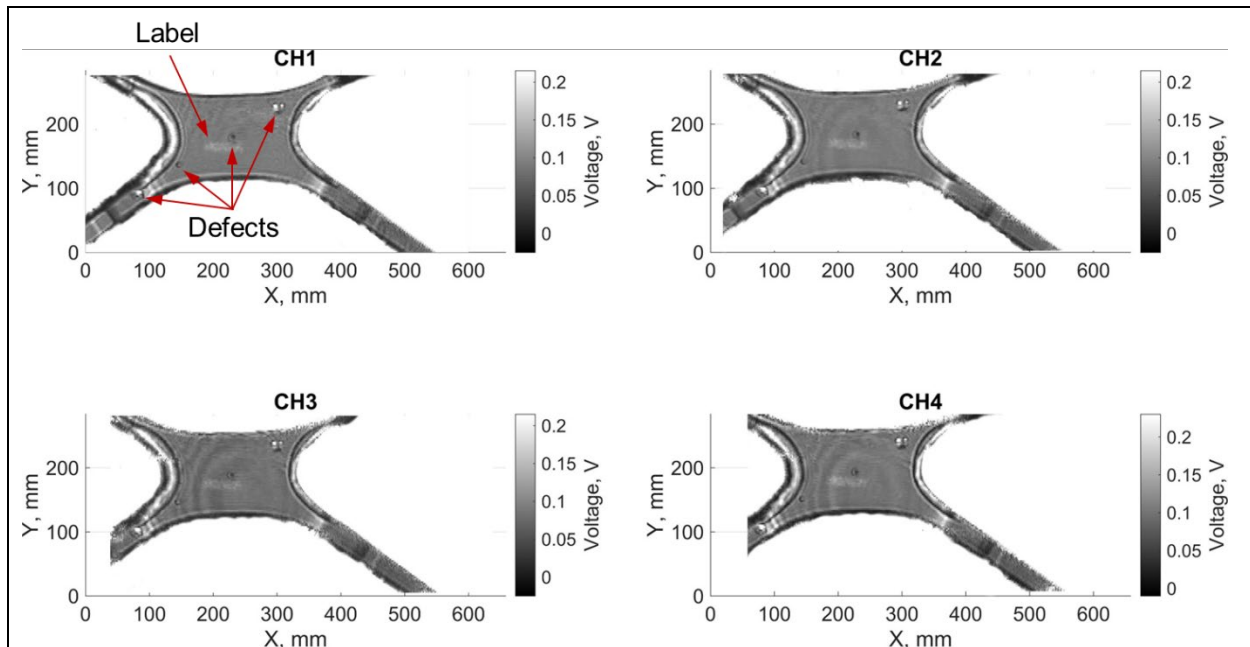


Figure 81. Multi-channel ACUT C-scan of X-brace #3. Scan increment: 2.5 mm.

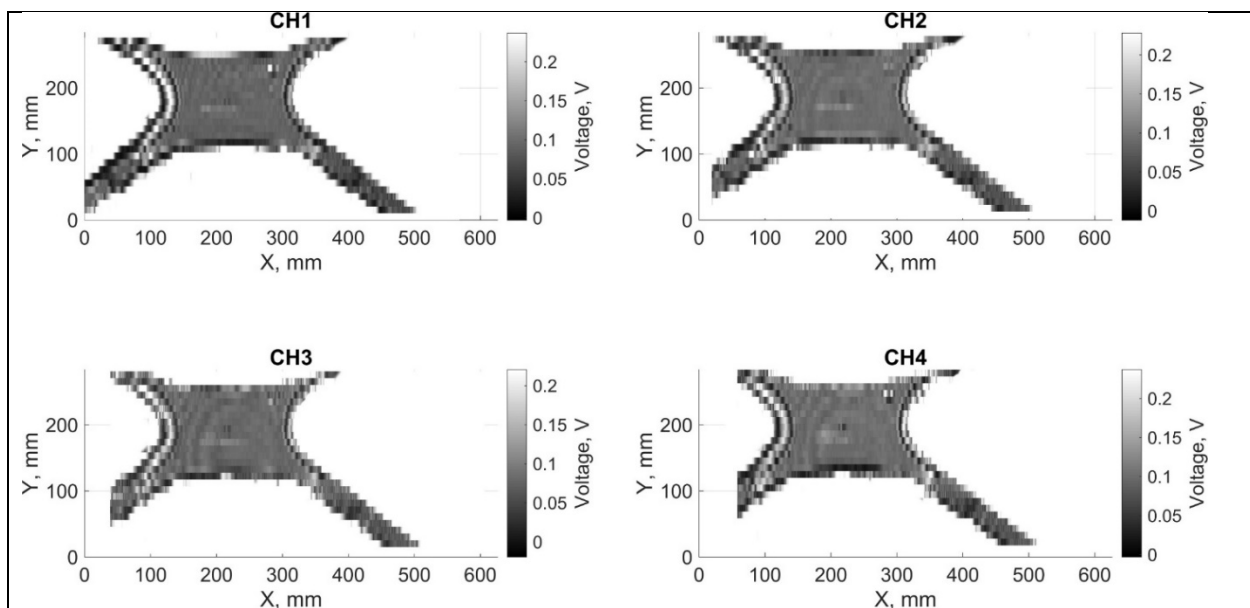


Figure 82. Multi-channel ACUT C-scan of X-brace #3. Scan increment: 10 mm.

Figure 83 provides comparisons of a single-channel C-scan and a merged multi-channel C-scan of X-brace #3. C-scan shown in Figure 83a was acquired with 2.5 mm step increments, and it corresponds to Channel 1 of the linear array (CH1 in Figure 81). The C-scan presented in Figure 83b is a merged version of all C-scans from Figure 82.

The total time for the acquisition of a C-scan in Figure 83a was ~6 min, whereas the total time for acquisition of a C-scan in Figure 83b was ~1 min 30 s. The scan area was $\sim 300 \times 650 \text{ mm}^2$. At this point, the bottleneck in reducing the scan time for the ACUT inspection is low maximum speed/acceleration of the XYZ gantry.

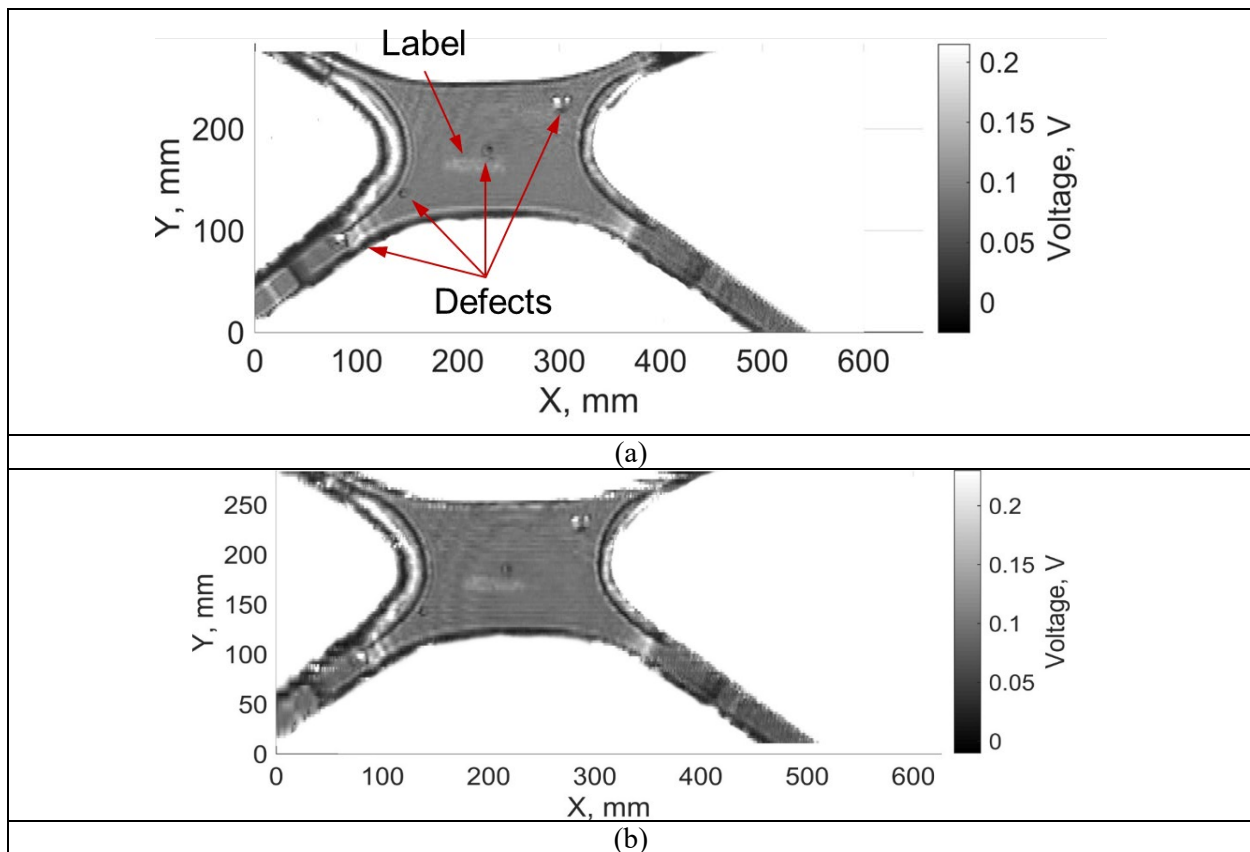


Figure 83. ACUT C-scans of X-brace #3: (a) single channel (CH1), scan increment 2.5 mm, scan time ~6 min; (b) merged multi-channel (CH1+CH2+CH3+CH4), scan increment 10 mm, scan time ~1 min 30 s.

All structural features and anomalies seen in Figure 83a are preserved after merging the multi-channel data Figure 83b. At the same time, the linear array acquires C-scans ~4 times faster than the single-element probe. In Figure 83b, amplitude variations between the channels are reduced by normalizing channel data by their respective average energies. Figure 83b shows some ripple, which can be removed by more sophisticated data equalization and signal processing algorithms.

Figure 84 and Figure 85 present C-scans of defect-free X-brace #1 acquired with 2.5 mm step increments and with 10 mm step increments, respectively.

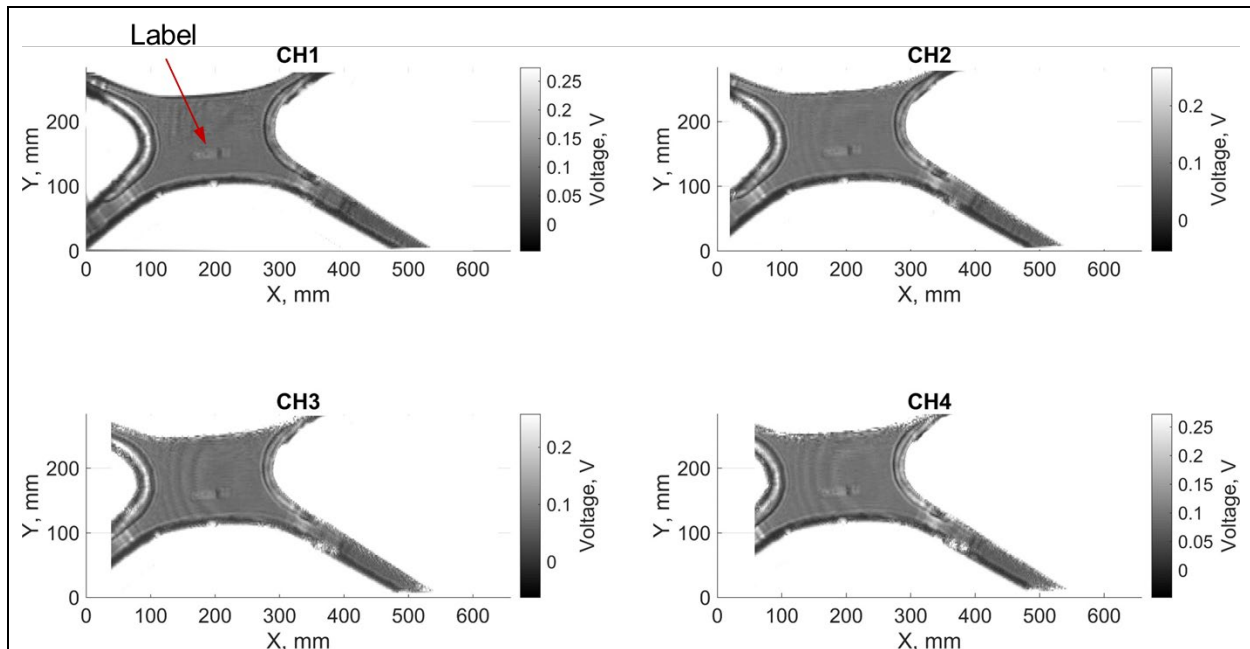


Figure 84. Multi-channel ACUT C-scan of X-brace #1. Scan increment: 2.5 mm.

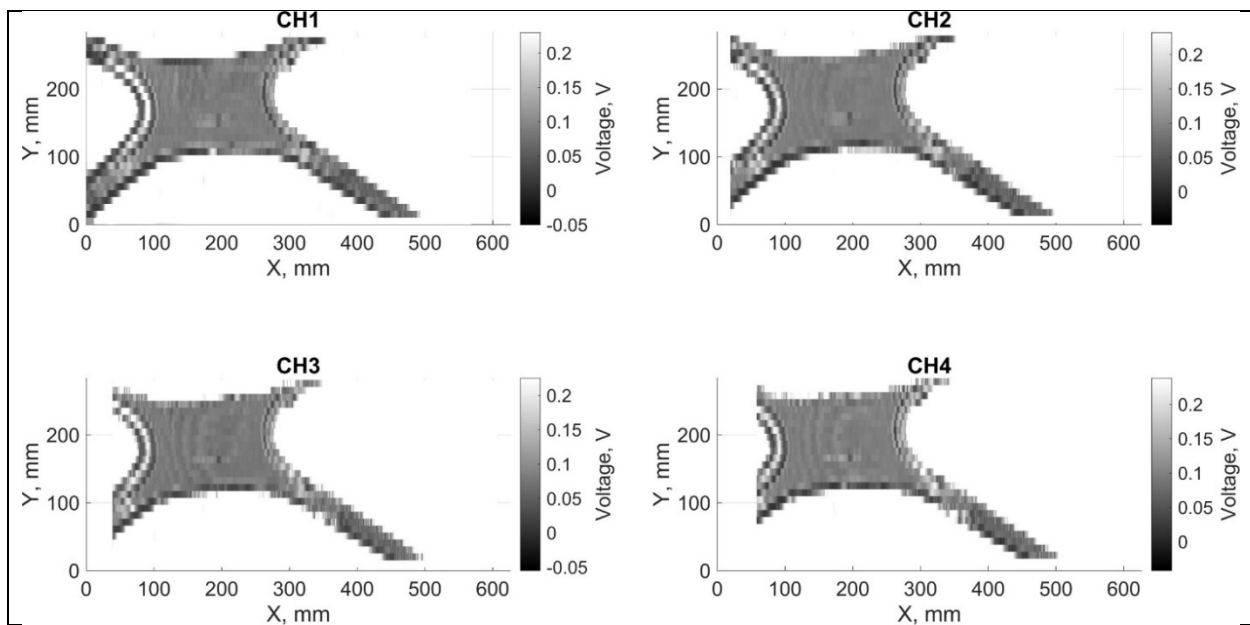


Figure 85. Multi-channel ACUT C-scan of X-brace #1. Scan increment: 10 mm.

Figure 86 provides comparisons of a single-channel C-scan and a merged multi-channel C-scan of X-brace #1. No defects are detected, but there is leftover glue from previously attached label.

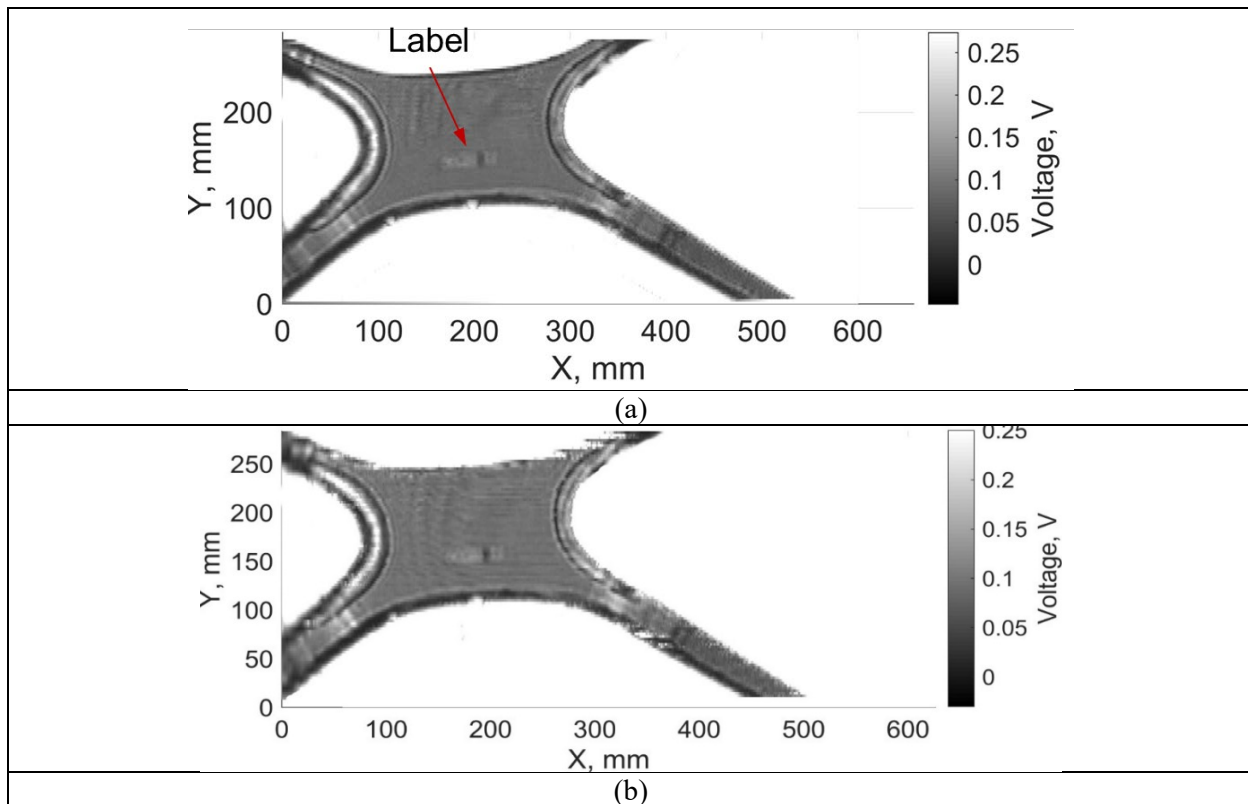


Figure 86. ACUT C-scans of X-brace #1: (a) single channel (CH1), scan increment 2.5 mm, scan time ~6 min; (b) merged multi-channel (CH1+CH2+CH3+CH4), scan increment 10 mm, scan time ~1 min 30 s.

TT-ACUT C-scans of CFRP panel #3

In Quarter VIII, the high-speed multi-channel ACUT system was further validated using the CFRP composite panel #3, which is shown in Figure 87. To the best of the author's knowledge, the CFRP panel #3 had no deliberately introduced defects, and it had not been previously scanned using either immersion UT or phased array UT.

The MSU team made multiple improvements to the experimental setup for TT-ACUT. In particular, automatic floating time gates were implemented in the software in order to enhance detectability of useful acoustic signals acquired on curved samples. Another update included the implementation of three types of digital filters: low-pass (LPF), high-pass (HPF) and band-pass (BPF). Having digital filters of high order allowed the MSU team to acquire clean ultrasonic signals in real-time without averaging the data that could potentially reduce the scan speed. In addition, the ultrasonic gantry was properly grounded, which improved the SNR of measurements.

For example, Figure 88 demonstrates the floating time gate that was automatically applied to the filtered ACUT signal. As the time-of-flight (ToF) of the ultrasonic wave may slightly change due to refraction in the curved sample, the adaptive time gating ensures the amplitude of the wave is extracted accurately at all times.

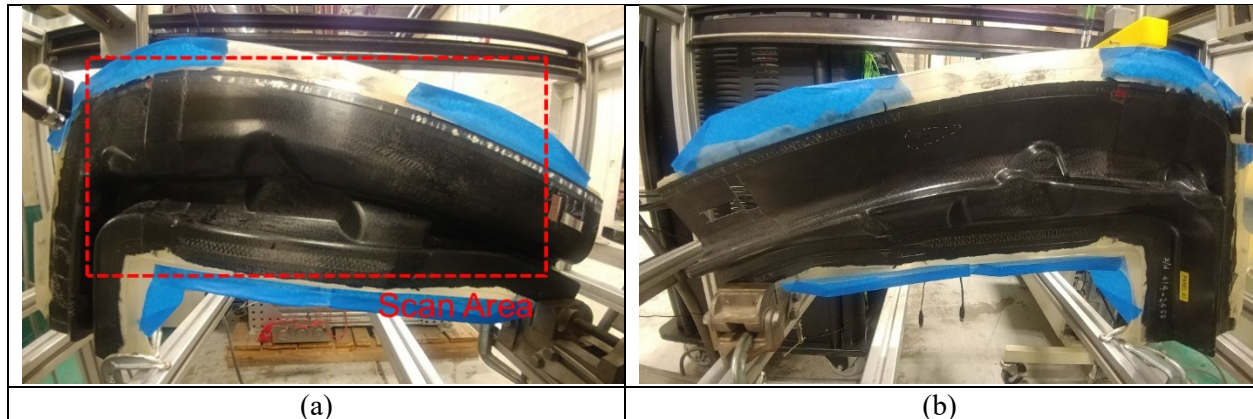


Figure 87. CFRP panel #3: (a) front view; (b) rear view.

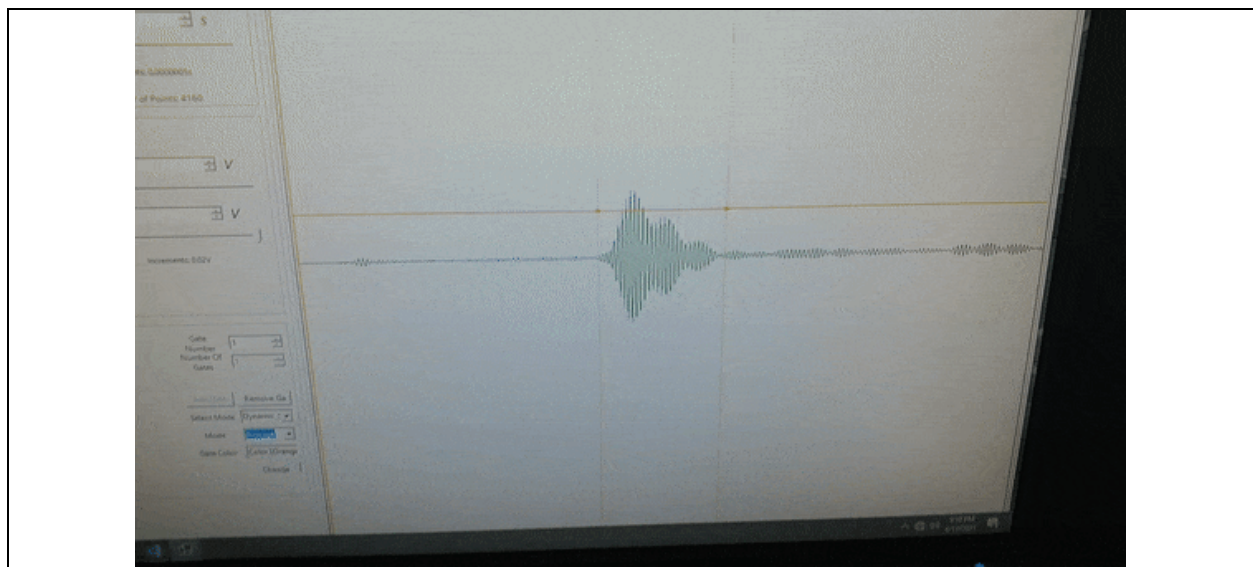


Figure 88. Implementation of floating time-gates for feature extraction from A-scans.

Figure 89 shows the multi-channel ACUT C-scan of panel #3, which was acquired at $f = 200$ kHz and $1 \text{ mm} \times 1 \text{ mm}$ resolution. The C-scan followed the geometrical features of panel #3 very well. In addition, wave reflections were observed in the top section of the panel and were marked using red arrows. These reflections were identified to be manufacturing flaws.

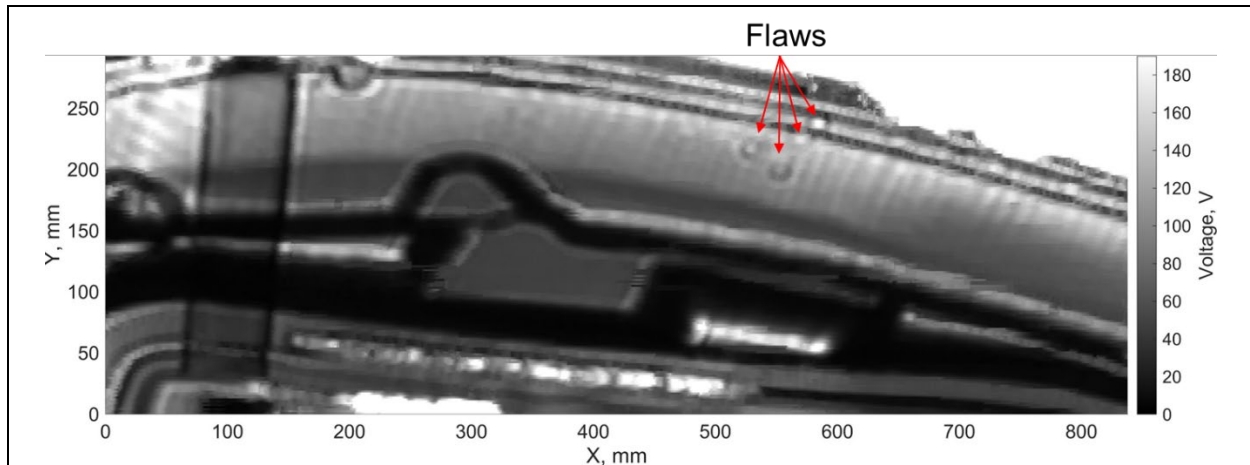


Figure 89. Multi-channel ACUT C-scan of CFRP panel #3 acquired in TT mode at 200 kHz.

The MSU team performed visual inspection of the ROI that corresponded to the detected ACUT irregularities. The photograph of the ROI of the test sample is presented in Figure 90a. It was discovered that defects could possibly be dry fibers and/or agglomerations of air bubbles that were introduced by imperfect curing. The approximate sizes of defects were in the range of [1-4] mm. The obtained results proved the sensitivity of the developed multi-channel ACUT system to manufacturing flaws and validated its performance on CFRP samples with fairly complex geometries.

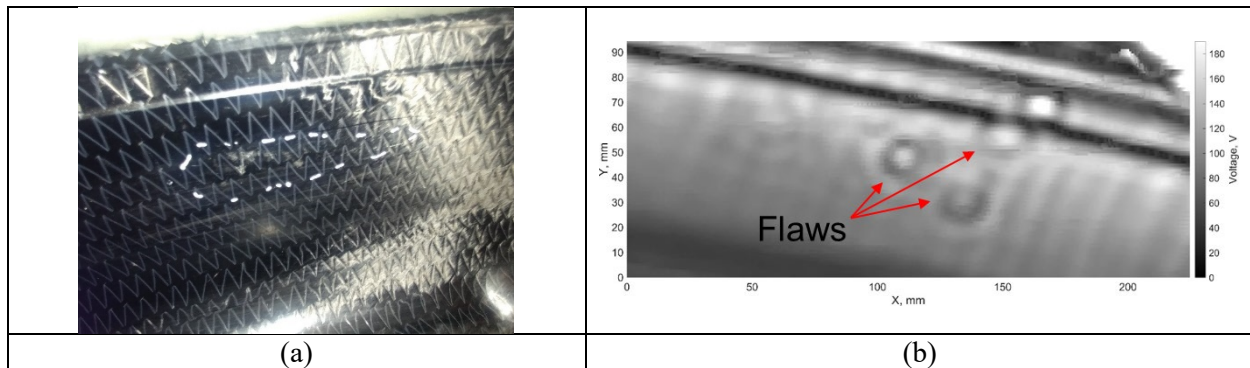


Figure 90. Manufacturing flaws in CFRP panel #3: (a) photograph of the ROI, region with defects is marked with white paint, possibly dry fibers and/or agglomeration of air bubbles; (b) corresponding ACUT C-scan showing acoustic reflections.

Evaluation of piezocomposite ACUT sensors in TT mode

MSU acquired one pair of CFC-230-D12 piezocomposite transducers ($f = 230$ kHz) from Sonotec for evaluation. Piezocomposite probes are manufactured using dice-and-fill technique, in which the piezoelectric crystal is diced and is later filled with epoxy. Piezocomposite probes have tighter beams compared to piezoceramic probes. However, they generate less acoustic pressure. In contrast to piezoceramic probes (e.g. CF-200), piezocomposite probes have slightly different resonant frequencies. Hence, the transmitter and receiver can't be swapped. The CFC-230 receiving probe acquired by MSU also had an embedded pre-amplifier that increased the outer diameter of its aluminum case to ~ 35 mm.

Figure 91 shows the setup for comparison of piezoceramic probes CF-200 and piezocomposite probes CFC-230 in the through-transmission mode. In both cases, the transmitter and receiver were ~ 135 mm apart, and the excitation voltage was 200 V. The central part of the X-brace #3 was raster scanned.

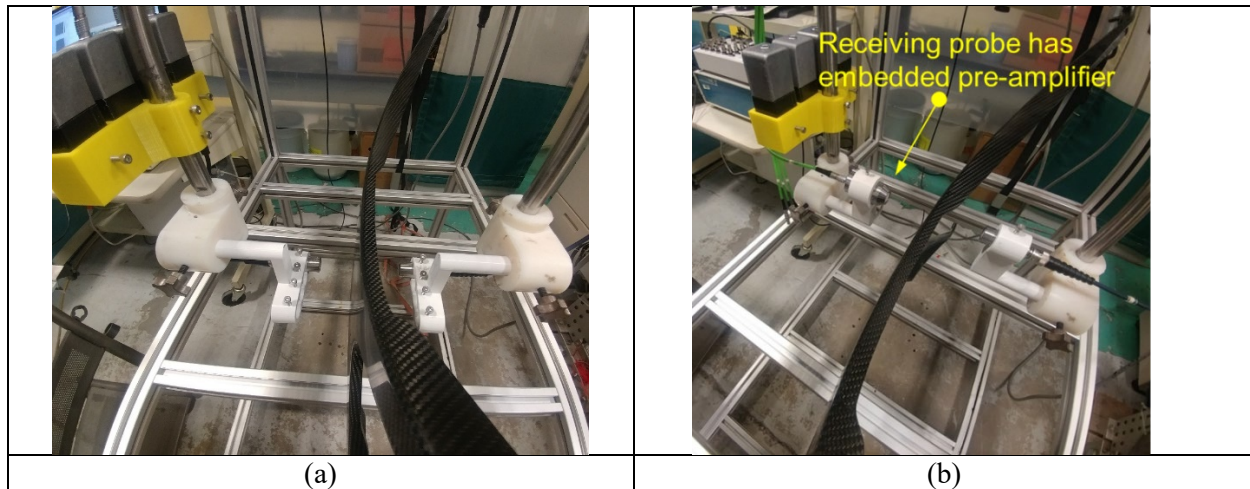


Figure 91. Setup for qualitative comparison of ACUT probes: (a) piezoceramic probes CF-200; (b) piezocomposite probes CFC-230.

Typical A-scans acquired with CF-200 and CFC-230 probes are shown in Figure 92. CF-200 transducers (Figure 92a) provide higher signal-to-noise ratio (SNR) compared to CFC-230 transducers (see Figure 92b). However, CFC-230 probes generate less surface reflections.

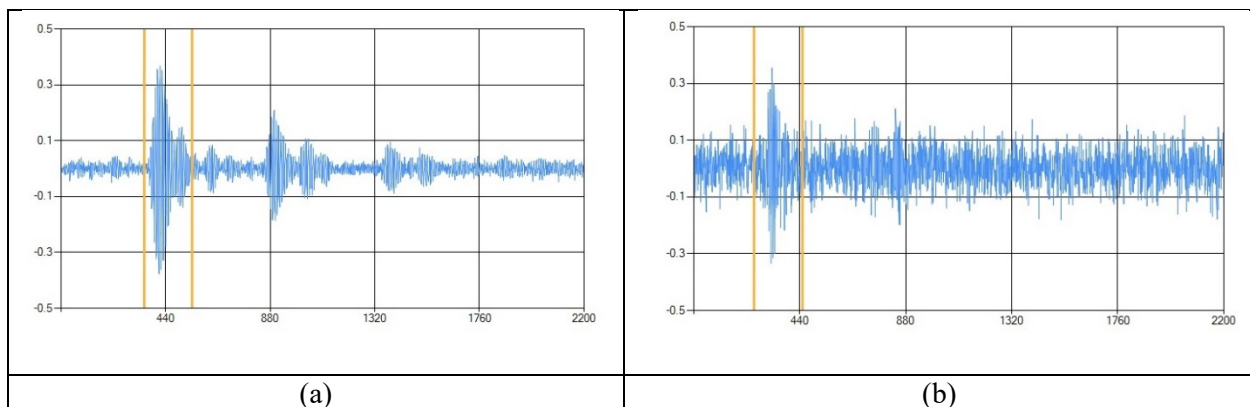


Figure 92. Comparison of piezoceramic and piezocomposite ACUT probes. Typical A-scans: (a) CF-200; (b) CFC-230.

Figure 93 shows C-scans of the X-brace #3 acquired with piezoceramic and piezocomposite ACUT probes. Obtained results demonstrate that the CF-200 probes produce diagnostic images with higher contrast. However, the CF-200 probes have more sidelobes in the acoustic beam. Hence, they tend to oversaturate C-scans around the edges. Damage indications in C-scans acquired using CFC-230 probes have smaller footprints, which means that CFC-230 probes have more focused acoustic beams.

However, for relatively thin CFRP samples like X-braces, standard piezoceramic transducers CF-200 seem to be a good option, since the advantages of CFC-230 with embedded pre-amplifiers come at a cost of increased size. CF-230 piezocomposite probes without embedded pre-amplifiers on the receiving side also could be considered, since this simpler modification provides the same size as CF-200 probes.

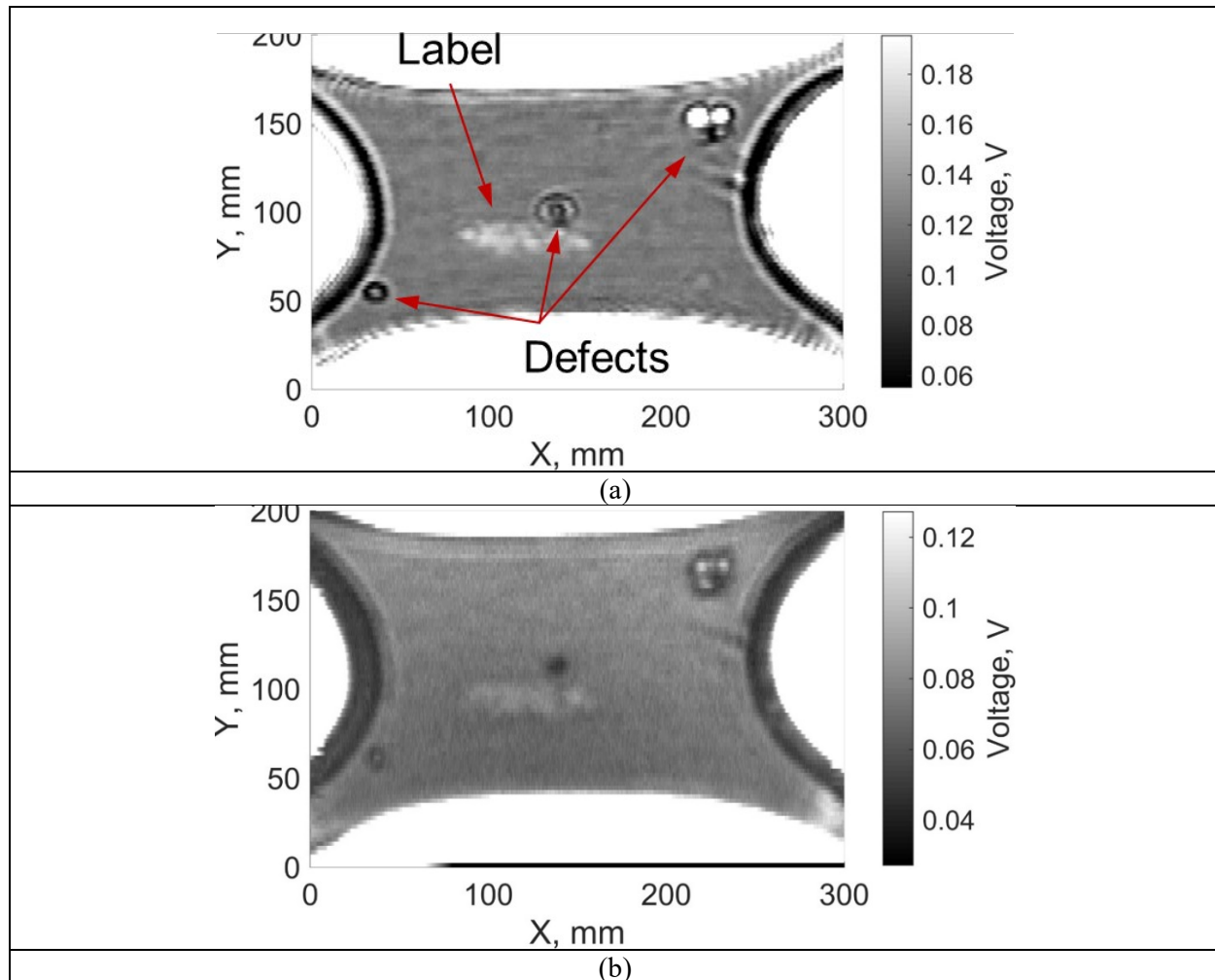


Figure 93. Comparison of piezoceramic and piezocomposite ACUT probes. C-scans of central section of X-brace #3: (a) CF-200; (b) CFC-230.

2.3.6. Design and development of SSA-ACUT probes

In Quarter VII, the MSU team used the developed multi-channel ACUT setup to confirm the feasibility of the single-side access inspection of CFRP specimens. Figure 94b shows a new fixture for holding two ACUT transducers. The ultrasonic waves are excited using the transmitting probe (T) and are picked up by the receiving probe (R). The direct path between the probes through the air is blocked by the absorbing cones so that the waves are forced to propagate through the sample.

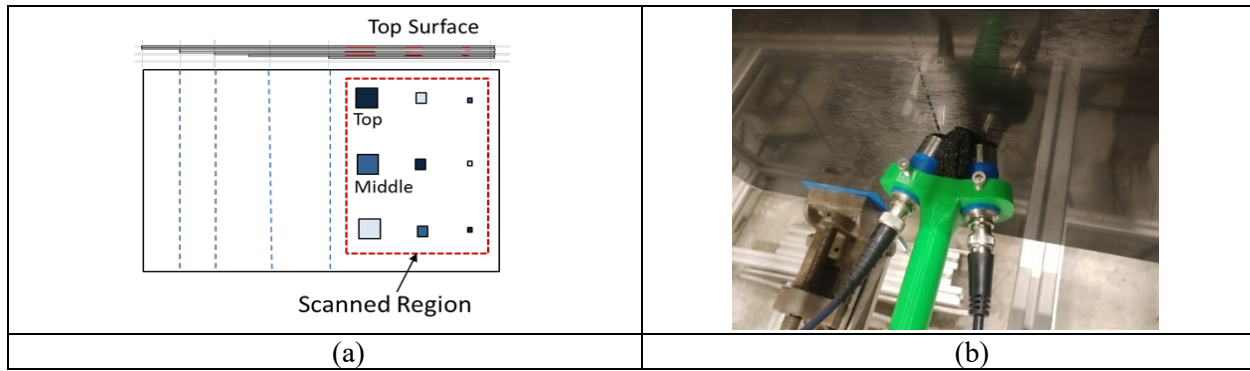


Figure 94. Single-side access ACUT of calibration panel #1: (a) locations of delaminations and scanned region; (b) configuration of the SSA-ACUT probe.

2.3.7. Validation of high-speed ACUT gantry system: 1-channel data acquisition in SSA mode

The developed single-side access ACUT setup was successfully validated on the calibration panel #1 as shown in Figure 94a. The sample was scanned using two pairs of CF-200 and CF-300 probes with 200 kHz and 300 kHz center frequencies, respectively. Raster scans were acquired at 50 mm/s and with 2 mm resolution. The corresponding results are presented in Figure 95.

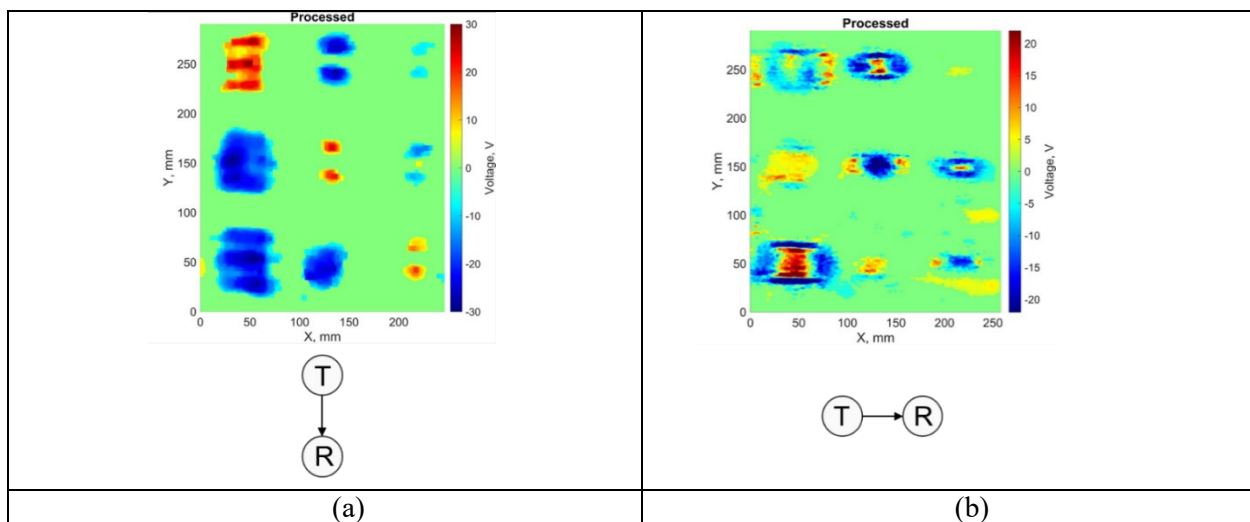


Figure 95. Experimental validation of single-side access ACUT on Calibration panel #1: (a) CF-200 probes, $f = 200$ kHz, vertical probe orientation; (b) CF-300 probes, $f = 300$ kHz, horizontal probe orientation. (T - transmitter, R - receiver).

Figure 95a shows the C-scan of calibration panel #1 acquired using a pair of CF-200 probes. All delaminations were successfully detected that validated the single-side access ACUT technique. In Figure 95a, the probes were positioned vertically; hence, vertical edges of delaminations were detected better than the horizontal edges. The guided waves in the test sample were sensed in one direction only, and the edge lobes appeared due to constructive and destructive interference of guided waves at the edges of interlaminar delaminations.

Figure 95b shows the C-scan of calibration panel #1 acquired using a pair of CF-300 probes. CF-300 probes have smaller aperture and lower acoustic pressure compared to CF-200 probes. Hence, the SNR of the acquired ACUT measurements is lower. In Figure 95b, the probes are positioned horizontally.

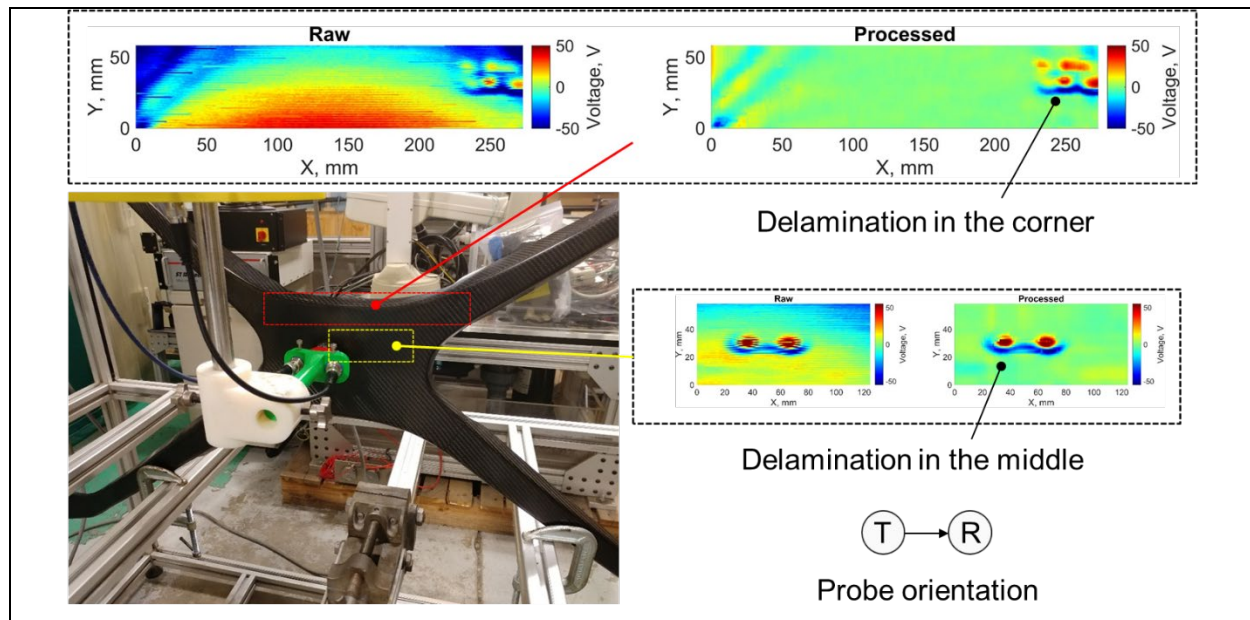


Figure 96. Experimental validation of single-side access ACUT on X-brace 3 (CF-200 probes, $f = 200$ kHz, horizontal probe orientation).

The single-side access ACUT setup was also successfully tested on the X-brace samples as shown in Figure 96. Two regions of the X-brace #3 with interlaminar delaminations were scanned using CF-200 probes. Floating gates were applied to track the acoustic signals, and MSU image processing was used to enhance defect signals. Two delaminations were detected as shown in the inserts in Figure 96. The results agreed well with water immersion C-scans of the same sample from Project 3.8 (Phase I).

3. ELECTROMAGNETIC (EM) NDE

Results obtained in IACMI Project 3.8 (Phase I) successfully demonstrated the feasibility of electromagnetic (EM) techniques for NDE of automotive parts. In Project 3.13 (Phase II), fiber damage and fiber irregularities were detected using coil sensors and eddy current testing (ECT), whereas matrix damage, matrix irregularities and interlaminar delaminations were detected by means of capacitive imaging (CI) and open-plate capacitive sensors. The MSU team also developed and successfully validated dual-mode sensors that synergistically combined benefits of ECT and CI. Validation of EM techniques for high-speed and high-volume NDE in Project 3.13 (Phase II) required completion of the following tasks:

- vii. development and/or acquisition of a measurement system that supported multiple sensing technologies (e.g. inductive, capacitive and/or hybrid sensors) and provided multiple channels for rapid inspection.
- viii. development and validation of finite element (FE) simulations for optimization of sensor design and enhancement of sensitivity to calibration flaws in CFRP and GFRP parts;
- ix. design, manufacturing and experimental validation of multi-element coil and capacitor array probes on rigid and flexible substrates;

3.1. Hardware for Rapid Eddy Current and Capacitive NDE of CFRP Parts

3.1.1. Experimental setup from Phase I

In Quarter II, the MSU team focused on the development and acquisition of hardware necessary to implement the electromagnetic sensing technology in the novel system for rapid NDE of CFRP parts. The original MSU benchtop setup for eddy current and capacitive sensing is shown in Figure 97a.

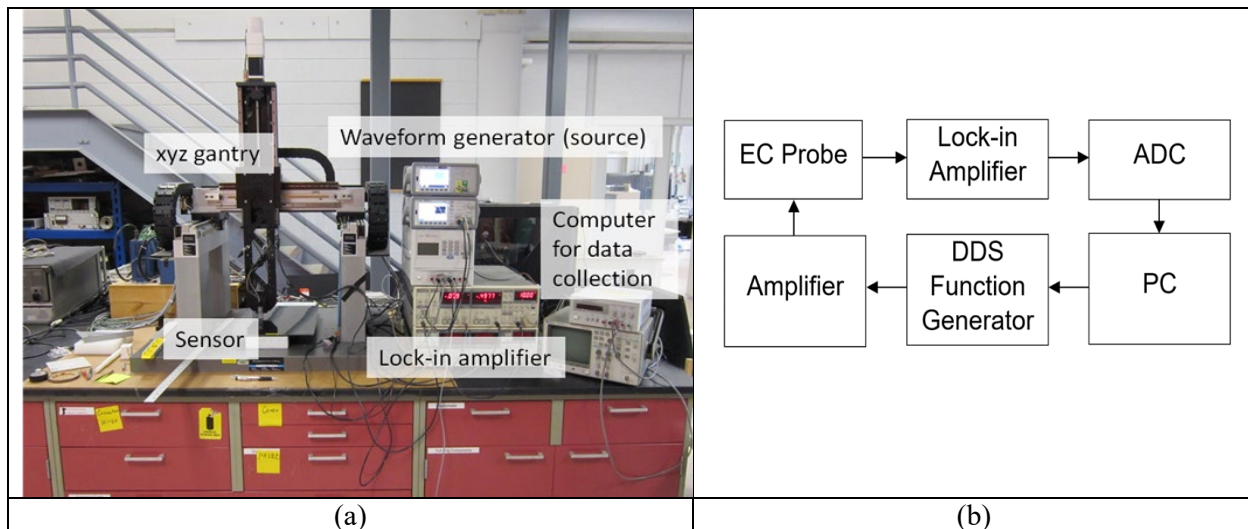


Figure 97. (a) Experimental setup for eddy current NDE and capacitive sensing from Phase I; (b) corresponding block-diagram.

In Project 3.8 (Phase I), defects in CFRP samples such as interlaminar delaminations and fiber damage were detected by registering the impedance changes of either coil or capacitive sensors. Corresponding block-diagram of the system is shown in Figure 97b. Sensors were driven by external source (e.g., DDS function generator) and resulting sensor responses were measured using a lock-in amplifier with high gain and high noise rejection.

3.1.2. Experimental setup for Phase II

Ectane 2 module

In Phase II, all functionality from Figure 97b needed to be combined in a single and ruggedized instrument. In addition, the electromagnetic measurement module had to acquire and process signals from multiple sensors for rapid inspections. The MSU team selected Ectane 2 from Eddyfi for further integration into the multi-modal robotized NDE system for composites (Task vii). The Ectane 2 instrument, shown in Figure 98, was delivered to MSU. Its key features are briefly summarized in Table 2.

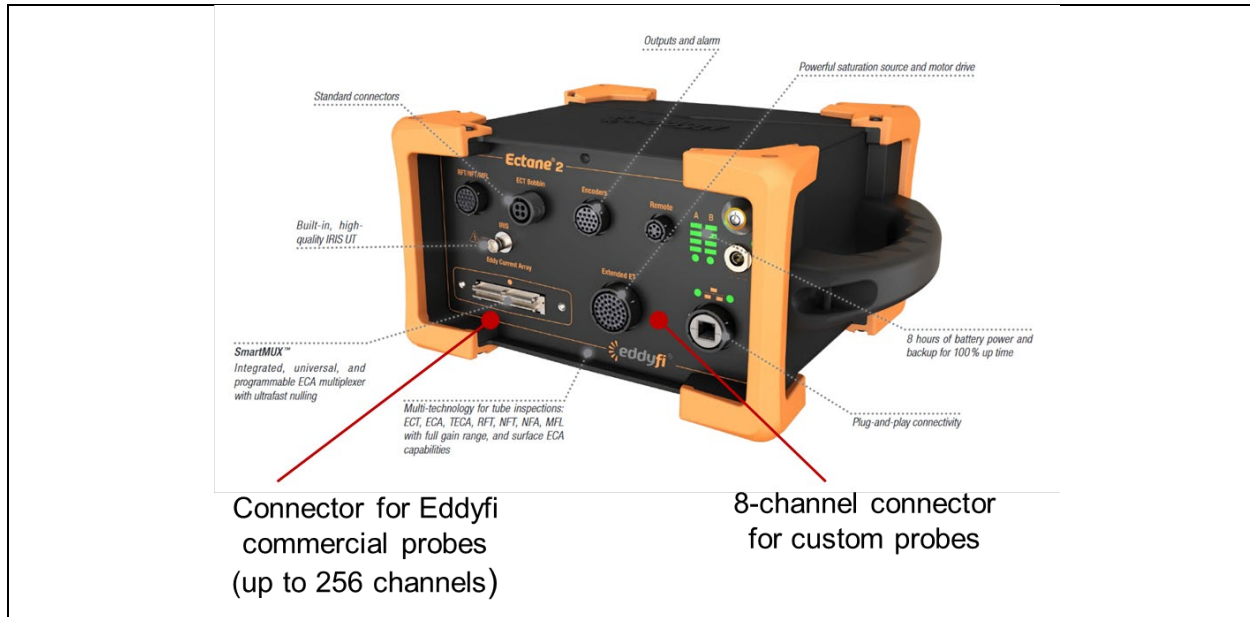


Figure 98. Ectane 2 system for EM NDE.

Feature	Value
Operating frequency range, Hz	5 Hz – 10 MHz
Independent channels	8
Analog-to-digital converter (ADC), bits	16
Sampling rate, kS/s	50
Coil drive, V	2 generators, up to 20 V _{pp}
Position encoder inputs	3
Receiver gain, dB	41
Multiplexer (commercial ECA connector)	SmartMUX, 64 channels

Table 2. Salient features of Ectane 2 system.

Ectane 2 has an 8-channel ADC whose inputs are connected straight to extended ET connector (41 pin, round in Figure 98) and to ECA connector through a multiplexer (256 pins, rectangular in Figure 98). The ECA connector is mostly used for probes with high channel count that require multiplexing, but the extended ET connector is more flexible for prototyping. The extended ET does not have any current limiting circuits and can drive additional external multiplexer, if necessary. The Extane 2 system has a digitally controlled resistor bank for impedance matching to user developed probes.

Custom cable for interfacing MSU array probes with ECA connector

In collaboration with Eddyfi, the MSU team fabricated a custom cable to interface array probes with the ECA connector. The cable supported 18 independent measurement channels and came with stripped ends on the side opposite to the ECA connector as shown in Figure 99a. The MSU team prepared a set of micro-BNC connectors meant to be placed on PCB boards. The micro-BNC cables and the main cable were connected using pins as shown in Figure 99b and Figure 99c. The snap apart design allowed for a single cable to be compatible with multiple MSU array probes. It was also advantageous for debugging the sensor boards and the multiplexer. The cross-section of the multi-channel cable and its mechanical and electrical properties are presented in Figure 100.

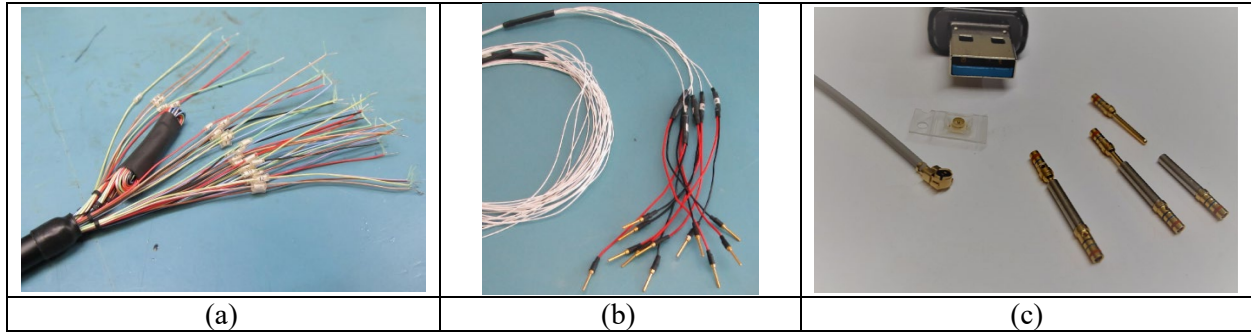


Figure 99. Cable for interfacing array probes with the ECA connector: (a) stripped wire ends; (b) pins attached to ends; (c) pins and μ BNC connection with PCB.

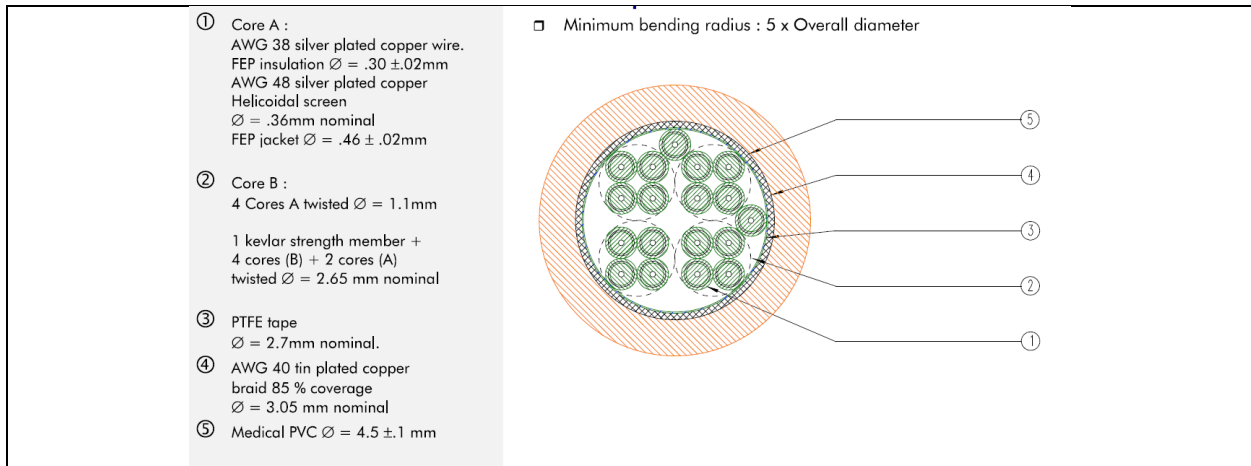


Figure 100. Cross section, electrical and mechanical properties of the cable.

3.2. Eddy Current Testing (ECT)

3.2.1. Modeling of coil sensors for NDE of CFRP and GFRP composites

Magnetic dipole representation of a coil sensor

A coil sensor can be thought of as a magnetic dipole, which is an elementary (ideal) source of the electromagnetic field. A present study investigates the structure of this field and its interaction with subsurface flaws in test samples. Specifically, in the near field zone, which is one of interest in most NDE applications, the electric field (**E**) and magnetic field (**H**) of the electric dipole are given by

$\begin{aligned} H_r &= \frac{m}{4\pi r^3} 2 \cos \theta + O\left(\frac{1}{r^2}\right) \\ H_\theta &= \frac{m}{4\pi r^3} \sin \theta + O\left(\frac{1}{r^2}\right) \\ E_\phi &= -\frac{j\omega\mu_0 m}{4\pi} \frac{1}{r^2} \sin \theta + O\left(\frac{1}{r}\right) \end{aligned}$	(2)
-----------------------------------------------------------------------------------------------------------------------------------------------------------------------------------------------------------------------------------------------------------------------------------	-----

where m is the magnetic moment and μ_0 is the free-space magnetic permittivity, ω is the angular frequency. The components of the electric and magnetic fields are given in spherical coordinates.

In the following section, finite element (FE) simulations are established in order to demonstrate the interaction of the coil sensor with insulating GFRP and CFRP with low through-thickness (cross-ply) electric conductivity. The goal is to optimize the sensitivity of coil sensors to fiber breakage and interlaminar delaminations (Task viii).

Finite element (FE) model of a coil sensor

A finite element model is developed in Comsol Multiphysics in order to simulate the distribution of the electric field in composite test specimens. A volumetric flaw is introduced as an air region. The coil sensor is placed with a small lift-off over the sample geometry and the impedance was then calculated at multiple positions close to the flaw. Here, we considered two sensor topologies: 1) single or absolute (ABS) coil sensor (large coil from Figure 101), and 2) single transmitter / differential receiver sensor STDR (all three coils shown in Figure 101).

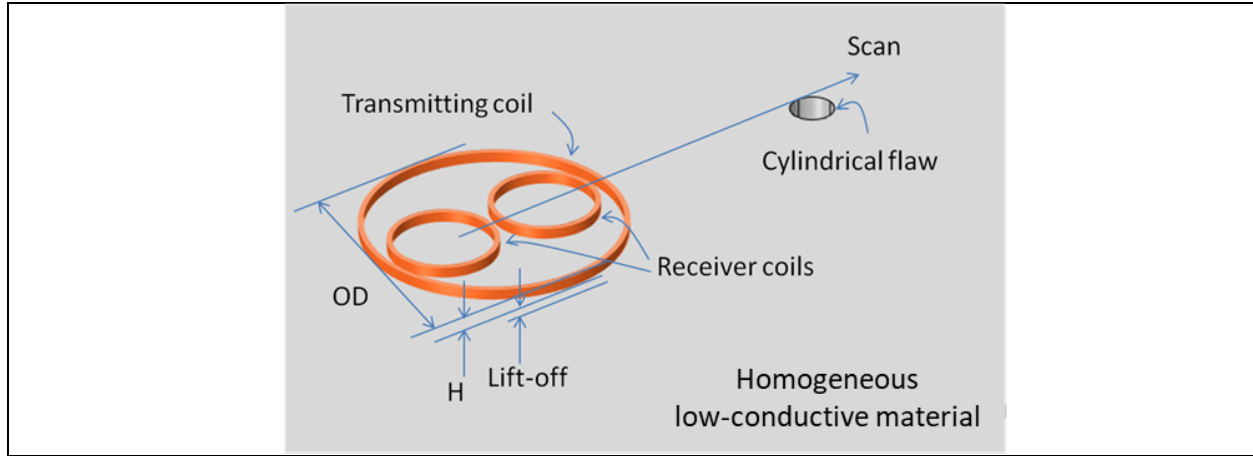


Figure 101. Schematics of the single transmitter / differential receiver (STDR) coil sensor.

The coil carries an imposed current density \mathbf{J}_e , and produces a large magnetic field and a small electric field as per Eq. 1. The fields are computed in the frequency ranges between 10 kHz and 10 MHz. The finite element model is formulated based on the following full-wave Maxwell equations:

$\begin{cases} \nabla \times \mathbf{E} = -j\omega\mathbf{B} \\ \nabla \times \mathbf{B} = \mu_0(\sigma\mathbf{E} + j\omega\epsilon\mathbf{E} + \mathbf{J}_e) \\ \nabla \cdot \epsilon\mathbf{E} = \rho \\ \nabla \cdot \mathbf{B} = 0 \\ + \text{regularity cond. at infinity} \end{cases}$	(3)
----------------------------------------------------------------------------------------------------------------------------------------------------------------------------------------------------------------------------------------------------------------------------------------------	-----

The boundary conditions are set on the outer boundary which truncate the infinite space where $\hat{\mathbf{n}} \times \mathbf{E} = 0$, $\hat{\mathbf{n}}$ being the exterior normal. The outer boundaries are reasonably far away from the region of interest in order to reduce their influence on the final solution. Note that the magnetoquasistatic model (MQS) is not appropriate for modelling the interaction of a coil with a low conductive CFRP or dielectric GFRP materials, since it does not account for the effect of the dielectric constant, ϵ . For the sake of simplicity, we do not consider the dielectric loss, anisotropy of the dielectric permittivity, and anisotropy of the electric conductivity.

Electric conductivity of a test specimen

In order to simplify the numerical computations, the model assumes homogeneous isotropic material with electrical conductivity σ on the order of [0–100] S/m. More sophisticated models can be developed by incorporating the conductivity tensor $\bar{\sigma}$ that accounts for anisotropy. For instance, $\bar{\sigma}$ of a unidirectional CFRP ply with fibers in x - y plane is given by Eq. 4:

$\bar{\sigma} = \begin{bmatrix} \sigma_L \cos^2 \theta + \sigma_T \sin^2 \theta & (\sigma_L - \sigma_T) \sin \theta \cos \theta & 0 \\ (\sigma_L - \sigma_T) \sin \theta \cos \theta & \sigma_L \sin^2 \theta + \sigma_T \cos^2 \theta & 0 \\ 0 & 0 & \sigma_{cp} \end{bmatrix},$	(4)
-----------------------------------------------------------------------------------------------------------------------------------------------------------------------------------------------------------------------------------------------------------------------------------	-----

where σ_L and σ_T are the conductivities in the fiber direction and transverse direction respectively, and σ_{cp} is the cross ply conductivity, θ is the fiber orientation with respect to the x axis.

Typically, σ_L lies between 5×10^3 and 5×10^4 S/m. Typical values of σ_T and σ_{cp} are between 1 S/m and 100 S/m for classical laminates (e.g., multiple unidirectional laminas stacked at different orientations). However, σ_T can be comparable to σ_L in case of plain weave laminates (e.g., stacked layers of plain weave fabrics), and σ_{cp} can be comparable to σ_L in case of 3D woven laminates. Note that the electrical conductivity of CFRP is a few orders of magnitude smaller than that of metals (e.g. $\sigma = 5 \times 10^7$ for copper), and the electrical conductivity of GFRP laminates approaches zero.

Effects of fiber breakage and interlaminar delaminations on measured signals

In the IACMI Projects 3.8 and 3.13, the MSU team developed NDE technologies for the samples provided by the US manufacturers of OEM automotive parts. The samples were classical CFRP laminates and plain weave CFRP laminates with low cross-ply electric conductivity, σ_{cp} . For these types of samples, it was anticipated that fiber breakage would result in measurable changes of the in-plane electric conductivities σ_L and/or σ_T , and negligibly small changes of σ_{cp} and the dielectric permittivity ϵ . However, in the case of the interlaminar delamination, defect detection using coil sensors could be far more challenging owing to the fact that an interlaminar delamination would only affect σ_{cp} and ϵ . Hence, the MSU team proposed a single transmitter/differential receiver coil sensor to address this problem.

Impedance of a single (absolute) coil sensor

For a single coil we can calculate the impedance based on Poynting's theorem:

$Z_{abs} = \frac{1}{I^2} \iiint_{\Omega} j\omega\mu H ^2 + j\omega\epsilon E ^2 + \sigma E ^2 dV$	(5)
---------------------------------------------------------------------------------------------------	-----

The integration is carried out over the whole model domain Ω . The magnetic energy (first term on the right-hand side (RHS)) is important considering CFRP with low σ_{cp} an insulating GFRP with $\sigma = 0$. The magnetic energy due to a magnetic dipole is much larger than the corresponding electric energy (second and third terms respectively, at the RHS of Eq.(5)). This is a drawback, because σ_{cp} and ϵ will mainly affect the electric energy and, therefore, the sensitivity of such sensor to interlaminar delaminations will be rather poor.

Impedance of a single transmitter/differential receiver (STDR) coil sensor

A single transmitter/differential receiver coil sensor is designed to eliminate the effect of the first term at the RHS of Eq.(5). We considered a probe that measures the differential impedance changes between two receiving coils placed in proximity of a third transmitting coil as shown in Figure 101. The change in transfer impedance between the transmitter (T) and receiver (R_i , $i=1,2$) due to a volumetric change in the dielectric properties of the bulk material is calculated as

$\Delta Z_{T/R_i} = \frac{-j\omega}{I^2} \iiint_{V_F} (\epsilon - \epsilon_{BG}) \mathbf{E} \cdot \mathbf{E}_{BG} dV,$	(6)
------------------------------------------------------------------------------------------------------------------------	-----

where I is the prescribed excitation current in the transmitter coil, and ϵ_{BG} is the dielectric permittivity of the specimen with no defects.

The transfer impedance change in Eq.(6) will increase with the angular frequency ω and with the square of the electric field. In the kHz frequency and MHz frequency range, the electric field is mainly proportional to ω and the impedance difference is then proportional to ω^3 . This can be exploited to increase the measured quantities. A high frequency and a high number of turns are therefore important in order to get good signal strength. However, an increase of both these variables will eventually build up large capacitive effects which must be considered carefully in an experimental setup.

In the FE model, the impedances of receiving coils (R_i , $i=1,2$) are calculated as ratios between the induced voltages over the induced currents:

$Z_{T/R_i} = \frac{V_i}{I_i}.$	(7)
--------------------------------	-----

The output of the sensor is differential, hence the difference between the receiver coil impedances is considered:

$\Delta Z_{T/R_{diff}} = \left(\frac{V_1}{I_1} - \frac{V_2}{I_2} \right).$	(8)
-----------------------------------------------------------------------------	-----

Relative impedance change

A volumetric change in the dielectric properties of the bulk material associated with a flaw will alter the fields and this will translate in a change of the impedance of the coil sensor. We considered the relative change of impedance due to the flaw as a sensitivity metric:

$\delta_s = \frac{\Delta Z_{DEF} - \Delta Z_{BG}}{\Delta Z_{BG}},$	(9)
--------------------------------------------------------------------	-----

where ΔZ_{DEF} is the impedance difference when the flaw is present, and ΔZ_{BG} denotes the impedance difference without the flaw. The sensitivity δ_s is dimensionless. The model represents an ideal measurement and does not include stray capacitances or inductances of wires and connectors.

3.2.2. FE simulations: ABS and STDR coil sensors, dielectric FRP

Distribution of the electric field in the transect of the test specimen

Test geometry given in Figure 101 was imported into the FE model. The test material was simulated as a dielectric with $\sigma = 0$. The transmitter coil had the following geometry: $N = 1$ turn, $OD = 5$ mm, $ID = 4.5$ mm, $H = 1$ mm, and lift-off = 1 mm. The prescribed excitation current was 1 A. Figure 102 shows the corresponding electric field around the coil.

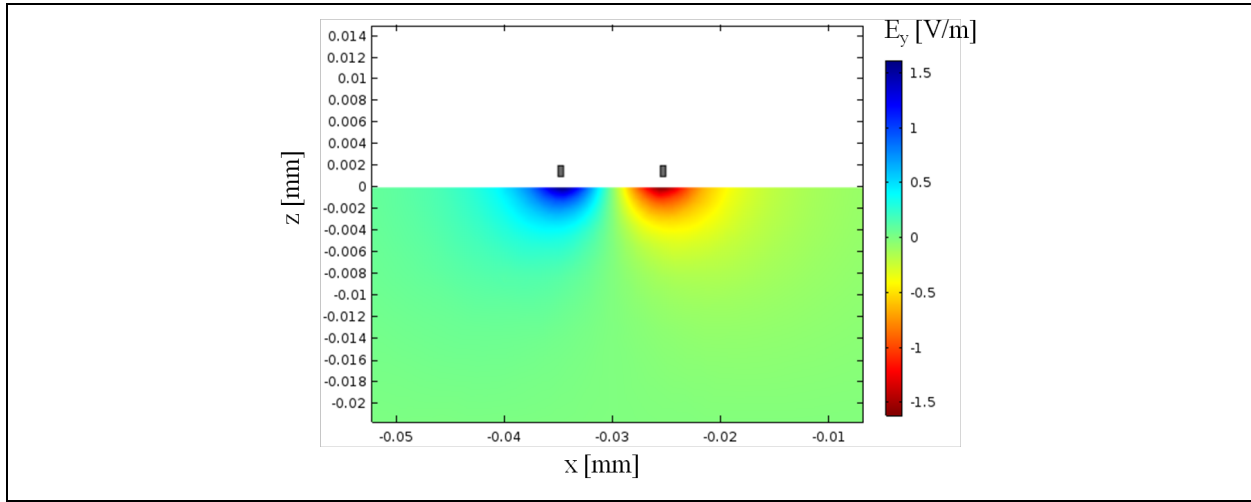


Figure 102. The electric field around the absolute coil (xz-cross section).

It is worth noting that the electric field produced by the coil is aligned along the circumferential direction and it is almost orthogonal to the field produced by the open plate capacitor. Indeed, these two different sensors can be used in a complementary manner regarding the directional properties of the applied electrical field.

C-Scan image of the volumetric defect

Figure 103 shows the change in inductance of the absolute coil at multiple positions around a cylindrical flaw. The dimensions for the coil were: $OD = 10$ mm, $ID = 9$ mm, height = 1 mm, liftoff = 1 mm, $N = 25$ turns, and the flaw radius was 2 mm. The test material was simulated as a dielectric with $\sigma = 0$.

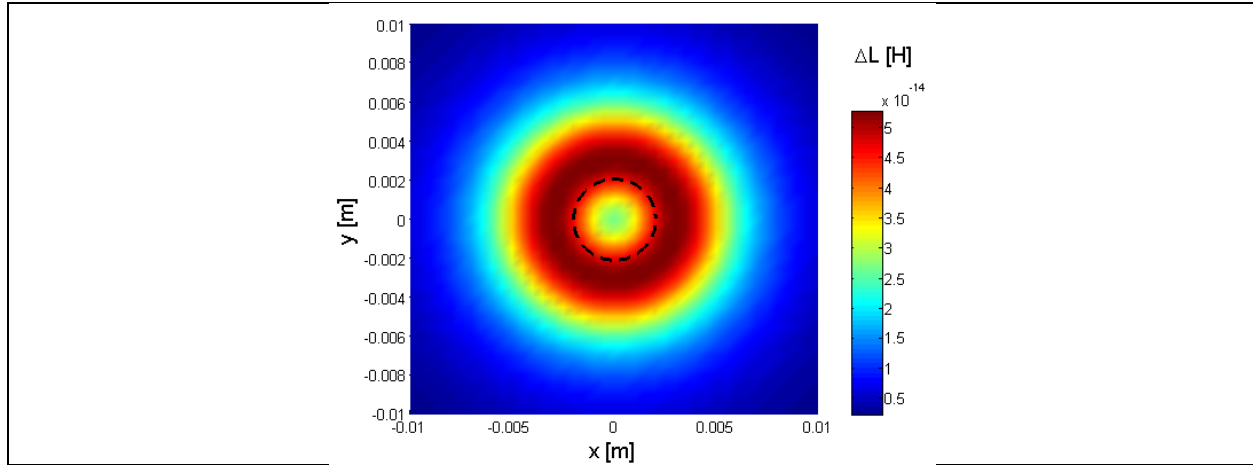


Figure 103. C-scan image over a hole with 2 mm radius (dashed line). Coil sensor with OD = 10 mm, ID = 9 mm, height = 1 mm, liftoff = 1 mm, N=25.

The geometrical properties (i.e., the footprint) of the coil influence the measured signal around the cylindrical flaw. The flaw produces a very small change of inductance, while background inductance is around 10 μH . This confirms that the underlying NDE problem is challenging: 1) equipment with high gain, high bitwise resolution and low noise is needed for data acquisition; and 2) inductance and stray capacitance of probe wires will affect the measurements.

Effects of sensor/defect geometries and lift-off on relative impedance change: single (absolute) coil

A series of FE simulations was carried out in order to compare different geometries of the absolute coil sensor and study the effects of defect size, defect depth under surface, specimen's permittivity, and sensor lift-off on the relative impedance change. Three different coil geometries were considered as presented in Figure 104.

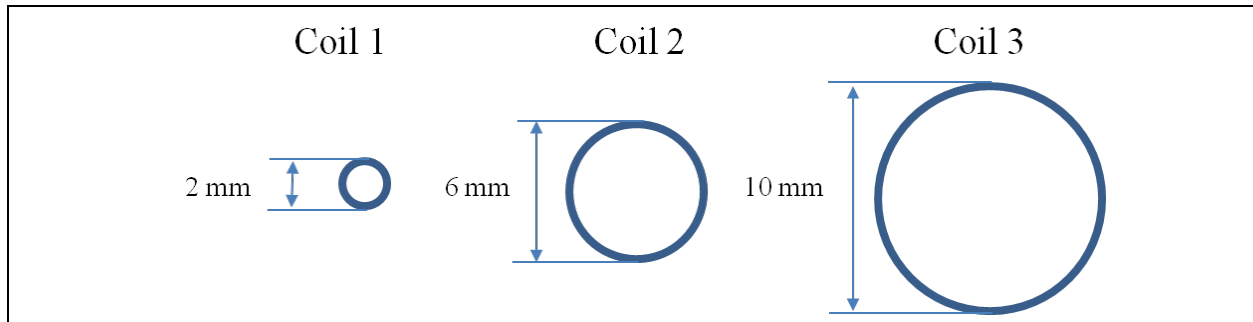


Figure 104. Three configurations of a single coil sensor.

The test material was simulated as a dielectric with $\sigma = 0$. For all FE simulations, a separate defect domain was created. It was either assigned the properties of the bulk material to simulate a baseline sensor response (defect-free case), or the properties of air to simulate a sensor response with defect present in the structure. The absolute coil sensor was placed above the surface of the sample and the center of the defect domain. Then, the relative impedance change from Eq.(9) was evaluated based on the acquired FE results. Four separate parameters were considered: 1) defect radius, 2) specimen's dielectric permittivity, 3) sensor lift-off, and 4) defect depth under the surface. Figure 105 shows the corresponding FE results for different sensor geometries from Figure 104 and the four test configurations mentioned above.

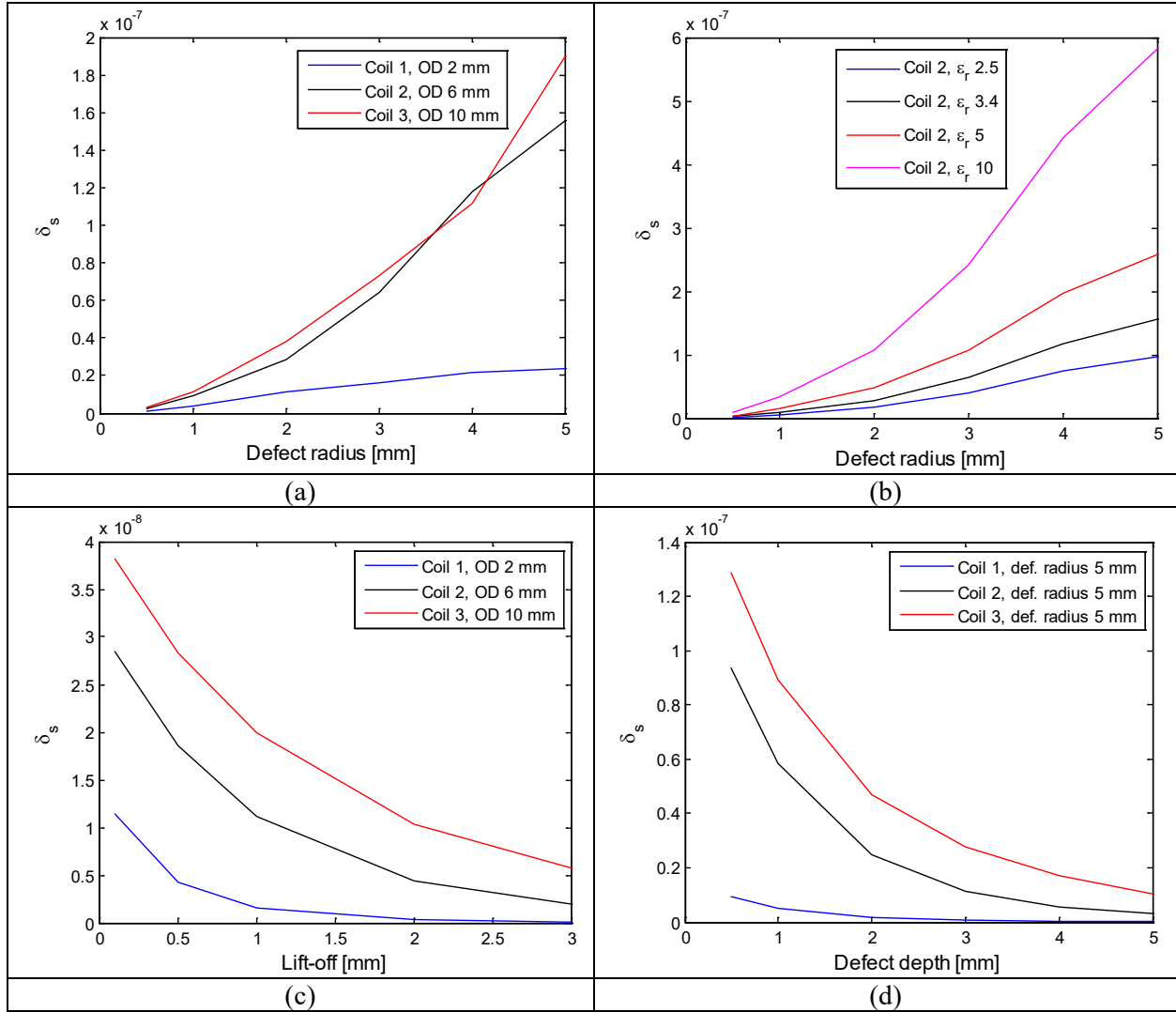


Figure 105. Sensitivity for different coil geometries (absolute sensor) as a function of: (a) defect radius, (b) dielectric constant of test material, (c) sensor lift-off (defect radius of 2 mm) and (d) defect depth under the surface (defect radius of 5 mm).

Figure 105a demonstrates that the relative impedance change of the absolute coil sensor increases with flaw size for all sensor geometries. Another outcome is that the sensitivity to a defect in the form of an air void increases with higher dielectric permittivity of the surrounding material as shown in Figure 105b. Increased lift-off reduces the sensitivity of all sensor configurations (see Figure 105c). Figure 105d presents the simulation results for different defect depths under the surface of the test specimen. With all other parameters equal, the sensitivity will drop faster as a function of defect depth under the surface for the coil sensor with smaller footprint. Larger coils generate stronger electric field that provides deeper penetration into the transect of the test specimen. However, the most significant result of the FE modeling is that the relative impedance change of an absolute coil is on the order of 10^{-7} , which is too small to be reliably measured in the experiments. The single transmitter/differential receiver coil sensor is designed to address this problem.

Three different designs of the single transmitter/differential receiver coil sensor are shown in Figure 106. Signals from smaller coils are subtracted in order to cancel out the effect of the first term in Eq.(5).

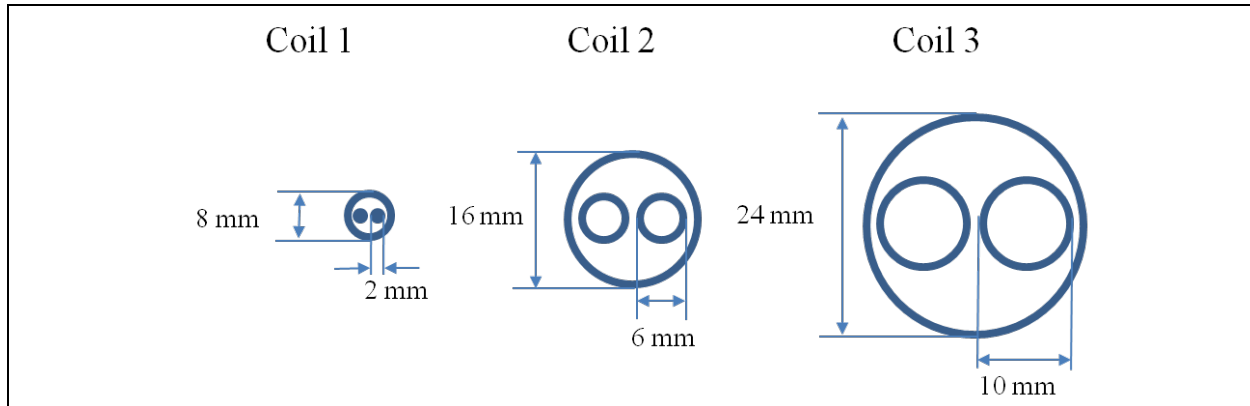


Figure 106. Three configurations of a single transmitter/differential receiver sensor.

A similar set of FE simulations was performed as in the case with the absolute coil in order to study the sensitivity of the new sensor design. The obtained results are shown in Figure 107.

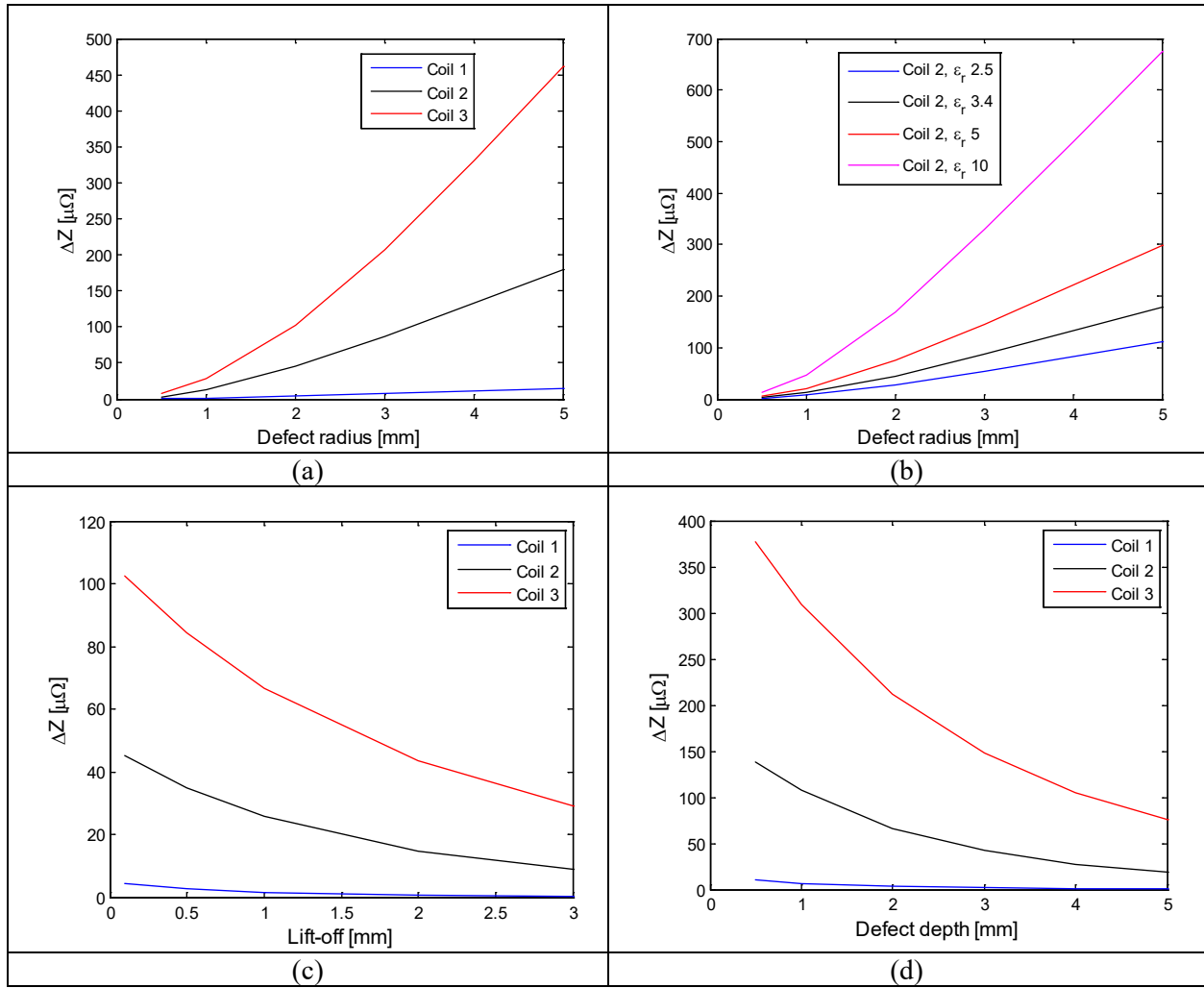


Figure 107. Sensitivity for different geometries of single transmitter/differential receiver coil as a function of: (a) defect radius, (b) dielectric constant of test material, (c) sensor lift-off (defect radius of 2 mm) and (d) defect depth under the surface (defect radius of 5 mm).

The overall trends are very similar to those described in Figure 105. However, the difference between receiver coil impedances is in the range of a fraction of $m\Omega$ and, thus, it can be properly measured. Single a transmitter/differential receiver sensor is promising for detecting the interlaminar delaminations. However, the design is more complex compared to conventional pancake coils. The MSU team focused on its fabrication only after implementation and optimization of the regular sensor topologies (e.g. multi-channel absolute, differential and T/R).

3.2.3. Configurations of array coil sensors

In IACMI Project 3.13, rapid EC inspection of CFRP test samples was accomplished using three different sensing configurations (topologies) compatible with Ectane 2 instrument:

1. absolute (ABS);
2. differential (DIFF);
3. reflection or transmit/receive (T/R):
 - a. short single driver (SSD)
 - b. short double driver (SDD)
 - c. long single driver (LSD)

All EC array probes used in experiments had one or multiple rows of coils to achieve large spatial coverage and rapid multi-channel data acquisition. Sensing configurations involved one or multiple coils for field excitation and field pick up.

The MSU team performed initial experiments by interfacing the developed eddy current sensors to the EET connector, which was suitable for parallel data acquisition using up to 8 channels. EC array probes with high channel counts were later interfaced to the ECA connector with the multiplexor (MUX). The MUX was programmed in order to support all time switching sequences. Since the electronic switching process was fast, multiple sensing topologies could be activated in one pass of the array probe.

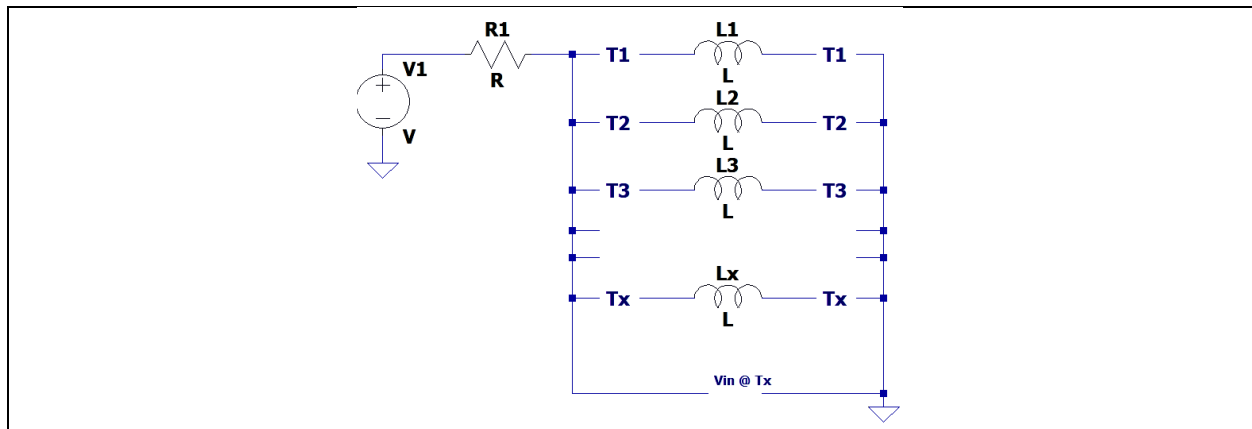


Figure 108. Electrical connection of coils of the array probe to MUX.

The electrical circuit depicted in Figure 108 shows how the driving coils are connected to the MUX. Coils L1 through Lx are activated sequentially at time gates T1 through Tx. In addition, it is possible to enable two coils at the same time (needed for the SDD topology) since the instrument has two synchronized direct digital synthesis (DDS) voltage sources.

Absolute topology (ABS)

Schematics of the absolute sensing topology is illustrated in Figure 109. The same coil is used as a driver and a receiver. Impedance of the coil changes due to the mutual inductance with the test sample. Hence, the voltage across the coil is sensitive to local imperfections of the test sample. ABS topology is the simplest to implement. Impedance measurements provide high sensitivity to flaws. However, the coils are also sensitive to lift-off variations, noise in the cables and thermal drifts. The output signal is always non-zero, and bias needs to be removed from measurements.

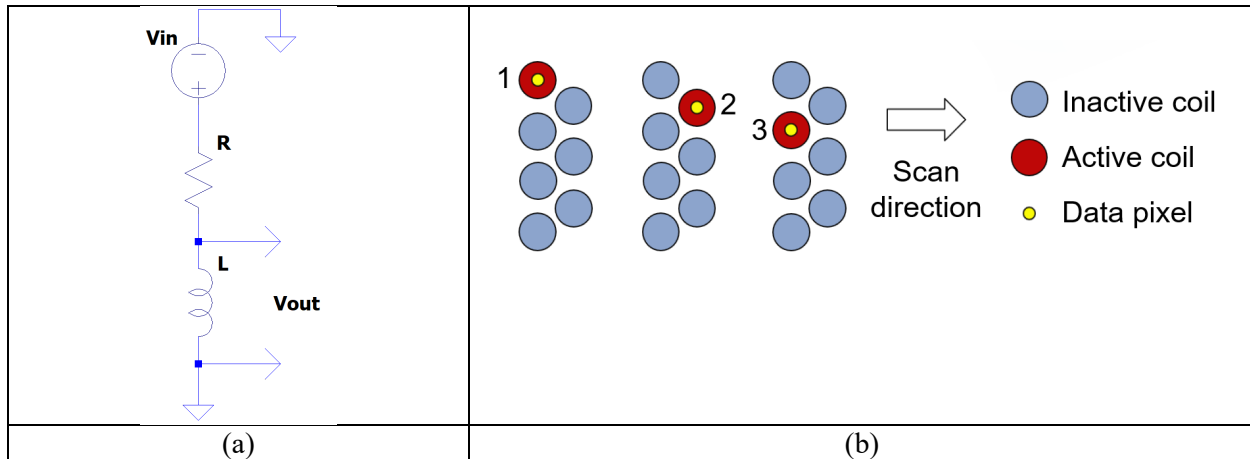


Figure 109. Absolute (ABS) sensing topology: 1) corresponding electric circuit for one channel; 2) switching sequence for measurements in time gates T1-T3.

Differential topology (DIFF)

Figure 110 illustrates the differential sensing topology. Two coils are connected in the Wheatstone bridge. The output of the bridge is near zero in the absence of structural flaws under the sensors. Non-zero signals are generated when the defect is under one of the coils, or if the bridge is not balanced. The virtues of the differential measurement are cancellations of voltage biases on coils and noise due to cables, as well as providing reduced thermal drift. Differential signal changes its polarity when the probe passes over opposing edges of a defect.

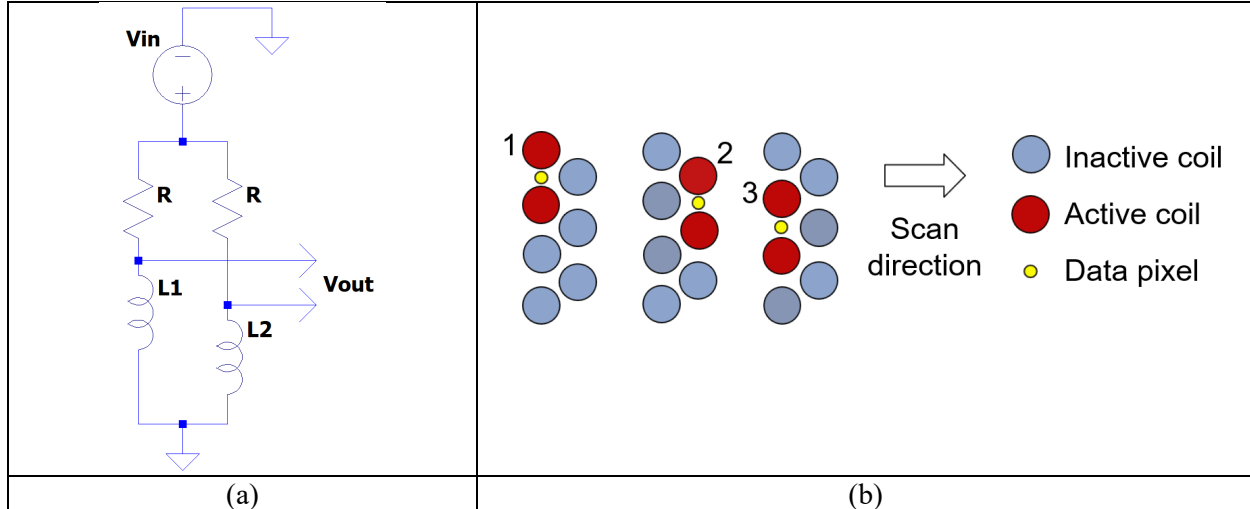


Figure 110. Differential (DIFF) sensing topology: 1) corresponding electric circuit for one channel; 2) switching sequence for measurements in time gates T1-T3.

Transmit/receive topology (T/R)

Schematics of the reflection sensing topology (transmit/receive – T/R, or pitch-catch) are highlighted in Figure 111. The transmitting coil L1 generates the excitation magnetic field, which induces the field in the test sample through eddy currents. The total field which is a superposition of the excitation field and the induced field, is picked up by the receiver L2. The array probes using the T/R topology can be designed such that the transmitters are placed either on top of the receivers, or both transmitters and the receivers are in the same plane parallel to the top surface of the test sample.

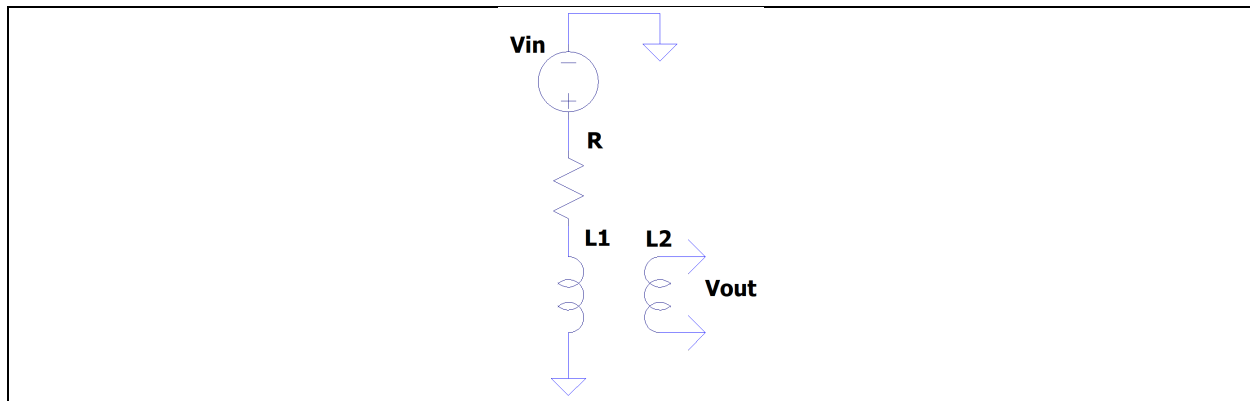


Figure 111. Reflection (T/R) sensing topology: electric circuit for one channel measurement using a single transmitter coil L1 and a single receiver coil L2.

Having two or more rows of coils in the array probe is advantageous for reflection sensing, because fields can be measured by the receivers in both longitudinal and transverse directions. Splitting sensing channels into axial and transverse groups effectively doubles the number of the acquired signals. Defects with preferred orientation (e.g., matrix cracks) will be better detected in one channel than in another.

Depending on the number and positions of activated transmitters and the distances between them to receivers, the reflection topology can be further subdivided into the SSD, SDD and LSD topologies as explained below.

Short Single Driver (SSD)

The SSD topology is the simplest T/R topology as it involves only one transmitting coil and one receiving coil as shown in Figure 111 and Figure 112. The SSD is suitable for detecting small surface breaking flaws and defects at medium depths in the transect of the test specimen. The SSD topology presented in Figure 112 would be more sensitive to flaws of horizontal orientation rather than to flaws of vertical orientation.

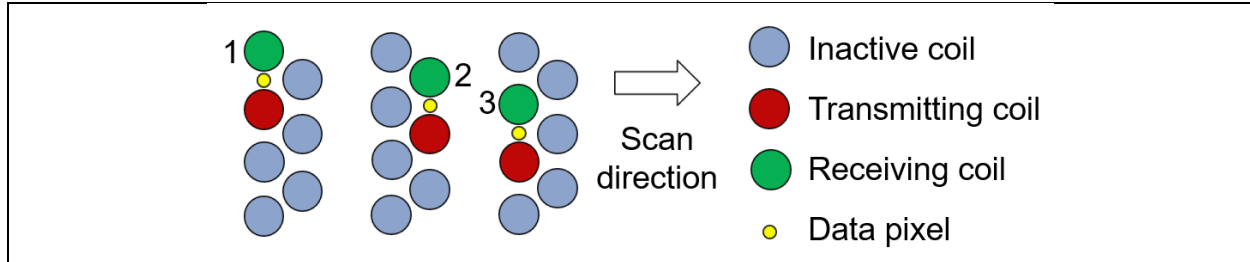


Figure 112. SSD sensing topology: switching sequence for measurements in time gates T1-T3.

Short Double Driver (SDD)

The SDD topology is similar to SSD. However, the T/R measurements are acquired in both axial and transverse directions as depicted in Figure 113 and Figure 114. Having orthogonal channel groups provides uniform sensitivity to flaws of all orientations. In SDD, two excitation coils are enabled simultaneously in order to increase the strength of the magnetic field in the test sample. For example, in the axial configuration, two adjacent coils in one row are driven simultaneously and the coil in the opposite row measures the resulting field. Each data pixel in the C-scan is placed in the geometrical center between the three coils as highlighted by a yellow dot.

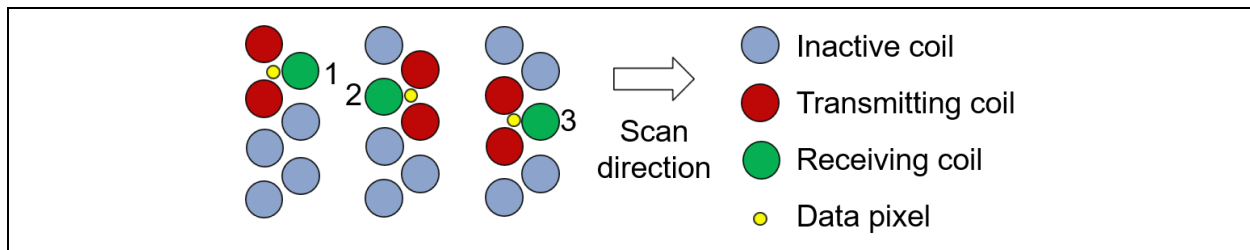


Figure 113. SSD axial topology: switching sequence for measurements in time gates T1-T3

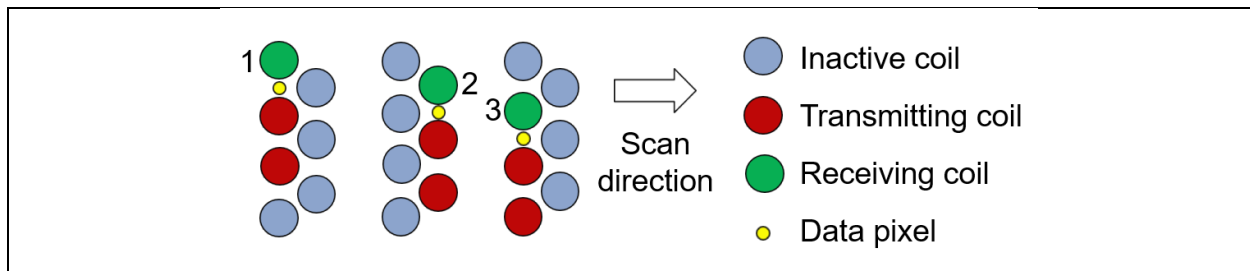


Figure 114. SSD transverse topology: switching sequence for measurements in time gates T1-T3

Long Single Driver (LSD)

The LSD topology provides the highest penetration depth of the field at the expense of reduced spatial resolution of the measurement. If the probe is set to operate as LSD, only one coil at a time is driven by the generator and only one coil is used as a receiver. The coils adjacent to the transmitter are disabled. The distances between the transmitter and the receiver are doubled compared to SSD and SDD topologies. The LSD topology also provides axial and transverse measurements as illustrated in Figure 115 and Figure 116.

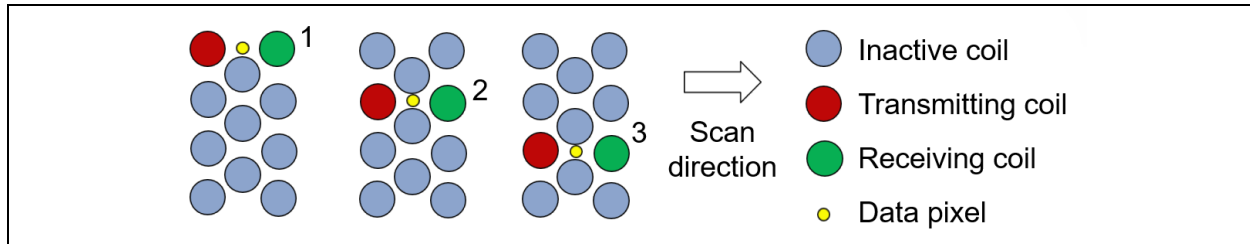


Figure 115. LSD axial topology: switching sequence for measurements in time gates T1-T3.

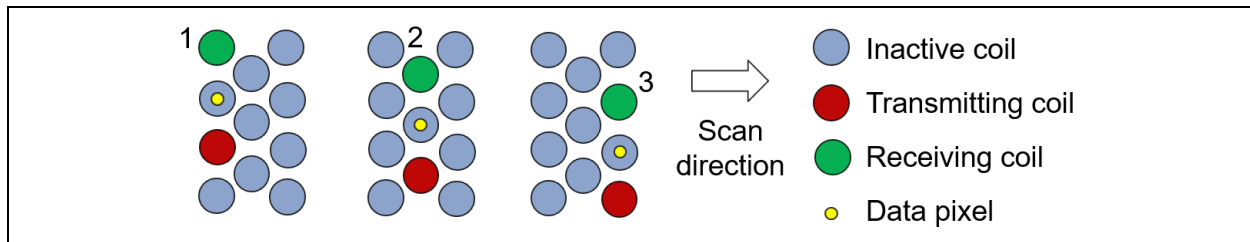


Figure 116. LSD transverse topology: switching sequence for measurements in time gates T1-T3

3.2.4. Commercial coil array probe

One of the standard flex probes from Eddyfi is shown in Figure 117. The probe has 64 coils embedded in a flexible substrate. The coils are physically wound using copper wires, and are arranged in two rows as shown in Figure 117a. Since the probe is flexible, it can follow curvatures of fairly complicated parts. Coil size of 5 mm provides reasonable sensitivity to small defects (~2.5 mm). Unfortunately, the probe's nominal operating frequency is only 250 kHz, which is not optimal for inspection of CFRP parts with low electric conductivity. Optimal excitation frequencies for eddy current NDE of carbon fiber composites generally lie in the range of 500 kHz – 10 MHz.

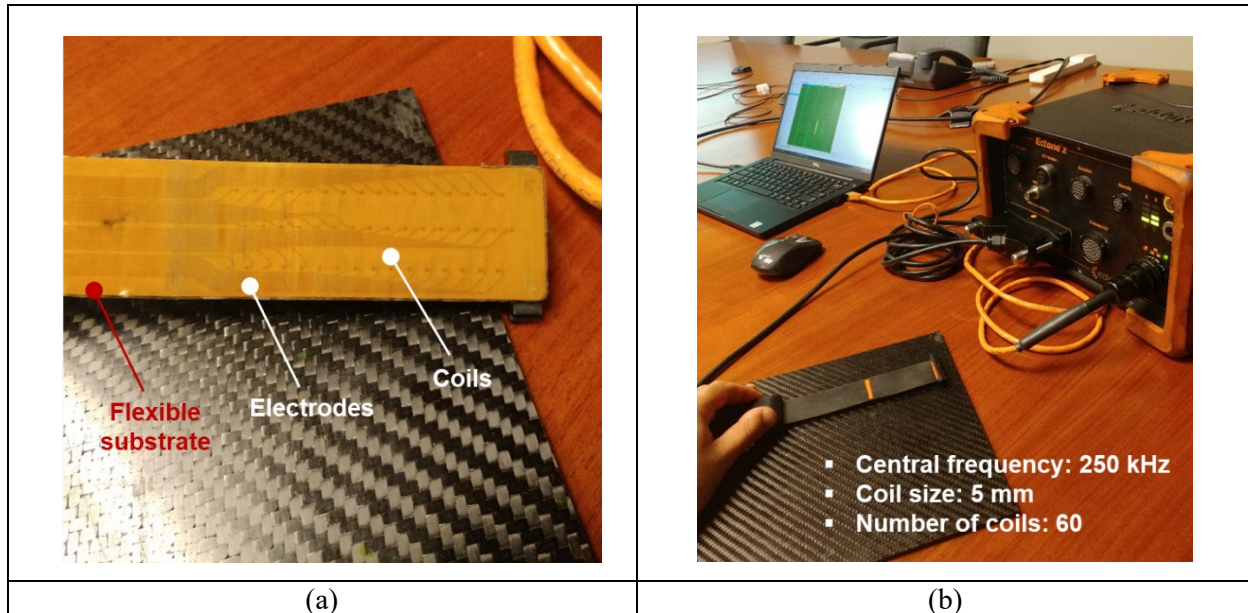


Figure 117. Commercial flex coil for detecting surface barking cracks in metallic parts; (b) manual scanning of CFRP sample with calibrated defects.

Ectane 2 with a commercial coil probe (see Figure 117) was tested on a plain weave CFRP panel with calibration defects (see Figure 118a and Figure 118b). Multiple cuts of different shapes, sizes and depths were created in the sample to simulated fiber damage. Figure 118c demonstrates schematic drawings and positions of all notches. The Eddyfi probe did not have position encoders, and C-scan of the top row of defects (see Figure 118b) was acquired from the clean side by dragging the probe manually. The probe was set to operate in LSD mode at 1 MHz. Corresponding results are presented in Figure 118d. C-scan in Figure 118d shows the real part of the signals. All three notches at 90°, 75° and 45° were highlighted. Optimization of the probe design was necessary in order to provide higher sensitivity to flaws.

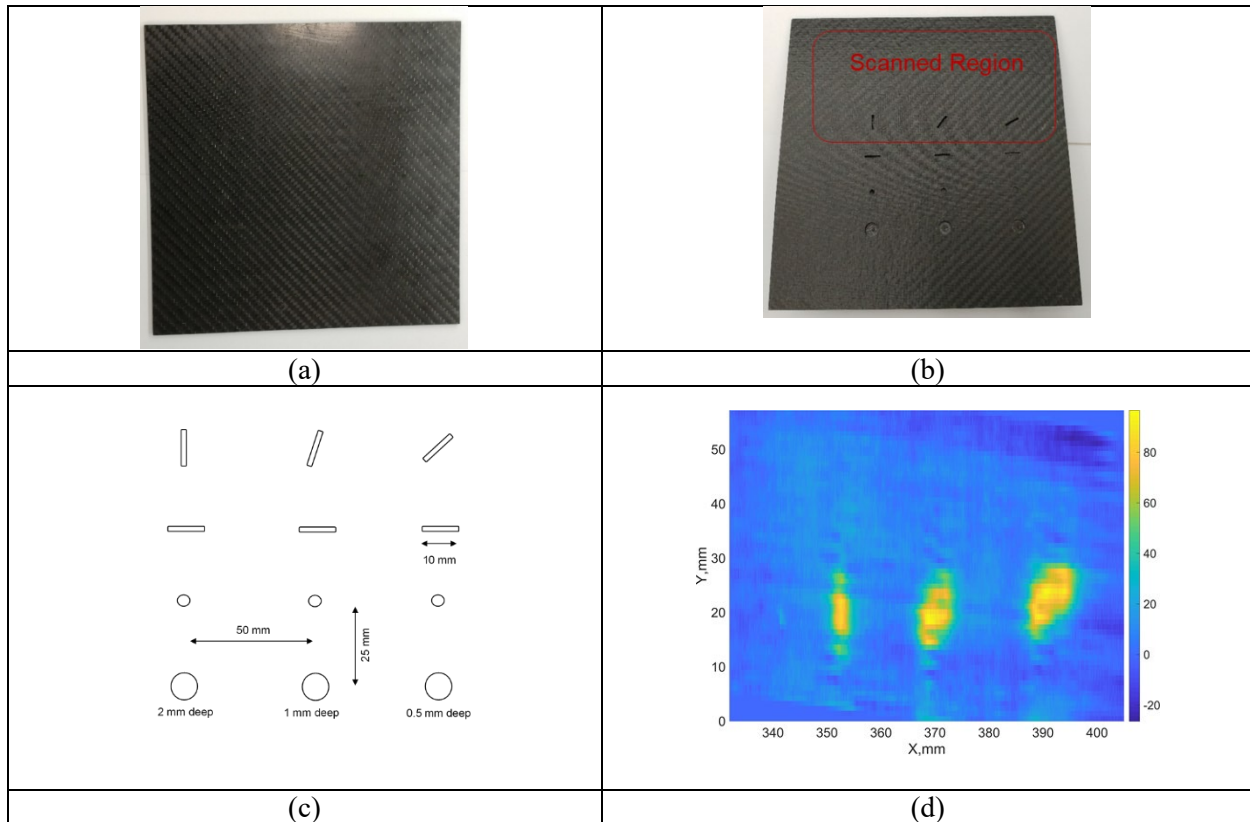


Figure 118. CFRP sample #7 with calibrated notches: (a) top view; (b) bottom view; (c) schematic drawing; (d) eddy current C-scan of top row of defects acquired at 1 MHz using Eddify flex probe with LSD topology.

3.2.5. MSU coil array probes for NDE of CFRP composites

Coil array probes E-1a and E-1b (8-coils)

Nominal operating frequencies of commercial probes are lower than optimal frequencies needed for inspection of CFRP components. Off-the-shelf array probes are usually tailored for detection of surface breaking cracks in metallic structures, such as pipelines, gas tanks and reservoirs. Low driving frequency can be a limitation, if small defects need to be identified in thin CFRP laminates. Therefore, the MSU team designed and built multi-element coil probes with resonant frequencies above 40 MHz.

The MSU team designed and fabricated two 8-element coil arrays for eddy current testing of CFRP parts as shown in Figure 119a. The first array E-1a had 10-mm diameter coils. In its second version E-1b, the coil size was reduced to 5-mm in order to improve the spatial resolution. Coils were fabricated on double-layer PCB. Wire traces were placed on the top and on the bottom of PCB as shown in Figure 119b. Top and bottom layer coils had the same winding directions, which provided more turns for increased signal output.

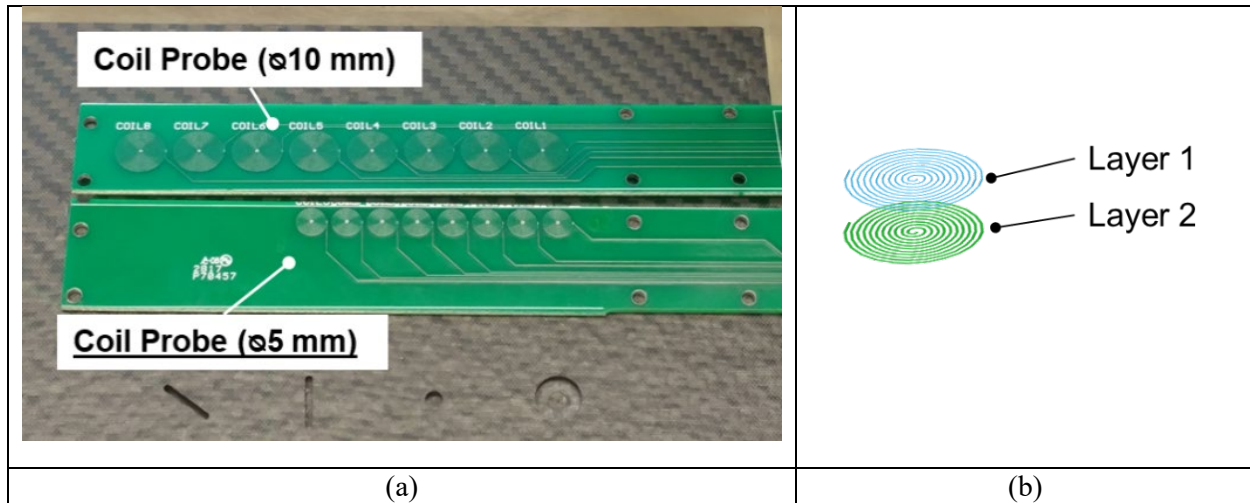


Figure 119. MSU array probes: (a) E-1a array (10 mm coils) and E-1b array (5 mm coils); (b) two-layer coil design, windings printed on top and bottom sides of PCB.

Impedance of E-1a coil sensors

One of the coils from the E-1a array was connected to the analyzer HP-4194A in order to measure its impedance in the frequency range up to 40 MHz. Results shown in Figure 120a demonstrated that the impedance plot fit the equivalent RLC circuit model of the sensor coil (see figure insert), and that the resonance was above 40 MHz. The lumped capacitor C in the equivalent circuit was introduced by parasitic capacitances between the wire traces. The sensor coil driven above the resonant frequency behaved as a capacitive sensor as shown in Figure 120b.

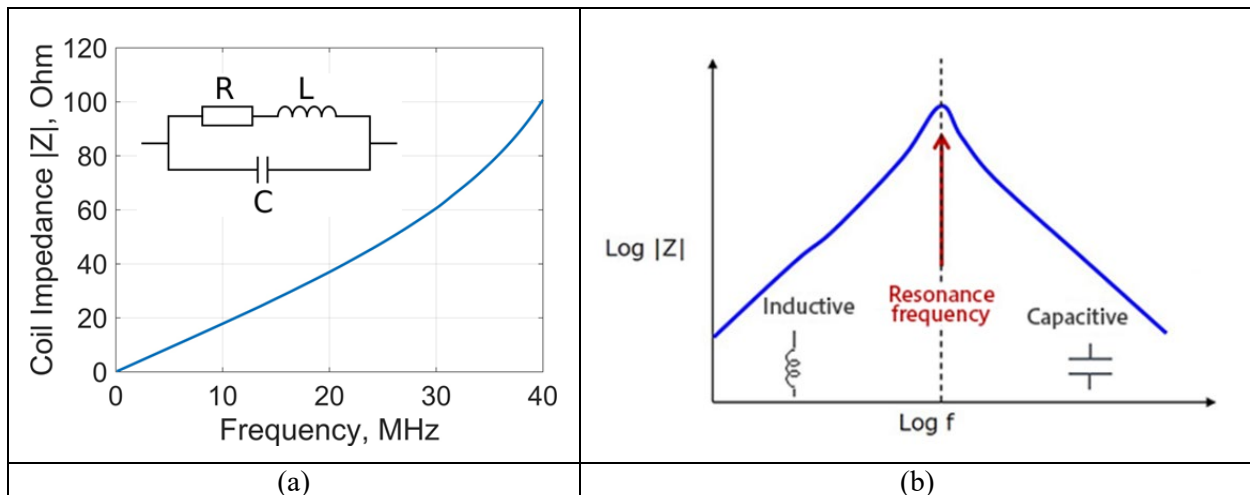


Figure 120. (a) Impedance of one coil from E-1a probe and its equivalent RLC circuit (shown as graph insert); (b) typical dependence of coil impedance $|Z|$ on excitation frequency.

Validation of E-1a and E-1b probes using lock-in amplifier (DIFF topology, 1 channel)

In Quarter III, the MSU team validated the E-1a and E-1b array probes using the experimental setup shown in Figure 121a, since the Ectane 2 system was not yet delivered. The MSU team used the benchtop lock-in amplifiers SR830 and SR844 paired with NI USB 6251 data acquisition device. Hardware front ends were interfaced with a PC, which was used to control the XYZ gantry.

A single channel raster scan was performed using the E-1b probe. Two identical E-1b PCBs were placed on a 3D printed fixture such that one PCB was parallel to the test specimen, and the other PCB was away from the specimen. The differential measurement was taken as shown in Figure 110a with coil L1 close to the surface of the sample and with coil L2 in the air.

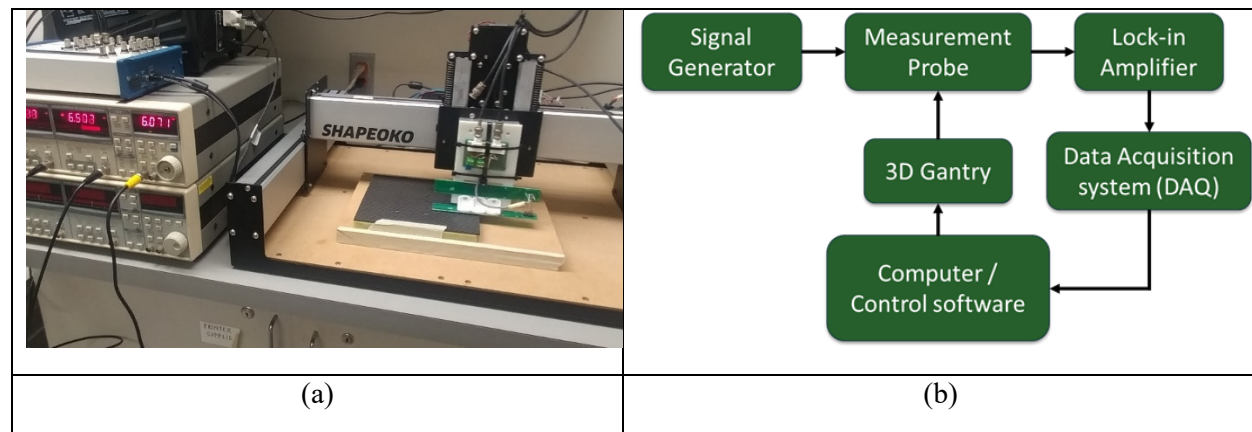


Figure 121. MSU experimental set-up for initial testing of E-1a and E-1b array probes: (a) gantry, lock-in amplifiers, ADC and probe fixtures; (b) schematic block-diagram.

The MSU team performed C-scans of the calibration CFRP test panel shown in Figure 122a. Schematics, locations, and sizes of defects are shown in Figure 122b. Array probe E-1b scanned the sample with 2 mm spatial resolution at 10 MHz and with a single activated channel. Corresponding C-scan is shown in Figure 122c after minor post-processing. Results demonstrated that all calibration notches were clearly detected. Deeper defects created more fiber damage, which translated into higher conductivity loss and stronger signals. Obtained results proved that the designed coil sensor probes were sensitive to carbon fiber damage and fiber irregularities

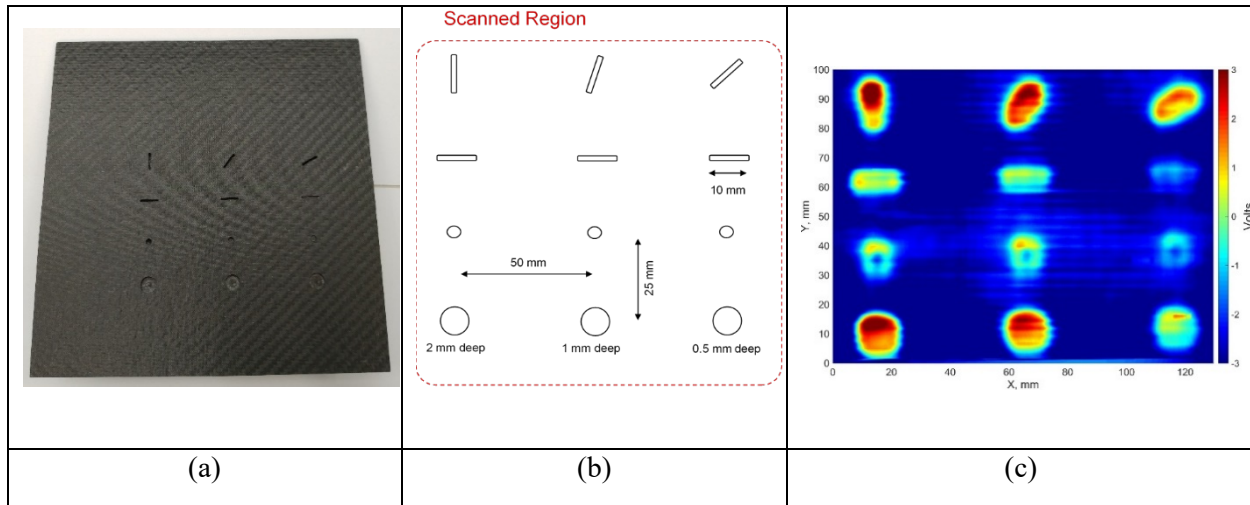


Figure 122. Experimental validation of E-1b probe in DIFF mode using lock-in amplifier: (a) CFRP sample #7 with defects that simulate fiber damage; (b) locations and sizes of machined defects; (c) corresponding C-scan acquired with a 5-mm coil at $f = 10$ MHz.

Validation of E-1a and E-1b probes using Ectane 2 system (SSD topology, EET connector, 2 channels)

In Quarter VI, the Ectane 2 system was delivered and was successfully interfaced with the XYZ gantry and position encoders. Substituting the lock-in amplifiers with the Ectane 2 enabled multi-channel measurements, multi-frequency measurements, automatic bias removal, higher gains, and extra features in real-time signal processing. However, the ECA cable (see Figure 99) was not yet available. Therefore, the MSU team could only use the Extended ET connector (EET). The EET connector is usually reserved for debugging purposes, because it was not interfaced to the multiplexor (MUX). The EET provides 2 voltage drivers and 8 parallel input channels. The MSU team interfaced the array probe E-1b with the EET using unshielded wires used for prototyping. Ectane 2 was configured to drive a single 5-mm coil and receive the signals from two surrounding coils in the T/R SSD mode. The corresponding setup is shown in Figure 123

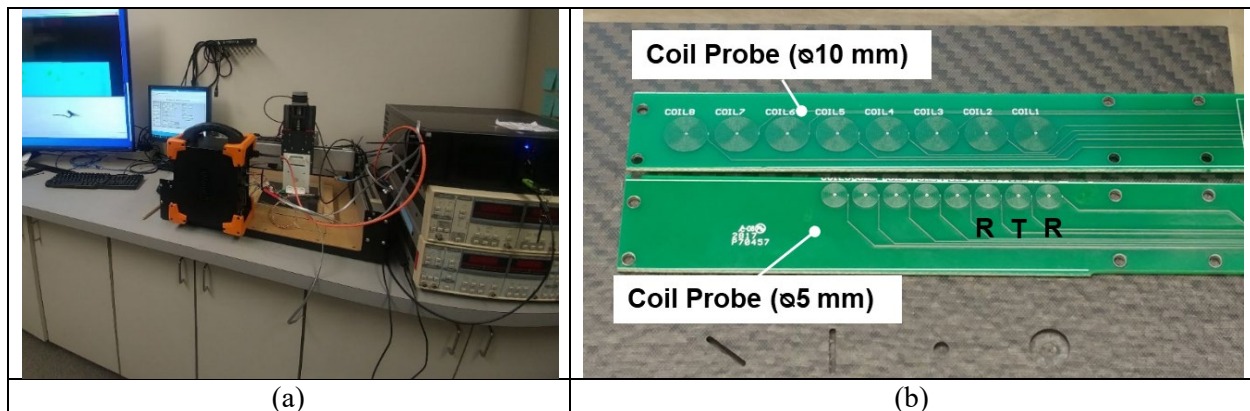


Figure 123. Experimental validation of E-1b probe in T/R SSD mode using Ectane 2: (a) experimental setup; (b) activated coils (T – transmitter, R – receivers).

The CFRP sample shown in Figure 124 was scanned at 5 MHz with spatial resolution of 1 mm and at a speed of 40 mm/s. Sensor lift-off was approximately 2 mm. Two C-scans were acquired corresponding to two receivers R, but only one of them is shown in order to avoid redundancy C-scans from top and bottom sides are shown in Figure 125 and Figure 126, respectively. Figure 126 shows that the excitation frequency of 5 MHz was too high to detect the smallest defects. The operating frequency needed to be lowered in order to increase the skin depth.

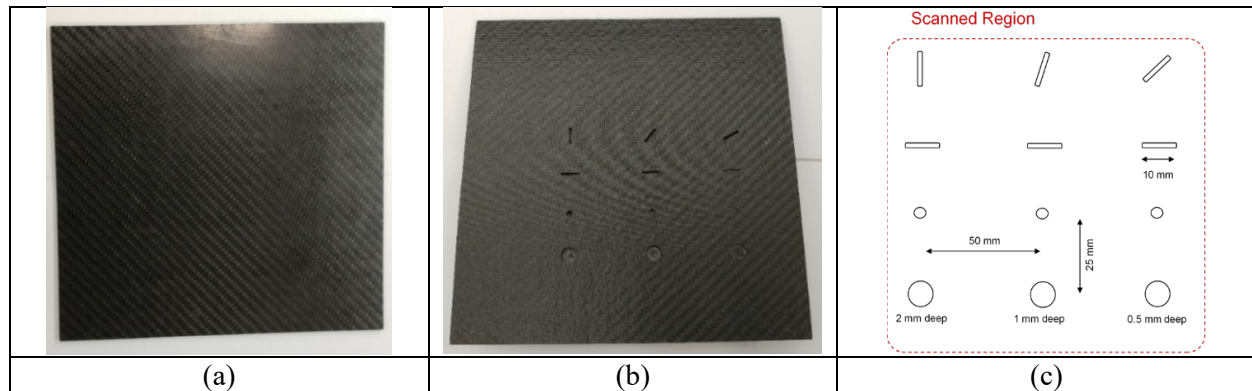


Figure 124. Calibration CFRP sample #7 with fiber damage: (a) top view; (b) bottom view; (c) schematics and locations of introduced notches.

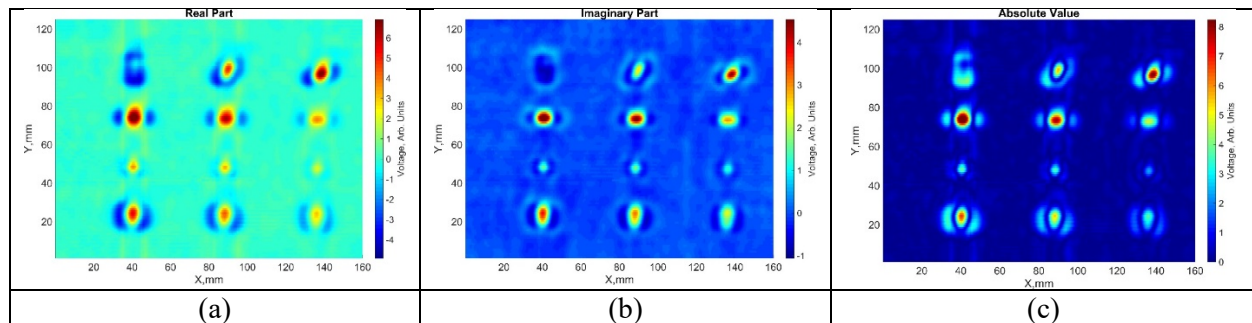


Figure 125. Validation of the E-1b probe connected through EET. C-scans of CFRP test sample from the bottom side (SSD topology, left receiver R, $f = 5$ MHz): (a) real part; (b) imaginary part; and (c) absolute value.

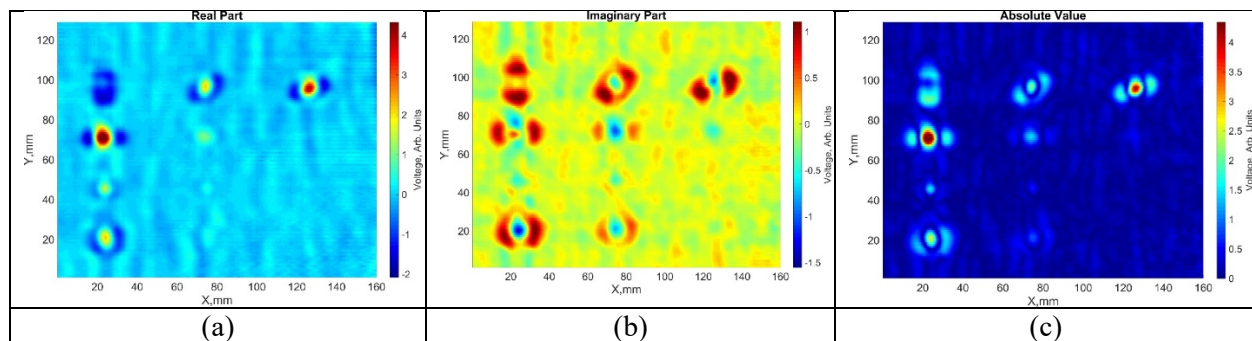


Figure 126. Validation of the E-1b probe connected through EET. C-scans of CFRP test sample from the top side (SSD topology, left receiver R, $f = 5$ MHz): (a) real part; (b) imaginary part; and (c) absolute value.

Coil array probe E-1c (8 top coils and 8 bottom coils)

Array probe E-1c is shown in Figure 127. The E-1c probe consists of two identical PCB E-1b placed on top of each other so that the driver coils would be above the receiver coils. The diameters of the coils were 5 mm. The probe was attached to a fixture and was interfaced to the EET connector.

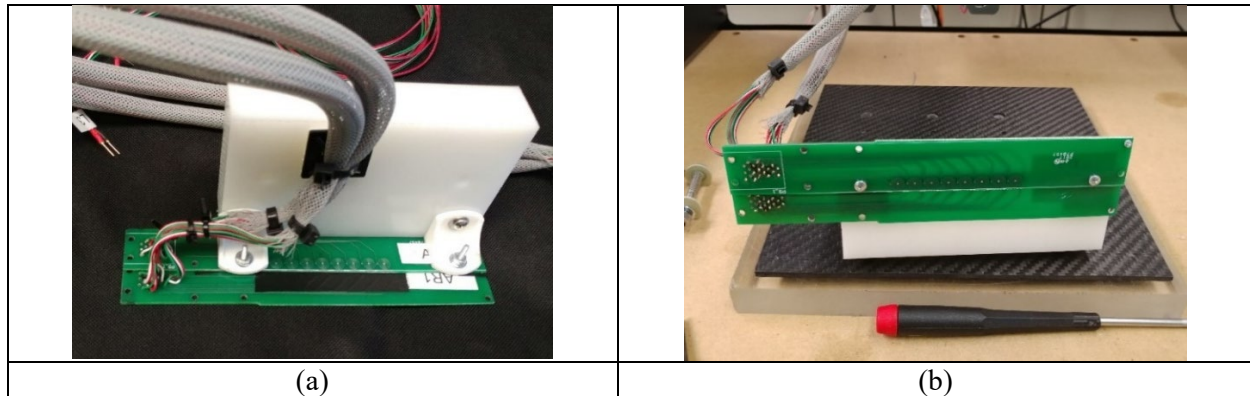


Figure 127. Array probe E-1c with driver coils on top of receiver coils: (a) top view; (b) bottom view.

Validation of E-1c probe using Ectane 2 system (SSD topology, EET connector, 8 channels)

The experimental setup for validation of the E-1c probe is shown in Figure 128. The EET connector did not support the MUX. Hence, the driving coils were activated simultaneously. The MSU team decided to utilize two available DDS generators and then interfaced four coils to each generator in series as shown in Figure 129. All 8 input channels were activated in parallel with the same gains.

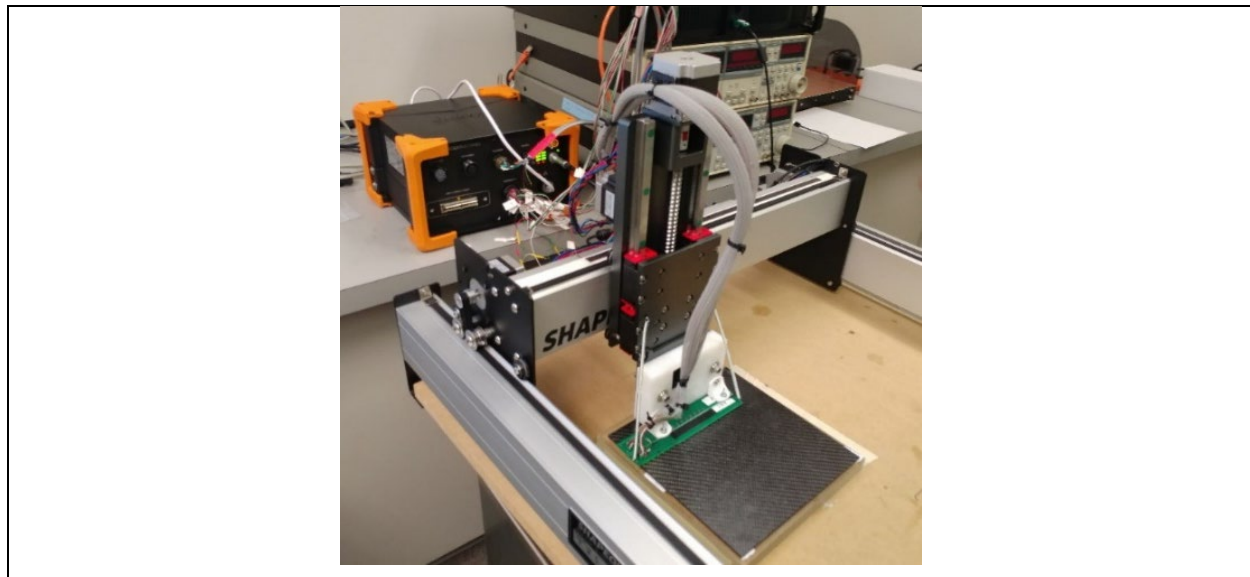


Figure 128. Experimental validation of E-1c probe in T/R SSD mode.

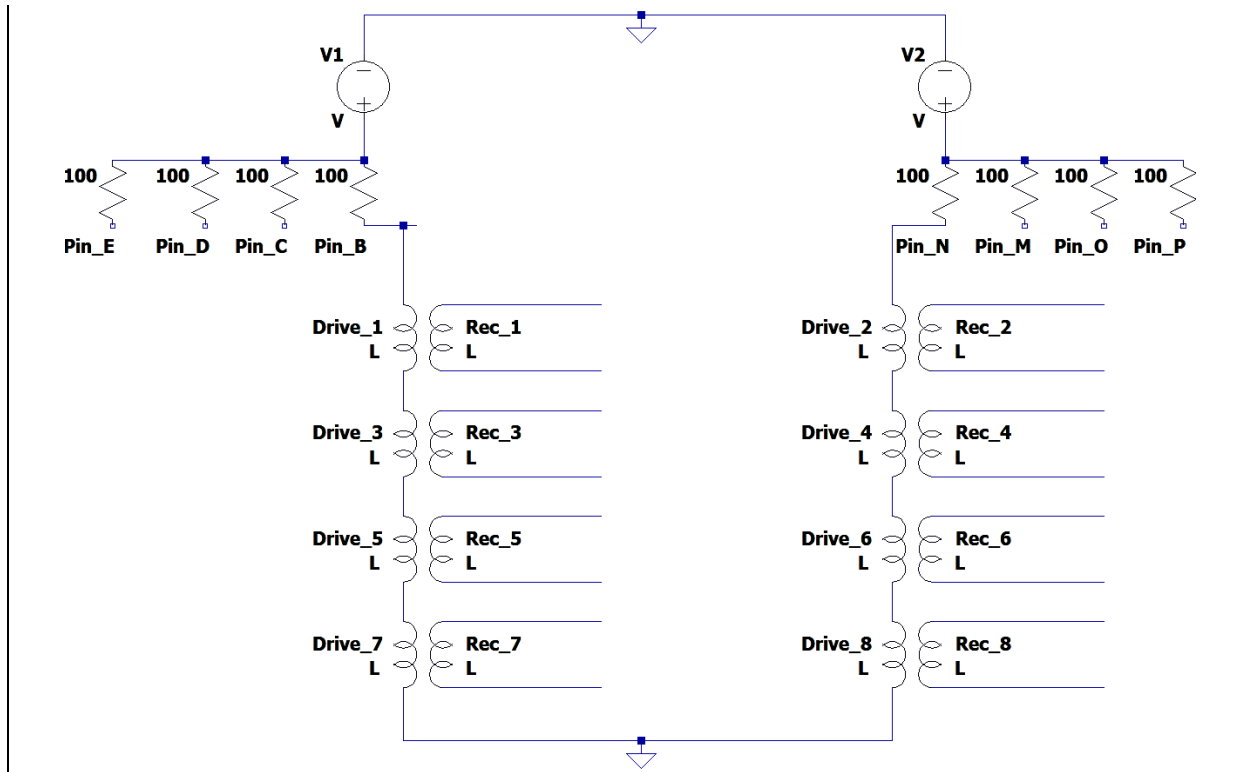


Figure 129. Electrical connections between the EET connector and E-1c array probe.

Raster scanning was performed on the calibration CFRP sample #7 (see Figure 124) at 2.5 MHz, and data from all 8 channels were acquired in parallel. The resulting C-scans are presented in Figure 131. Note that the data from individual channels were not merged together. All channels except channel #7 showed uniform signal amplitudes and sensitivities to the defects. The C-scan corresponding to channel #7 was noisy owing to a bad solder joint on the PCB board. Figure 130 demonstrates a typical C-scan acquired from the top side.

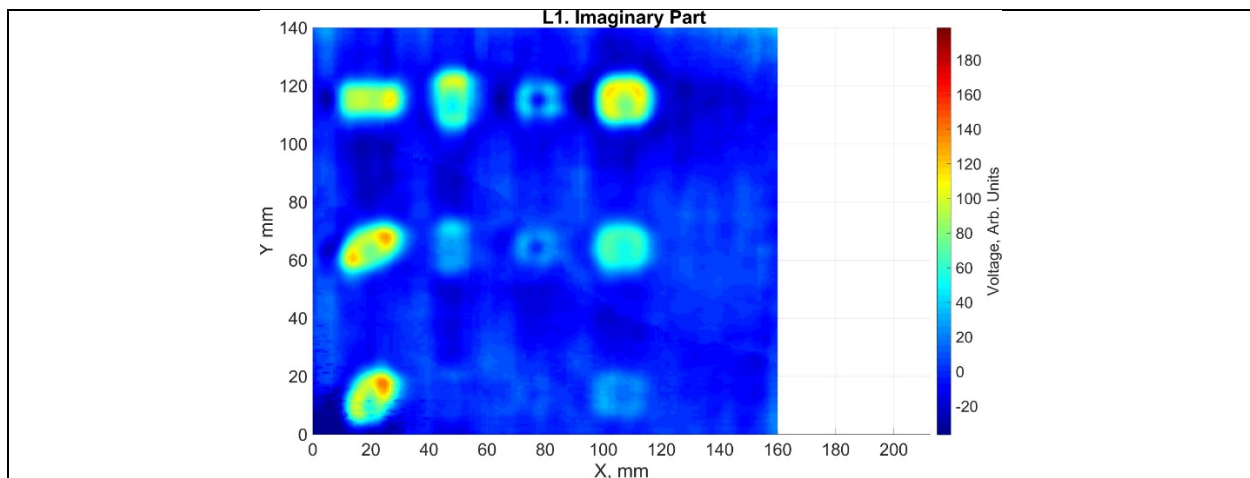


Figure 130. Two row 8-channel coil array operating in the T/R mode. Transmitters on the top, receiver on the bottom. C-scans of CFRP test sample from the top side, $f = 2.5$ MHz, CH1.

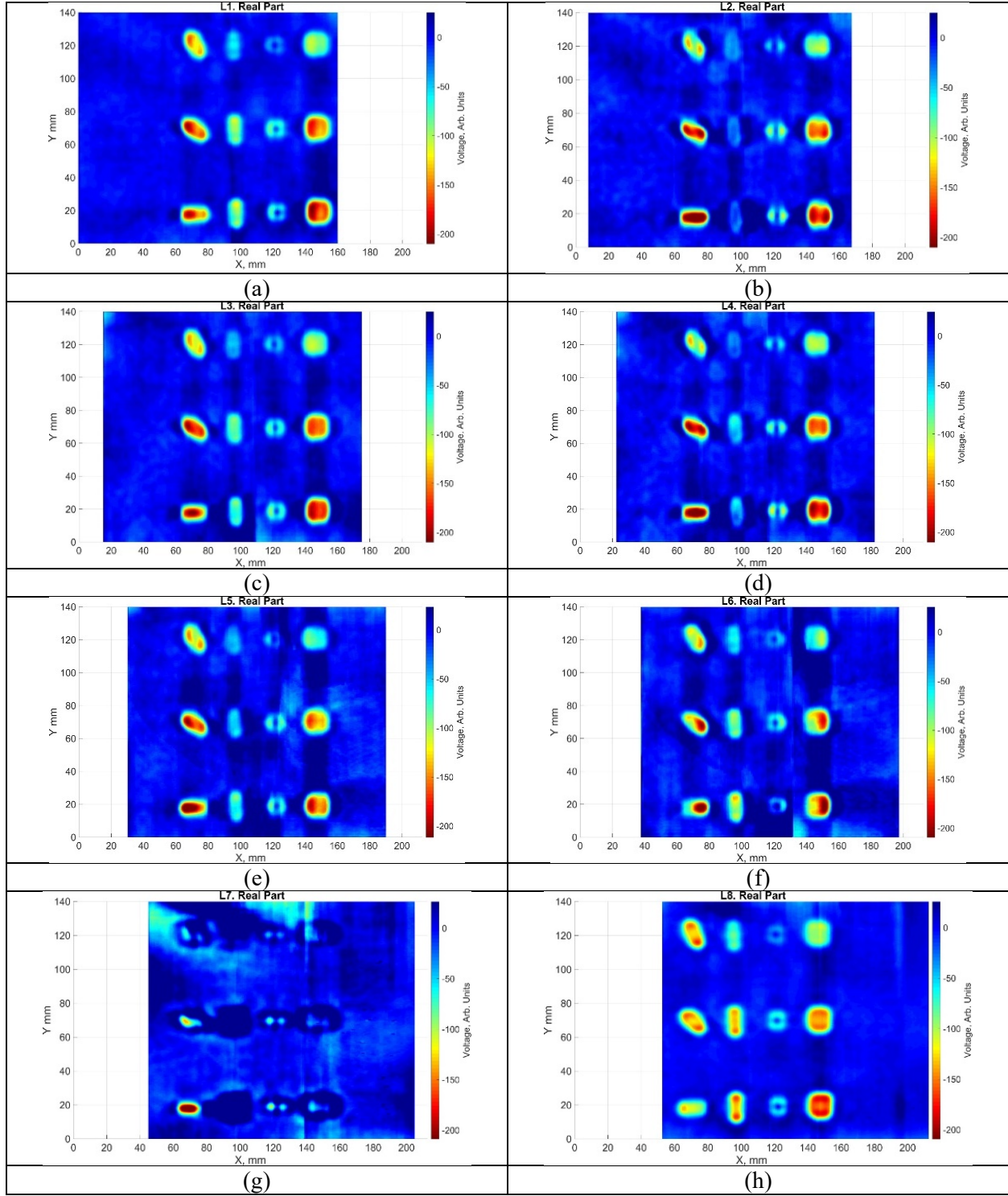


Figure 131. Two row 8-channel coil array operating in the T/R mode. Transmitters on the top, receiver on the bottom. C-scans of CFRP test sample from the bottom side (absolute value, 2.5 MHz): (a) CH1; (b) CH2; (c) CH3; (d) CH4; (e) CH5; (f) CH6; (g) CH7; and (h) CH8.

Coil array probe E-2a (18 coils)

In Quarter VII, the MSU team designed the array probe E-2a, which was fully compatible with the ECA connector and MUX. Compared to the prototypes from the first batch, which were all linear arrays, the updated probe E2-a had two rows of coils. The design of the E-2a PCB board is shown in Figure 132a. Arranging the coils in two staggered rows effectively doubled the spatial resolution of the array for single-pass scanning (Task ix). The PCB was also designed with traces for micro-BNC connectors as illustrated in Figure 132b. This allowed each coil to be individually accessed which provided the possibility to detach the probe from a cable. In addition, the coax cables were superior to previously used cables in terms of shielding and electromagnetic noise reduction. The board had extra space for solder joints and filter capacitors in order to tune the Q-factor and resonance frequencies of the sensors.

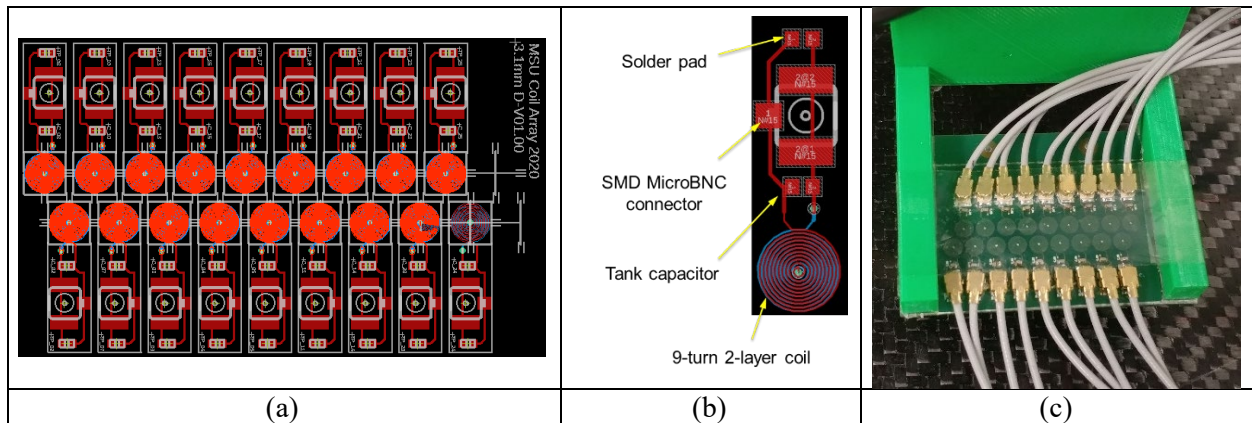


Figure 132. Prototype E-2a: (a) PCB design of a staggered 18-CH array; (b) PCB design of a single channel with solder pads for μ BNC connector; (c) fabricated array interfaced to the Ectane.

The fabricated coil array E-2a is shown in Figure 132c. The micro-BNCs were soldered onto the 2-layer board in a reflow oven. The overall size of the array was ~ 36 mm and the distance between two neighboring coils in the same row was ~ 4 mm. Thus, the staggered design provided the effective spatial resolution of 2 mm.

An additional advantage of the new PCB design was the absence of protrusions for contact soldering on the bottom of the board. All micro-BNC connectors were soldered to the top layer traces, which helped to keep the bottom of the board smooth. Thus, the array sensor could scan CFRP sample at low lift-offs.

Table 3 provides a comparison of the prototype E-2a against the earlier prototype E-1c in terms of sensor geometry and electrical properties. With increased self-inductance and sensitivity, the overall size of a single coil in the array was reduced from 5 mm to ~ 3.5 mm.

Feature\Probe	E-1c	E-2a
Coil diameter, mm	5	3.43
Number of layers	2	2
Number of turns	8×2	9×2
Feature size, mm	0.139	0.0762
Self-inductance, μH	0.488	0.52
External capacitance, pF	1000	1000
Resonance with capacitor, MHz	7.2	6.9
DC resistance, Ohm	0.5	0.5
Maximum current, mA	1.96	1.7

Table 3. Comparisons of coil properties for the probes E-1c and E-2a.

Validation of E-2a probe using Ectane 2 system (ABS and SDD topologies, ECA connector, 18 channels)

The cable for the ECA connector (rectangular in Figure 133a) connected to the E-2a probe is shown in Figure 133b. The E-2a array sensor developed at MSU was attached to an XYZ-gantry using a 3D printed fixture as shown in Figure 133c.

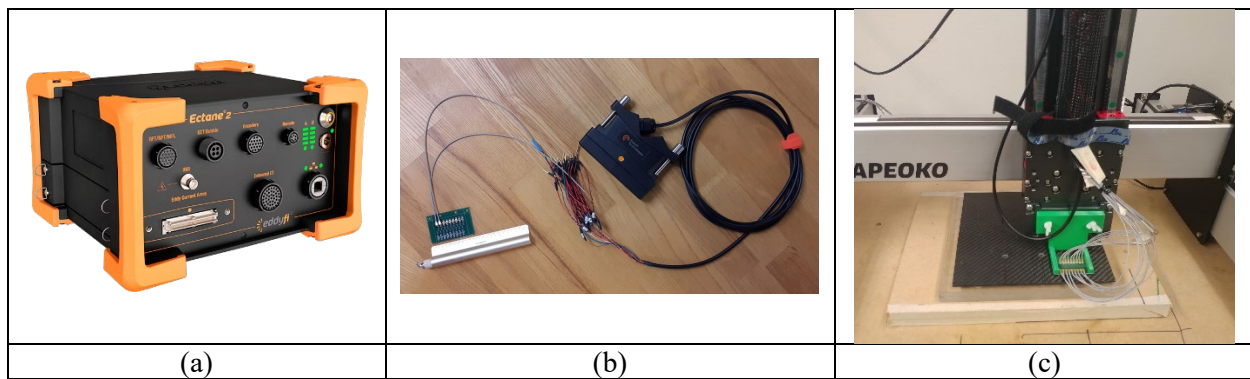


Figure 133. Interfacing array probe E-2a with the Ectane: (a) the ECA connector on the Ectane's front panel; (b) cable with the E-2a probe attached; (c) E-2a probe scanning a CFRP sample.

The calibration sample #7 was scanned from top and bottom sides for validation. The area of the scan was $150 \text{ mm} \times 150 \text{ mm}$, and the scan resolution was 2 mm (half-distance between the coils in one row). The array probe moved at 116.7 mm/s. The inspection frequencies were 1.3 MHz and 2.0 MHz for top and bottom sides, respectively. Figure 134 contains a “gif” video of the actual scan process that took only ~10 s. The video shows how calibration defects are being successfully detected in real-time. However, the scan speed shown in Figure 134 is not maximal and is mostly limited by the XYZ gantry. Placing the array probes on robotic manipulators may reduce the scan time while providing the capability to scan non-flat specimens.



Figure 134. Fast scanning of the CFRP calibration sample #7 using the array probe E2-a ($t = 10.7$ s). Note that the figure includes a gif video.

Table 4 provides comparisons of the times required to scan the CFRP calibration sample #7 using different sensor prototypes at different stages of the project. The progression from ~9 min to ~10 s was achieved by developing array sensors and implementing the multi-channel multiplexing.

Project 3.8 (Phase I):	Project 3.13 (Phase II): E-1c	Project 3.13 (Phase II): E-2a
9 min 4 s	2 min 20 s	10.7 s

Table 4. Comparisons of times required to scan a calibration CFRP sample #7 using different MSU probes (150 mm \times 150 mm scan area, scan resolution of 2 mm).

Validation of E-2a array probe: ABS topology

Calibration CFRP sample #7 was used for probe validation. The MSU team successfully implemented the ABS measurement topology using the E-2a sensor array and Magnify software. In the ABS topology, each coil was excited individually and the resulting changes of the impedance due to defects were registered. The C-scans were acquired by merging data from 18 independent measurement channels.

Figure 135 presents a C-scan of the bottom side of the test specimen. In order to enhance defect images, the x and y gradients of both real and imaginary parts were computed as shown in Figure 136 and Figure 137, respectively. The C-scan of the top side of the sample is presented in Figure 138. Obtained experimental results demonstrated that taking measurements in the ABS mode was effective in detecting calibration defects.

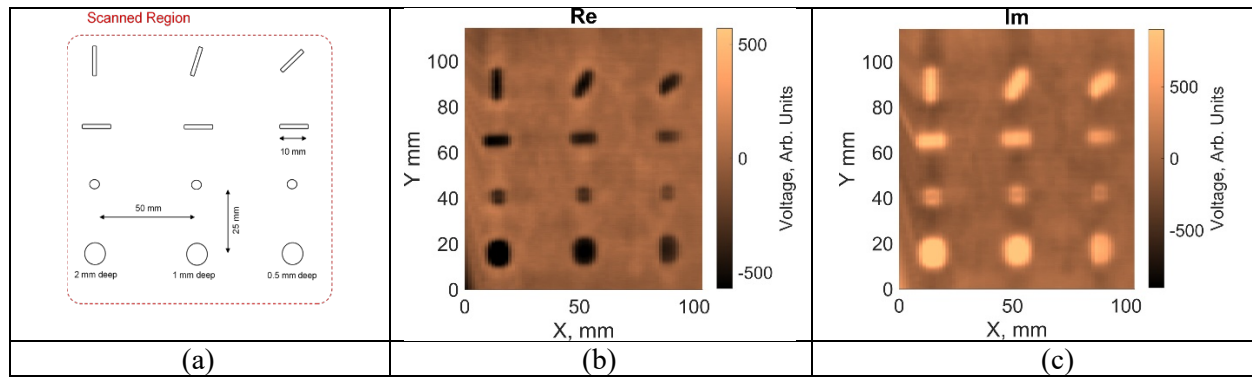


Figure 135. C-scan of the calibration CFRP sample using the array probe E-2a, bottom side, $f = 2$ MHz in the ABS mode: (a) locations of defects; (b) real part (RE); (c) imaginary part (IM).

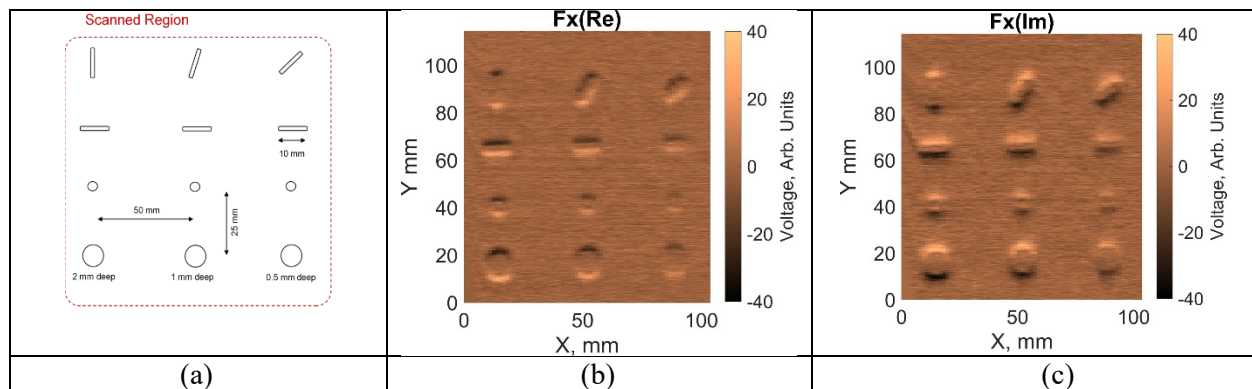


Figure 136. C-scan of the calibration CFRP sample using the array probe E-2a, bottom side, $f = 2$ MHz in the ABS mode: (a) locations of defects; (b) x-gradient of the real part (RE); (c) x-gradient of the imaginary part (IM).

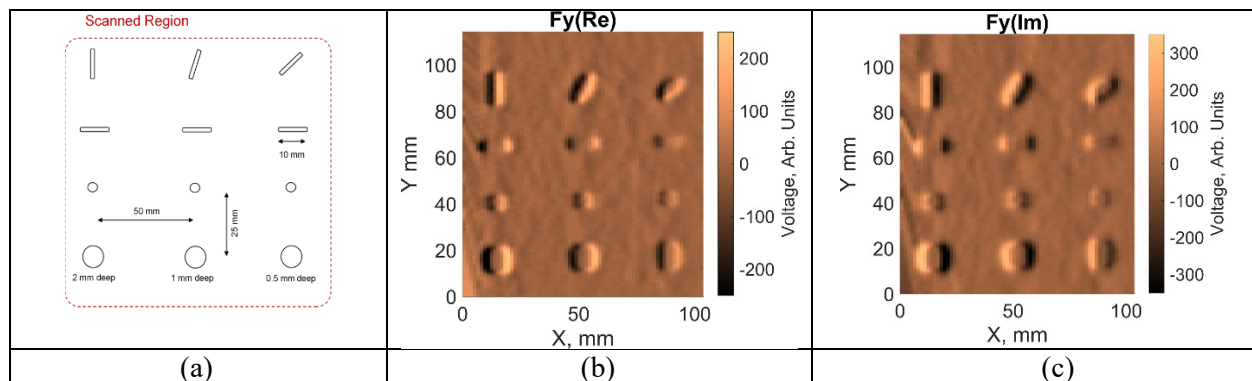


Figure 137. C-scan of the calibration CFRP sample using the array probe E-2a, bottom side, $f = 2$ MHz in the ABS mode: (a) locations of defects; (b) y-gradient of the real part (RE); (c) y-gradient of the imaginary part (IM).

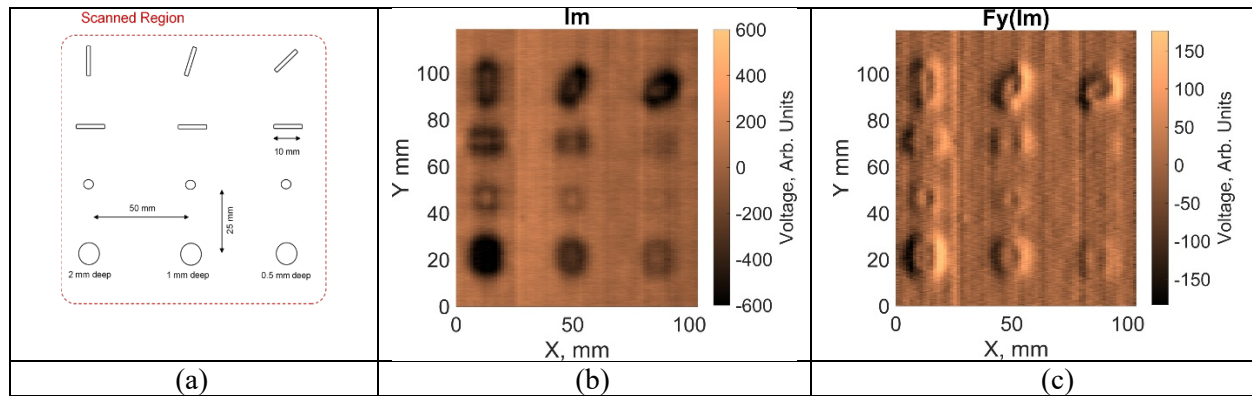


Figure 138. C-scan of the calibration CFRP sample using the array probe E-2a, top side, $f = 1.3$ MHz in the ABS mode: (a) locations of defects; (b) the imaginary part; (c) y-gradient of the imaginary part.

Validation of E-2a array probe: SDD axial topology

The second measurement topology implemented by the MSU team was the SDD. Figure 139, Figure 140, Figure 141 and Figure 142 present typical C-scans of the CFRP calibration panel #7 acquired in the SDD axial mode using the scan settings described previously. The scan direction is highlighted by the white arrow (also see video in Figure 134). Obtained results are similar to those using the ABS mode; however, the fields due defects in the specimen look different owing to the transmit-receive configuration of measurements.

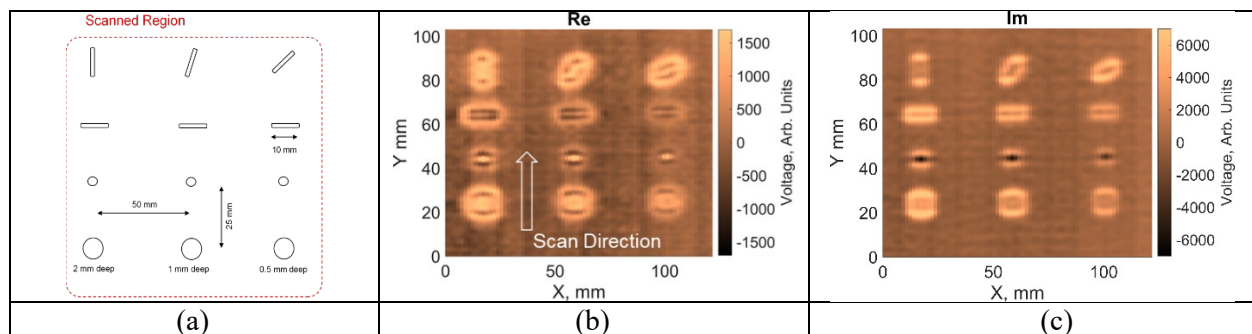


Figure 139. C-scan of the calibration CFRP sample using the sensor array E-2a, bottom side, $f = 2$ MHz in the SDD axial mode: (a) locations of defects; (b) the real part; (c) the imaginary part.

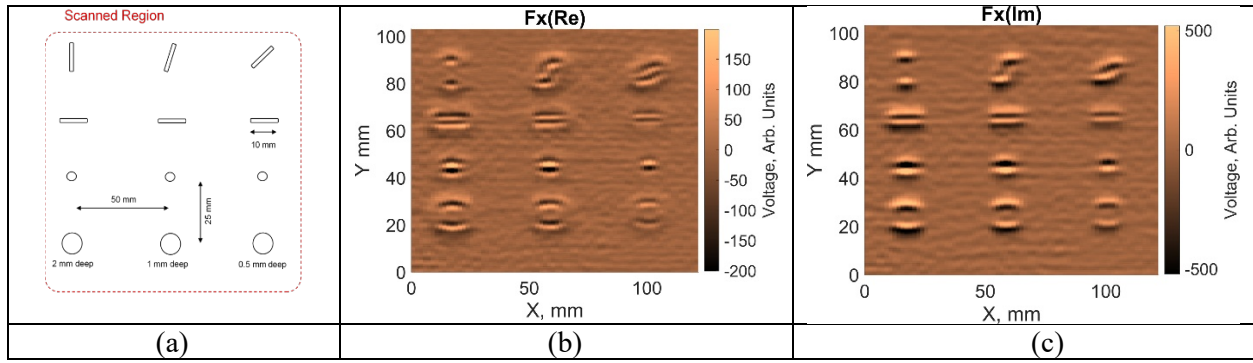


Figure 140. C-scan of the calibration CFRP sample using the sensor array E-2a, bottom side, $f = 2$ MHz in the SDD axial mode: (a) locations of defects; (b) x-gradient of the real part; (c) x-gradient of the imaginary part.

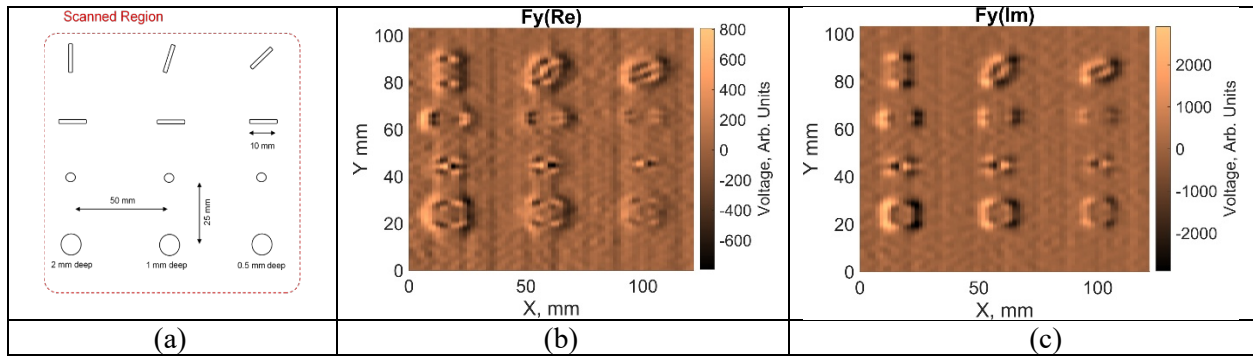


Figure 141. C-scan of the calibration CFRP sample using the sensor array E-2a, bottom side, $f = 2$ MHz in the SDD axial mode: (a) locations of defects; (b) y-gradient of the real part; (c) y-gradient of the imaginary part.

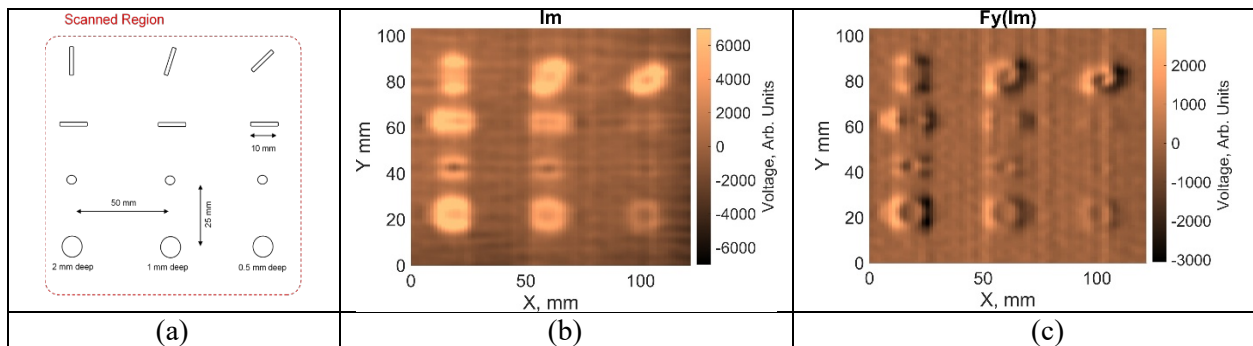


Figure 142. C-scan of the calibration CFRP sample using the sensor array E-2a, top side, $f = 1.3$ MHz in the SDD axial mode: (a) locations of defects; (b) the imaginary part; (c) y-gradient of the imaginary part.

Validation of E-2a array probe: SDD transverse topology

The transverse SDD is complementary to the axial SDD in the sense that both excitation and receiving coils are in the same row as shown in Figure 114. Such configuration allows to orient fields in the direction orthogonal to the axial SDD. Figure 143, Figure 144, Figure 145 and Figure 146 represent typical C-scans of the CFRP calibration panel #7 acquired in the SDD transverse mode. It is worth noting that all C-scans presented for the ABS, SDD axial, and SDD transverse modes were acquired during a single 10.7 s experiment.

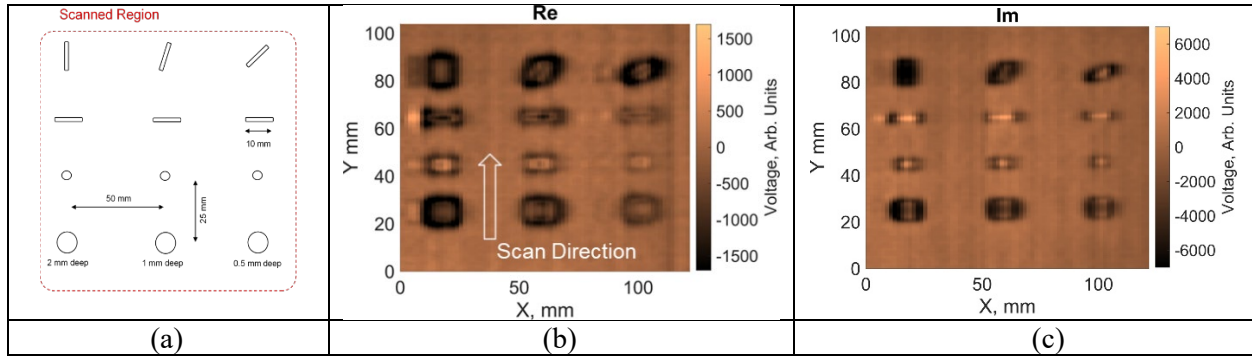


Figure 143. C-scan of the sample #7 using the E-2a array, bottom side, $f = 2$ MHz in the SDD transverse mode: (a) locations of defects; (b) the real part (RE); (c) the imaginary part (IM).

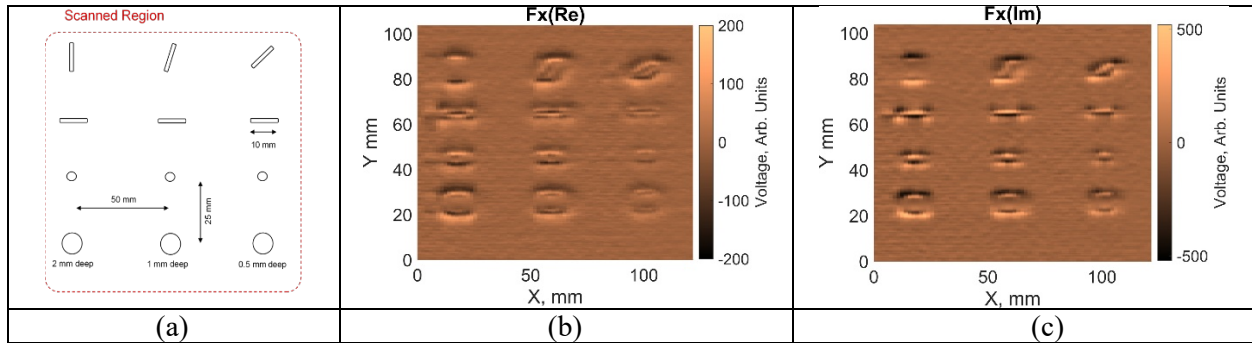


Figure 144. C-scan of the CFRP sample #7 using the E-2a array, bottom side, $f = 2$ MHz in the SDD transverse mode: (a) locations of defects; (b) x-gradient of RE; (c) x-gradient of IM.

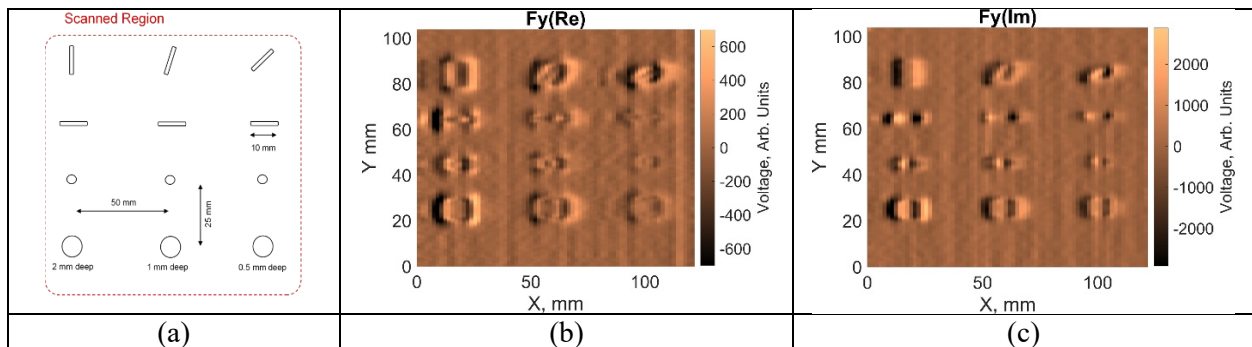


Figure 145. C-scan of the calibration CFRP sample using the E-2a array, bottom side, $f = 2$ MHz in the SDD transverse mode: (a) locations of defects; (b) y-gradient of RE; (c) y-gradient of IM.

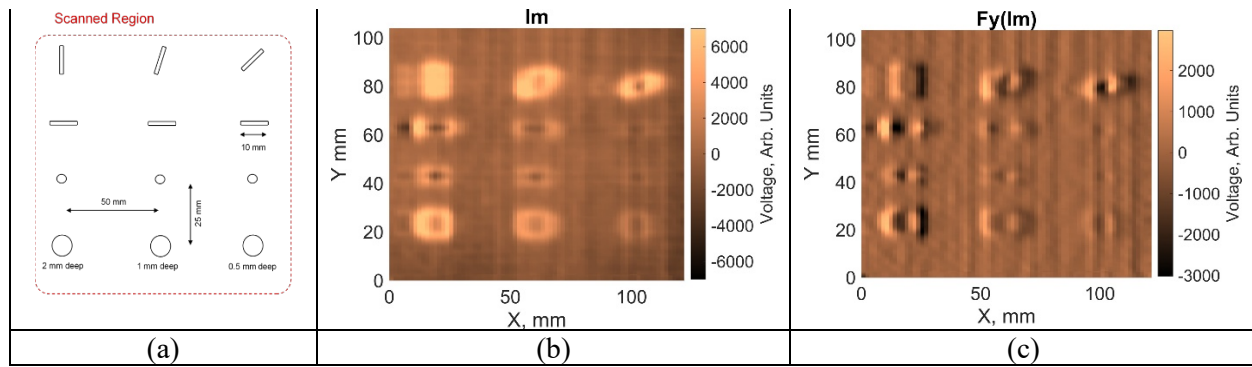


Figure 146. C-scan of the calibration CFRP sample using the sensor array E-2a, top side, $f = 1.3$ MHz in the SDD transverse mode: (a) locations of defects; (b) the imaginary part; (c) y-gradient of the imaginary part.

Array probes E-2b and E-2c

The MSU team optimized earlier PCB board designs in order to improve sensor performance. The PCB of the updated prototypes E-2b (4-layer) and E-2c (2-layer) are shown in Figure 147. In the new design, the micro-BNC connectors are shifted towards the centers of the coils, which minimizes the overall width of the array.

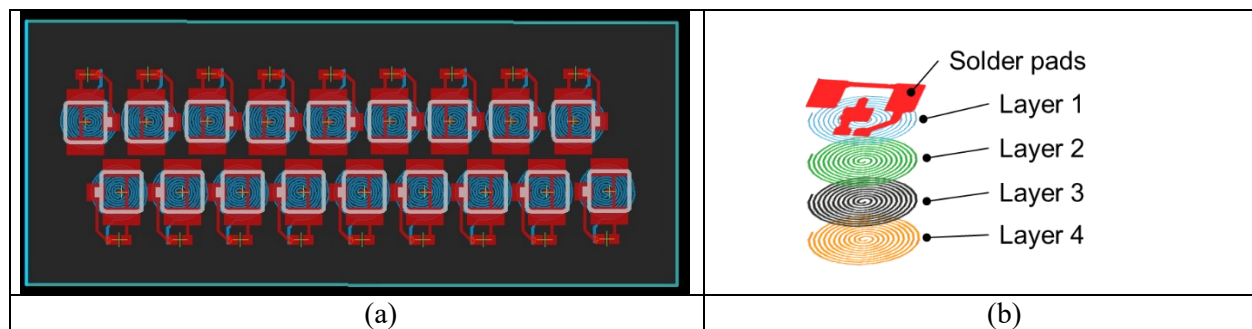


Figure 147. Drawings of array probes E-2b (4-layer) and E-2c (2-layer): (a) PCB top view; (b) multi-layer PCB structure.

In addition, the thickness of the board is reduced in order to keep the layers with copper traces closer to each other, which increases the inductance. It is planned that the prototype E-2b is going to be fabricated with four layers of coils, and the prototype E-2c is going to be fabricated with two layers of coils deposited on a flexible substrate.

3.3. Capacitive Imaging (CI)

Capacitive sensors are complementary to eddy current coil sensors in the sense that they can better detect matrix imperfections such as interlaminar delaminations. Typical designs of the rectangular and disk capacitive sensors are presented in Figure 148. Capacitor probes generate the electric field that penetrates the test sample (GFRP or CFRP with low conductivity), and changes of the dielectric permittivity (e.g., matrix cracking, inclusions or interlaminar delaminations) affect the impedance of the probe.

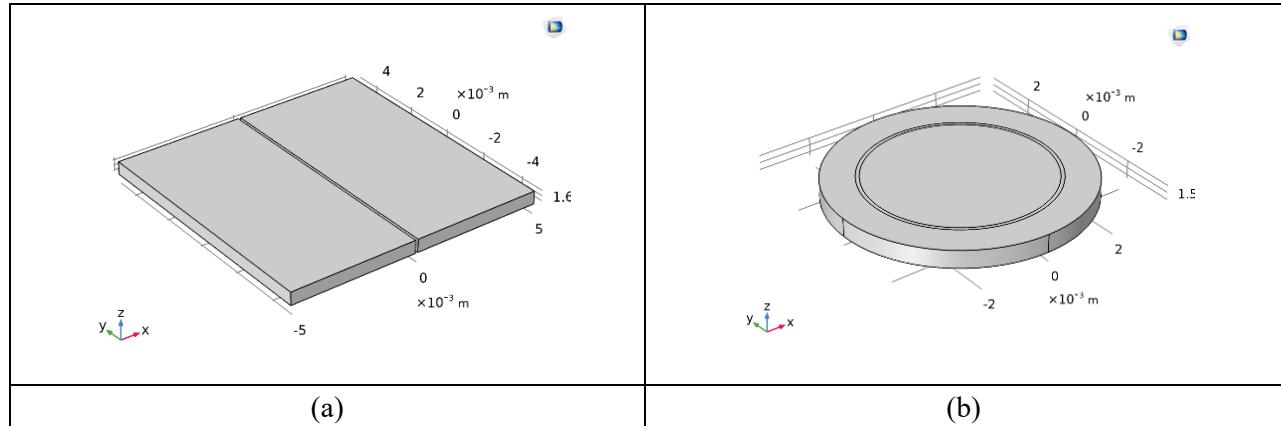


Figure 148. Designs of capacitive sensors for NDE of FRP composites: (a) capacitor with rectangular electrodes; (b) capacitor with disk electrodes.

The main advantage of a circular capacitor compared to a rectangular capacitor is its uniform sensitivity to flaws in all orientation. However, circular capacitors provide measurements that are integrated over the circumference of an air gap, which is longer than a straight air gap of open-plate rectangular capacitor of similar size.

In Quarter VII, the MSU team developed FE models and performed parametric studies in order to:

- 1) visualize electric fields in the air generated by capacitors of different geometries and sizes;
- 2) understand interactions of the electric field with structural defects in CFRP and GFRP samples;
- 3) investigate synchronized group excitation of electrodes in order to facilitate the development of multi-resolution capacitive sensor arrays; and
- 4) simulate multiplexing process in capacitive array probes.

3.3.1. Modeling of capacitive sensors for NDE of FRP composites

Electric dipole representation of an open-plate capacitor

An open-plate capacitor can be thought of as a short electric dipole, which is an elementary (ideal) source of the electromagnetic field. The foundation of the present study lies in investigating the structure of this field and its interaction with subsurface flaws in test samples. Specifically, in the near field zone, which is one of interest in most NDE applications, the electric field (**E**) and magnetic field (**H**) of the electric dipole are given by:

$E_r = \frac{p}{4\pi\epsilon_0 r^3} 2 \cos \theta + O\left(\frac{1}{r^2}\right)$ $E_\theta = \frac{p}{4\pi\epsilon_0 r^3} \sin \theta + O\left(\frac{1}{r^2}\right)$ $H_\phi = \frac{j\omega p}{4\pi r^2} \sin \theta + O\left(\frac{1}{r}\right)$	(10)
----------------------------------------------------------------------------------------------------------------------------------------------------------------------------------------------------------------------------------------------------	------

In the following sections, finite element (FE) simulations are undertaken in order to demonstrate the interaction of the open-plate capacitor with insulating GFRP and CFRP with low through-thickness electric conductivity. The goal is to optimize the sensitivity of such sensors to dielectric changes in test samples. For simplicity, the dielectric loss and anisotropy of the dielectric permittivity are not considered.

Finite element model of an open-plate capacitor

A finite element model was developed to simulate the distribution of the electric field in a lossless material. A volumetric flaw is introduced as an air region. The open plate capacitor is placed with a small lift-off over the sample geometry and the impedance is then calculated at multiple positions close to the flaw. Here, we consider only a capacitor with rectangular plates of different sizes as shown in Figure 149.

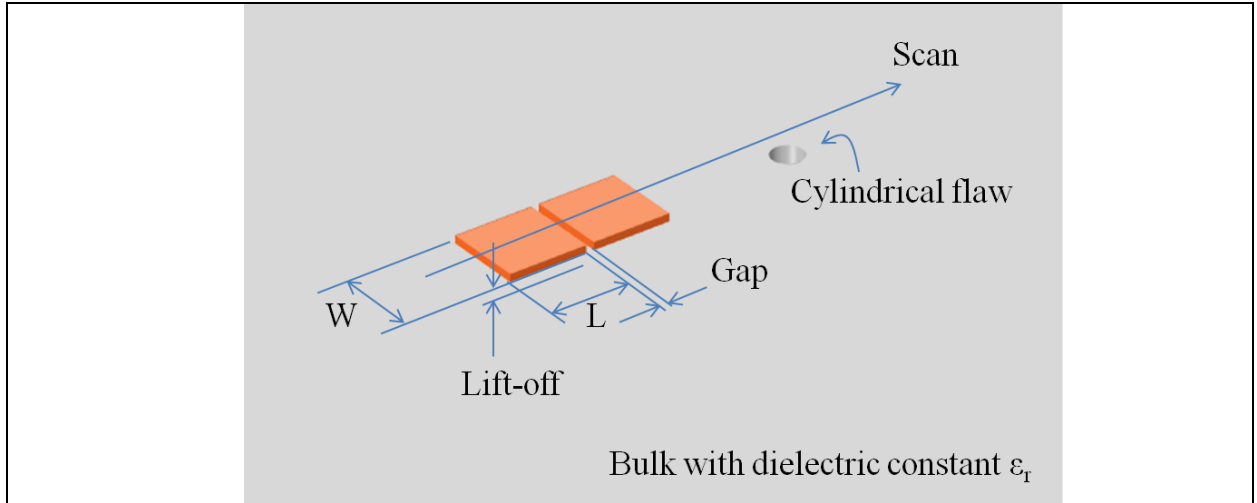


Figure 149. Schematics of the open-plate capacitor and surface breaking defect.

The electro-quasistatic (EQS) model was used to simulate the open plate capacitor operating in the frequency range from few kHz up to few MHz. This is because we found from experimental results that other couplings were negligible, and the model solving full Maxwell's equation was redundant. The EQS model is described by the following boundary value problem (BVP):

$\begin{cases} \nabla \times \mathbf{E} = 0 \\ \nabla \times \mathbf{B} = \mu_0(\sigma \mathbf{E} + j\omega \varepsilon \mathbf{E} + \mathbf{J}_e) \\ \nabla \cdot \varepsilon \mathbf{E} = \rho \\ \nabla \cdot \mathbf{B} = 0 \\ + \text{regularity cond. at infinity} \end{cases},$	(11)
----------------------------------------------------------------------------------------------------------------------------------------------------------------------------------------------------------------------------------------------------------------------------------------	------

where σ is the electrical conductivity, ε is the permittivity, J_e is the external current density, ρ is the electric charge density and \mathbf{B} is the magnetic flux density. The formulations are valid as long as the term $j\omega \mathbf{B}$ can be ignored so that the electric field is essentially curl free. Moreover, if the electrical conductivity σ is small, the EQS model reduces to the electrostatic (ES) model.

Anisotropic electric conductivity of composite test samples

In order to simplify the numerical computations, the model assumes homogeneous isotropic material with electrical conductivity σ on the order of [0–100] S/m. More sophisticated models can be developed by incorporating the conductivity tensor $\bar{\bar{\sigma}}$ that accounts for anisotropy. For instance, $\bar{\bar{\sigma}}$ of a unidirectional CFRP ply with fibers in x - y plane is given by Eq. (12):

$\bar{\bar{\sigma}} = \begin{bmatrix} \sigma_L \cos^2 \theta + \sigma_T \sin^2 \theta & (\sigma_L - \sigma_T) \sin \theta \cos \theta & 0 \\ (\sigma_L - \sigma_T) \sin \theta \cos \theta & \sigma_L \sin^2 \theta + \sigma_T \cos^2 \theta & 0 \\ 0 & 0 & \sigma_{cp} \end{bmatrix},$	(12)
-----------------------------------------------------------------------------------------------------------------------------------------------------------------------------------------------------------------------------------------------------------------------------------------	------

where σ_L and σ_T are the conductivities in the fiber direction and transverse direction respectively, and σ_{cp} is the cross-ply conductivity, θ is the fiber orientation with respect to the x axis. Typically, σ_L lies between 5×10^3 and 5×10^4 S/m. Typical values of σ_T and σ_{cp} are between 1 and 100 S/m. Note that the electrical conductivity of CFRP laminates is a few orders of magnitude smaller than that of metals (e.g., $\sigma = 5 \times 10^7$ for copper), and the electrical conductivity of GFRP laminates approaches zero.

The open plate capacitor has a strong electrical field and a weak magnetic field associated with it. This is similar to the field generated by the electric dipole described by Eq.(10). The numerical model of such source was developed in Comsol Multiphysics®. The boundary conditions were defined on the two plates of the capacitor (1V and 0V, respectively) and on the outer boundaries, which truncated the infinite space, $\hat{\mathbf{n}} \cdot \mathbf{D} = 0$, where $\hat{\mathbf{n}}$ was the exterior normal. The outer boundaries were reasonably far away from the region of interest in order to reduce their influence on the final solution.

Relative impedance change of an open-plate capacitor

The impedance of the capacitor was calculated as the voltage over the current at the terminal. It is associated with the capacitance C between the plates:

$$Z = \frac{V}{I} = \frac{1}{j\omega C}. \quad (13)$$

Here V and I are the voltage and current, respectively, at the terminal, and C is the capacitance. Note that the impedance is purely imaginary, if $\sigma = 0$. A volumetric change in the dielectric properties of the bulk material associated with a flaw will alter the fields and this will translate in a change of the impedance of the capacitor. We consider the relative change of impedance due to the flaw as a sensitivity metric:

$$\delta_s = \frac{Z - Z_{BG}}{Z_{BG}} = \frac{\Delta Z}{Z_{BG}}, \quad (14)$$

where Z_{BG} denotes the impedance without the flaw. The sensitivity δ_s is dimensionless. The model represents an ideal measurement and does not include stray capacitances of wires and connectors.

Distribution of the electric field in the transect of the test specimen

The test geometry given in Figure 149 was imported into the FE model. The main dimensions were $W = L = 10$ mm, lift-off = 1 mm and gap = 1 mm. Figure 150 shows the corresponding electric field around the open plate capacitor. The field lines are directed from one electrode of the open-plate capacitor to another electrode. The field is the strongest near the gap between the plates, and its magnitude reduces with penetration depth. The distribution of the field will depend on the geometry of the electrodes and lift-off with respect to the top surface of the test sample.

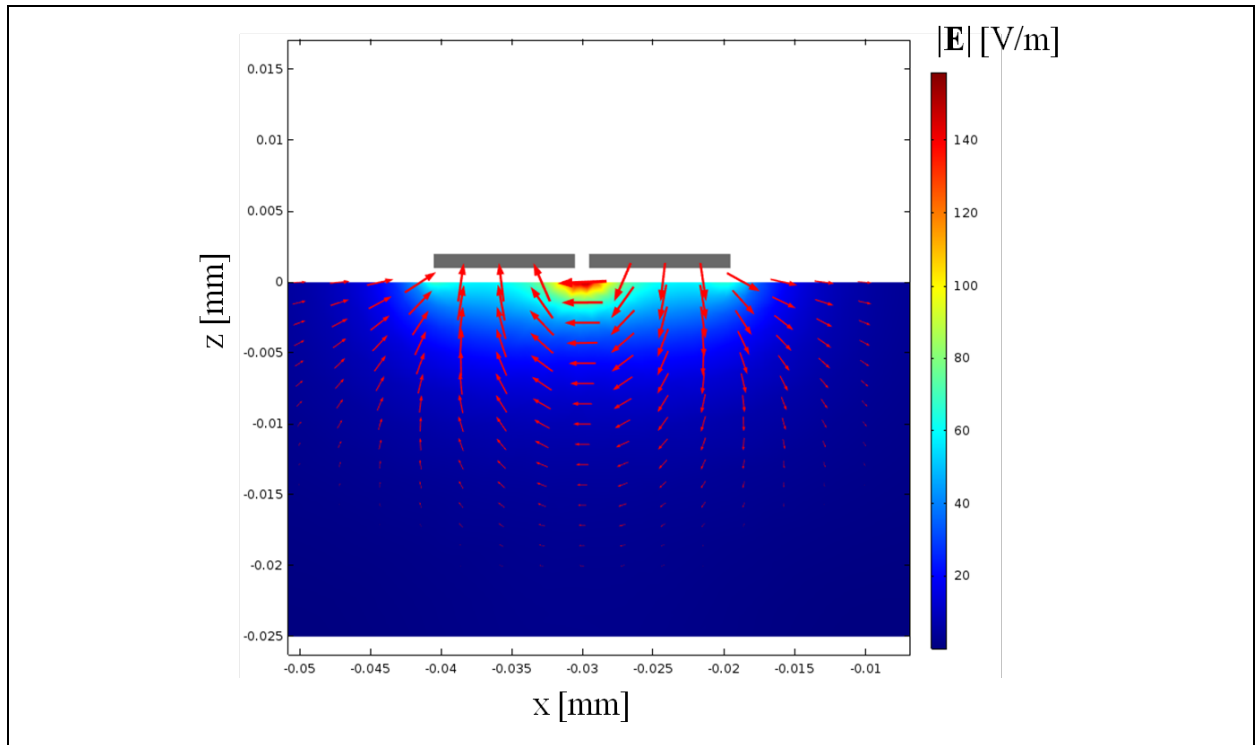


Figure 150. The electric field in the sample under the open plate capacitor (xz -cross section).

C-Scan of the volumetric defect

Figure 151 shows the change in capacitance (see Eq.(13)) of an open-plate capacitor at multiple positions around a cylindrical flaw. The dimensions for the capacitor were $W = L = 10$ mm, lift-off = 1 mm, gap = 1 mm, and the flaw radius was 2 mm.

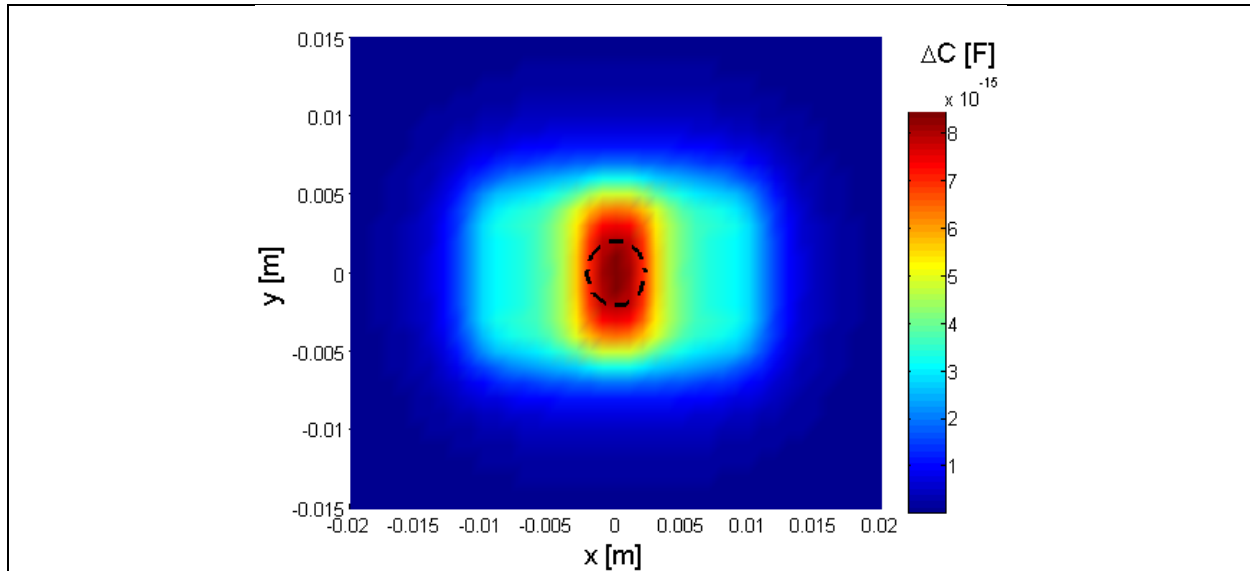


Figure 151. Capacitive C-scan over a hole with 2 mm radius (dashed line). Capacitive sensor with $W=L=10$ mm, lift-off=1 mm, gap=1 mm.

The geometrical properties (i.e., the footprint) of the capacitor influence the measured signal around the cylindrical flaw as the resulting C-scan seems to have rectangular shape. The flaw produces a small, but measurable change of capacitance, while the background capacitance is around 50 pF. This confirms that the underlying NDE problem is challenging, and as a result equipment with high gain and low noise is needed for data acquisition.

Effects of sensor/defect geometries on the impedance change of rectangular capacitor

A series of FE simulations was carried out in order to compare different geometries of the open-plate capacitor and study the effects of defect size, defect depth under surface, specimen's permittivity, and sensor lift-off on the relative impedance change. Five different geometries of capacitors were considered as presented in Figure 152. The gap between the plate electrodes was 1 mm.

For all FE simulations a separate defect domain was created. It was either assigned the properties of the bulk material to simulate a baseline sensor response (defect-free case), or the properties of air to simulate a sensor response with defect present in the structure. The open-plate capacitor was placed above the surface of the sample and the center of the defect domain. Then, the change in the relative impedance from Eq.(14) was evaluated based on the acquired FE results. Four separate parameters were considered: 1) defect radius, 2) specimen's dielectric permittivity, 3) sensor lift-off, and 4) defect depth under the surface. Figure 153 shows the corresponding FE results for different sensor geometries from Figure 152 and the four test configurations mentioned above.

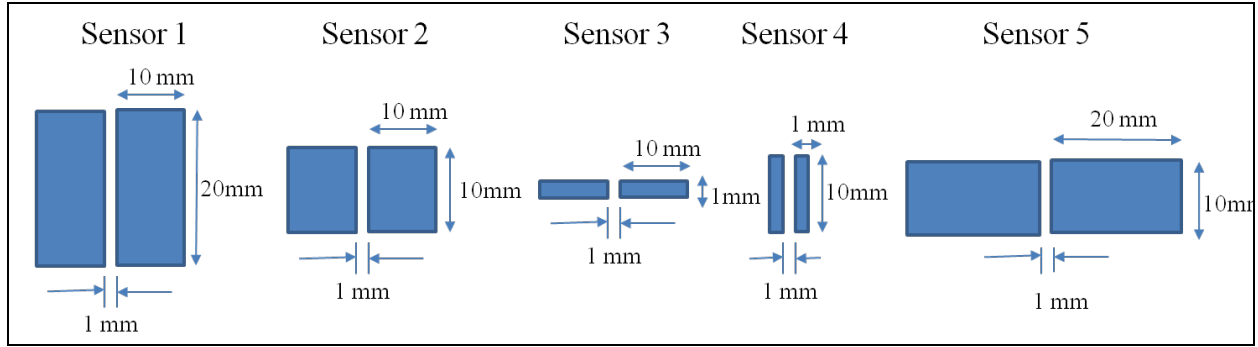


Figure 152. Five configurations of open-plate capacitors used in FE simulations.

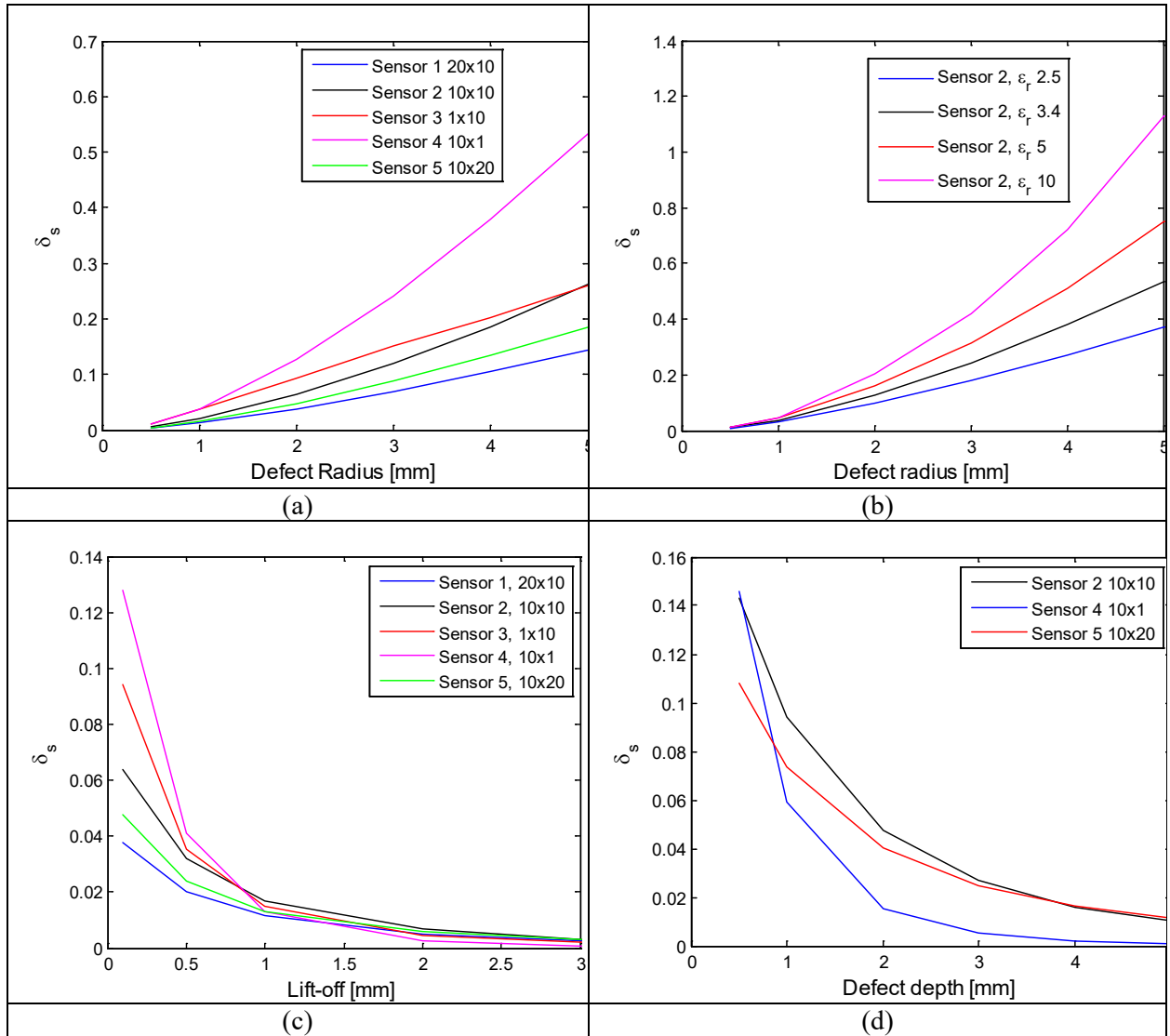


Figure 153. Sensitivity for different capacitor geometries as a function of: (a) defect radius, (b) dielectric constant of test material, (c) sensor lift-off (defect radius of 2 mm) and (d) defect depth under the surface (defect radius of 5 mm).

Figure 153a demonstrates that the relative impedance change of the open-plate capacitor increases with flaw size for all sensor geometries. However, the highest sensitivity is achieved with sensor configuration 4. In this configuration, the plates are narrow (1 mm). They cover mostly the defect area and much less of the rest of the specimen. Another outcome is that the sensitivity to a defect in the form of an air void increases with higher dielectric permittivity of the surrounding material as shown in Figure 153b. Increased lift-off reduces the sensitivity of all sensor configurations, and δ_s drops to about 1% for lift-offs above 1.5 mm (see Figure 153c). Figure 153d presents the simulation results for different defect depths under the surface of the test specimen. With all other parameters equal, the sensitivity will drop faster as a function of defect depth under the surface for the open-plate capacitor with smaller footprint. Larger capacitors generate stronger electric fields that provide deeper penetration into the transect of the test specimen.

Adjusting the gap between the plates provides the trade-off between the penetration depth of the field and the sensitivity to defects as shown in Figure 154b and Figure 154c. The electric field excited using the capacitor with the narrow gap is focused closer to the top surface of the test sample. For the capacitor with a wider gap, the electric field strength is reduced. However, the field penetrates deeper into the transect of the test sample.

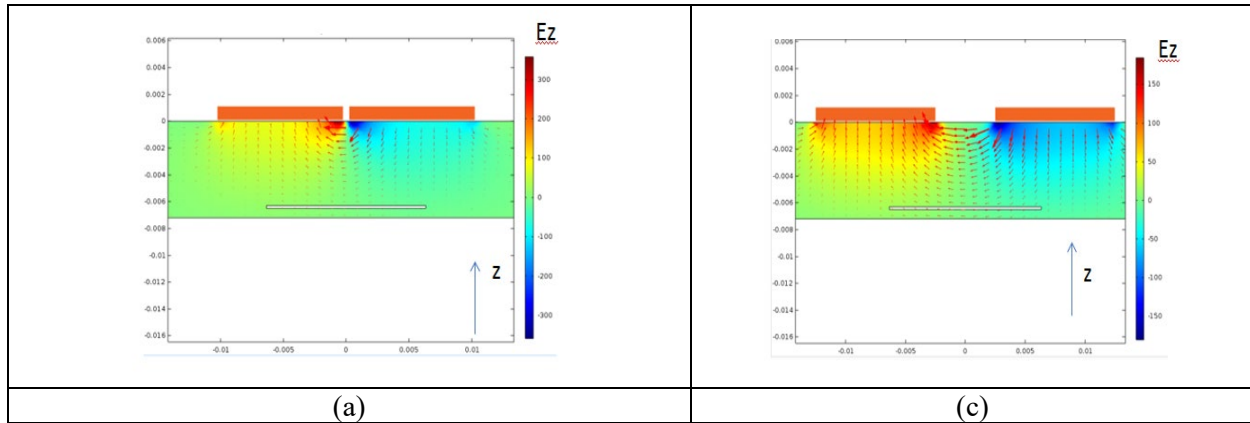


Figure 154. Electric field in the transect of the test specimen generated by: (a) capacitor with narrow gap; (b) capacitor with wide gap.

Overall, the results of the FE studies provide useful insights into how the geometry of the open-plate capacitor can be optimized so as to improve defect detection in FRP composites.

Absolute and differential topologies of rectangular capacitive sensors

The MSU team validated two designs of the capacitive sensors with rectangular electrodes: absolute (ABS) and differential (DIFF). Schematics of both types of the probes are shown in Figure 155. The absolute capacitive probe has one positive and one negative electrode, while the differential probe has two positive electrodes surrounding the negative electrode.

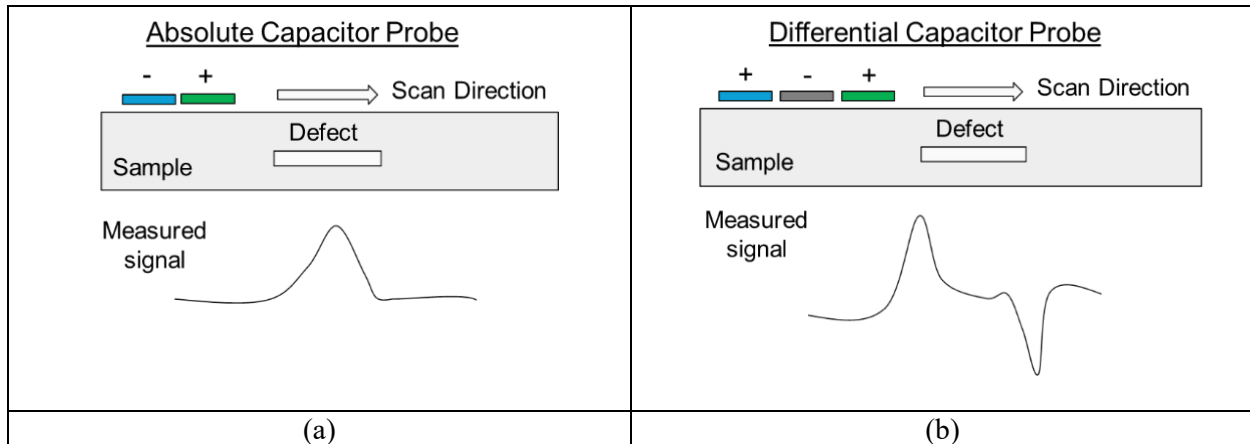


Figure 155. Open-plate capacitive probes: (a) absolute topology; and (b) differential topology.

Absolute and differential capacitor probes can be driven by the Ectane instrument similarly to the absolute and differential coils sensors. Analogous to coils, an absolute capacitive probe will always generate a bias signal, and the differential probe will generate signals with opposite polarities as it passes across the defect site.

3.3.2. Design and optimization of capacitive array probes

Capacitive sensor arrays with rectangular electrodes

Optimization of the electrode size is one of the major issues in capacitive sensor development. Larger electrodes provide deeper field penetration into a composite test specimen; however, smaller electrodes provide better spatial resolution of the measurement. This trade-off is schematically illustrated in Figure 156. An open-plate capacitor can be formed by connecting two consecutive electrodes to positive and negative voltage terminals as illustrated in Figure 156a. Narrow electrodes allow for more channels in the probe and switching can be accomplished with a finer stepping.

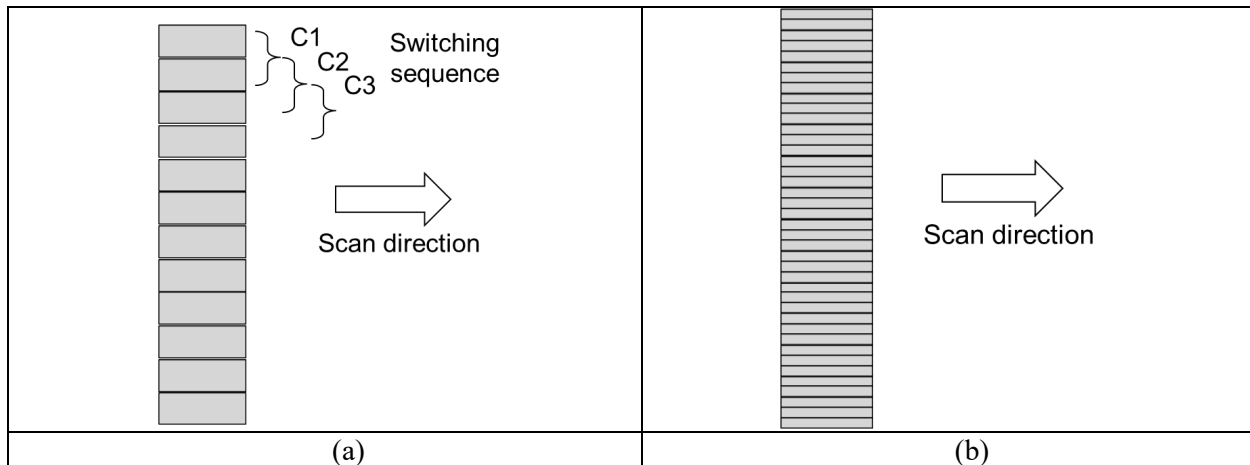


Figure 156. Schematics of linear capacitor arrays with rectangular electrodes: (a) wide electrodes; (b) narrow electrodes.

The disadvantage of having small electrodes can possibly be eliminated if electrodes can be excited in groups. For instance, a larger open-plate capacitor can be formed by exciting multiple narrow electrodes. In this case, the step between the sensors can be as fine as the distance between the narrow electrodes, and the effective size of the capacitor can be increased by activating multiple adjacent electrodes at the same time. The MSU team investigated the feasibility of this idea using FEM (Tasks viii-ix).

Figure 157a illustrates a reference open-plate capacitor with two $10\text{ mm} \times 5\text{ mm}$ electrodes with a 0.2 mm air gap between them. The corresponding electric field in the air is shown in Figure 157b. In the model, the capacitor was excited at 1 V and the frequency was 10 kHz .

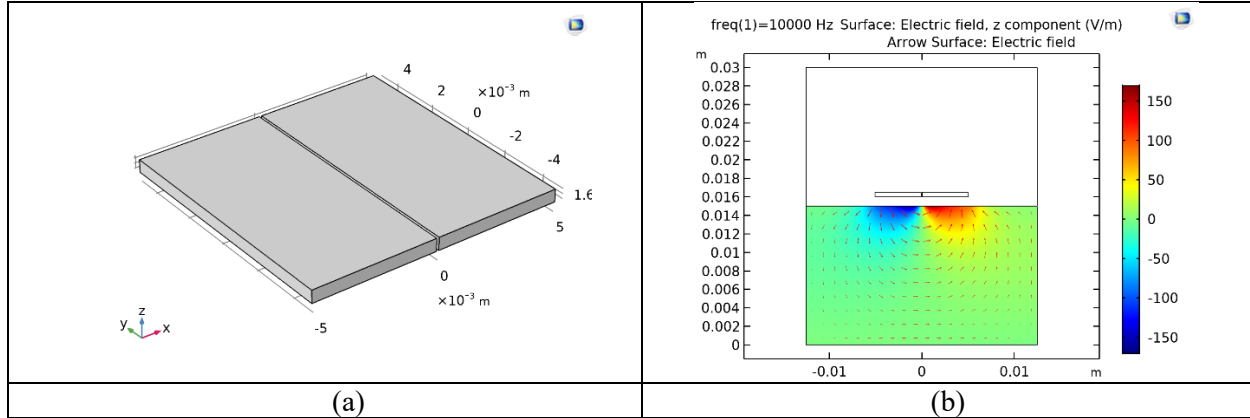


Figure 157. A typical design of a 2-electrode open-plate capacitor: (a) schematic geometry; (b) electric field distribution in the air (xz-plane) at 10 kHz .

Figure 158a illustrates the split geometry in which both left and right capacitor electrodes are split in halves along the y -axis. In this model, the left pair of electrodes was excited at 1 V and the right pair of electrodes is grounded. The simulation results reveal that the electric field shown in Figure 158b is nearly identical to the electric field generated by the reference capacitor.

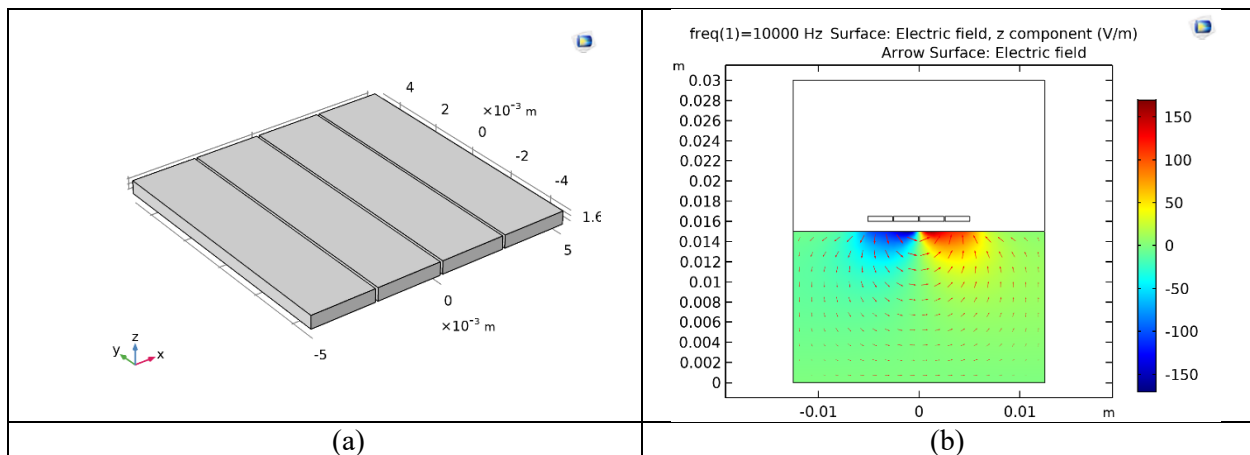


Figure 158. The 2-electrode open-plate capacitor after splitting the electrodes along the y -axis: (a) schematic geometry; (b) electric field distribution in the air (xz-plane).

Figure 159a demonstrates the second model in which the electrodes of the reference capacitor were split in halves along the x -axis. Similar to the results obtained in Figure 157b and Figure 158b, there were no appreciable differences in the electric field distributions.

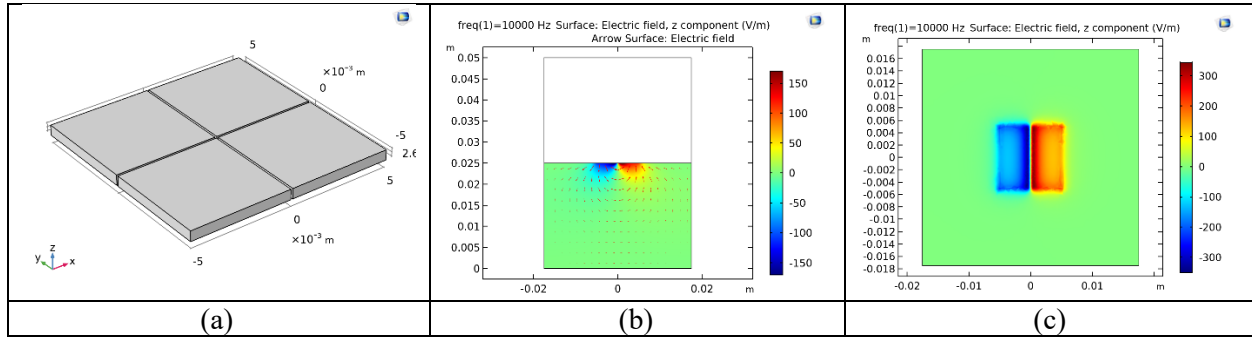


Figure 159. The 2-electrode open-plate capacitor after splitting the electrodes along the x -axis: (a) schematic geometry; (b) electric field distribution in the air (xz -plane); (c) electric field distribution in the air right under the electrodes (xy -plane).

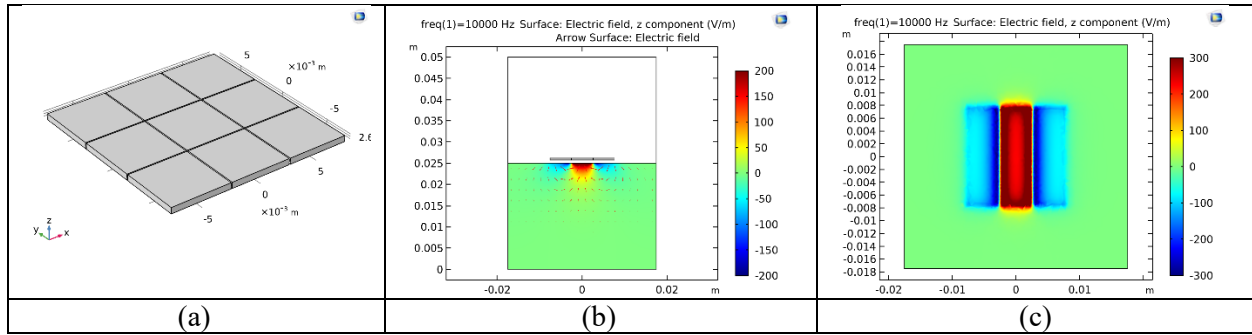


Figure 160. The differential open-plate capacitor with 3 split electrodes: (a) schematic geometry; (b) electric field distribution in the air (xz -plane); (c) electric field distribution in the air right under the electrodes (xy -plane).

The same effect was observed in the model of a differential capacitor with three electrodes shown in Figure 160a. In this case, two splits were introduced along the x -axis. Three middle electrode partitions at $x = 0$ were grounded while all other electrode partitions were subjected to a 1 V electric potential. The electric field in both xz - and xy -planes seemed to be consistent with that of an ordinary differential capacitor without splits. Hence, the FE models confirmed that an open-plate capacitor of a larger size can be designed by grouping multiple electrodes of smaller sizes.

Figure 161 depicts a 10-electrode capacitive array probe which is configured to acquire measurements in the differential (DIFF) topology. Since 3 electrodes are needed to form an elementary differential capacitor (channel), only 8 channels are available. Figure 161b provides an animation of the electric field change as individual channels are activated sequentially (time division multiplexed) from left to right. For every frame, an index electrode is subjected to 1V electric potential, and all remaining electrodes are grounded. There are no visible differences in the electric fields generated by all channels.

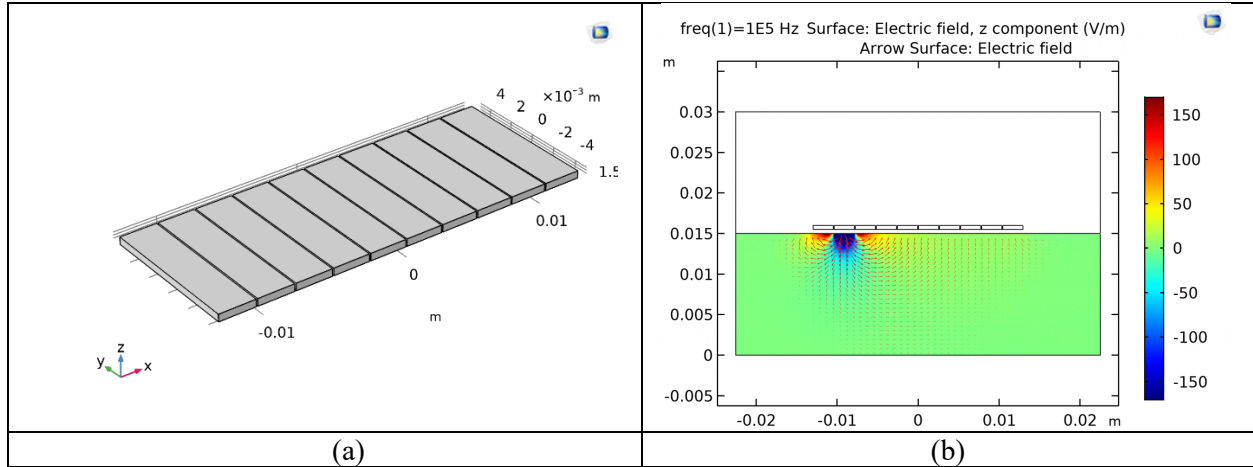


Figure 161. A linear 10-electrode capacitor array with differential (DIFF) measurement topology: (a) schematic geometry; (b) multi-channel switching sequence. Note that the figure contains a gif video.

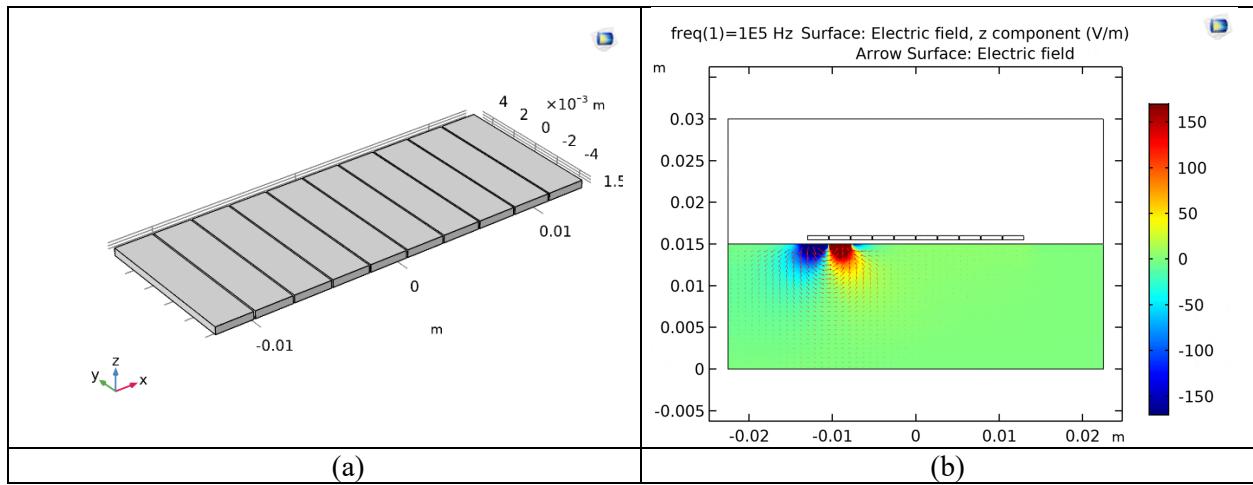


Figure 162. A linear 10-electrode capacitor array with absolute (ABS) measurement topology: (a) schematic geometry; (b) multi-channel switching sequence. Note that the figure contains a gif video.

Similar modeling was performed for the 10-electrode capacitive array with the absolute (ABS) measurement topology (see Figure 162a). In this case, the elementary capacitor needed to have only two electrodes. Hence, 9 measurement channels could be formed. The animation of the electric field and multi-channel multiplexing is shown in Figure 162b. The left and right index electrodes of the elementary capacitor were connected to +1V and -1V, respectively. Every other electrode was grounded. The results demonstrated that the generated electric fields in the different time frames were similar. Slight differences in the field distributions were observed for the capacitors at the edges of the probe, which means that measurements corresponding to these channels would need to be normalized with respect to the other channels prior to the data acquisition process. However, this problem is minor since channel normalization is an embedded feature in the Magnify software.

Capacitive sensor arrays with circ electrodes

In order to minimize the size of the circular capacitor, which is critical for making compact array probes, the MSU team carried out a parametric FE study. Two circular capacitors were simulated as illustrated in Figure 163a and Figure 164a. Both capacitors had a central disk electrode of 2.5 mm radius. At the same time, the width of the outer ring electrode was different: 2.4 mm and 0.8 mm, respectively. The electric fields generated by circular capacitors are shown in Figure 163b and Figure 164b. As evident from the results, the difference between the fields is minimal. Hence, the width of the outer ring electrode can be kept small in all designs.

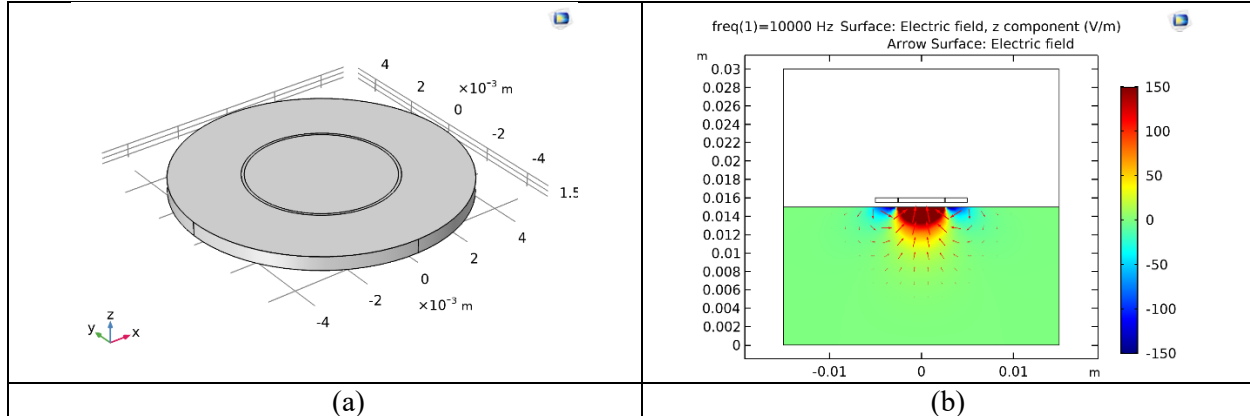


Figure 163. A circular 2-electrode capacitor with wide outer ring electrode: (a) schematic geometry; (b) electric field distribution in the air (xz-plane).

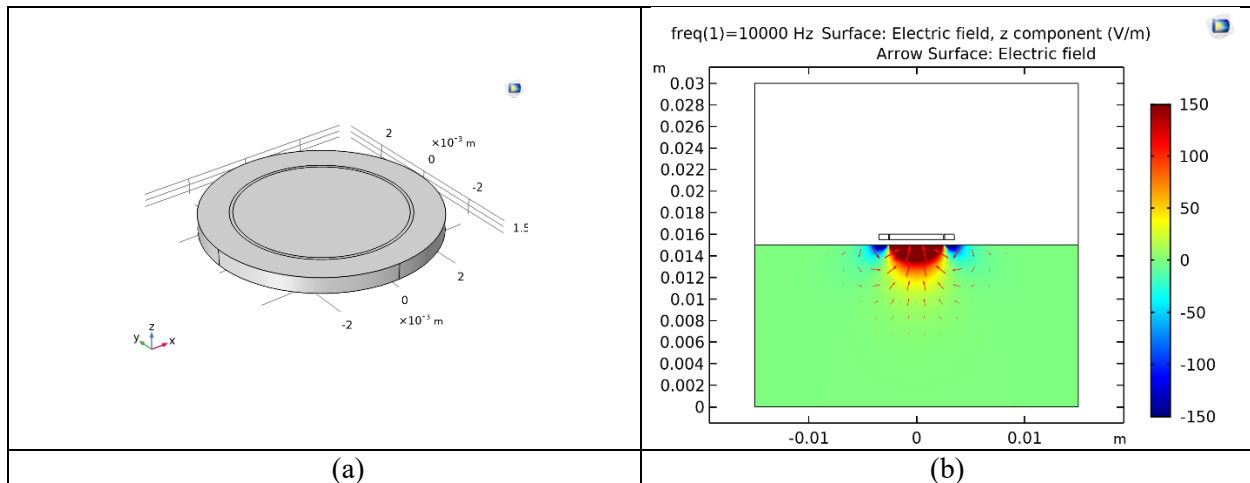


Figure 164. A circular 2-electrode capacitor with narrow outer ring electrode: (a) schematic geometry; (b) electric field distribution in the air (xz-plane).

Figure 165a demonstrates the design of an 18-channel array capacitive probe with circular electrodes. Radii of the inner disk electrodes are 2 mm, and the ring electrodes are replaced with a single ground electrode, which surrounds the disks. The design in Figure 165a is compatible with the Ectane's ECA connector and MUX settings for the ABS coil topology. In addition, the ground electrode provides the opportunity to eliminate 17 wires.

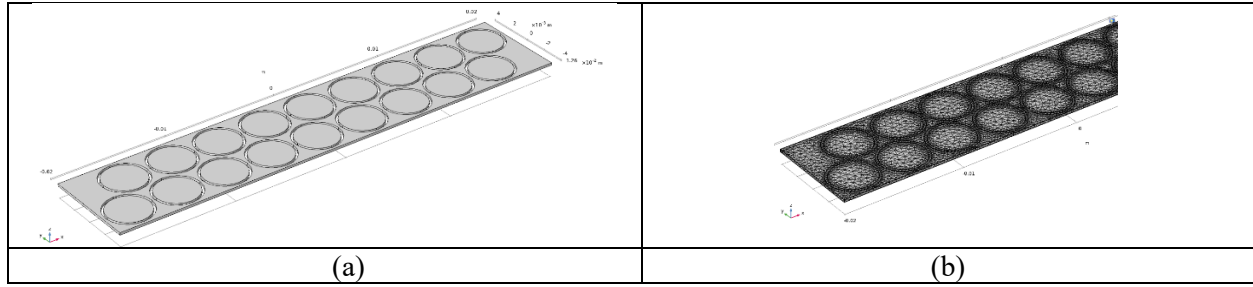


Figure 165. An 18-channel circular capacitor array with common ground electrode: (a) schematic geometry; (b) mesh for finite element simulations.

Figure 165b shows the corresponding mesh for FE simulations. In the present model, all disk electrodes were excited simultaneously with 1V electric potential. The electric field in the xy -plane beneath the probe is shown in Figure 166. Similarly, the electric field in the xz -plane that dissected one row of capacitors is presented in Figure 167. The simulation results revealed that the field was fairly uniform despite the simultaneous excitation of all capacitors. The only differences in the field patterns were observed around the edge elements of the probe, which were insignificant.

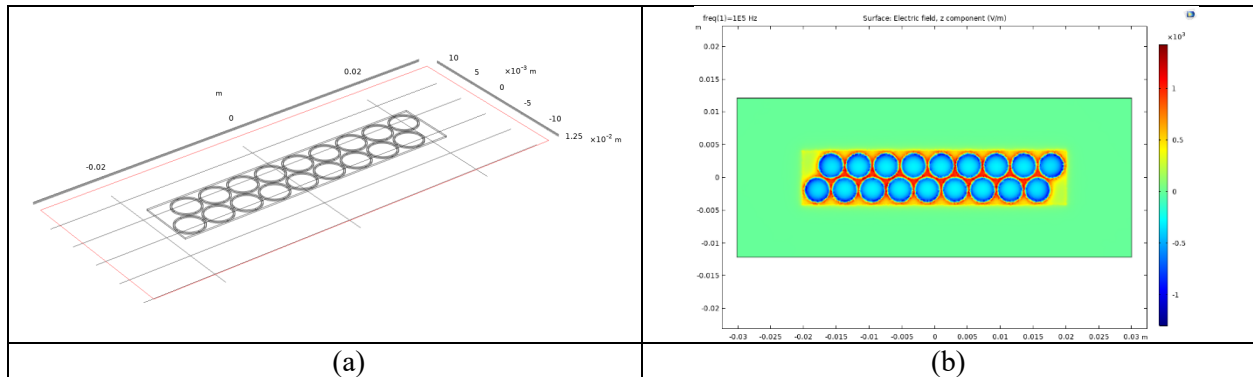


Figure 166. FEM result, electric field distribution in the air: (a) cut xy -plane; (b) z -component of the electric field.

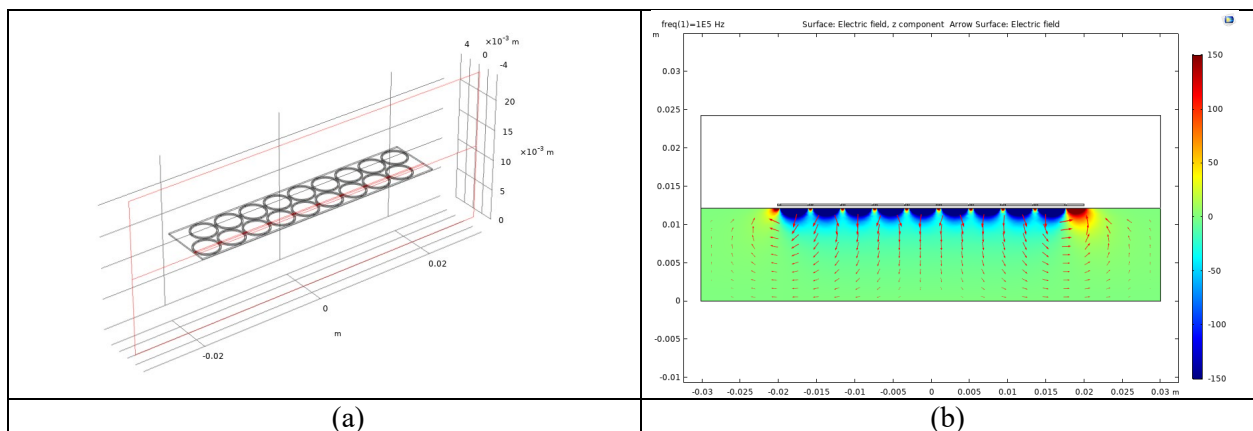


Figure 167. FEM result, electric field distribution in the air: (a) cut xz -plane; (b) z -component of the electric field.

3.3.3. MSU capacitor array probes for NDE of FRP composites

Capacitive array probe C-1a

Schematics of the C-1a capacitive probe fabricated by MSU are shown in Figure 168a. Four 10 mm × 2 mm copper stripes were cut from a copper coated panel. Left and right pairs of electrodes formed open-plate capacitors C1 and C2, respectively.

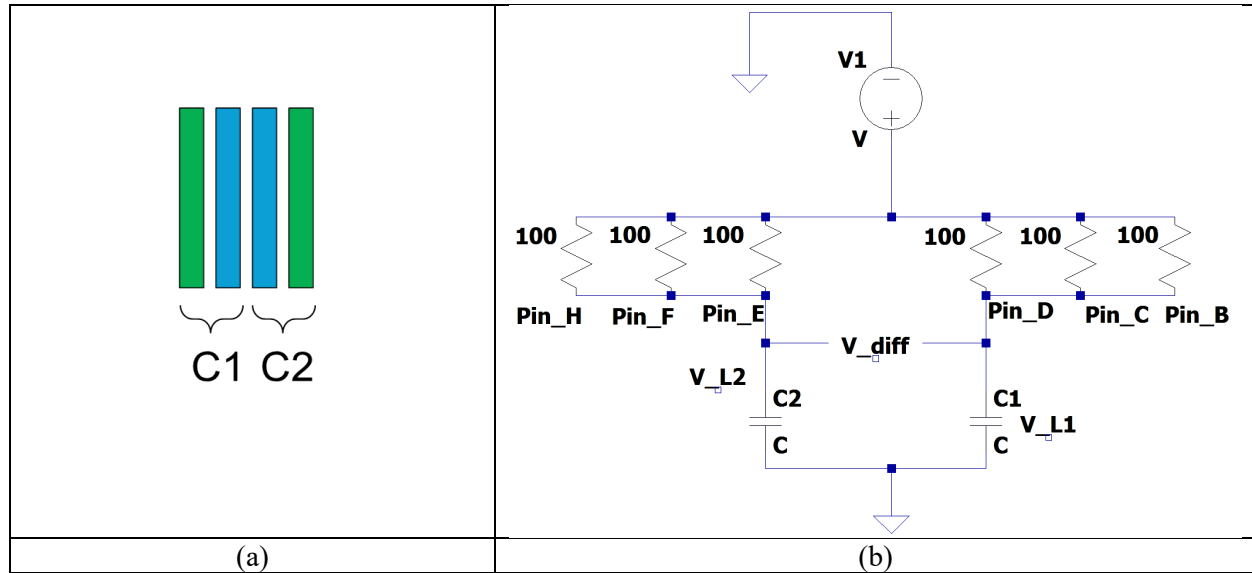


Figure 168. Capacitive probe C-1a: (a) schematics; (b) driving circuit (EET connector)

The electrical circuit interfacing the Ectane 2 with C1 and C2 through the EET connector is illustrated in Figure 168b. Both C1 with C2 capacitors were connected to the same voltage source as two balanced arms of the bridge. At the same time, three input channels were activated for data acquisition: CH1 and CH2 for taking the absolute measurements V_{C1} and V_{C2} , and CH3 for taking the differential measurement $V_{DIFF} = V_{C1} - V_{C2}$.

Validation of C-1a probe (ABS topology, 2 channels; DIFF topology, 1 channel)

Selected region of the CFRP panel #7 with notches was scanned using the C-1a probe as shown in Figure 169. The excitation frequency was 10 MHz, scan resolution was 1 mm, scan speed was 40 mm/s, and sensor lift-off was ~1.5 mm. The corresponding results for CH1, CH2, and CH3 are shown in Figure 170. The obtained results demonstrated that defects in the form of fiber damage (notches) were successfully detected with the capacitor probe C-1a. Both absolute and differential channels provided measurements as predicted in Figure 155, thereby validating the design of the probe.

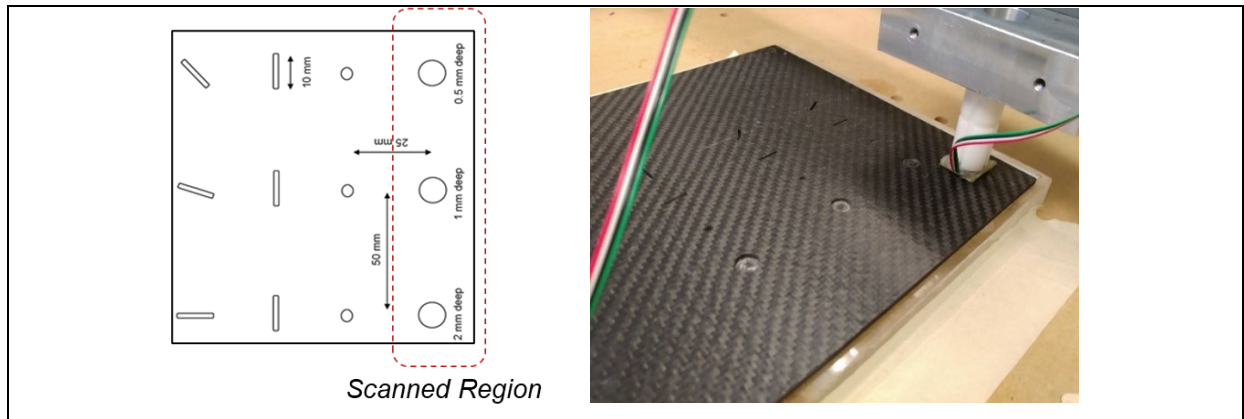


Figure 169. Region of the CFRP test panel #7 scanned using capacitor probe C-1a.

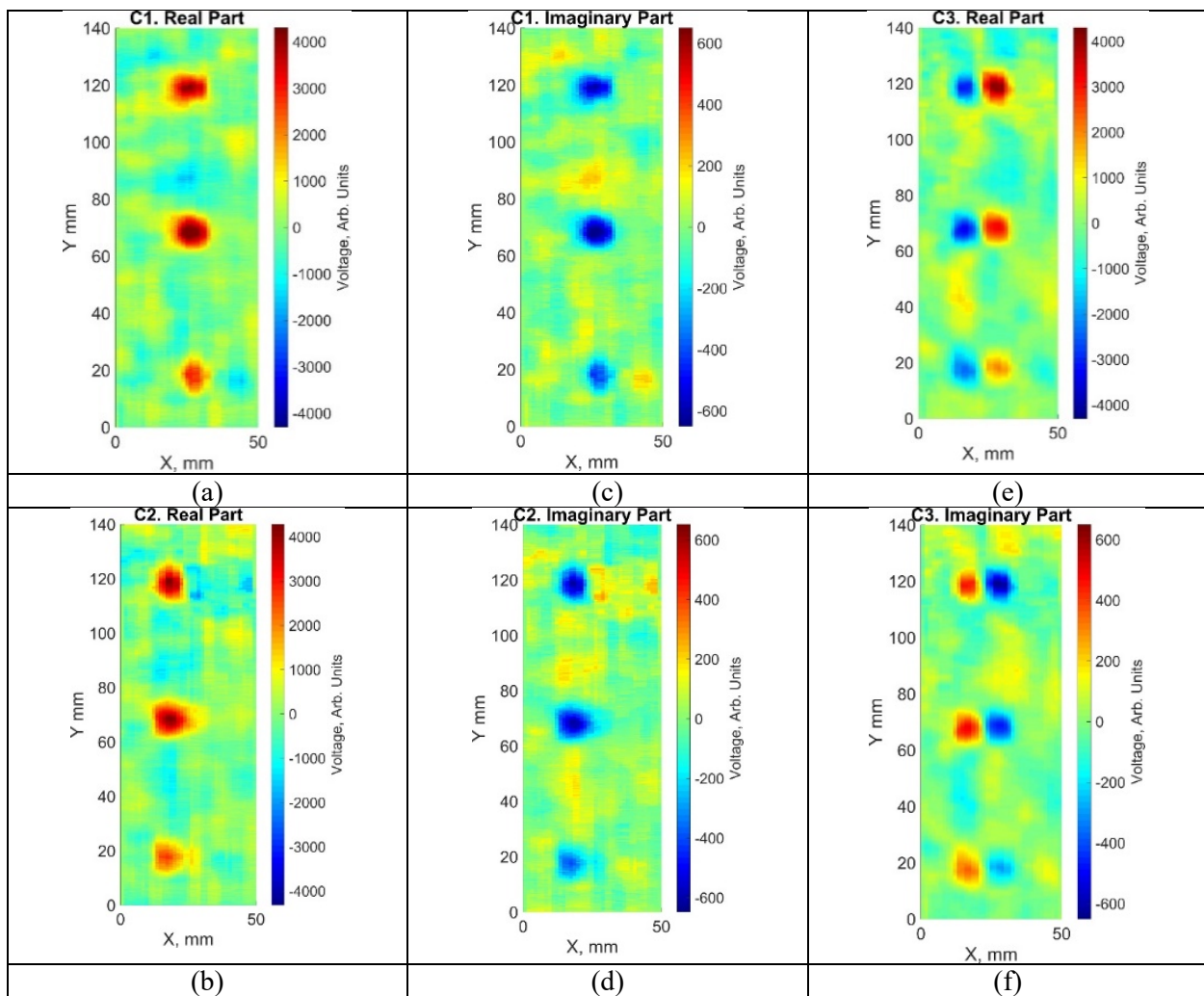


Figure 170. Capacitor probe C-1a. C-scans of selected region on CFRP test panel: (a) CH1 real part; (b) CH1 imaginary part; (c) CH2 real part; (d) CH2 imaginary part; (e) CH3 real part; (f) CH3 imaginary part. CH1 and CH2 are ABS, CH3 is DIFF.

Capacitive array probes C-1b and C-1c

In contrast to the probe C-1a, the capacitive probes C-1b and III C-1c had only three copper electrodes as shown in Figure 155b, Figure 171b and Figure 171c. The output of both probes was differential (see Figure 171a). Probe C-1b was designed for deeper penetration of the electric field into the test sample, and probe C-1c was supposed to have higher spatial resolution and higher sensitivity to defects located closer to the top surface of the test sample. Dimensions of the electrodes were $10\text{ mm} \times 5\text{ mm}$ for the probe C-1b, and $10\text{ mm} \times 2\text{ mm}$ for the Probe C-1c.

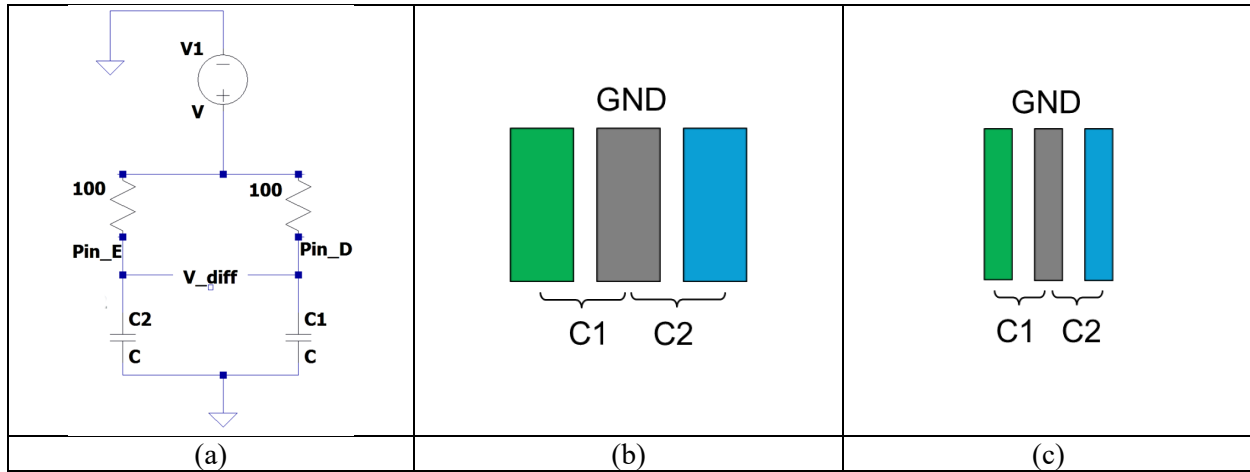


Figure 171. Differential capacitive probes: (a) electric circuit showing connection to the EET connector; (b) C-1b; and (c) C-1c.

Impedance of C-1b probe

The complex impedance of the C1 open-plate capacitor (see Figure 171a) was measured with the help of the impedance analyzer HP4194. The results are shown in Figure 172. Similar to coil sensors, capacitive probes could also be represented as an equivalent RLC circuit with main capacitance plus parasitic inductances and resistances. The anti-resonance of the capacitor C-1b was observed at $f \sim 26\text{ MHz}$. At frequencies above 26 MHz, the probe essentially behaved as an inductor owing to the lumped inductance introduced by the attached non-coax cables.

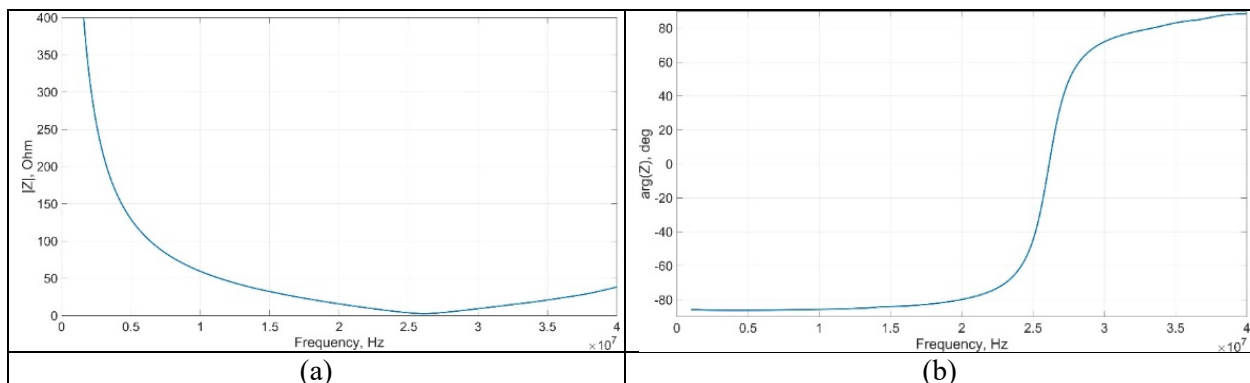


Figure 172. Impedance of C1 open-plate capacitor in C-1b probe: (a) magnitude; (b) phase.

Validation of C-1b and C-1c probes (DIFF topology, 1 channel)

Performance of capacitor probes C-1b and C-1c was validated on the Calibration CFRP Panel #1 shown in Figure 173. The panel had a stepped profile. Nine delaminations (Teflon inserts) were introduced between different plies as illustrated in Figure 174. Delaminations were square shaped with sizes of 1 in \times 1 in, 0.5 in \times 0.5 in, and 0.25 in \times 0.25 in.

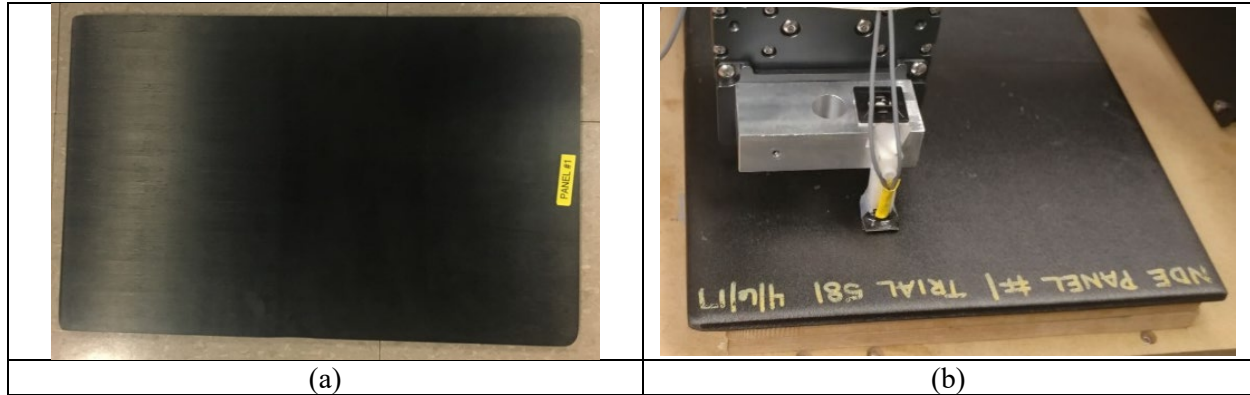


Figure 173. Calibration panel #1: (a) top view; (b) bottom view.

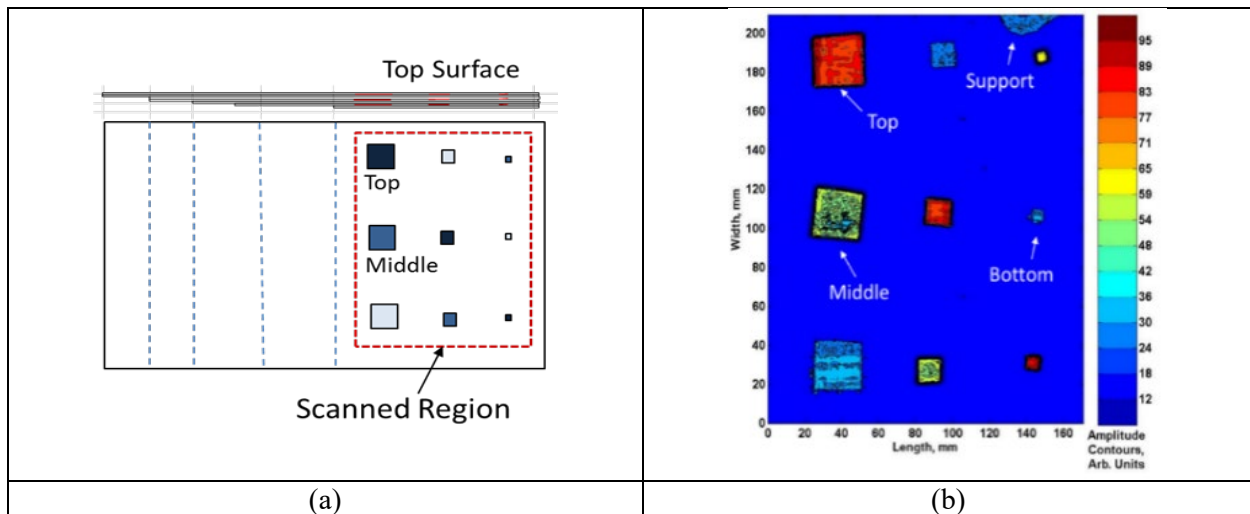


Figure 174. Baseline UT imaging of Calibration Panel #1: (a) locations of delaminations; (b) ultrasonic pulse-echo C-scan at 2.25 MHz.

C-scans of the Calibration Panel #1 were acquired using the capacitor probe C-1b at 9.9 MHz and 6.4 MHz with a lift-off of 1.5 mm and at a scan speed of \sim 30 mm/s. Scan resolution was 1 mm and scans were acquired from bottom side as shown in Figure 173b. Corresponding results are found in Figure 175 and Figure 176.

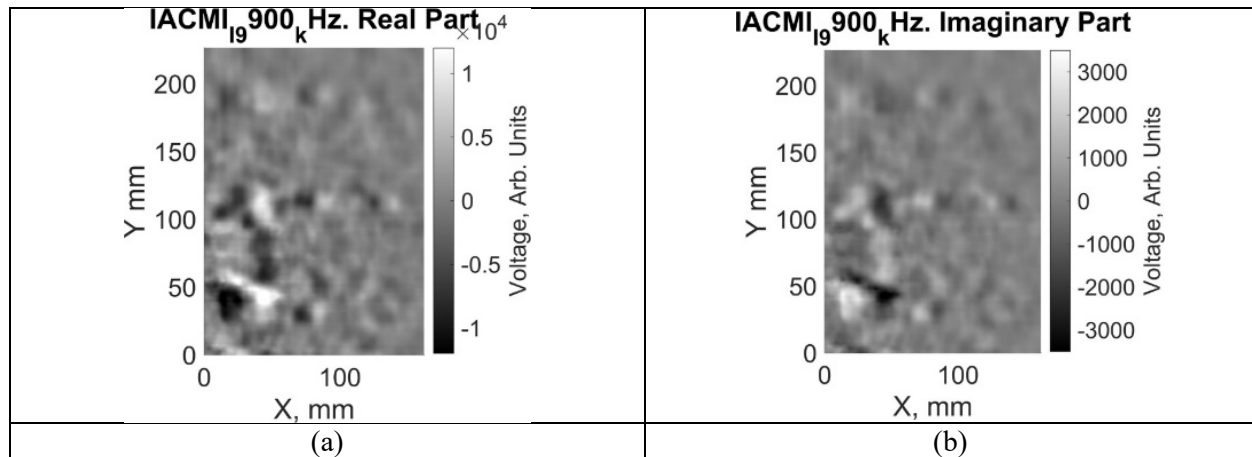


Figure 175. Capacitive C-scans of Calibration Panel #1 acquired using C-1b probe at 9.9 MHz: (a) real part; (b) imaginary part.

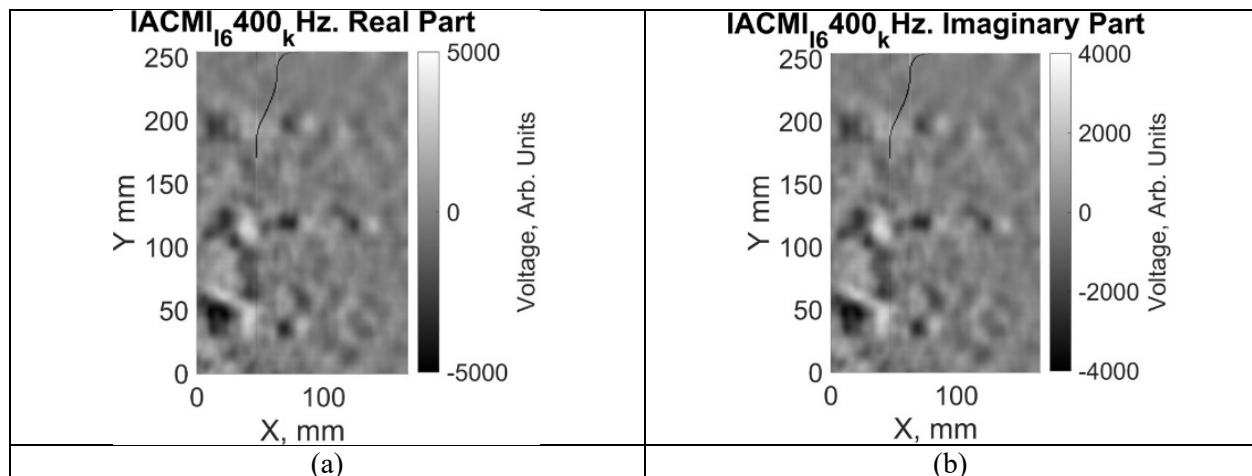


Figure 176. Capacitive C-scans of Calibration Panel #1 acquired using C-1b probe at 6.4 MHz: (a) real part; (b) imaginary part.

Seven out nine delaminations are visible in Figure 175 and Figure 176. They are highlighted as bumps with bright and dark edges. The Capacitive C-scans also revealed the variations of dielectric properties of the test sample. However, one of the main challenges in data acquisition was imperfect shielding and noise introduced by cable movement. Hence, only coax cables were used for future probe designs.

The MSU team also acquired C-scans of mid-size and small delaminations at a finer spatial resolution of 0.5 mm. The results are presented in Figure 177 and Figure 178. Delaminations are better visible, and they manifest themselves as a pair of bright and dark lobes in the images.

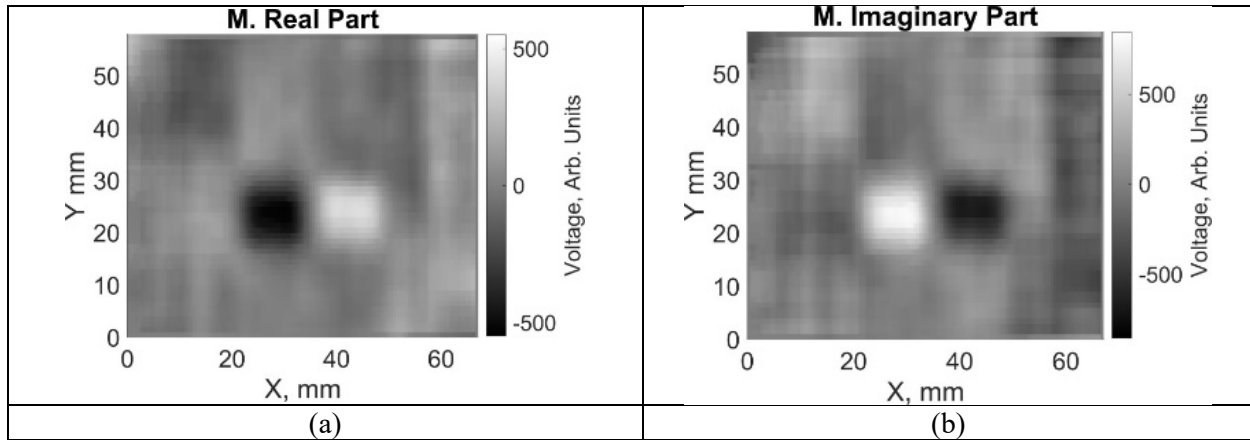


Figure 177. Capacitive C-scan of mid-size (0.5 in \times 0.5 in) delamination “M” close to the top surface of Calibration Panel #1. Data acquired using probe C-1b at 1 MHz.

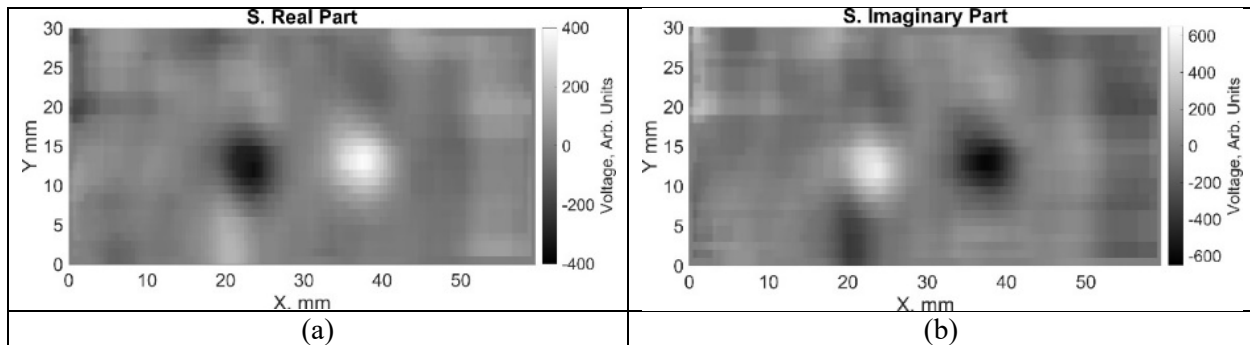


Figure 178. Capacitive C-scan of a small (0.25 in \times 0.25 in) delamination “S” close to the top surface of Calibration Panel #1. Data acquired using probe C-1b at 1 MHz.

Capacitor probe C-1c was used to acquire a C-scan of the calibration CFRP sample #7 with fiber damage as shown in Figure 179. Sensor lift-off was 1.5 mm and scan step size was 1 mm.

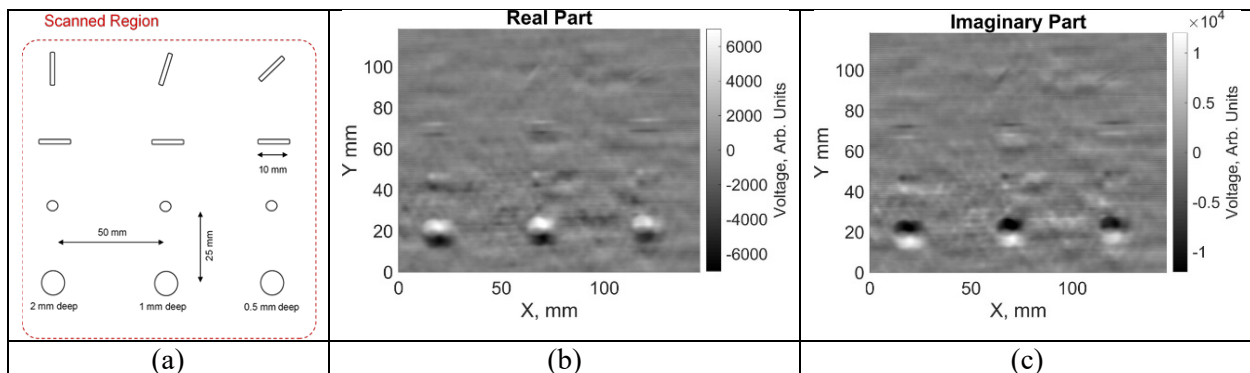


Figure 179. Capacitive C-scan of the CFRP panel with fiber damage (notches). Data acquired using probe C-1c at 1 MHz: (a) scanned region; (b) real part; (c) imaginary part.

Capacitive probes C-2a and C-2b

In Quarter VII, a pair of new capacitive probes was fabricated by MSU. The rectangular probe C-2a with $10\text{ mm} \times 5\text{ mm}$ copper tape electrodes was designed to operate in the ABS mode (see Figure 180a). The main differences between this probe and previous prototypes were: 1) higher quality of manufacturing, 2) low-noise micro-BNC connection and 3) the absence of solder joints on the bottom faces of the electrodes. The circular probe C-2b shown in Figure 181a consisted of two ring electrodes with outer radii of 4 mm and 7 mm, respectively. The widths of both rings were 2 mm.

Both probes were attached to the XYZ gantry in order to raster scan the calibration sample #1 that contained 9 interlaminar delaminations as illustrated in Figure 180b. The C-scans were acquired at 5 MHz with 1 mm resolution. Corresponding results are presented in Figure 180c and Figure 181c, respectively.

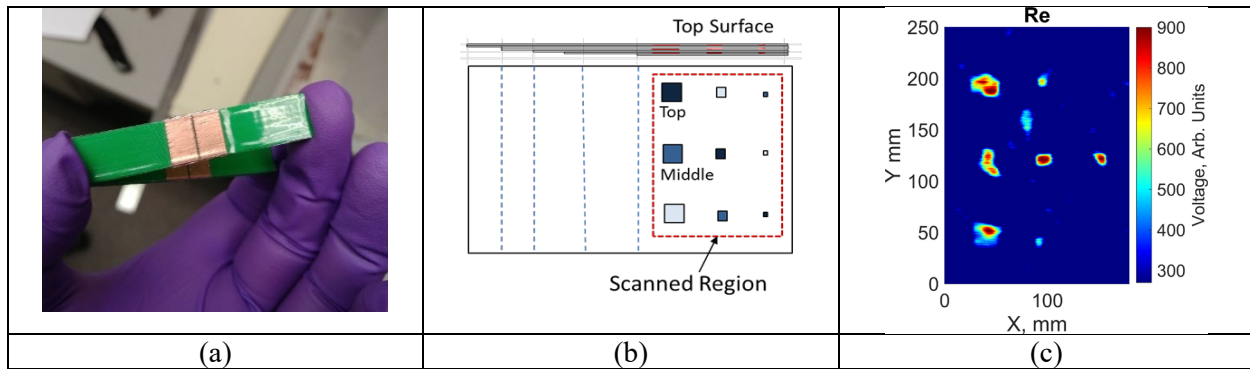


Figure 180. Capacitive imaging of interlaminar delaminations using capacitor prototype C-2a: (a) capacitive sensor with $10\text{ mm} \times 5\text{ mm}$ rectangular electrodes; (b) CFRP laminate; (c) processed C-scan image ($f = 5\text{ MHz}$) highlighting delaminations and variations of dielectric constant of the laminate.

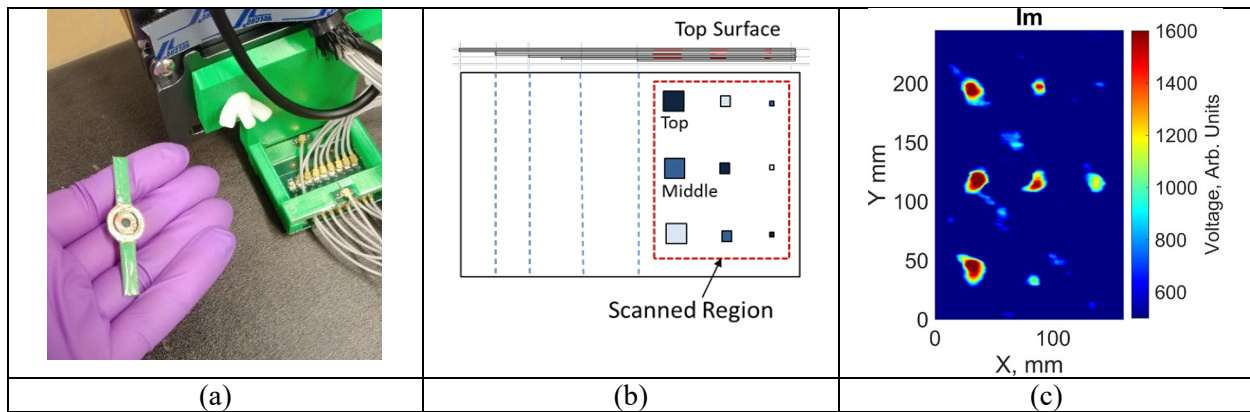


Figure 181. Capacitive imaging of interlaminar delaminations using capacitor prototype C-2b: (a) capacitive sensor with ring electrodes (inner radius of 4 mm, outer radius of 7 mm, ring width of 2 mm); (b) CFRP laminate; (c) processed C-scan image ($f = 5\text{ MHz}$) highlighting delaminations and variations of dielectric constant of the laminate.

The circular probe C-2b demonstrated slightly more uniform sensitivity to flaws. However, most delaminations were successfully detected by both probes. The only misses were two smallest defects between the middle and the bottom plies of the CFRP laminate. The C-scans also revealed sensitivity of the probes to internal fiber/matrix irregularities in the test specimen. Some repeatable indications of the irregularities were observed in the defect-free regions with no embedded delaminations. This can be explained by local variations of the dielectric properties of the material.

Capacitive array probe C-3a (18 rectangular capacitors)

Based on the results of the FE modeling and experimental testing of previous prototypes, the MSU team developed the third batch of novel capacitive array probes compatible with the Ectane ECA connector and MUX. The capacitor array probe C-3a is shown in Figure 182. The array consisted of 36 rectangular electrodes and 18 measurements channels, since one channel required two electrodes. The height of the electrodes was 10 mm, and the width of the electrodes was only 1.5 mm. The prototype C-3a was compatible with Ectane instrument, which was operated in the ABS mode.

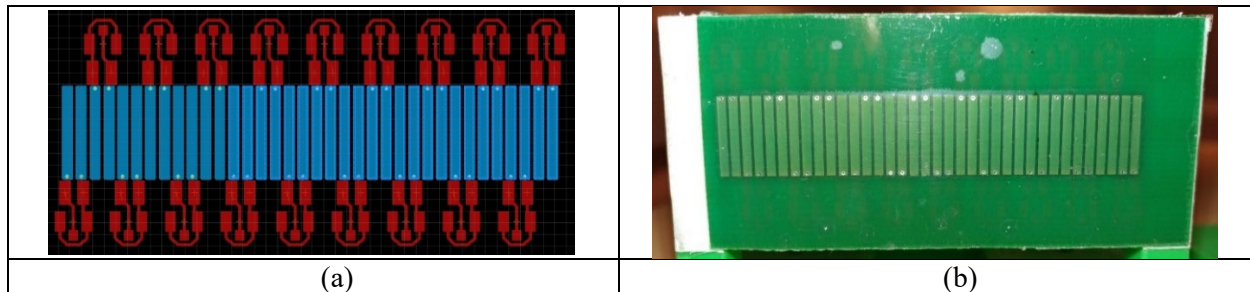


Figure 182. Array probe C-3a with rectangular capacitor electrodes: (a) PCB design; (b) fabricated prototype.

The experimental setup for validating the C-3a array using the Ectane instrument is illustrated in Figure 183. The array was attached to an XYZ gantry, and was first tested on the 15-mm thick GFRP sample with revolved cuts as shown in Figure 183b. A calibration was performed in order to make sure that the array was properly defined in the Ectane/Magnify software and that the sensor coordinates were specified correctly.

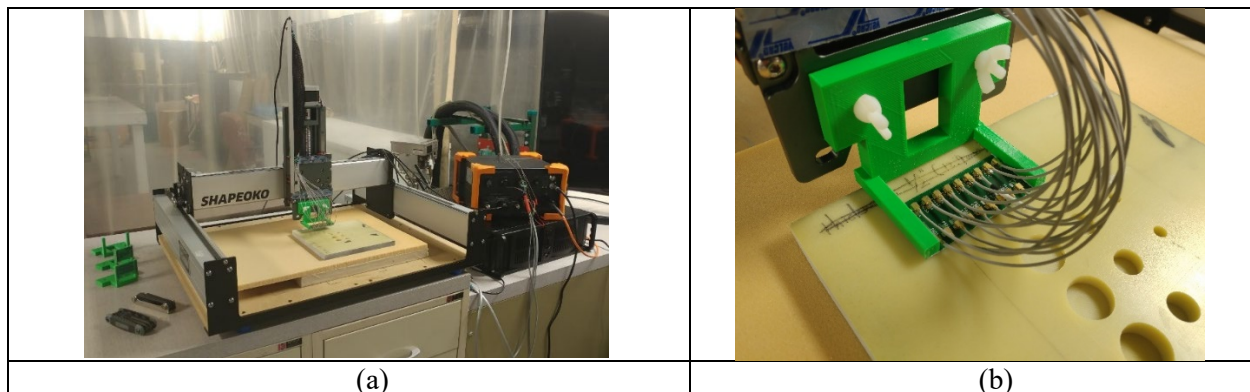


Figure 183. Experimental setup for calibration of C-3a capacitive array: (a) XYZ gantry with Ectane system; (b) array probe on top of GFRP sample with defects.

Experiments demonstrated that solder traces of the micro-BNC connectors (see red traces in Figure 182a) increased the effective heights of rectangular electrodes by 2 mm. Hence, this issue was accounted for when

specifying the channel (x;y) coordinates in the Ectance/Magnify. Considering the effect of connector electrodes helped avoid image striping. Typical C-scans of the calibration GFRP sample are presented in Figure 184. In this case, parallel 18-channel data acquisition was performed. The C-3a array probe was moved at a linear speed of 35 mm/s. The array probe touched the surface of the test sample. The gantry was programmed so as to perform line scans along the height of the electrodes. The space increment between the lines was only 0.2 mm. After 15 lines, the gantry would make a long increment equal to the length of the whole array probe in order to avoid rescanning of the same regions of the sample, but with different sensor channels.

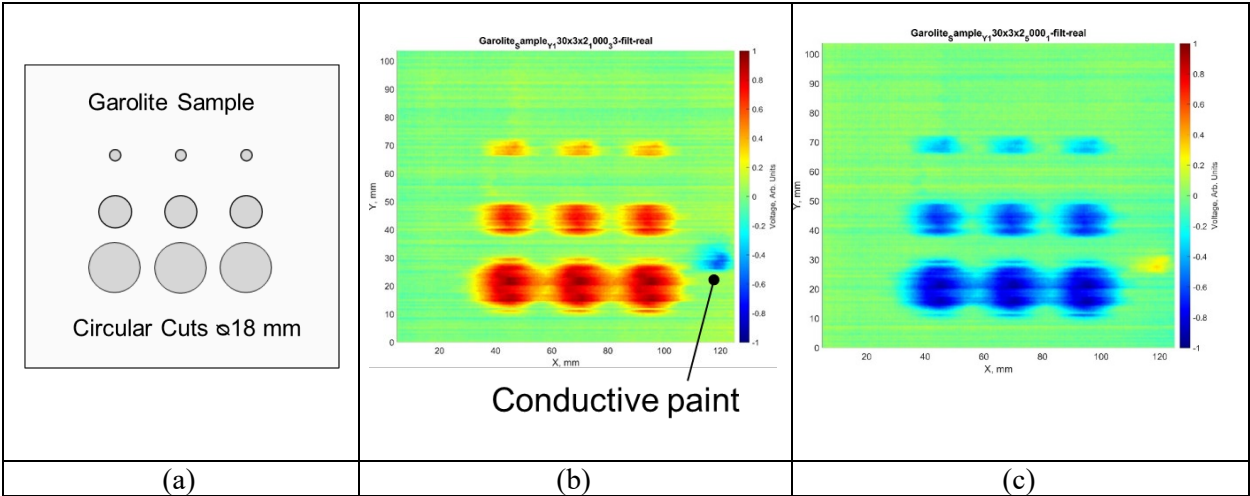


Figure 184. Validation of array probe C-3a on GFRP calibration sample: (a) locations of defects; (b) C-scan at f = 1 MHz (real part, normalized); (c) C-scan at f = 5 MHz (real part, normalized).

Results shown in Figure 184b and Figure 184c demonstrate that the calibration holes are successfully detected using the capacitive array probe. The contrast between the defects and healthy regions is high irrespective of driving frequency. In addition, the probe picked up the signal from conductive paint that was unintentionally left on the surface of the GFRP sample.

Figure 185 presents validation of the C-3a capacitive array on the Calibration Panel #1 with interlaminar delaminations of different sizes. The region with 6 delaminations was scanned as shown in Figure 185a. The excitation frequency was 1 MHz in order to increase the penetration depth of the electric field into the test specimen. Other scan settings were similar to the previous study in Figure 184. The resulting C-scan is shown in Figure 185c. MSU image processing was applied in order to enhance defect signals by reducing the noise, and by suppressing the variations of lift-off and variations of channel sensitivity.

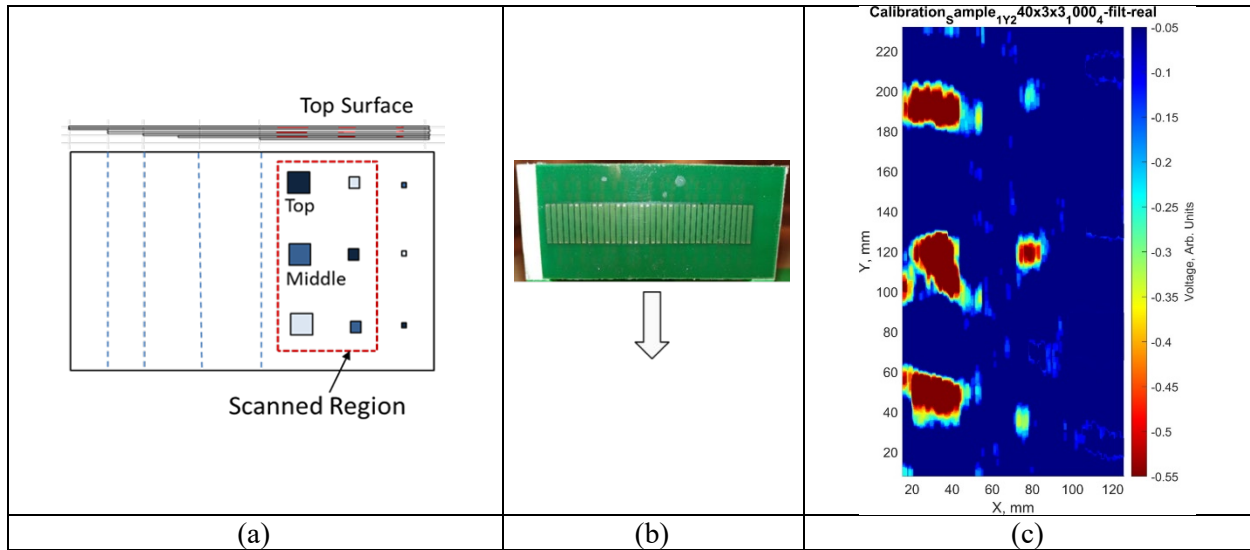


Figure 185. Validation of array probe C-3a on CFRP calibration sample #1: (a) locations of delaminations and scanned region; (b) direction of line scans; (c) typical C-scan (real part), $f = 1$ MHz.

Capacitive array probe C-3b (18 circ capacitors)

Fabricated capacitor array probe C-3b is shown in Figure 186. The array consisted of 18 circ capacitors. The OD of the outer ring electrodes was 6.5 mm. The prototype C-3b was compatible with the Ectane instrument, which was operated in the ABS mode.

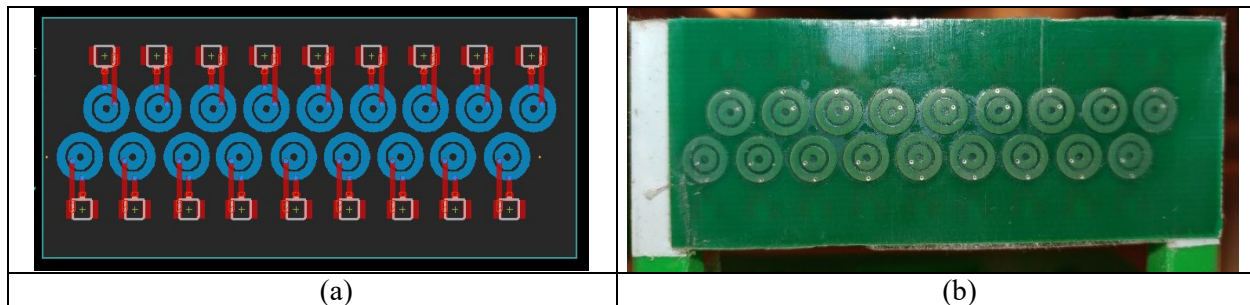


Figure 186. Array probe C-3b with circ capacitor electrodes: (a) PCB design; (b) fabricated prototype.

Similar to the C-3a array, the array C-3b was attached to the XYZ gantry, and was first tested on the 15-mm thick GFRP sample with revolved cuts as shown in Figure 183b. The calibration was performed in order to make sure that the array was properly defined in the Ectane/Magnify software and the sensor coordinates were specified correctly.

Typical C-scans of the calibration GFRP sample are presented in Figure 187. In this case, a parallel 18-channel data acquisition was performed. The C-3b array probe was moved at a linear speed of 35 mm/s. The array probe touched the surface of the test sample. The gantry was programmed so as to perform line scans along the height of the electrodes. The space increment between the lines was only 0.25 mm. After 13 lines, the gantry would make a long increment equal to the length of the whole array probe in order to avoid rescanning the same regions of the sample, but with different sensor channels. Figure 187b and Figure 187c show the acquired C-scans before and after MSU image processing, respectively. Results presented in Figure 187 demonstrate that the calibration holes are successfully detected using the capacitive array probe.

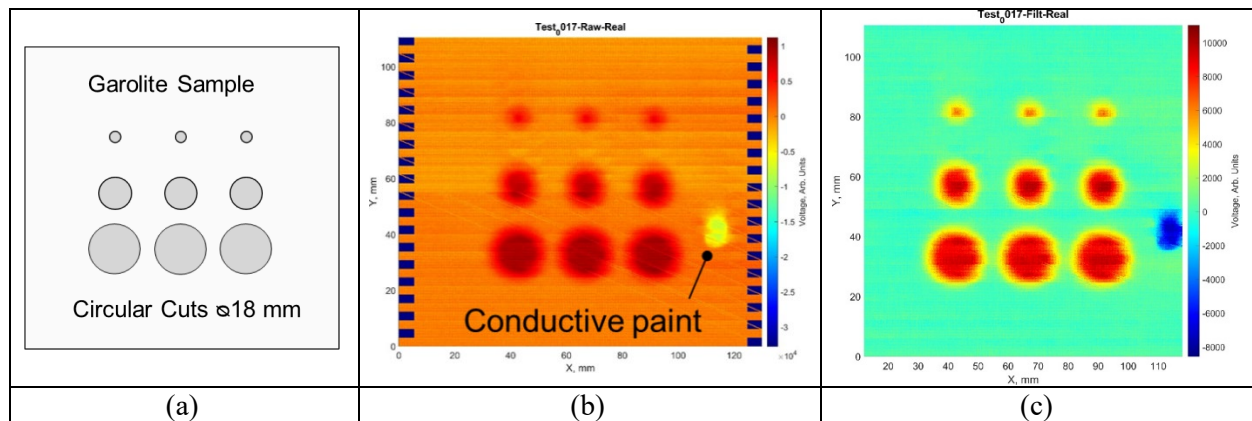


Figure 187. Validation of array probe C-3b on GFRP calibration sample: (a) locations of defects; (b) C-scan at $f = 1$ MHz (real part, raw image); (c) C-scan at $f = 1$ MHz (real part, processed image).

Figure 188 presents validation of the C-3b capacitive array on the CFRP calibration panel #1 with interlaminar delaminations of different sizes. The region with 6 delaminations was scanned as shown in Figure 188a. The excitation frequency was 1 MHz in order to increase the penetration depth of the electric field into the test specimen. Other scan settings were similar to the previous study depicted in Figure 187. The resulting C-scan is shown in Figure 188c. The MSU image processing was applied in order to enhance defect signals by reducing the noise, and by suppressing the variations of lift-off and variations of channel sensitivity.

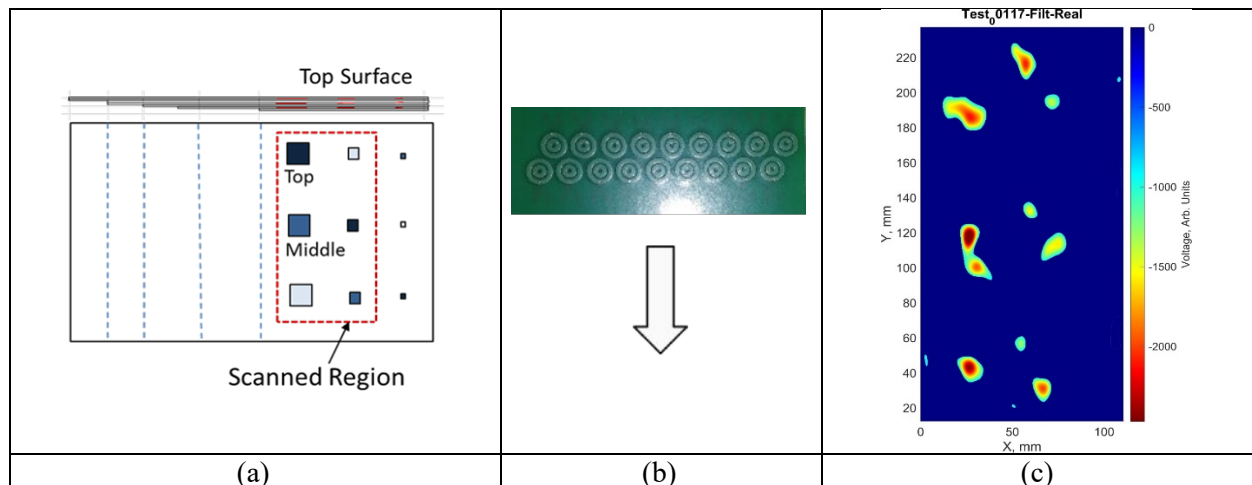


Figure 188. Validation of array probe C-3b on CFRP calibration sample #1: (a) locations of delaminations and scanned region; (b) direction of line scans; (c) typical C-scan (real part).

3.4. Dual-Mode Imaging (Inductive + Capacitive)

In Quarter VII, the MSU team proposed a new measurement technique (patent pending) that synergistically combines the benefits of inductive and capacitive sensing for rapid NDE of FRP composite structures. NDE of FRP is performed using arrays of hybrid (dual-mode) inductive/capacitive sensors. The hybrid array sensors are made of conductive electrodes deposited on multilayer printed circuit boards (PCB) with flexible substrates. Geometry of electrodes, respective electrode connections, and switching are optimized so as to provide: 1) eddy current imaging; 2) capacitive imaging; 3) uniform sensitivity to surface and subsurface flaws in all directions; 4) minimized sizes of the arrays; and 5) multichannel and multifrequency measurements for reduced inspection time.

3.4.1. Dual-mode sensing technique for NDE of FRP

Fiber damage and fiber irregularities in FRP are detected by configuring hybrid sensors as coil sensors. Similarly, matrix damage, matrix irregularities, and interlaminar delaminations are detected by configuring hybrid sensors as capacitive sensors. ECT and CI are performed sequentially by means of electronic switching. Hence, this procedure eliminates the need for mounting two separate sensor arrays on the probe.

ECT using coils furnishes information about local changes of the electric conductivity of FRP. On the other hand, CI using open-plate capacitors is a complementary modality, which is sensitive to local changes of the dielectric constant of FRP. Combining ECT and CI techniques together provide the necessary synergy to detect different types of flaws simultaneously (e.g., fiber breakage and interlaminar delaminations) that wouldn't be otherwise all detectable by only one technique.

Schematic design of a dual-mode sensor is presented in Figure 189. The sensor consists of two concentric coils that are adjacent to each other. The sensor operates in the ABS configuration by providing two independent inductive measurements and a single capacitive measurement as indicated in Figure 190. The open-plate capacitor is formed by connecting the windings of Coil 1 to a positive voltage terminal of the driver and the windings of Coil 2 to a negative voltage terminal of the driver. Thus, switching between the operation modes requires a MUX that is programmed according to the rules from Table 5.

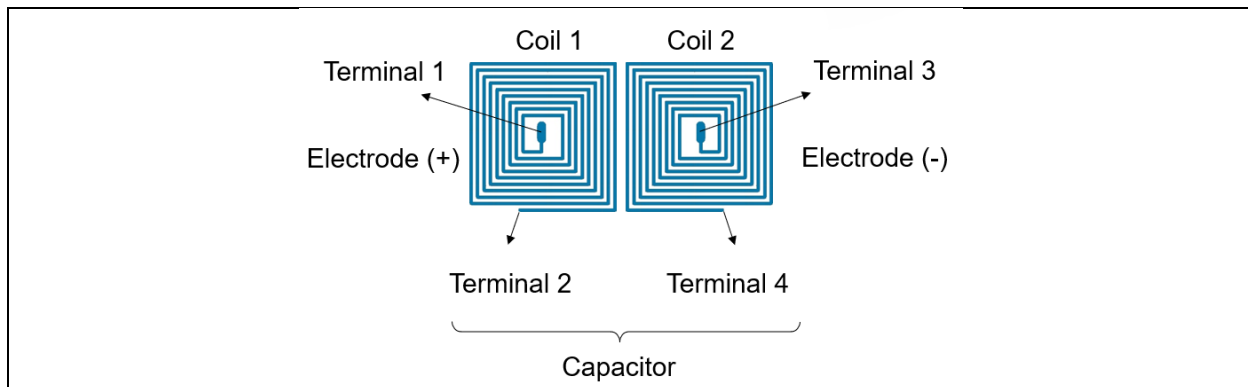


Figure 189. A dual-mode sensor comprising of two rectangular coils and one open-plate capacitor.

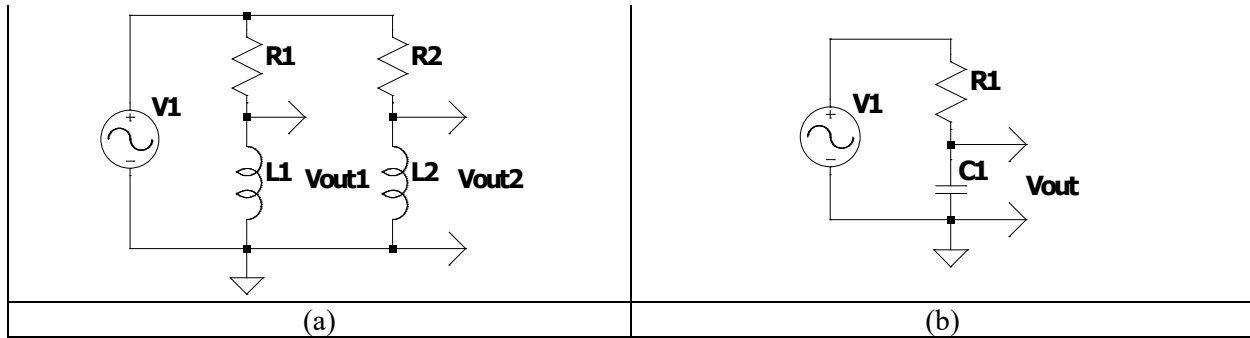


Figure 190. A circuit diagram for: (a) driving the rectangular coil sensors in the absolute mode; (b) driving the open-plate capacitor formed by two rectangular coils as electrodes.

	Terminal	Connection			Terminal	Connection	
	T1	R1			T1	R1	
	T2	Ground			T2	Open or T1	
	T3	R2			T3	Ground	
	T4	Ground			T4	Open or T3	
	(a)				(b)		

Table 5. Connections of terminals corresponding to: (a) driving two rectangular coil sensors; (b) driving the open-plate capacitor formed by two rectangular coils as electrodes.

3.4.2. Array implementation of dual-mode sensing

The array implementation of the dual-mode sensing NDE technique can be expanded to include axial (+45°) and transverse (-45°) capacitive channels. This concept is schematically illustrated in Figure 191. Hence, the dual-mode array shown in Figure 191 will furnish 18 ABS inductive measurements, 16 SDD axial inductive measurements, 16 SDD transverse inductive measurements, 9 axial capacitive measurements, and 8 transverse capacitive measurements in one pass. The initial PCB design of the probe D-1a is shown in Figure 192.

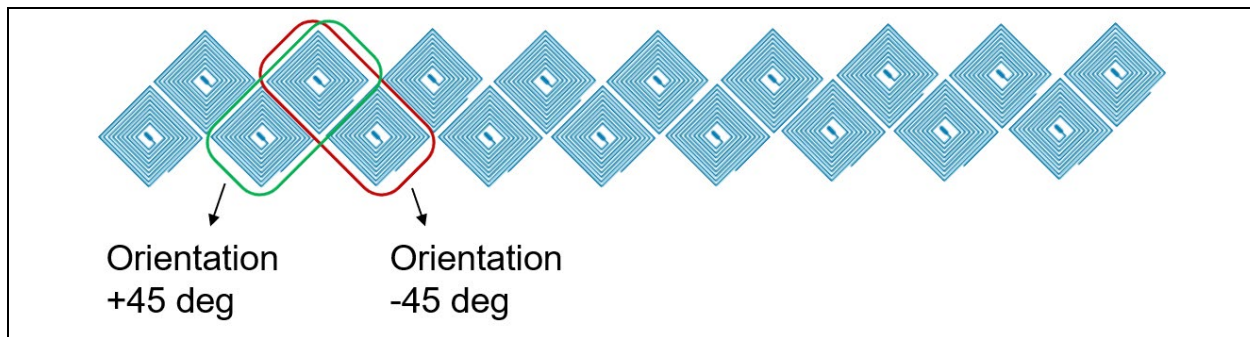


Figure 191. Dual-mode array sensor prototype: an array of rectangular coil/capacitive sensors that supports two orthogonal orientations of measurements. (An example of the open-plate capacitor with +45° orientation is highlighted as a green box. The open-plate capacitor with -45° orientation is highlighted as a red box).

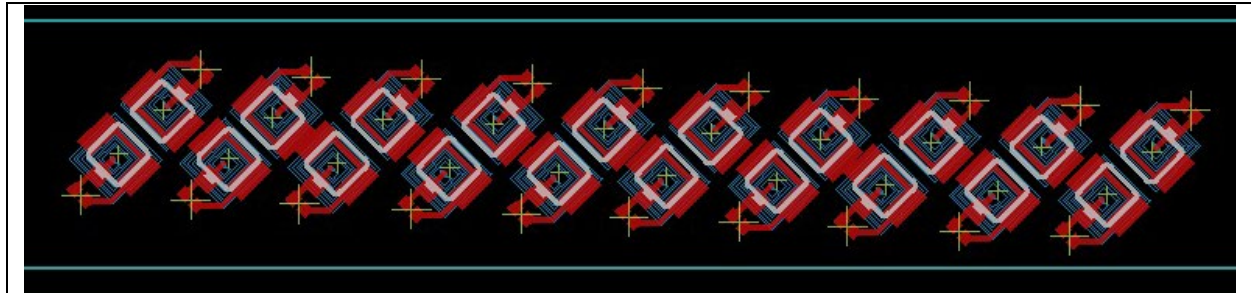


Figure 192. Possible PCB design of the array dual-mode sensor prototype.

3.4.3. MSU dual-mode probe for NDE of FRP composites

The dual-mode probe D-1a was fabricated for initial testing and concept validation. Hence, it had only 2 channels. The design of the dual-mode (hybrid) probe D-1a is shown in Figure 193. The salient feature of the D-1a is that it is suitable for inspection of both CFRP laminates (weak electrical conductors) and GFRP laminates (electrical insulators). The probe operates as a single transmitter and a dual receiver (STDTR). Hence, it consists of three coils. The driving coil is in the top PCB layer. The receiving coils are D-shaped and are in the bottom PCB layer. The receiving coils also have opposite windings. The STDTR configuration provides the capability to acquire multiple ECT measurements such as absolute (impedance), differential, transmit/receive (reflection), and differential transmit/receive. In addition, the D-shaped coils can be configured for CI measurements as an open-plate capacitor in order to enhance sensitivity of the probe to interlaminar delaminations in CFRP test samples.

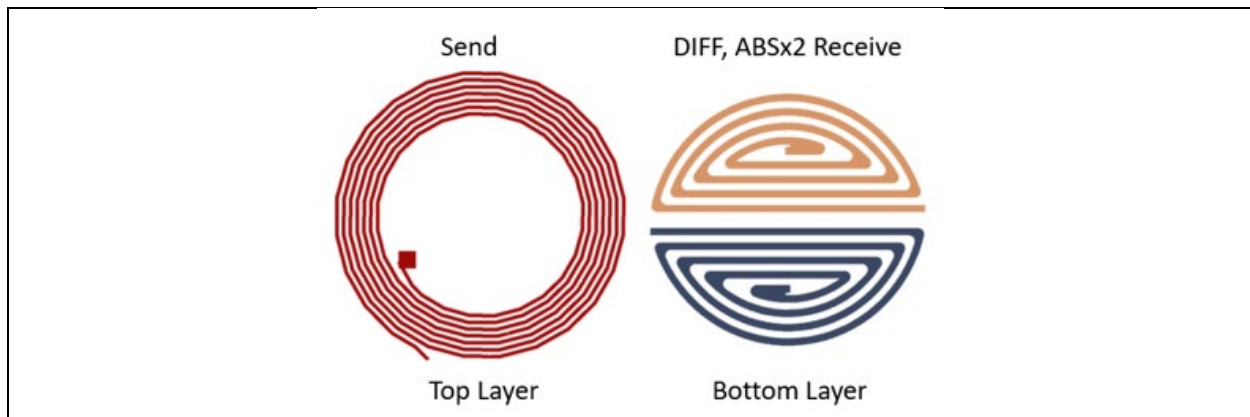


Figure 193. Design of the dual-mode (hybrid) probe D-1a (single transmitter / dual receiver).

The D-1a probe was fabricated with other array sensors on the same PCB as shown in Figure 194. Figure 195 shows a pair of the D-1a probes orthogonal to each other. For testing purposes, only one D-1a probe was activated, and its three coils were individually accessed using micro-BNC connectors. The OD of the driving coil was 9 mm. Since the D-1a probe had copper electrodes in both PCB layers, some extra connections to the micro-BNC ports needed to be soldered manually.

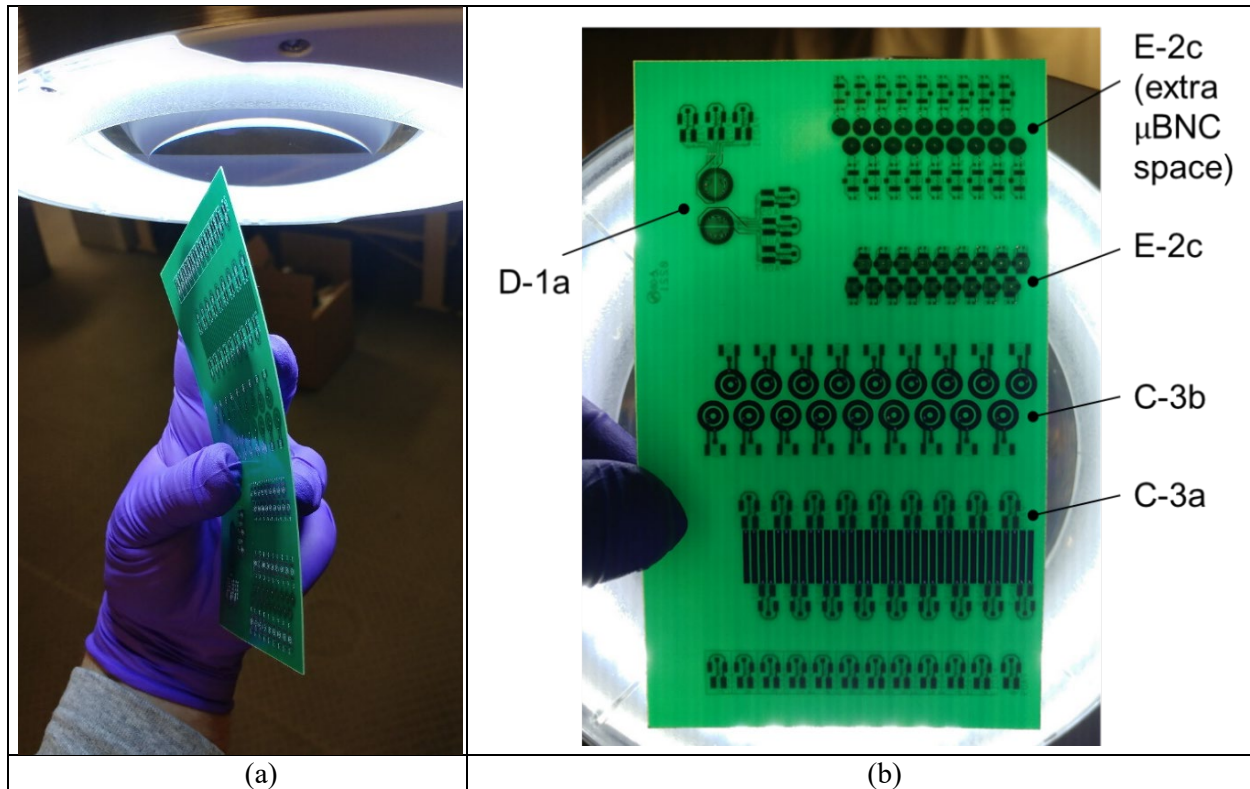


Figure 194. Fabricated 2-layer PCB with multiple sensors: (a) side view; (b) front view.

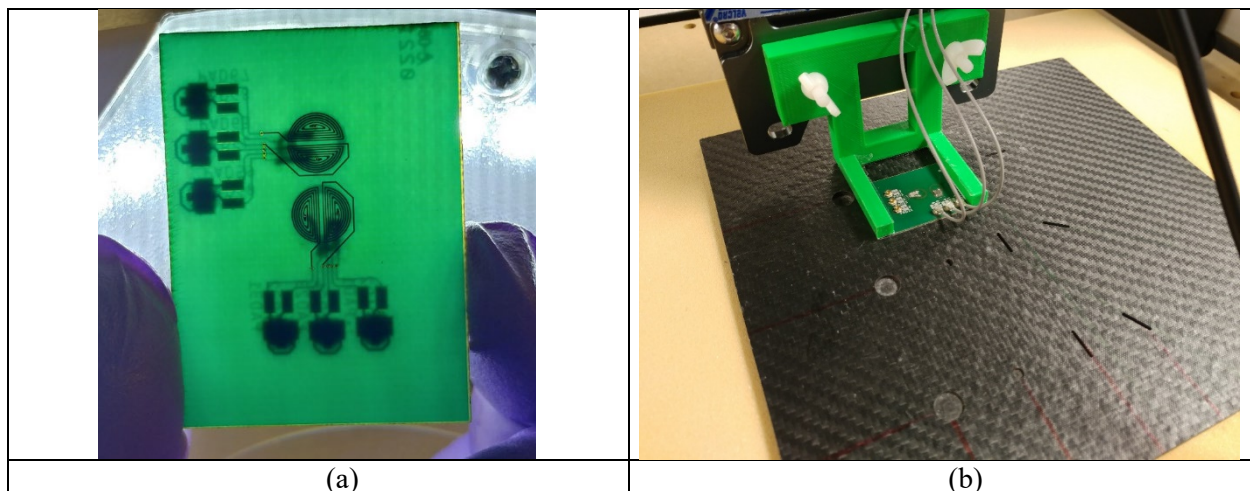


Figure 195. Fabricated hybrid probe D-1a: (a) PCB; (b) fixture and connectors.

Experimental validation of D-1a probe interfaced to Ectane's EET connector

D-1a in ECT mode; T/R 2 channels; STDR 1 channel; CFRP sample with fiber damage

The performance of the fabricated D-1a probe was first validated on the calibration sample #7 as shown in Figure 195b. The probe was interfaced to the Extended ET connector of the Ectane instrument. The driving coil was connected to a voltage source and receiving coils were connected to two separate data acquisition channels. Hence, two sets of transmit/receive measurements were acquired: one for the receiver coil 1 and

another for the receiver coil 2. This was done in order to verify that the coils were fabricated properly. The calibration sample #7 was raster scanned at 2 MHz with spatial resolution of 0.5 mm. C-scans corresponding to a Transmitter/Receiver 1 pair are shown in Figure 196, and C-scans corresponding to a Transmitter/Receiver 2 pair are shown in Figure 197.

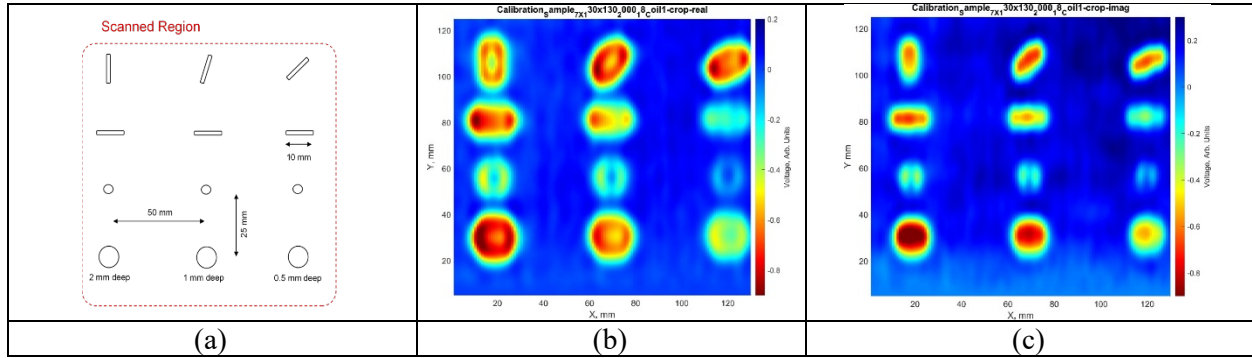


Figure 196. Validation of hybrid probe D-1a on CFRP calibration sample #7: (a) locations of notches; (b) receiver coil 1 (real part); (c) receiver coil 1 (imaginary part), $f = 2$ MHz.

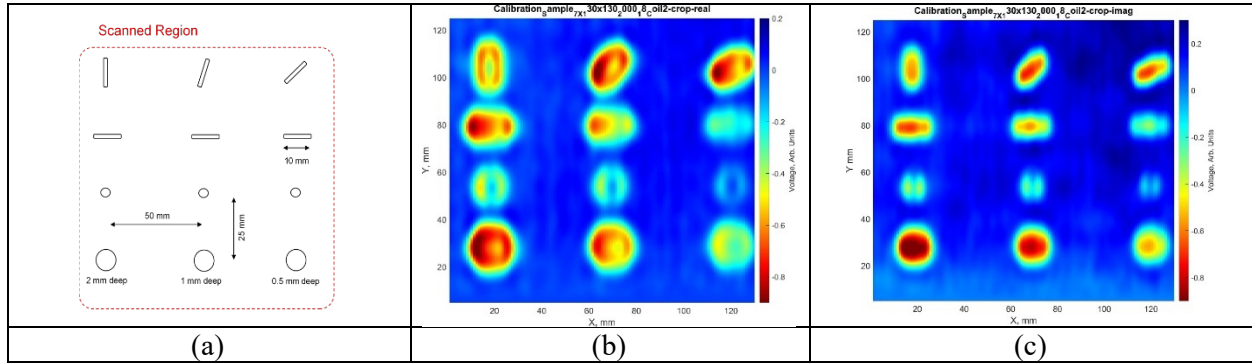


Figure 197. Validation of hybrid probe D-1a on CFRP calibration sample #7: (a) locations of notches; (b) receiver coil 2 (real part); (c) receiver coil 2 (imaginary part), $f = 2$ MHz.

The results demonstrated that transmit/receive measurements using the D-1a probe were highly sensitive to calibration notches on the CFRP test sample. C-scans corresponding to both transmit/receive pairs were nearly identical in amplitudes, which confirmed that receiver coil 1 and receiver coil 2 had similar impedances at the driving frequency. In addition, the images of the notches were shifted by ~ 1.5 mm since the D-shaped receiver coils were not in the geometrical center of the D-1a probe.

Figure 198 shows difference images in which the C-scans from Figure 197 were subtracted from the corresponding C-scan from Figure 196. Note that the C-scans in Figure 197 and in Figure 196 were normalized by their respective peak magnitudes prior to the subtraction. The C-scans in Figure 198 are analogous to a differential transmit/receive measurement [Driver/Coil 1 – Driver/Coil 2] that can be obtained experimentally by electrically connecting the receiver coils at a mid-point and by feeding the output to a single measurement channel. Such measurement reduces noise, and it is less sensitive to lift-off variations of the probe and temperature drifts. Moreover, the differential transmit/receive configuration may provide sensitivity to matrix defects in addition to carbon fiber breakage/imperfections. Figure 198b and Figure 198c demonstrate that real and imaginary parts of differential transmit/measurement have positive and negative lobes at calibration notches as expected for differential ECT images.

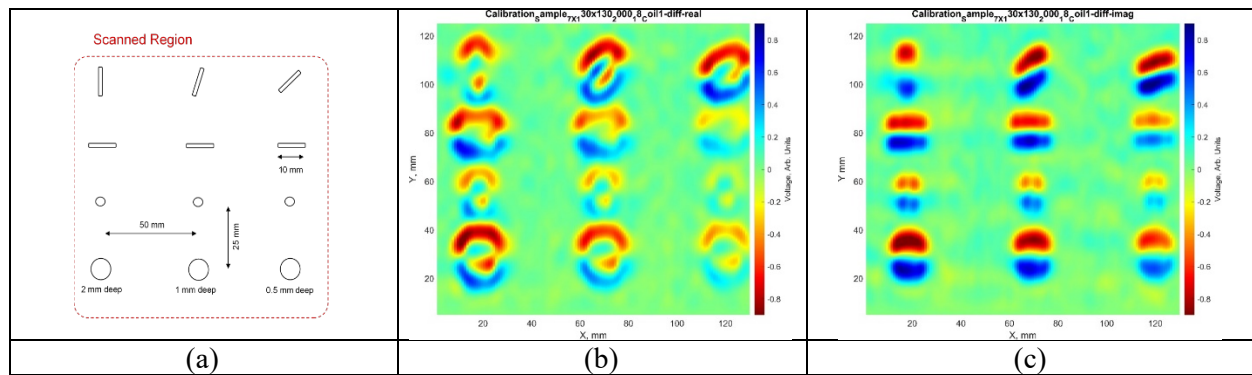


Figure 198. Validation of hybrid probe D-1a on CFRP calibration sample #7: (a) locations of notches; (b) difference [coil 1 – coil 2] (real part); (c) difference [coil 1 – coil 2] (imaginary part), $f = 2$ MHz. Images normalized by peak magnitude.

D-1a in ECT mode; STDR 1 channel; CFRP sample with interlaminar delaminations

Figure 199 presents validation of the D-1a probe on the calibration panel #1 with interlaminar delaminations of different sizes. The region with 6 delaminations was scanned as shown in Figure 199b. The sample was scanned at $f = 2$ MHz and with 2 mm spatial resolution. The D-1a probe was configured as differential transmitter/receiver. The resulting C-scan is shown in Figure 199c. The MSU image processing was applied in order to enhance defect signals by reducing the noise, and by suppressing the variations of lift-off. The results obtained in Figure 199 demonstrate that the D-1a probe is sensitive to interlaminar delaminations as well as to local variations of the electrical conductivity and dielectric constant of the test sample.

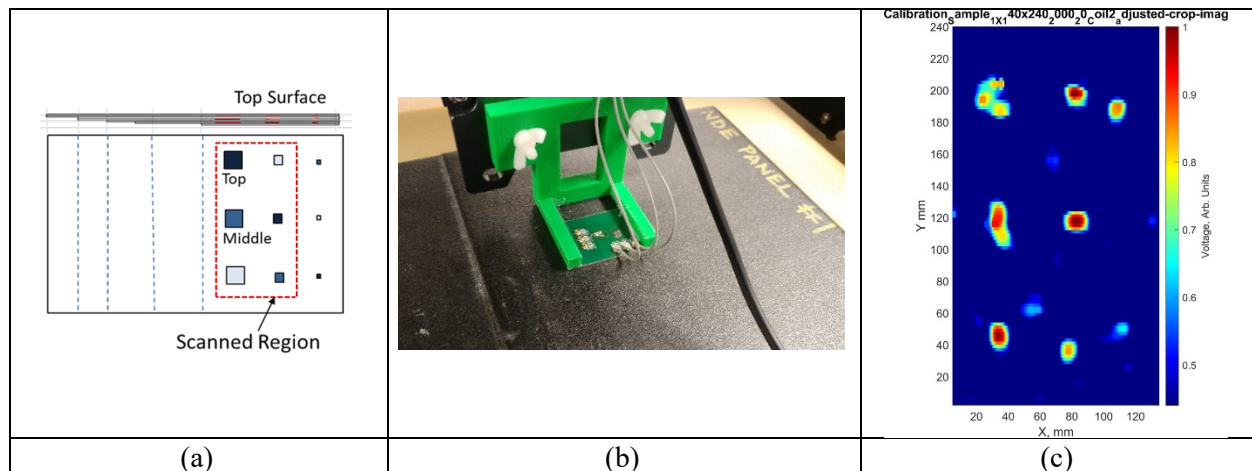


Figure 199. Validation of hybrid probe D-1a on CFRP calibration sample #1: (a) locations of delaminations and scanned region; (b) probe scanning the sample; (c) typical C-scan acquired in differential STDR mode, $f = 2$ MHz. Only positive lobes are shown.

D-1a in CI mode; ABS 1 channel; CFRP sample with interlaminar delaminations

In this experiment, the D-1a probe was configured as a capacitive sensor in ABS mode as explained in Figure 189 and Figure 190b. A raster scan was performed on calibration panel #1 with resolution of $1 \text{ mm} \times 0.2 \text{ mm}$. The measurements were acquired at $f = 1 \text{ MHz}$. The resulting C-scan is shown in Figure 200c. The MSU image processing was applied in order to enhance defect signals by reducing the noise, and by suppressing the variations of lift-off. The obtained results showed that the D-shaped coils could be successfully used as electrodes for the capacitor in the dual-mode inspection. The D-1a probe in its CI configuration was also sensitive to interlaminar delaminations as theoretically predicted.

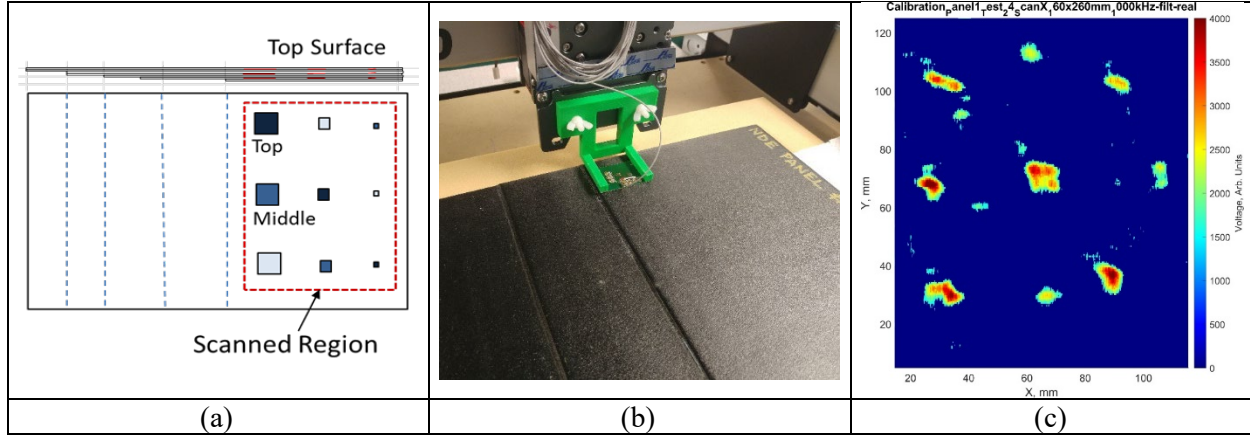


Figure 200. Validation of hybrid probe D-1a on CFRP calibration sample #1: (a) locations of delaminations and scanned region; (b) probe scanning the sample; (c) typical C-scan in CI mode, $f = 1 \text{ MHz}$.

D-1a in ECT mode; T/R 1 channel; GFRP sample with volumetric defects

In contrast to previous validation studies with the D-1a probe, the test sample #8 in the current experiment was made of GFRP composite with zero electric conductivity ($\sigma = 0 \text{ S/m}$). The sample was 16 mm thick and had 9 circular cuts of different sizes and depths as shown in Figure 201a and Figure 201b. It was anticipated that the ECT inspection using coil sensors wouldn't render any results, since there would be no eddy currents induced in the GFRP.

The D-1a probe was configured as a T/R sensor, in which the round coil in the top layer was used as a transmitter and one of the D-shaped coils in the bottom layer was used as a receiver for field pick up. A raster scan was performed with resolution of $1 \text{ mm} \times 0.2 \text{ mm}$, and the measurements were acquired at $f = 2 \text{ MHz}$. Corresponding C-scan is presented in Figure 201c. The results demonstrated that there was no variation in the measured voltage on the receiving coil. Hence, the D-1a probe should be configured as a capacitor in order to register defects in the non-conductive GFRP sample.

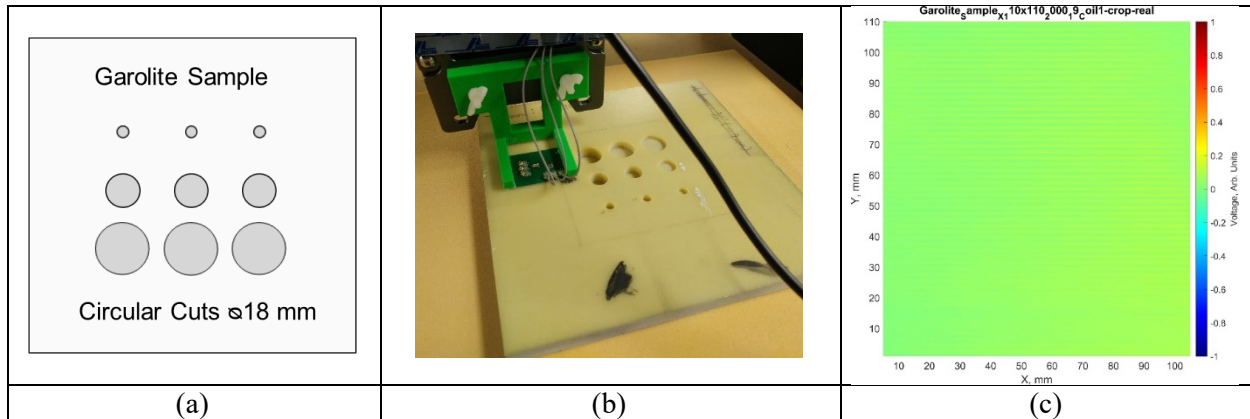


Figure 201. Validation of hybrid probe D-1a on GFRP calibration sample #8: (a) locations of delaminations and scanned region; (b) probe scanning the sample; (c) typical C-scan in T/R mode, $f = 2$ MHz, real part.

D-1a in ECT mode; T/R 1 channel; GFRP sample with volumetric defects

Figure 202 presents validation of the D-1a probe in CI mode on the GFRP calibration panel #8. A raster scan was performed at $f = 1$ MHz with resolution of $1 \text{ mm} \times 0.2 \text{ mm}$. The probe was configured as an ABS capacitor. In contrast to the ECT mode, the CI mode provided good sensitivity to the volumetric flaws in the electrically insulating GFRP as shown in Figure 202c. All calibration holes were successfully detected. However, the images of the defects were doubled. Image doubling occurred owing to the micro-BNC connector solder pads added to the PCB for the ease of interfacing the D-1a probe with Ectane's EET connector (see Figure 195a). The solder pads acted as extra capacitors and will be removed in the future designs of dual-mode probes.

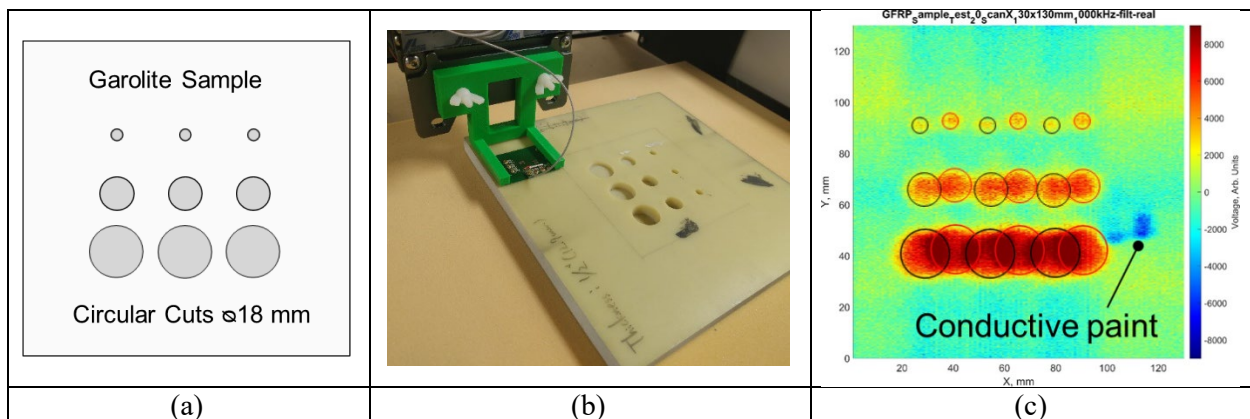


Figure 202. Validation of hybrid probe D-1a on CFRP calibration sample #8: (a) locations of delaminations and scanned region; (b) probe scanning the sample; (c) typical C-scan in CI mode, $f = 1$ MHz, real part.

4. ROBOTIC NDE PLATFORM

The MSU team developed a robotic platform for high-speed multi-technique NDE of automotive parts. The main goal behind the development of the platform was to overcome the limitations of the previously designed XYZ gantries, which were largely applicable only for scanning flat composite samples or samples with small curvatures. Placing acoustic and electromagnetic sensors on robotic manipulators helped to follow large curvatures and enabled the capability of NDE of parts with complex shapes.

4.1. Robotic NDE Platform Development

4.1.1. Robotic NDE platform design

A schematic from the CAD drawing of the platform is shown in Figure 203. The platform was designed to have a pair of 6-axis robots that could either operate independently or could be synchronized using a PC interface. The test part was attached to a holder or a table, which was placed in the center of the platform where robot envelopes overlapped. Robot motion range was large enough so that the test sample could be reached by both arms. The base of the platform and fixturing for composite parts were proposed to be designed using standard profiles. Such platform design allows for implementing SSA-ACUT, TT-ACUT, and EM NDE techniques for FRP samples of complex shapes.

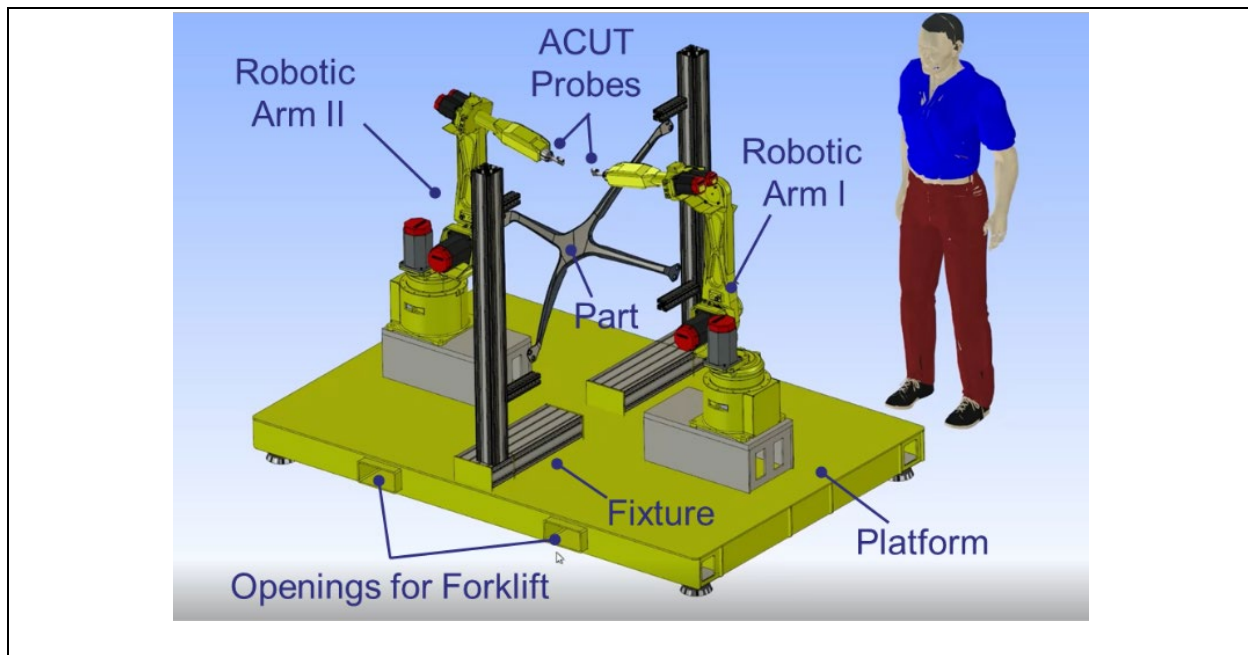


Figure 203. Design of the robotic platform for high-speed ACUT and EM NDE.

In the case of the SSA-ACUT or EM inspection, the arms are able to scan the test sample independently from different sides without real-time synchronization of their positions. The sample scan surface could be partitioned into non-overlapping subregions with different subregions assigned to different arms in order to scan in parallel and reduce the inspection time. In the case of the TT-ACUT, the transmitters would be attached to the master arm and the receivers would be attached to the slave arm in order to excite the ultrasonic waves on one side of the test sample and sense the through-transmitted waves on the opposite side. The scan paths of the robotic arms would need to be actively synchronized via a script, since the ACUT transmitters and receivers need to be accurately aligned.

4.1.2. Acquisition of robotic manipulators

MSU purchased two pre-owned industrial robots Fanuc ArcMate 100iB with R-J3iB motion controllers. Table 6 provides detailed specifications of the acquired manipulators. Fanuc's ArcMate series were used previously as high-precising and high-dexterity 6-axis welding robots that fit the requirements of the Project. Each axis of the robotic arm could move with high angular speeds, and the max linear speed was 2000 mm/s. In addition, the end effectors could carry payloads up to 6 kg, which was perfect for rapid ACUT NDE.

Robot Specs		Axis		
Value/Type		Speed		
Axes		Motion Range		
Payload		J1	150 °/s (2.62 rad/s)	±165°
H-Reach		J2	160 °/s (2.79 rad/s)	+135° - 75°
Repeatability		J3	170 °/s (2.97 rad/s)	+150° - 140°
Robot Mass		J4	400 °/s (6.98 rad/s)	±190°
Structure		J5	400 °/s (6.98 rad/s)	±140°
		J6	520 °/s (9.08 rad/s)	±320°

Table 6. Specifications of the acquired Fanuc ArcMate 100iB robots: (a) general; (b) angular speeds and motion ranges of the axes.

The MSU team outsourced the platform manufacturing and robot refurbishment to Slipstream LLC (Chattanooga, TN) in order to speed up NDE technology development. In Quarter III, the robots were transported to Slipstream for major cleaning, testing, maintenance, and repairs (see Figure 204). The MSU team made a trip to Slipstream in order to help with platform development and to receive training in robot handling, control, and programming.

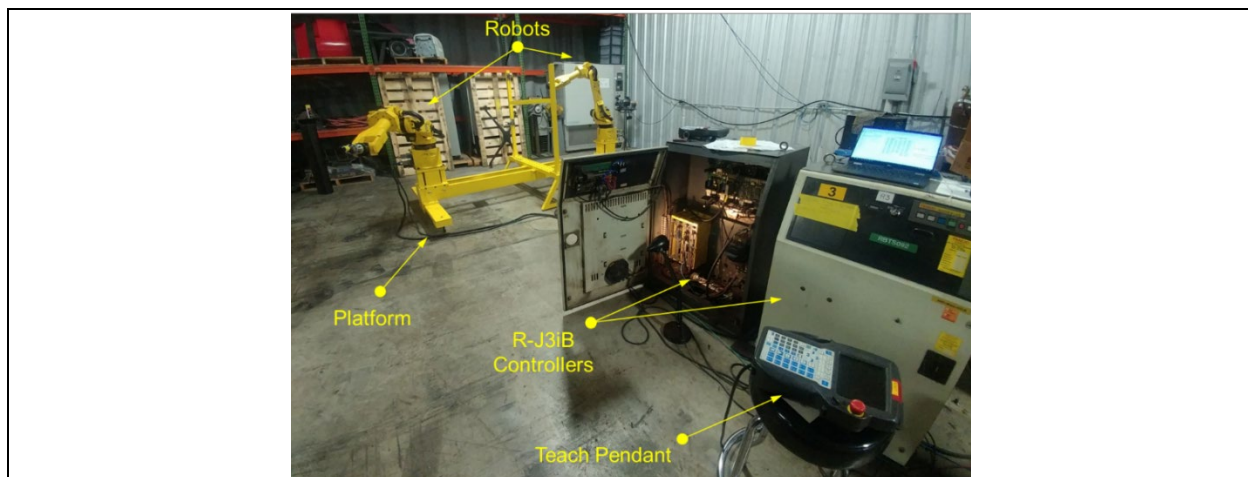


Figure 204. Robotic platform assembly and testing at Slipstream Technologies' warehouse (Chattanooga, TN).

4.1.3. Installation of robotic workcell at MSU/CVRC

In Quarter IV, the robotic platform was delivered to MSU/CVRC. MSU allocated lab space for dual robots and developed detailed floor plans of the surrounding environment. A robotic workcell was created as shown in Figure 205, and 3-phase 480V power lines were installed in order to power up the robots with controllers. The MSU team also replaced grease in robot joints and touch up painted the frames. Both robots

where zero mastered and calibrated.



Figure 205. Installation of robotic workcell at MSU/CVRC (Lansing, MI).

Workcell safety features

Multiple safety features were added in order to establish a safe workcell. These included: 1) physical barriers; 2) floor markings indicating the boundaries of robot envelopes; 3) mechanical and electrical safety signs; 4) 3-color tower light indicating different regimes of robot operation; 4) extra emergency stop buttons, and 5) special insulating tools for handling 480V bus boxes.

The MSU team acquired the necessary documentation from Fanuc regarding robot handling, programming, and maintenance. The user manual describing the standard operating procedures (SOP) in the workcell was written by the principal investigators (PI) and was later approved by the MSU Environmental and Human Safety (EHS) Department.

Core software upgrades and PC driver

The necessary hardware components (e.g., cables, PCMCIA memory cards, adapters) and software packages were purchased in order to establish a PC interface with one robot controller. The ArcTool V6.4 core software, which was originally installed on the R-j3iB, was replaced with the Handling Tool V6.4 software. The upgrade was necessary, since only Handling Tool V6.4 supported all Fanuc software packages required to control the robot via a PC. The software packages ordered from Fanuc included: 1) socket messaging; 2) PC interface; 3) KAREL; 4) ASCII upload; 5) ethernet IP; 6) singularity avoid; 7) motion optimization, and many others.

The MSU team selected the Fanuc PC development kit (PCDK) as a driver for robot controllers, since it provided all necessary functionality to control robot moves, change system variables/registers, and query the coordinates of the end effector in real-time. The C# version of Fanuc PCDK was used to establish ethernet data transfer with the R-j3iB. Since the update time of R-j3iB was 8 ms, the robot state could be queried at a maximum rate of ~125 Hz.

4.2. Robotic NDE Pipeline

A robotized inspection of automotive parts is a multi-step process, and is more complex compared to NDI using XYZ gantries. The robotized NDE implemented by the MSU team included the following steps:

- 1) Obtain/Reconstruct outer surfaces of the inspected part
The simplest way to accomplish this task is to use CAD drawings provided by the manufacturer. However, if the CAD drawings are not available, 3D reconstruction of part's surfaces using stereo cameras is an alternative option. Stereo cameras are attached to the robots that pre-scan the part before running the inspection.
- 2) Generate optimal toolpath for the NDE sensor
This task is accomplished using the MSU team's developed scripts. Tool paths on complex geometries can be also generated using commercial software (e.g. SprutCAM).
- 3) Generate/Upload/Run robot program & Acquire NDE data
For independent robot operations, the KAREL and Teach Pendant programs are compiled and uploaded to the controllers using the RoboDK API. For synced motions, robots are controlled via Fanuc PCDK. Data acquisition using the NDE sensors is always synced with robot position.
- 4) Visualize & Process NDE data
Inspection data is represented as a colorized point cloud or a mesh with colored surfaces. Data rendering is performed using the CloudCompare library.

A detailed description of the MSU team's robotic NDE and developed software modules is provided below.

4.2.1. Part's profile reconstruction using stereovision

MSU acquired an Intel RealSense D435i stereo depth camera system for experiments with part's profile reconstruction (see Figure 206a). The stereo depth cameras operate based on the principles shown in Figure 206b. The distance between the optical camera centers is called the stereo baseline. The overlapping area of both images contains the same information observed from slightly different views defined by the stereo baseline as presented in Figure 206b (left). The resulting optical parallax of corresponding points in both stereo images is used to calculate depth information, which is inversely proportional to the parallax as shown in Figure 206b (right). Multiple snapshots of the structure are taken for the 3D reconstruction of the imaged surface (see Figure 206c).

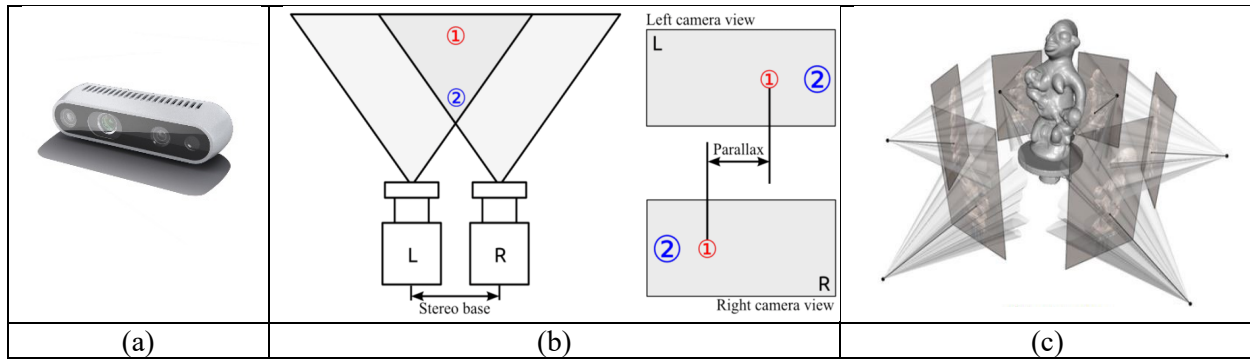


Figure 206. Part profile reconstruction using a stereo camera: (a) Intel RealSense D435i stereo depth camera; (b) principle of a stereo camera setup (adapted from S. Grehel *et al*, 2015 <https://www.researchgate.net/publication/303307354>); (c) reconstruction using multiple view angles.

Figure 207 depicts the implementation of the surface reconstruction using dual robots and stereographic imaging. Both robotic arms move along the predefined target positions on the imaginary sphere encapsulating the part. A few depth images are taken and are merged together in order to form a single RGB/depth point cloud using the OpenTK library. Part surfaces are extracted from this data using the CloudCompare library.

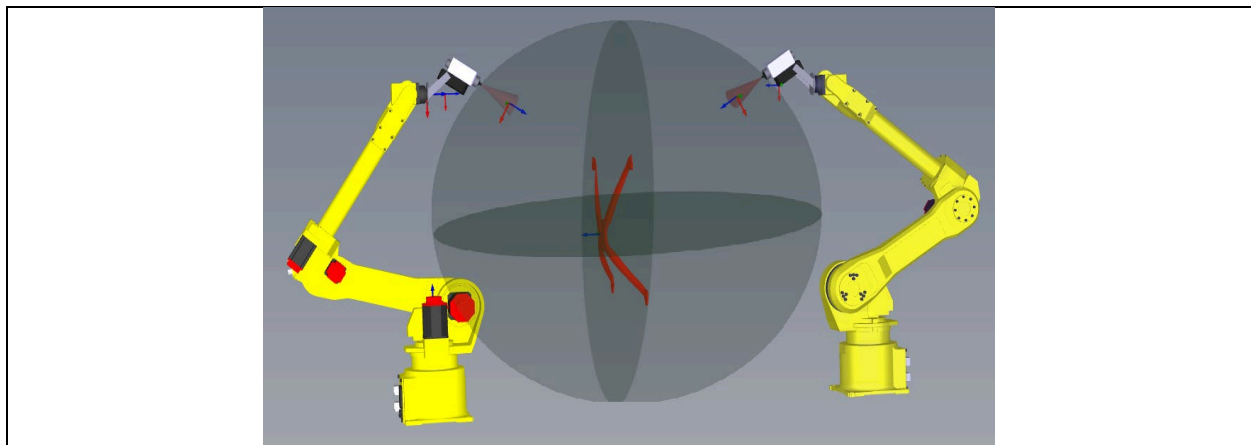


Figure 207. Stereo cameras taking depth images of the test part at a few locations on the imaginary sphere that encapsulates the test part.

Figure 208 shows the validation of the depth imaging using the Intel RealSense D435i stereo camera. Images of student's face are taken when the position of the camera is fixed, and the camera can be only rotated about its axis slightly. Holes in the images can be patched by moving the camera to other positions and appending the point cloud with new data.

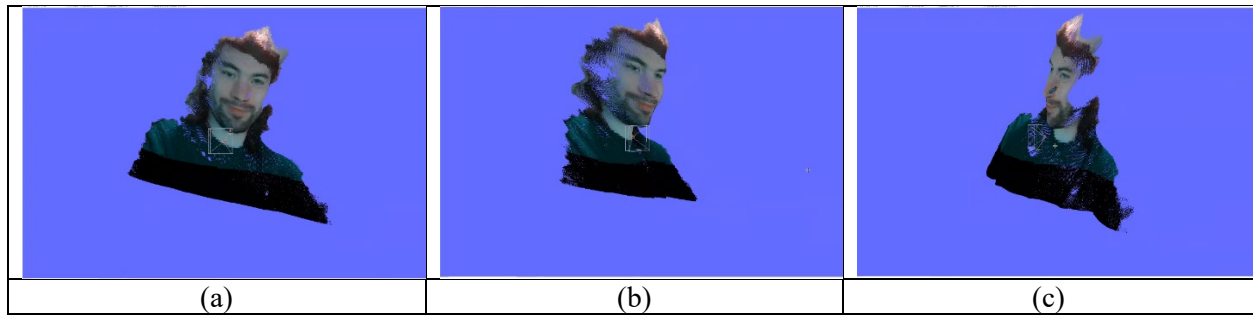


Figure 208. Reconstructed 3D face profile using stereo camera rotation at a fixed position: (a) front view; (b) view from the left; (c) view from the right.

Examples of 3D stereo images of CFRP parts from Phase I of the Project are presented in Figure 209. The stereo images were acquired from a few snapshots around the parts, and image data were merged using the iterative closest point (ICP) algorithm.



Figure 209. Stereo images of CFRP parts: (a) composite panel #3; (b) composite panel #4 (front splitter section) with embedded honeycomb structure.

4.2.2. Automated toolpath generation for NDE sensors

The MSU team developed a custom algorithm for scan path generation on 3D surfaces. As a first step, the algorithm seeds position targets on part's surfaces by intersecting the surfaces with multiple rays as shown in Figure 210a. In the second step, the targets are sequentially connected to each other such that a continuous scan path is created. Current version of the algorithm supports two options to connect the targets: 1) traveling salesman, and 2) zig-zag. The traveling salesman would join the targets with the goal to minimize the overall scan path length. In contrast, the zig-zag option would provide uniform motion pattern, which is better suited for the NDE array probes. An example of generated zig-zag is presented in Figure 210b.

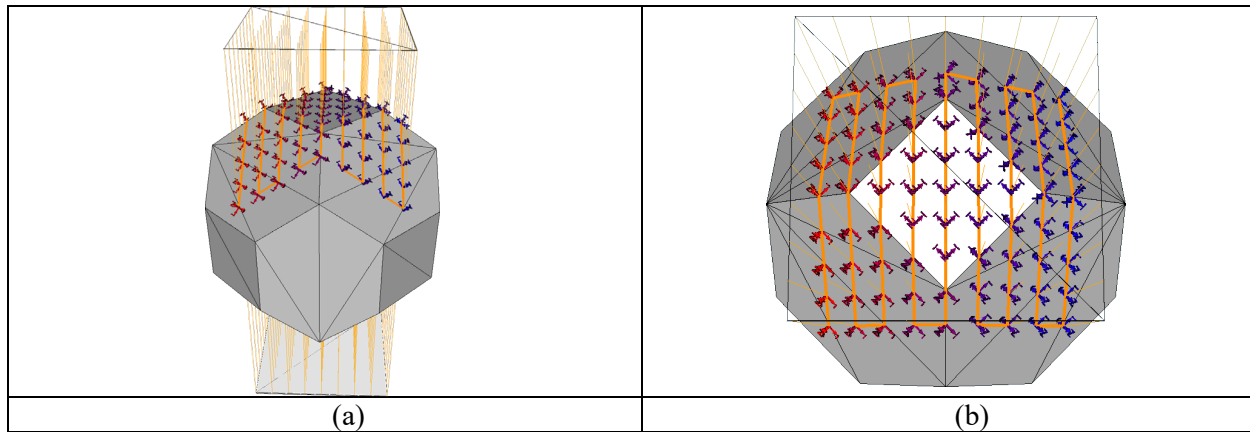


Figure 210. Zig-zag scan pattern formed by rays intersecting a 3D test object: (a) front view; (b) top view.

The biggest advantage of a zig-zag pattern is the user-controlled offset between the scan lines (distance between the vertical orange line scans in Figure 210b). The offset can be set so as to match the required spatial coverage of the ACUT or EM array probes. In addition, the offset stays fixed during the whole scan, which helps avoid over-sampling or under-sampling. However, one of the drawbacks of the zig-zag pattern is that it would have multiple transitions between the lines when scanning narrow parts. This drawback may limit the maximal speed that the end effector could reach between the scan targets.

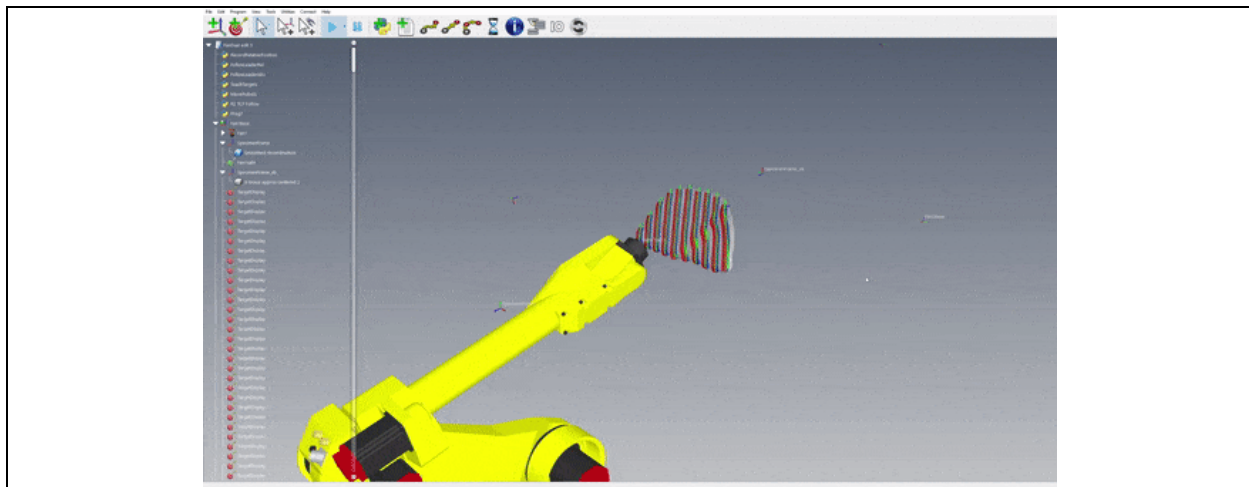


Figure 211. A demo showing a zig-zag tool path for composite panel #4. Simulation executed in RoboDK for Fanuc Arc Mate 120iB robot with no sensor attached to the end effector.

The MSU team's zig-zag path planning algorithm applied to a 3D surface profile of a CFRP composite panel #4 is shown in Figure 211. Figure 211 contains a gif demo showing the execution of a typical zig zag in the RoboDK. Note the robot doesn't have a sensor attached to its end effector, and the axis of the end effector (Joint #6) stays normal to the surface of the sample at every target position. The surface of the part is given by the stereo image from Figure 209b.

4.2.3. Execution of scan programs and parallel data acquisition

The MSU team developed scripts for controlling Fanuc robots using an industrial PC and successfully merged them with respective codes for controlling the NDE instruments (e.g., Sonoair pulser-receiver). The scripts were written in C# language and utilized the RoboDK API as well as the Fanuc PCDK. Both standalone single robot operations and synced dual-robot operations were supported. The MSU team could successfully create Teach Pendant (TP) programs as well as KAREL programs for robot controllers.

TP programs are human readable programs that can be executed from a teach pendant step by step. TP programs provide versatile tools for robot control and can be easily written by an operator without having access to a PC. On the other hand, KAREL is a complicated low-level programming language that provides access to all sorts of useful built-ins for things the user may not be able to do with TP. For KAREL programs, the source must be translated from a KAREL source file (.KL) into p-code (.PC) before it can be loaded and executed on the controller. Once a KAREL program has been loaded onto the controller, it acts like a black box; and the user can't step through it like a TP program.

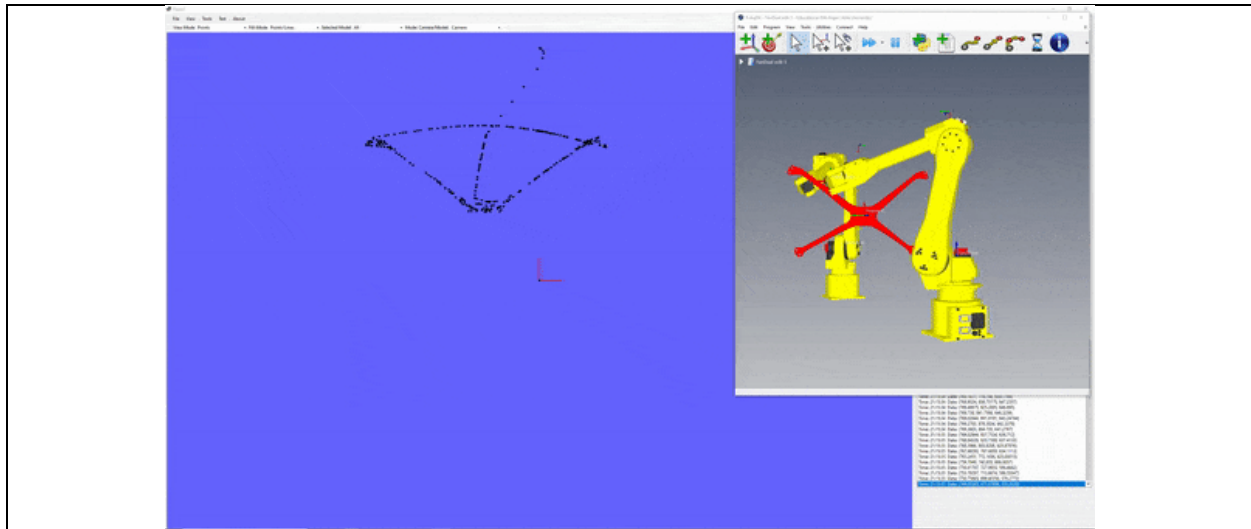


Figure 212. MSU software (based on RoboDK API and OpenTK) for scan simulation and real-time data display: main window – 3D point cloud showing scan positions of the lead end effector; insert – dual robots scanning the X-brace.

Figure 212 shows the snapshot from the real-time RoboDK simulation, in which two robotics arms synchronously scanned the X-brace part. Since there was no NDE data generated, the simulation only outputted the target xyz -positions of the lead end effector as a data cloud. The data cloud was visualized in 3D using the OpenTK library. The follow robot was synchronized with the lead robot such that both end effectors were aligned. After a move was completed by the lead robot, the script ensured that target positions of both robots were matched prior to executing the next move from the sequence. The number of target positions in each scan line or curve could be adjusted so as to provide the required synchronization accuracy and motion speed. When working with real Fanuc robots equipped with multiple ACUT and/or EM sensors, the cloud would contain data points from multiple sensors. Hence, the XYZ coordinates and rotations of the tool center point (TCP) also should be saved.

4.2.4. 3D data rendering and defect detection

The MSU team developed scripts for rendering the inspection scan data in 3D using the CloudCompare library. Figure 213a shows the pseudo-colored point cloud with XYZ coordinates from robotic scan simulation. Green points in the synthetic data simulate defect-free material and a white MSU logo simulates a defect. In order to provide a smooth image of part's surface, a triangular mesh is created using Delaunay's triangulation technique. Faces of the triangular elements are colorized based on the point values at respective vertices. A processed 3D image is shown in Figure 213b. This display is going to be provided in the updated version of the GUI, so that the user could easily drag, rotate, and zoom the images acquired after the nondestructive inspection of complex parts.

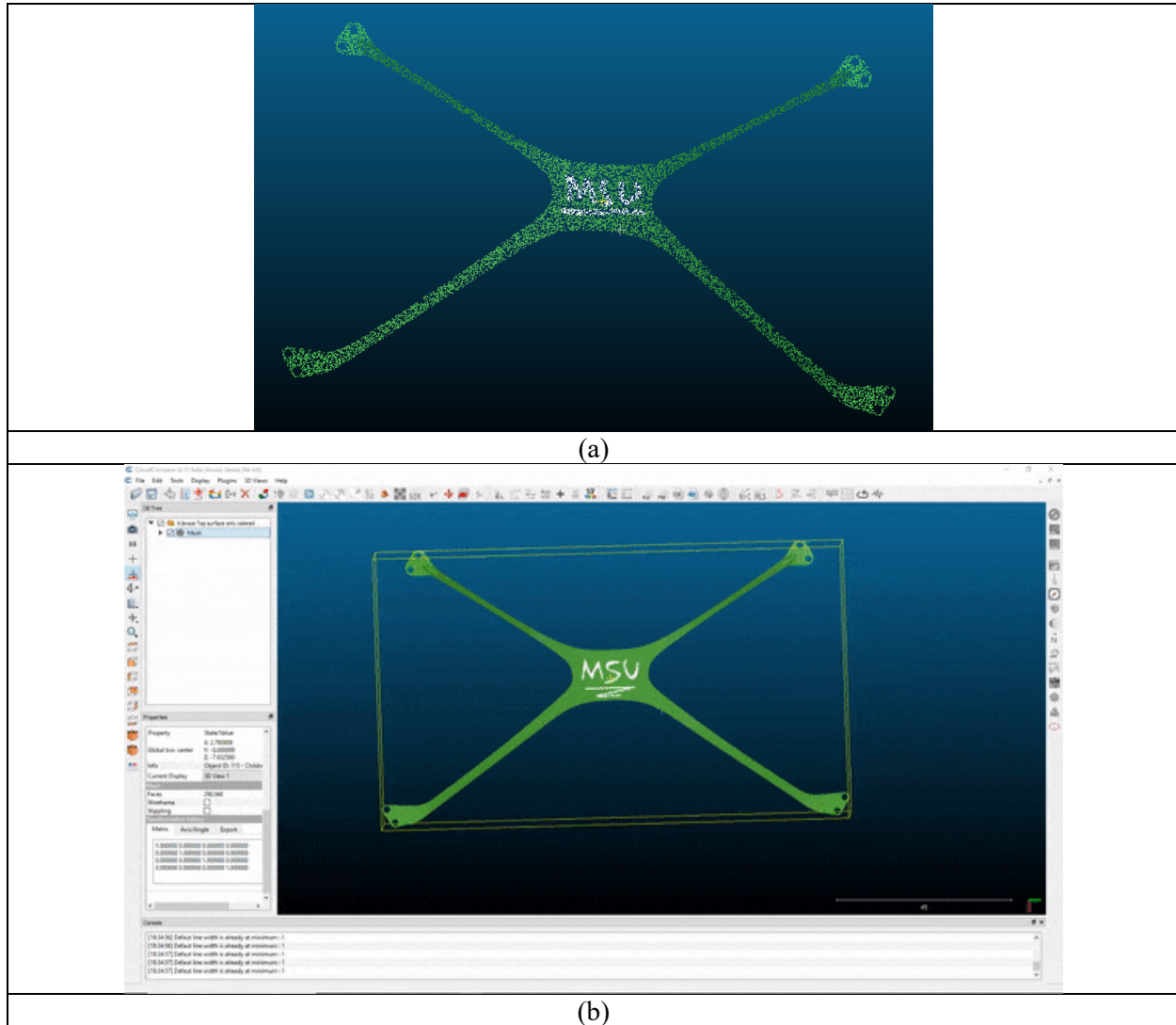


Figure 213. MSU 3D visualization of simulated scan data: (a) point cloud; (b) gif demo of the colored surface obtained after Delaunay triangulation.

4.3. Robotic SSA-ACUT

4.3.1. ACUT hardware and software integration with robotic platform

In Quarter VIII, the MSU team installed the acoustic sensors on one robotic arm in order to implement the single-side access ACUT NDE. The industrial PC and Sonoair pulser-receiver were placed on a movable rack stand, and ACUT cables were routed along the robotic arm as shown in Figure 214a and in Figure 214b. The fixtures for ACUT probes had bolted joints that allowed for manual adjustment of the angle of attack in 15° increments (see Figure 215). Attaching adjustable fixtures to robot flanges helped to avoid motion singularities since joints #6 were kept at 30° w.r.t. their zero joint coordinates. The MSU team also designed holders for ACUT preamplifiers, which were kept close to the ACUT probes.

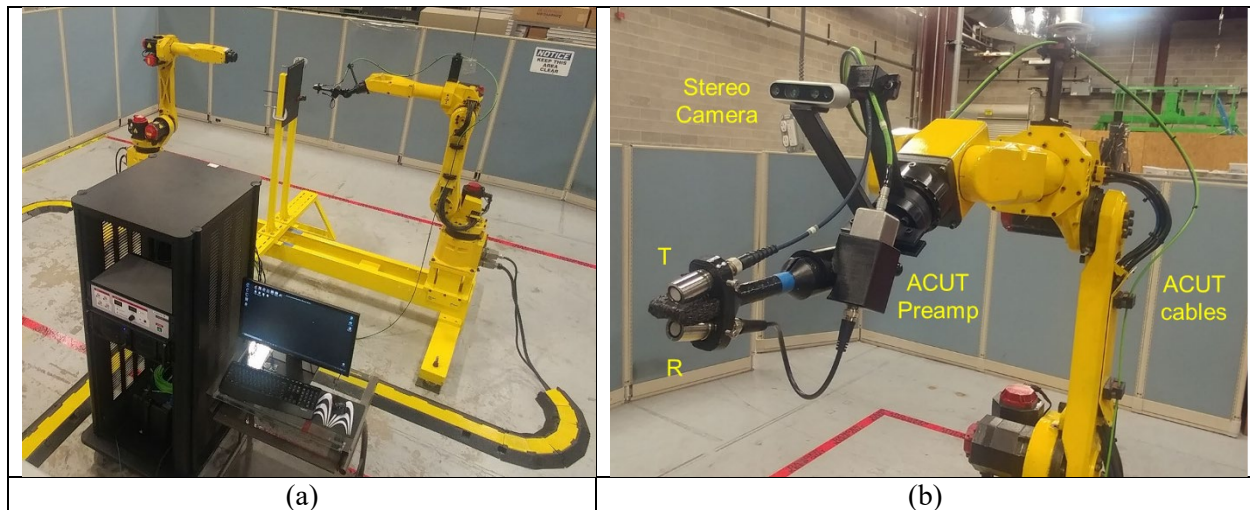


Figure 214. Robotic workcell configured for 1 channel single-side access ACUT NDE: (a) rack stand with ACUT hardware; (b) ACUT fixturing, probes and the preamplifier attached to the robot flange.

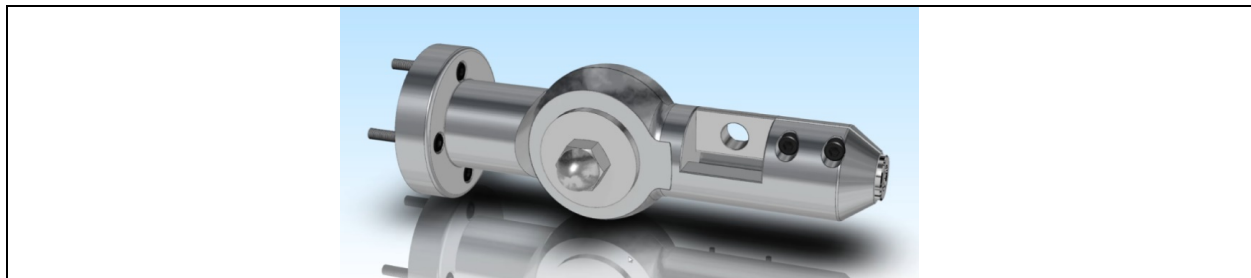


Figure 215. Aluminum fixtures for ACUT probes with adjustable angle of attack.

The MSU team developed scan software, which implemented path planning and synchronized the ACUT data acquisition with robot world coordinates. The TP and KAREL files for R-j3iB controllers were generated programmatically. The MSU team configured multiple robot settings (e.g., user/tool frames, position registers, collision guard, continuous moves, etc.) for seamless operation and smooth motion of the ACUT probes.

4.3.2. Experimental validation of robotic SSA-ACUT

Robotic SSA-ACUT inspection of CFRP calibration panel #1 (1 channel)

The robotic SSA-ACUT setup was first validated on the CFRP calibration panel #1. The panel was scanned using a 1-channel probe as shown in a video in Figure 216. A raster scan was acquired with 2 mm resolution. The ultrasonic actuator was driven at 250 Vp and at $f = 200$ kHz. The pulse repetition frequency (PRF) was 60 pulses/s. The angle of wave incidence was adjusted such that the fundamental A0 mode was excited in the test sample. Measured ultrasonic signals were band-pass filtered and time gated in order to extract the amplitude data.

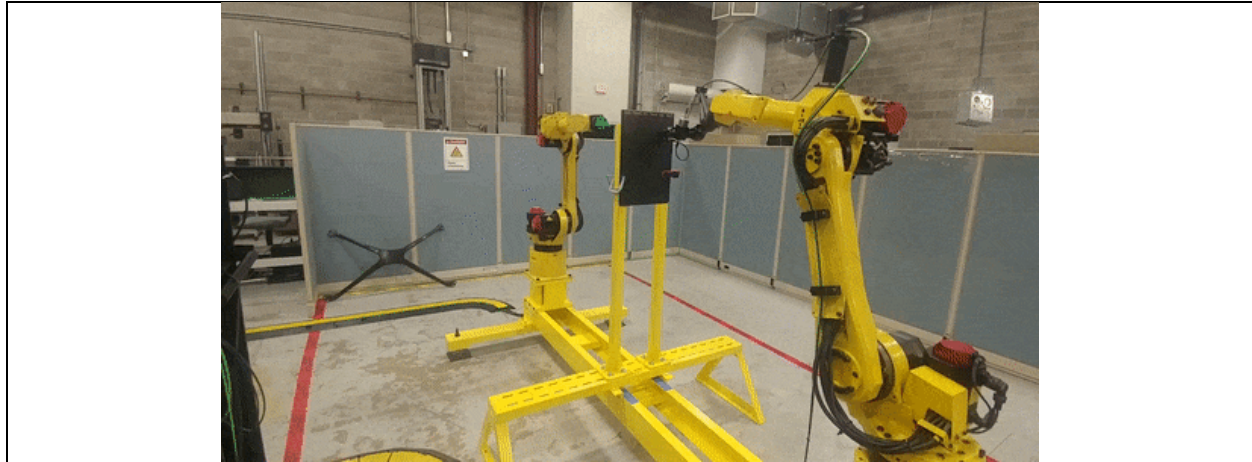


Figure 216. Robotic SSA-ACUT scan of calibration panel #1 (1 channel).

The corresponding results are presented in Figure 217. All interlaminar delaminations in the panel were successfully detected using the SSA-ACUT technique. Hence, the SSA-ACUT demonstrated good capability for robotic NDE

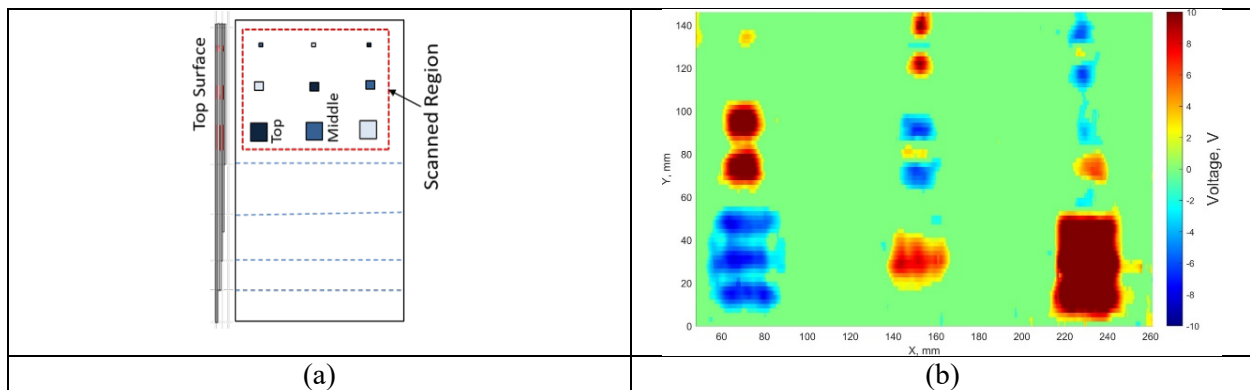


Figure 217. Robotic SSA-ACUT results on CFRP panel #1: (a) sample geometry showing scanned region and location of interlaminar delaminations; (b) C-scan at 200 kHz after automated MSU image processing (1 channel).

Robotic SSA-ACUT inspection of CFRP X-brace #3 (1 channel)

The robotic SSA-ACUT was validated on CFRP test samples with curved geometries. X-brace #3 with embedded defects was chosen for NDE. Surface profile for path planning was extracted from the CAD model. Horizontal and slanted zig-zag scan paths were programmed for Fanuc robot, which demonstrated flexibility of the MSU team's developed software.

Horizontal zig-zag

Figure 218 shows the RoboDK simulation of the scan process using the horizontal zig-zag pattern. Note that the central axis of the SSA-ACUT probe was collinear with the surface normal of the X-brace at all scan points. The rotation of the ACUT probe about its axis could be specified by the user. In this case, the rotation was 0° such that the transmitter would be above the receiver just like in Figure 214b. The program from the simulation was successfully executed on the R-j3iB controller. The video of the scan is shown in Figure 219. The robot was programmed to move at a linear speed of ~ 250 mm/s. The increments between the zig-zags were 2.3 mm (see Figure 220a).

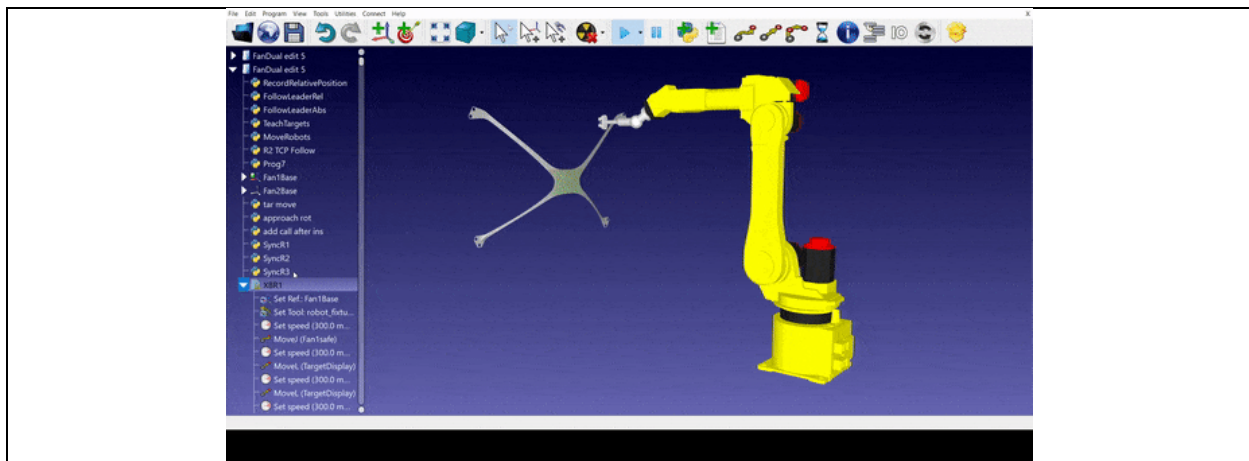


Figure 218. RoboDK simulation showing horizontal zig-zag scan of central part of X-brace #3.

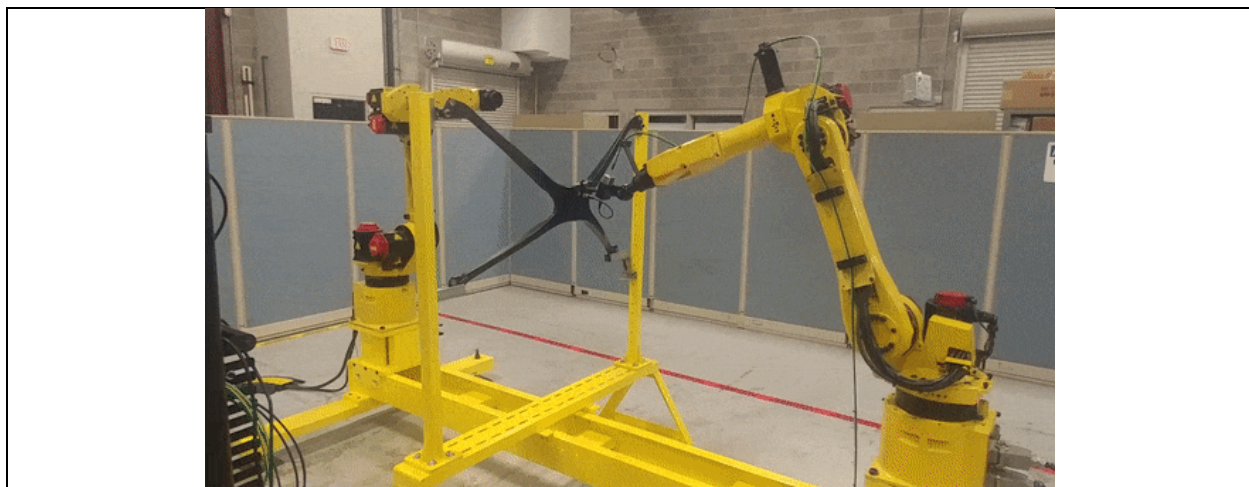


Figure 219. Validation of robotic SSA-ACUT on X-brace #3 (horizontal zig-zag pattern, 1 channel).

The acquired 3D point cloud is presented in Figure 220b. The results shown in Figure 220b correspond to the raw NDE data without post-processing. Three defects were successfully identified, which agreed well with the results of immersion UT inspection carried out in Phase I.

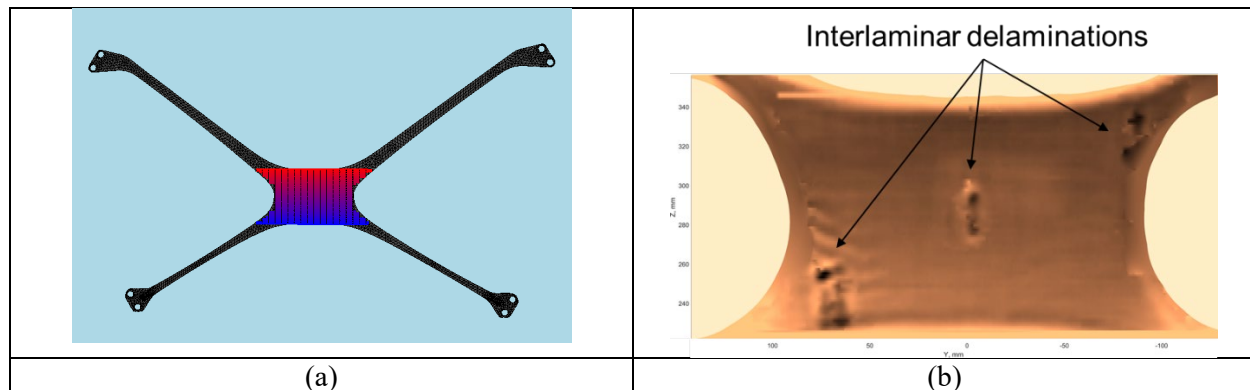


Figure 220. Robotic SSA-ACUT inspection of X-brace #3: (a) horizontal zig-zag scan pattern (motion from red to blue); (b) corresponding 3D image of X-brace #3 (1 channel).

Slanted zig-zag

The MSU team programmed Fanuc robot to perform a slanted zig-zag as shown in the RoboDK simulation in Figure 221. The rotation of the SSA-ACUT with respect its central axis was kept at 0° . The scan path covered the region with three defects in X-brace #3, which was identified earlier. The video of the scan is shown in Figure 222. The robot was programmed to move at a linear speed of ~ 250 mm/s. The increments between the zig-zags were 2.3 mm (see Figure 223a).

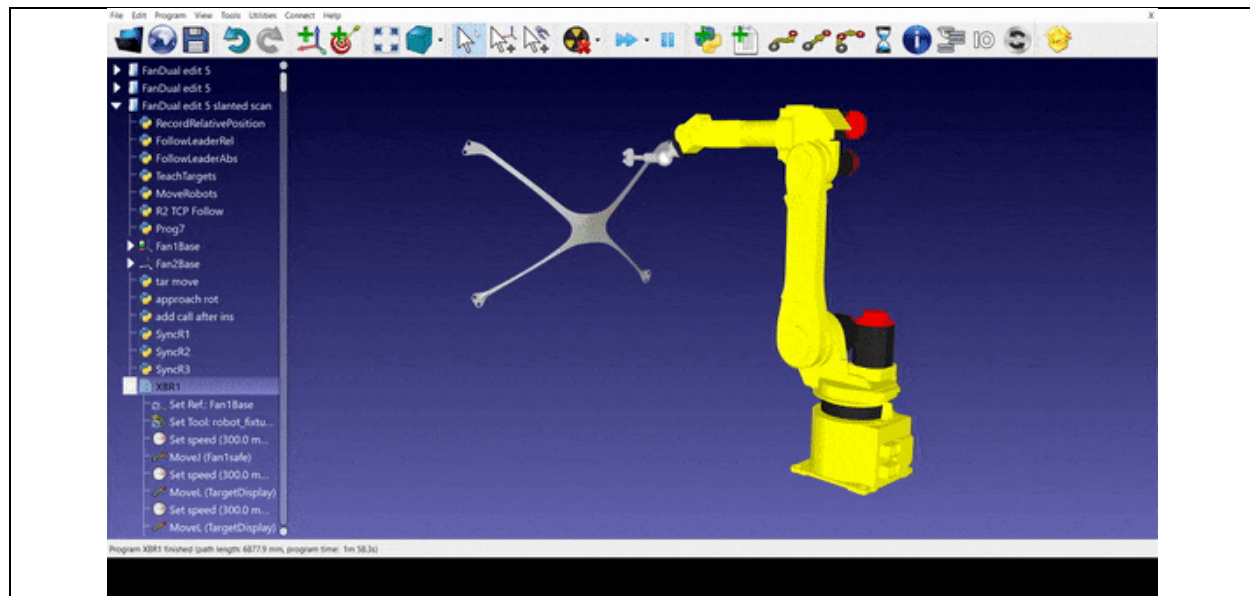


Figure 221. RoboDK simulation showing slanted zig-zag scan of central part of X-brace #3.

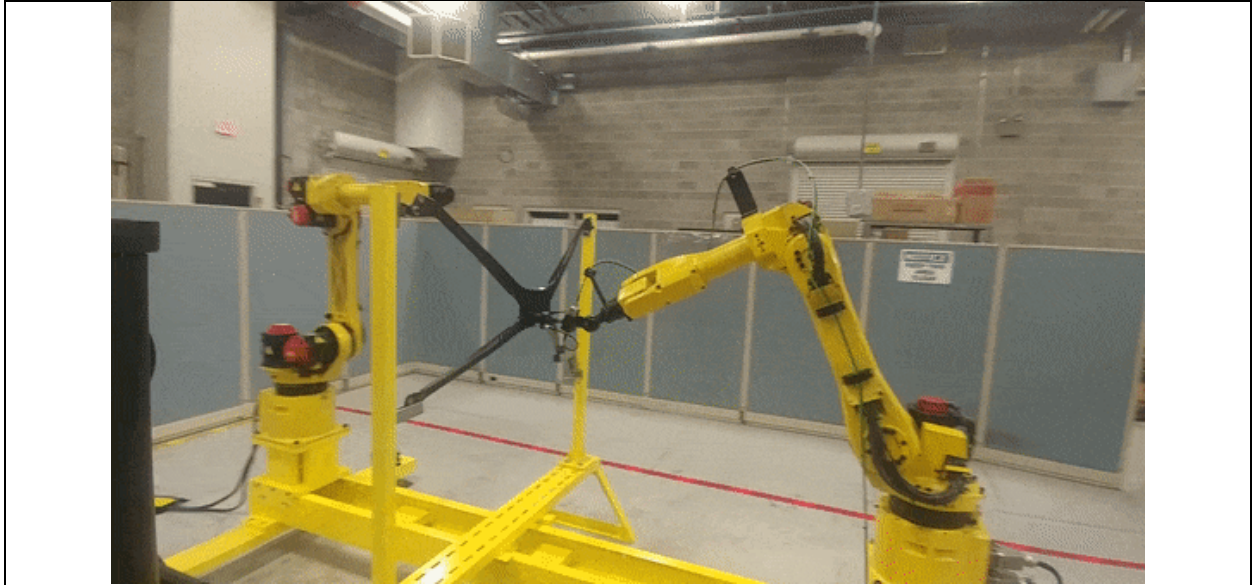


Figure 222. Validation of robotic SSA-ACUT on X-brace #3 (slanted zig-zag pattern, 1 channel).

The acquired 3D image of the X-brace #3 is presented in Figure 222. The image represents a point cloud without post-processing. In addition to three defects identified previously, there was the fourth indication of a defect in the upper right corner of the image. This fourth indication needs to be validated by running a larger SSA-ACUT scan and/or by taking a phased array UT image.

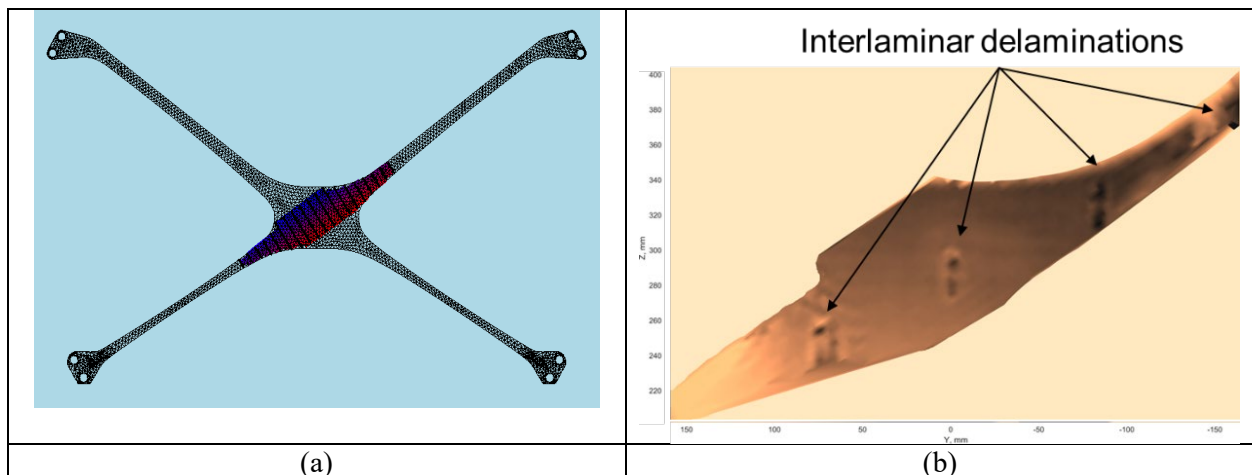


Figure 223. Robotic SSA-ACUT inspection of X-brace #3: (a) slanted zig-zag scan pattern (motion from red to blue); (b) corresponding 3D image of X-brace #3 (1 channel).

Robotic SSA-ACUT inspection of CFRP X-brace #3 (3 channel)

The MSU team developed a 3-channel SSA-ACUT probe for high-speed NDE of FRP composites. The design of the probe is shown in Figure 224. The probe had one transmitter (T1) for exciting UT waves and three independent receivers (R1, R2 and R3) for signal pick up. Such a design provides a wider coverage compared to a 1-channel probe and provides shorter inspection times. Three preamplifiers were installed close to the ACUT receivers. The zig-zag scan pattern and the probe's orientation w.r.t. its axis were optimized so as to provide the best inspection results.

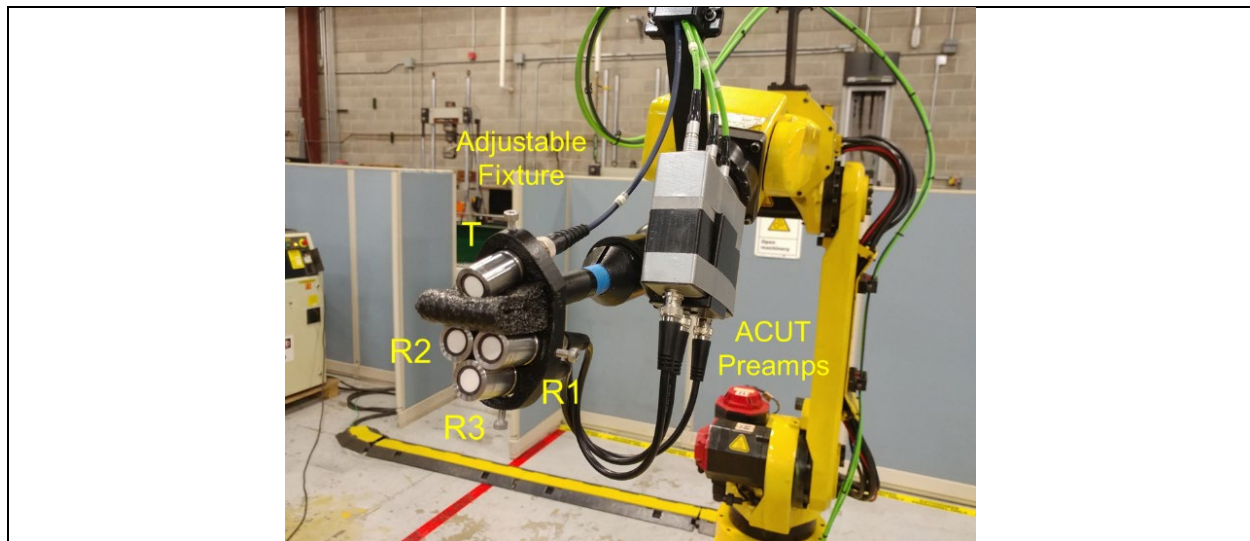


Figure 224. SSA-ACUT probe with 1 transmitter and 3 receivers for high-speed NDE.

A typical 3D image of the X-brace #3 acquired using a multi-channel SSA-ACUT probe is presented in Figure 225. Three point-clouds corresponding to three receivers were merged together. All defects were successfully detected, which validated the NDE technique.

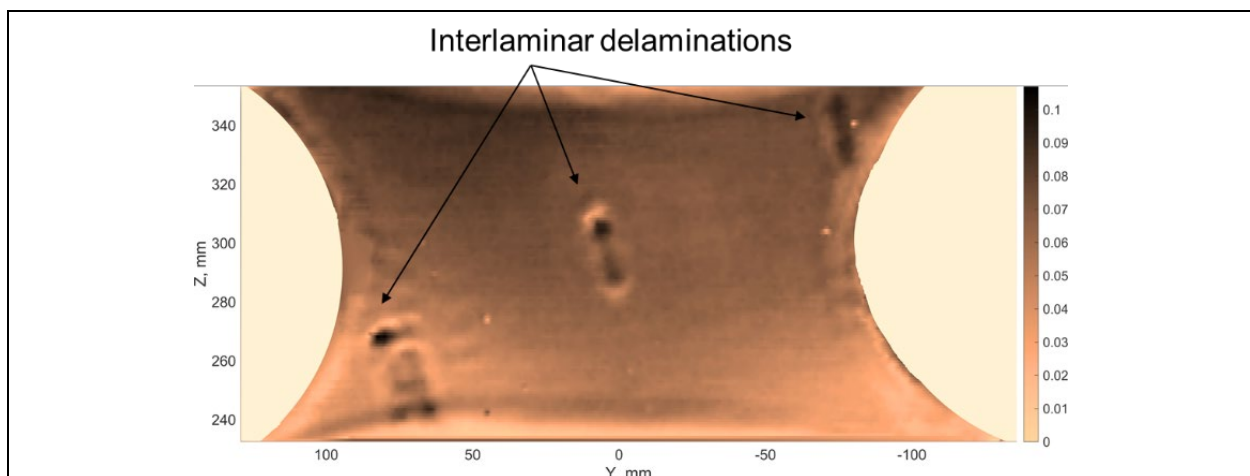


Figure 225. Robotic SSA-ACUT inspection of X-brace #3: 3D image of X-brace #3 (3 channels).

5. CONCLUSIONS AND RECOMMENDATIONS FOR FUTURE WORK

The development and optimization of ACUT and EM sensing techniques for high-speed NDE of CFRP parts are important outcomes of Project 3.13. Array probes for the TT-ACUT and SSA-ACUT were optimized to have small crosstalk and were demonstrated to successfully detect interlaminar delaminations and other flaws in CFRP test samples. Similarly, EM techniques including ECT, CI, and Dual Mode Imaging were shown to detect fiber and matrix imperfections. EM sensor arrays were designed to operate at frequencies optimized for NDE of CFRP. Integration of the developed sensor technologies with the robotic platform enabled the inspection of curved parts. ACUT and EM NDE could be performed rapidly by implementing parallel data acquisition.

Future work for ACUT NDE includes more extensive validation and optimization of TT-ACUT using synced robots since in this project the core software of only one robot controller was updated. MSU is planning to purchase and install the new version of core software on the second controller and debug dual-robot motion scripts. ACUT data acquisition is going to be optimized in order to facilitate the TT-ACUT inspection at linear speeds higher than 250 mm/s.

The next steps in the development of the EM techniques are: 1) design and acquisition of the ECA cable that would support up to 64 coil and/or capacitive sensors instead of current 18 in order to use the full capability of the Ectane 2 instrument with MUX; 2) place the Ectane 2 on Joint #3 of one of the robots such that flex EM probes could be validated on the robotic platform; 3) obtain the SDK for Ectane 2 and merge EM data acquisition scripts with main MSU software for robot control and ACUT. AN update and debugging of the scripts for 3D data visualization and image processing are also needed to enhance robotic NDE.

Finally, ACUT and EM NDE need to be validated on a larger number of CFRP parts manufactured using different technologies. A rationale for the types of defects of concern in automotive CFRP composite parts needs to be correlated to a structural integrity metric.

6. COMMERCIALIZATION PLAN

The IAMCI Project 3.13 is an important step towards positioning the automotive industry (and others including compressed gas, wind, medium and heavy-duty truck manufacturing, ATV, boating, etc.) for future lightweighting success with composites, which includes:

- i. ACUT and EM inspection techniques that have been demonstrated to detect an array of flaws in structural composites for high volume and high speed production;
- ii. array sensors and hardware that are robust and reliable to enable continuous operation in an automotive manufacturing environment;
- iii. proof of concept validation through development of a robotic platform for multi-technique and high-speed NDE compatible with 1-3 min production takt times.

The developed ACUT and EM technology for high-speed NDE of CFRP parts/components can be launched into the U.S. marketplace. The proof-of-concept robotic NDE system from Project 3.13 can be scaled by OEM and Tier 1 suppliers to a production ready NDE system for commercial manufacturing use. This will allow suppliers of such equipment to offer custom and off-the-shelf NDE solutions to molders of composites for multiple industries. The results of the project will be disseminated to all IACMI members

and members of the U.S. automotive supply chain through IACMI member meetings, technical presentations, and publications for use with composite materials.

7. ACADEMIC IMPACT

Project 3.13 resulted in an important workforce training/development for MSU/CVRC. Two graduate students and one undergraduate student were extensively trained in manufacturing of CFRP composites, NDE of composite structures, sensor development, FE modeling, signal processing, and robotics. Results from the project are going to be included in the respective PhD dissertations. The results of the project also include two journal manuscripts in preparation and an invention disclosure titled “Hybrid inductive/capacitive sensor arrays for rapid NDE of fiber reinforced polymer composites”.

8. REFERENCES

[1] Final Technical Report PA-16-0349-3.8-01, “Development of Tools for High Volume, High Speed Non-Destructive Inspection of Carbon Fiber Reinforced Plastics”, prepared by Institute for Advanced Composites Manufacturing Innovation (IACMI) for the U.S. Department of Energy, 2017.